Nanoparticles for Targeting Cancer Tissue: Detection and Imaging

By

Luke Simon Watson

A Thesis submitted to

The University of Birmingham

For the degree of

DOCTOR OF PHILOSOPHY

School of Chemistry
College of Engineering and Physical Sciences
University of Birmingham
November 2022

UNIVERSITY OF BIRMINGHAM

University of Birmingham Research Archive

e-theses repository

This unpublished thesis/dissertation is copyright of the author and/or third parties. The intellectual property rights of the author or third parties in respect of this work are as defined by The Copyright Designs and Patents Act 1988 or as modified by any successor legislation.

Any use made of information contained in this thesis/dissertation must be in accordance with that legislation and must be properly acknowledged. Further distribution or reproduction in any format is prohibited without the permission of the copyright holder.

Abstract

Gold nanoparticles have been widely used for a plethora of applications including bio-imaging agents through reflectance based microscopy, conjugation of luminescent metal complexes and specific targeting through the conjugation of proteins, antibodies and small molecules. Luminescent metal coated gold nanoparticles offers many advantages including dual emission through the triplet metal-to-ligand charge transfer (^{3}MLCT) and by reflectance of the gold, reduced toxicity and issues concerning cellular uptake. Three ruthenium(II) complexes were evaluated for their photophysical properties in aerated water, in the presence of a fluorosurfactant and decorated on 13 nm gold nanoparticles. The selection of the ruthenium(II) decorated gold nanoparticle system expressing the greatest photophysical properties was explored for its ability as a live cell imaging probe. It was found that the phenanthroline ruthenium(II) complex displayed longer luminescence lifetimes and higher quantum yields in agreement with previous studies. Live cell imaging in A549 cells were performed revealing localisation in the cytoplasm and perinuclear compartments. Additionally, a novel osmium(II) complex based on its previously made bipyridine counterpart for the attachment onto gold nanoparticles was synthesised for live cell imaging. Upon binding to the gold nanoparticles, luminescence of the osmium(II) complex was detected yielding, to our knowledge, the first example of a luminescent osmium(II) decorated gold nanoparticle. Upon confirmation of the phenanthroline ruthenium nanoprobes ability to image live cells, 13 nm gold nanoparticles were conjugated directly to the CD20 monoclonal antibody, Rituximab, for specific targeting of B-cell malignant cells. Three cell lines (Jurkat – T-lymphocyte, Raji – B-cell Burkitt lymphoma, and Karpas 422 – B-cell Non-Hodgkin lymphoma) were evaluated with the Rituximab and ruthenium(II) functionalised gold nanoparticles to determine preference towards the overexpressed B-cell receptor of interest, CD20. Flow cytometry analysis confirmed preference

towards B-cell lines overexpressing CD20 with Rituximab gold nanoparticles however the difference in intensity could not be statistically analysed based on one biological repeat. Confocal microscopy imaging of these particles on tonsil tissue revealed stronger intensities in fluorescence with the particles containing Rituximab than those without. Further proof of specific targeting of the ruthenium(II) and Rituximab nanoprobe was ascertained from mass spectrometry imaging yielding a higher ion intensity map in both the central and outer-part of the tissue sections. These results demonstrate the application of this nanosystem as a dual imaging nanoprobe for bio-imaging and mass spectrometry imaging.

Acknowledgements

Thank you for reading my thesis and I hope Ru enjoy it! ;)

I would like to dedicate this thesis to my late father, Anthony Leo Watson who passed away in the beginning of my journey of my PhD.

Firstly, I would like to thank my supervisors, Professor Zoe Pikramenou and my second supervisor Professor Michael Hannon for their continued guidance, suggestions, support and input into my PhD. I am very grateful to both especially when I had hit brick walls. I'd also like to thank Professor Paul Murray for his input in the antibody work.

I would also like to thank the support of my past and present group members: Andrew Carrod, Sunil Claire, Zhilin Guo, Jamie Bradley, Sajni Haria, Menisha Manhota, Sarah Akponasa, Elena Del Giorgio, Patricia Girio, Asier Rodriguez Muguruza, Maria Odyniec, Irene Theofilou, Joe Hughes and Grace Ball for their continued support, advice, guidance and laughs for when I was feeling down. A special thanks to Andrew for helping me get started on the synthesis and training and Sunil for the endless advice on gold nanoparticles and antibodies. I'd also like to thank those in the Hannon group for their input during group presentations especially Hugo Williams and James Craig. Additionally, I would like to thank past and present members of Professor John Fossey group, Alex Quy, Dr Fernanda Meloni, Harry Bird and Dr George Williams for making the office a happy place and their input in synthesis.

I'd like to thank members of the Murray group, Eva Lles, Dr Tracey Perry, Matthew Pugh and Ciara Leahy for training me in cell culture, flow cytometry, tonsil tissue sectioning, staining and analysis. I'd also like to thank Dr Garrett Rochford for running my MTT assays when the timing was terrible.

I would like to thank and acknowledge the RSC and the School of chemistry, University of Birmingham for financial support throughout my PhD and for expenses on conferences.

I would like to thank the analytical facility, Dr Cecile Duff, Dr Chi Tsang, Dr Christopher Williams, Miss Bridget Tang and Dr Louise Male for their continued encouragement, support and help throughout my PhD in MS and NMR. I would also like to thank Dr Theresa Morris and Dr Ludwig Schneider for training me in TEM and running samples for me. From the University of Warwick, I would like to thank Dr Lijiang Song for running the ICP-MS samples in a very timely manner and Dr Alessandro Di Maio from BALM for training me on the confocal microscope. A big thank you to all the staff in the chemistry department namely Bernard Tudor, Iain Wilkinson, Ian Bodfish, Richard Petford, Katherine Webb and John Wilkie for their support in issues I have encountered during my studies. I would also like to thank the wellbeing team for constantly checking in with me when I was at my lowest.

I would like to thank all of my fellow PhD members for standing by me and encouraging me to push on. I would like to thank my housemates James Fowke, Akil Yunus, Isabel Hunt and Blanca Sandoval Bueno for taking care of me and making home life enjoyable and fun. I would also like to thank my friends outside of university life, my snooker team and my family, Adi Saputra, Samuel White, Louis Miranda-Smedley, Robert Noakes, Leo Ashby, James Nunns, Boson Das, Dominic Mackey, George Corbin, Dr Daniel Jones, Dr Sam Parkinson, Daniel Watson, Fiona Watson, Charlotte Watson, Guy Chamberlain and Beth Gould. I would like to thank my grandad, Peter Orton for making me laugh and having the odd game of snooker and his partner Beth Allsopp for proof reading my thesis.

Finally, Putri Piesca Salsabila, thank you for everything. Without her, I wouldn’t have carried on.

Table of Contents

1.0 Introduction 1

1.1 Ruthenium(II) metal complexes for optical and mass spectrometry imaging 1

1.1.1 Mass spectrometry imaging using ruthenium 7

1.2 Osmium(II) polypyridyl complexes for cellular imaging and anticancer activity ... 10

1.3 Properties and uses of ruthenium(II) decorated gold nanoparticles in imaging and cancer applications 15

1.4 Gold nanoparticles in mass spectrometry imaging 19

1.5 Antibody labelled gold nanoparticles for anticancer and imaging applications 22

1.5.1 Ruthenium(II) and antibody labelled nanoparticles for imaging applications 28

1.5.2 Rituximab labelled gold nanoparticles for imaging applications 31

1.6 Thesis outline 34

1.7 References 36

2.0 General Methods 49

2.1 Materials 49

2.2 Synthesis techniques 49

2.3 Nanoparticle characterisation techniques 49

2.4 Photophysical characterisation techniques 50

2.5 Cell viability assays 50

2.6 Flow cytometry 51

2.7 Confocal microscopy and mass spectrometry imaging 51

3.0 Evaluation of Ruthenium Coated Gold Nanoparticles for Applications in Optical Microscopy and Mass Spectrometry Imaging 53

3.1 Introduction 53

3.2 Chapter outline 63

3.3 Results and Discussion 64

3.3.1 Evaluation of ruthenium(II) metal complexes 64

3.3.1.1 Synthesis 64

3.3.1.2 Photophysical characterisation of ruthenium(II) metal complexes 66

3.3.1.3 Influence of fluorosurfactant for improving photophysics of ruthenium(II) metal complexes 69

3.3.2 Coating of 13 nm gold nanoparticles with fluorosurfactant and metal complexes 72

3.3.2.1 Synthesis of 13 nm and 25 nm gold nanoparticles 72

3.3.2.2 Labelling of ruthenium(II) complexes on 13 nm gold nanoparticles 75

3.3.2.3 Evaluation and selection of ruthenium via luminescence studies on Z•AuNP13 79

3.3.3 Labelling and characterisation of RuPhenSS on 25 nm gold nanoparticles 81

3.3.4 Biological Studies of 13 nm and 25 nm RuPhenSS coated gold nanoparticles in A549 cells 84

3.3.5 Mass spectrometry of RuPhenSS coated 13 nm gold nanoparticles 88

3.4 Conclusion 90

3.5 Experimental 91

3.5.1 Materials 91

3.5.2 13 nm and 25 nm gold nanoparticle synthesis and coating 91

3.5.3 Ligand synthesis 93

3.5.4 Synthesis of ruthenium metal complexes 101

3.5.5 Cell culture 108

3.5.6 MTT assays 108

3.5.7 Confocal microscopy of live A549 cells 109

3.5.8 Mass spectrometry of RuPhenSS•AuNP13 110

3.6 References 111

4.0 Luminescent Osmium Gold Nanoparticles for Imaging in Cells 119

4.1 Introduction 119

4.2 Chapter outline 128

4.3 Results and Discussion 129

4.3.1 Synthesis and luminescence characterisation of OsPhenSS 129

4.3.1.1 Synthesis of OsPhenSS 129

4.3.1.2 Luminescence studies of OsPhenSS 131

4.3.1.3 Luminescence studies of OsPhenSS in the presence of Zonyl FSA 134

4.3.2 Coating of OsPhenSS on 13 nm and 25 nm gold nanoparticles 136

4.3.3 Biological studies of 13 nm and 25 nm gold nanoparticles 140

4.3.3.1 Cell viability assays of OsPhenSSAuNP in A549 cells 140

4.3.3.2 Luminescence imaging of 13 nm and 25 nm OsPhenSS•AuNP in live A549 cells 141

4.4 Conclusion 145

4.5 Experimental 146

4.5.1 Synthesis of BpySS 146

4.5.2 Synthesis of *Bis*-(1,10-phenanthroline)-Osmium dichloride 146

4.5.3 Synthesis of OsPhenSS 147

4.5.4 Synthesis of 13 nm and 25 nm c-AuNP 148

4.5.5 Coating of 13 nm and 25 nm OsPhenSS•AuNP13 148

4.5.6 Cell culture of A549 cells 150

4.5.7 MTT assays 150

4.5.8 Confocal microscopy 151

4.5.9 Transmission electron microscopy 151

4.5.10 Inductively coupled mass spectrometry 152

4.6 References 153

5.0 Luminescent Rituximab Labelled Gold Nanoparticles for Detection and Imaging ... 161

5.1 Introduction 161

5.1.1 Optical detection of gold nanoparticles for targeting tumour cells 163

5.1.2 Mass spectrometry imaging in cancer 167

5.2 Chapter Outline 170

5.3 Results and Discussion 171

5.3.1 Modification of Rituximab for attachment onto gold nanoparticles 171

5.3.2 Coating of Rituximab and RuPhenSS onto gold nanoparticles 173

5.3.2.1 Synthesis of gold nanoparticles 173

5.3.2.2 Attachment of Rituximab and RuPhenSS onto gold nanoparticles 175

5.3.2.3 Characterisation of gold nanoparticles in the absence and presence of Rituximab 181

5.3.2.4 Determining the presence of Rituximab on gold nanoparticles 182

5.3.3 Luminescent and biological studies of functionalised gold nanoparticles 184

5.3.3.1 Detection of ruthenium emission on RuPhenSS•PEG•AuNP and RuPhenSS•RXB•AuNP 184

5.3.3.2 Cell viability assays of Rituximab labelled gold nanoparticles 185

5.3.3.3 Flow cytometry of Rituximab labelled gold nanoparticles 186

5.3.4 Detection of functionalised gold nanoparticles in tonsil tissue 191

5.4 Conclusion 200

5.5 Experimental 201

5.5.1 Materials 201

5.5.2 Modification of Rituximab 201

5.5.3 Metal complex synthesis 202
5.5.4 Synthesis of AuNPs 202
5.5.5 Transmission electron microscopy 204
5.5.6 Check&Go strip test 205
5.5.7 Cell culture 205
5.5.8 Cell viability assay 205
5.5.9 Flow cytometry 206
5.5.10 Cytospins 206
5.5.11 Tonsil staining 207
5.5.12 Confocal microscopy 208
5.5.13 Mass Spectrometry Imaging 208
5.6 References 209
6.0 General conclusions and future Work 217
7.0 Appendix ..... - 1 -
7.1 Synthesis characterisation: NMR and MS ..... - 1 -
7.1.1 BpySS ligand ..... - 1 -
7.1.2 S8 ligand ..... - 14 -
7.1.3 $Ru(Bpy)_2Cl_2$ ..... - 27 -
7.1.4 $Ru(Phen)_2Cl_2$ ..... - 30 -
7.1.5 $Os(Phen)_2Cl_2$ ..... - 32 -
7.1.6 RuBpySS ..... - 34 -
7.1.7 RuPhenSS ..... - 40 -
7.1.8 RuS8 ..... - 45 -
7.1.9 OsPhenSS ..... - 49 -
7.2 IR spectrum of ruthenium complexes ..... - 56 -

7.3 Luminescence lifetimes of ruthenium complexes (χ^2 values between 1.0 – 1.2) - 57 -

7.3.1 RuBpySS (left), RuPhenSS (middle) and RuS8 (right) in aerated water .....- 57 -

7.3.2 RuBpySS (left), RuPhenSS (middle) and RuS8 (right) in the presence of Zonyl FSA in aerated water .....- 58 -

7.3.3 RuBpySS (left), RuPhenSS (middle) and RuS8 (right) on 13 nm gold nanoparticles in aerated water .....- 58 -

7.4 Hoescht 3368 staining of live A549 cells for RuPhenSS 13 nm and 25 nm gold nanoparticles .....- 59 -

7.5 Luminescence lifetimes of OsPhenSS (χ_2 values between 1.0 – 1.2) .....- 59 -

7.5.1 Luminescence lifetime of OsPhenSS in aerated water .....- 59 -

7.5.2 Luminescence lifetime of OsPhenSS in the presence of Zonyl in aerated water..... .....- 60 -

7.5.3 Luminescence lifetime of OsPhenSS on 13 nm gold nanoparticles in aerated water .....- 60 -

7.6 Z-stacks of RuPhenSS 25 nm gold nanoparticles in live A549 cells .....- 61 -

7.7 Z-stacks of OsPhenSS 25 nm gold nanoparticles in live A549 cells .....- 62 -

7.8 Fixed cell images of OsPhenSS 25 nm gold nanoparticles in A549 .....- 62 -

7.9 Confocal images of RuPhenSS•PEG•AuNP and RuPhenSS•RXB•AuNP on OCI-LY3 cytospins .....- 63 -

7.10 Images of H&E stained tonsil tissue .....- 63 -

7.11 Images of RuPhenSS•PEG•AuNP and RuPhenSS•RXB•AuNP after MSI.....- 64 -

7.12 Gold nanoparticle concentration calculation from UV-Vis .....- 64 -

7.13 Conferences and papers .....- 64 -

List of Abbreviations

ADCC – Antibody dependent cellular cytotoxicity

AuNP – Gold nanoparticle

Bpy – 2,2'-bipyridine

BSA – Bovine serum albumin

c-AuNP – Citrate capped gold nanoparticles

DAPI – 4′,6-diamidino-2-phenylindole

DCM – Dichloromethane

DESI – Desorption Electrospray Ionisation

DLS – Dynamic Light Scattering

DMF – Dimethylformamide

DMSO – Dimethyl sulfoxide

DNA – Deoxyribonucleic acid

Dppz – dipyrido[3,2-a:2′,3′-c]phenazine

ECL – Electrochemiluminescence

EDTA – Ethylene diaminetetraacetic acid

EGFR – Epidermal growth factor receptor

EPR – Enhanced permeability and retention

ESI – Electrospray Ionisation

FACS – Fluorescence activated cell sorter

FBS – Fetal bovine serum

H&E – Haematoxylin and eosin

HER2 – Human epidermal growth factor receptor 2

HMBC – Heteronuclear Multiple Bond Correlation

HSQC – Heteronuclear Single Quantum Coherence

ICG – Indocyanine green

ICP-AES – Inductively coupled plasma atomic emission spectroscopy

ICP-MS – Inductively coupled plasma mass spectrometry

IgG – Immunoglobulin G

IR – Infra red

ITO – Indium Tin Oxide

LC – Ligand centre

LC-MS – Liquid chromatography mass spectrometry

LDI-MS – Laser Desorption Ionisation Mass Spectrometry

MALDI – Matrix Assisted Laser Desorption Ionisation

MFI – Median fluorescence intensity

MLCT – Metal-to-Ligand Charge Transfer

MSI – Mass Spectrometry Imaging

MTG – Mitotracker green

MTT – 3-(4,5-dimethylthiazol-2-yl)-2,5-diphenyltetrazolium Bromide

MUC1 – Mucin 1

NHL – Non-Hodgkin lymphoma

NIR – Near-infra Red

NK – Natural killer

PBS – Phosphate buffer saline

PCP – Pentachlorophenol

PDI – Polydispersity index

PEG – Polyethylene glycol

RNA – Ribonucleic acid

RXB – Rituximab

SIMS – Secondary Ion Mass Spectrometry

SPR – Surface Plasmon Resonance

TEM – Transmission electron microscopy

THF – Tetrahydrofuran

ToF – Time of flight

UV-Vis – Ultra-Violet Visible

Z·AuNP – Zonyl Coated Gold Nanoparticles

χ – Lifetime fit

τ – Lifetimes

Φ – Quantum yield

1.0 Introduction

1.1 Ruthenium(II) metal complexes for optical and mass spectrometry imaging

Ruthenium(II) metal complexes containing 2,2'-bipyridine and 1,10-phenanthroline ligands have attracted extensive research. These complexes have been shown to possess favourable properties such as intense luminescence in solution at room temperature in the visible spectrum, good singlet oxygen generation, high photostability, large Stokes shifts and long luminescent lifetimes into the nanosecond region.[1-3] Due to the favourable qualities possessed by ruthenium(II) complexes, they have been studied as bio-imaging agents, sensing agents, anticancer agents and photo-redox catalysts.[4-9] Ruthenium(II) complexes exhibit a broad absorption range in the blue region of the visible spectrum due to excitation of the singlet metal to ligand charge transfer (^{1}MLCT) band. When the ^{1}MLCT is excited, this gives rise to the unstable ^{3}MLCT band typically seen in the red region. Due to the large Stokes shift (difference between excitation wavelength and emission wavelength) this provides no emitting light to be reabsorbed making the process efficient. Since ^{3}MLCT is a spin forbidden state, the relaxation back to the ground state typically provides long luminescent lifetimes to occur as long as no underlying energy states impede the efficiency of the ^{3}MLCT state. A plethora of ruthenium(II) bis(2,2'-bipyridine) and ruthenium(II) bis(1,10'-phenanthroline) complexes have been studied owing to their spectroscopic and electrochemical properties. The most widely used and researched ruthenium(II) complexes are $[Ru(bpy)_3]^{2+}$ and $[Ru(phen)_3]^{2+}$.[10-12] Phenanthroline based ruthenium complexes display greater photophysics, longer luminescence lifetimes and higher molar extinction coefficients whilst minorly blue shifting the ^{1}MLCT and ^{3}MLCT bands.[13] $[Ru(bpy)_3]Cl_2$ displays a ^{3}MLCT emission in aerated water at 628 nm with a strong extinction coefficient at 452 nm (ε = 14000 $M^{-1}cm^{-1}$) whereas $[Ru(phen)_3]Cl_2$ displays a ^{3}MLCT

profile at 604 nm with an enhanced extinction coefficient at 447 nm (ε = 18100 $M^{-1}cm^{-1}$) in comparison.[12]

Intracellular imaging of transition metal complexes requires the ability to permeate the cell efficiently. Typically, most dicationic ruthenium complexes do not tend to passively diffuse across the cell membrane and therefore need the addition of a lipophilic modification in order to permeate the cell.[14,15] Specifically targeting cellular compartments is of great interest for imaging to visualise localisation of the lumophores in a biological setting. Ruthenium(II) as well as other transition metal complexes offers no direct targeting moieties to enter specific compartments within a cell and therefore require other moieties to direct them. Initially, targeting of cellular compartments requires transport agents to direct ruthenium(II) metal complexes into the cellular compartments such as the cytoplasm, mitochondria and nucleus.[16] Mitochondria targeting has become of great interest for imaging and anticancer applications. Being able to selectively target mitochondria and disrupt the electron transport chain in cancer cells is highly advantageous to induce apoptosis.[17,18] The incorporation of triphenylphosphine substituents has been used for the targeting of mitochondria.[17] Alternatively, the employment of bioactive molecules including proteins, carbohydrates and peptides has been used in conjunction with metal complexes for specific targeting of cellular compartments. Additionally, protein targeting can be achieved through indole derivatives.[19]

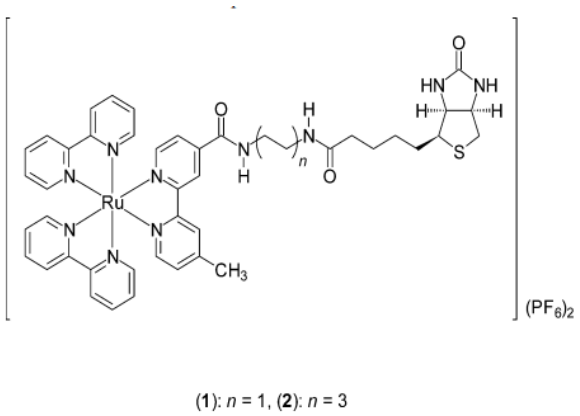

Figure 1.1.1. Chemical structures of biotin conjugated ruthenium complexes. Figure taken from Lo *et al.*[20]

Modification of biotin on biomolecules has been shown to have very little effect on the biological activity and functionality. Therefore two ruthenium(II) bipyridine complexes containing a biotin targeting moiety have been characterised for the targeting of avidin using numerous assays whilst being considered to be non-invasive imaging probes (Figure 1.1.1).[20] These complexes display intense emission in aerated methanol at ~630 nm whilst displaying lifetimes on the microsecond scale.[20]

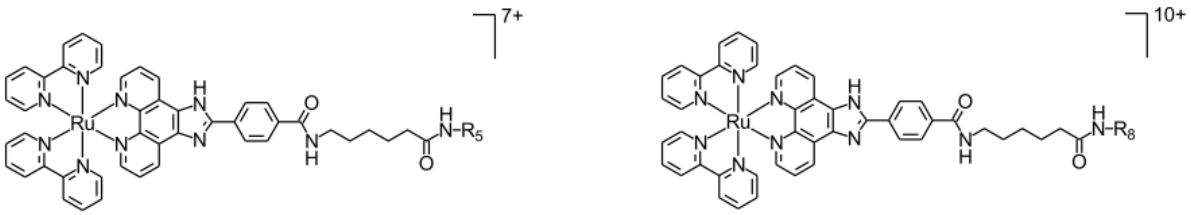

Figure 1.1.2. Chemical structures of ruthenium(II) pentaarginine (left) and ruthenium(II) octaarginine (right) complexes. Figure taken from Neugebauer *et al.*[21]

The first example of ruthenium(II) complexes appended to a peptide conjugate for cell permeation was implemented in 2008. Studies involving polyarginine conjugated to ruthenium(II) complexes have been shown to transport efficiently and rapidly across the cell

membrane into the cytoplasm (Figure 1.1.2).[22,23] Ruthenium(II) penta-arginine and octa-arginine complexes exhibited long, intense and oxygen sensitive emission and were readily transported across the cellular membrane into the cytoplasm in comparison to their parent complex, $[Ru(bpy)_2(picH_2)]^{2+}$.[21]

Previously, nuclear localisation of ruthenium complexes within cells was rarely reported due to low nuclear uptake.[24,25] A nuclear localisation signal (NLS) peptide derived from the transcription factor NF-kB was appended to two ruthenium(II) complexes, $[Ru(dpp)_2PIC]ClO_4$ and $[Ru(bpy)_2PIC]ClO_4$, where PIC is 2-(4-carboxyphenyl)-imidazo-[4,5-f][1,10]-phenanthroline, dpp is 4,7-diphenyl-1,10-phenanthroline and bpy is 2,2'-bipyridine, via a β-alanine bridge (Figure 1.1.3).

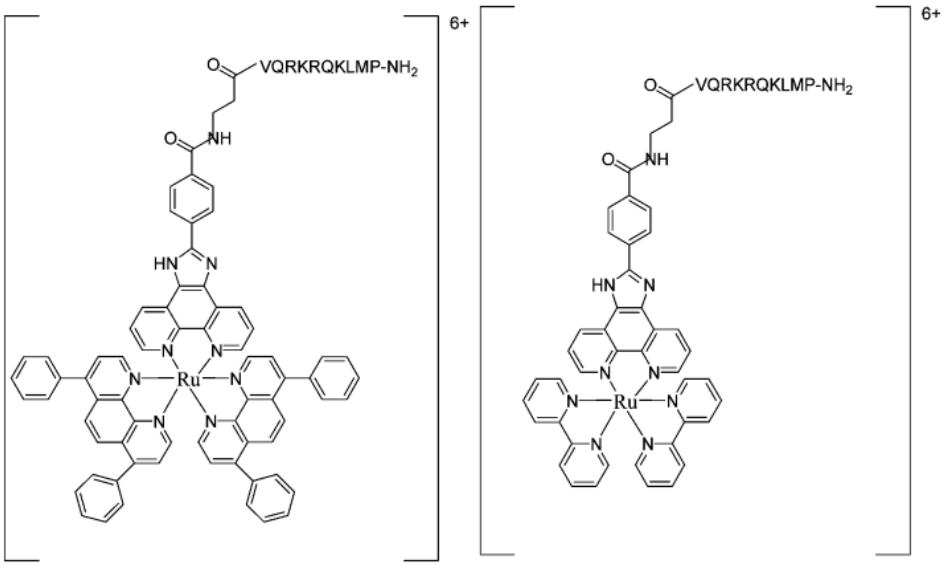

Figure 1.1.3. Chemical structures of $[Ru(dpp)_2PIC\text{-}bAla\text{-}NF\text{-}kB]^{6+}$ and $[Ru(bpy)_2PIC\text{-}bAla\text{-}NF\text{-}kB]^{6+}$. Figure taken from Blackmore *et al.*[16]

NF-kB has been previously reported to be a transmembrane molecular cargo carrier and the NLS peptide used was VQRKRQKLMP–NH_2.[26,27] Through this, it was found that the more hydrophilic ruthenium(II) bipyridine complex was directed into the nucleus whilst the more

lipophilic ruthenium(II) 4,7-diphenyl-1,10-phenanthroline complex was found to concentrate in the nucleolus in live CHO cells. This was co-localised through the use of a known nuclear organic dye, DAPI. On the other hand, nuclear localisation can be achieved through the incorporation of planar ligands (e.g. dipyridophenazine, dppz) that can bind to DNA grooves under physiological conditions.[3,28] Ruthenium(II) dppz metal complexes are known as molecular 'lightswitches' for DNA. Although the properties of these complexes can serve into therapeutic and diagnostic applications, the cellular uptake is generally very poor and restricts them for the use in live cells. However, recent studies have shown that ion pairing can play a key role in cellular uptake.[29] Alternatively, dinuclear ruthenium(II) complexes have been shown to stain the DNA of eukaryotic and prokaryotic cells for luminescence confocal microscopy and transmission electron microscopy (Figure 1.1.4).[30]

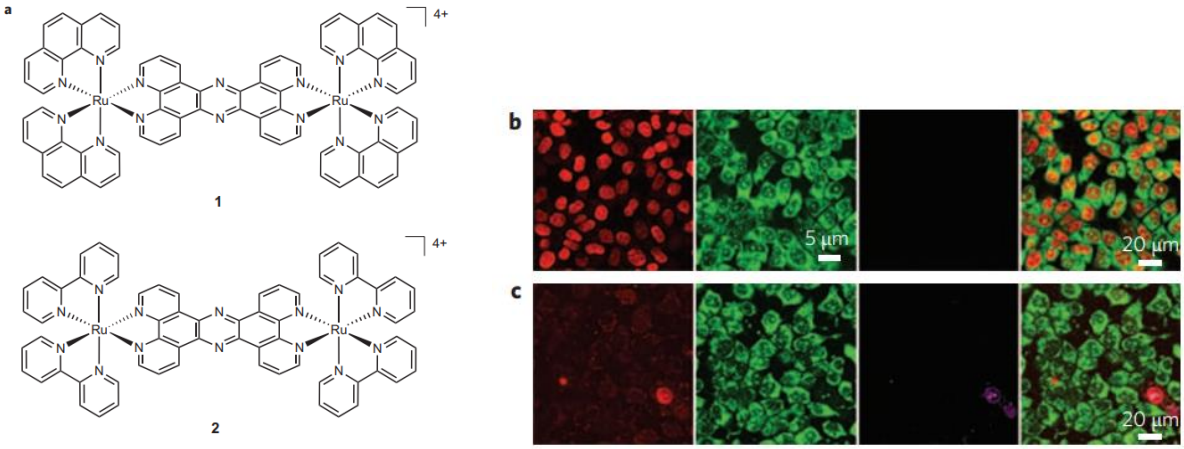

Figure 1.1.4. Chemical structures of dinuclear ruthenium complexes (a) and confocal luminescence in MCF-7 cells of complex 1 (500 mM, 1 h) (red) SYTO 9 (green), propidium iodide (purple) and overlay (b) and complex 2 (500 mM, 1 h) (c). Figure taken from Gill *et al.*[30]

Both complexes are non-emissive in water upon irradiation at 458 nm but display an intense luminescence signal when bound to DNA. These two complexes were incubated in MCF-7 cells

and imaged via confocal microscopy and was seen that upon irradiation at 458 nm, emission between 670 – 700 nm corresponding to the ^{3}MLCT band was observed.[30]

Alternatively to dppz, anthraquinone is a viable substitute for binding to DNA structures and for sensing applications.[31,32] Despite quinones having been shown to be excellent electron acceptors and efficient quenchers of numerous lumophores, conversion of quinones into hydroquinones through formation in protic media do not quench luminescence of nearby lumophores.[33] Combination of a luminescent ruthenium(II) complex with the redox-active and hypoxia sensing quinone group was utilised for two photon imaging for the cycling of hypoxia in A549 cells (Figure 1.1.5).

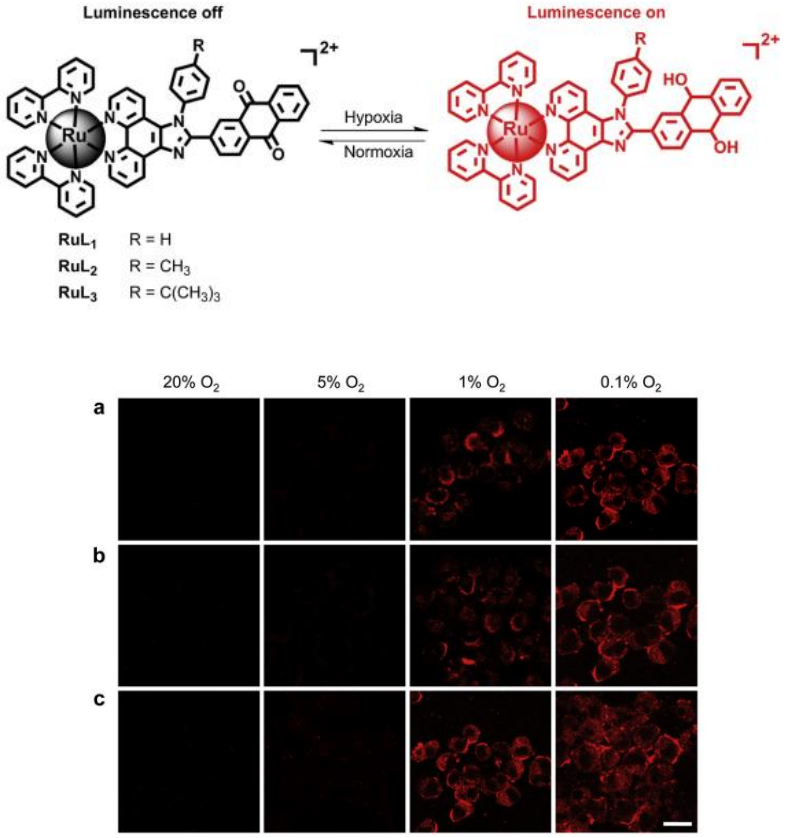

Figure 1.1.5. Schematic illustration of the ruthenium(II) anthraquinone complexes for cycling hypoxia imaging (top) and two-photon luminescence confocal microscopy images of A549 cancer cells incubated (a-RuL1; b-RuL2; c-RuL3) at various oxygen concentrations for 1 h. (bottom). The excitation and emission wavelengths were 800 nm and 560-680 nm, respectively. Scale bar: 30 µm. Figure taken from Zhang *et al*.[34]

It was found that the reduction of the quinone moiety on the ruthenium(II) complexes to hydro-anthraquinone by reductases under hypoxic conditions gave rise to two photon luminescence and was able to obtain image hypoxia via luminescent images in live cells and in vivo.

1.1.1 Mass spectrometry imaging using ruthenium

Ruthenium(II) complexes have been widely used in bio-imaging applications but rarely investigated for its use as a mass spectrometry imaging (MSI) agent. In matrix absorption laser desorption ionisation (MALDI) a matrix is required to prevent degradation of the analyte of interest and to preserve tissue morphology from the high laser power.[35,36] However, limitations in the exploration of transition metals as MSI agents are due to signal suppression arising from the interference of the matrix and/or biomolecules in the sample.[37] With this in mind, other limitations arising from MALDI are presented in matrix preparation, for example non-homogenous deposition and reproducibility.[38,39] Therefore, choosing a matrix and the deposition of the matrix for transition metal complexes in MSI is paramount. Typically, staining of biological tissue consists of haematoxylin and eosin (H&E) staining for viewing tissue morphology. This is required due to tissue samples being virtually non-fluorescent.[40,41] However, transition metal complexes have been used in substitution of H&E staining, namely osmium tetroxide and ruthenium tetroxide. An example of ruthenium tetroxide has been utilised as a counterstain in mass spectrometry imaging revealing tissue morphology and imaging (Figure 1.1.1.1).[42] By counterstaining with ruthenium tetroxide, not only it allows the visualisation of tissue morphology but it can also bind to tissue components.[43]

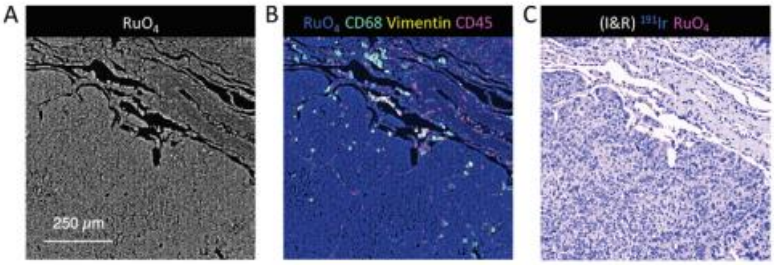

Figure 1.1.1.1. Mass cytometry imaging of formalin fixed paraffin embedded lung cancer tissue stained with ruthenium tetroxide. All ruthenium isotopes (a) ruthenium counterstain for other antigens (b) and iridium and ruthenium counterstain mimicking H&E staining (c). Figure taken from Catena *et al*.[42]

It was found that staining with ruthenium tetroxide portrayed a homogenous stain throughout the tissue than the standard conventional methods employed with H&E and other anionic dyes explored in this study.[42] Additionally, it was found that the ruthenium tetroxide counterstain did not interfere with metal labelled antibodies and the analytes of interest did not suffer from ion suppression. Traditionally, ruthenium tetroxide has been utilised in electron microscopy to visualise organic molecules such as fatty acids. An advantage for ruthenium tetroxide in mass spectrometry imaging is that it can aid in preserving tissue morphology via forming crosslinking with lipid bilayers.[42] Additionally, ruthenium tetroxide does not affect alternate staining including antibody staining thereby being able to maintain antibody signals.[42,44] Alternatively to ruthenium tetroxide, photocleavable ruthenium(II) complexes have been employed in MSI as mass tags for the imaging of αβV3 integrin through the use of laser desorption ionisation mass spectrometry (LDI-MS) in human cancer tissue (Figure 1.1.1.2).[45] Overcoming issues arising from sample preparation, namely matrix choice, deposition and embedding of tissue samples using formalin fixed paraffin embedding can be achieved through the use of mass barcodes. These barcodes are unique to the system employed and allow distinguishable fingerprints from background and molecular ions in the sample. Such mass tags are typically low in weight and have a high ionising ability. Therefore, designing ruthenium(II)

photocleavable complexes that can bind to a directed target of interest within the tissue that, upon irradiation, cleaves a mass tag for detection is advantageous.[46,47] Three ruthenium complexes (**1**, $[Ru(terpy)(bpy)Cl]^{+}$, **2**, $[Ru(terpy)(bpy)(D\text{-}biotin)]^{2+}$ and **3**, $[Ru(terpy)(bpy)(D\text{-}biotin)(cyc(RGDfK))]^{2+}$) were incubated on hypopharynx tumour tissue and imaged through LDI-MS.

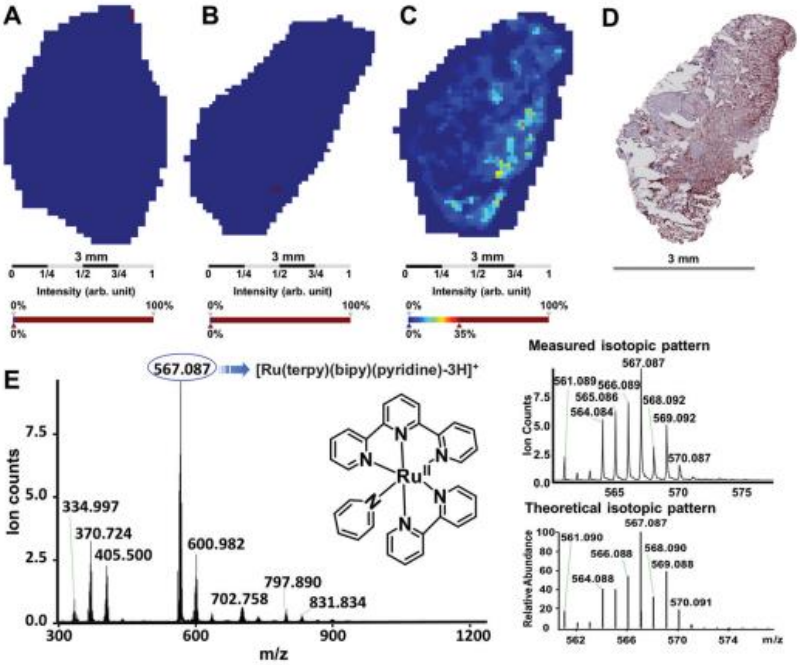

Figure 1.1.1.2. LDI-MSI images of mass tag from hypopharynx tumor tissue sections incubated with PBS (a), complex 2 (b) and complex 3 (c). Haematoxylin and immunohistochemistry stained section of a hypopharyngeal squamous cell carcinoma section (d). LDI mass spectrum of the mass-tag signal related to complex 3 comparing experimental and theoretical isotope pattern (e). Figure taken from Han *et al.*[45]

Images of tissue sections incubated with PBS, complex 2 and complex 3 in the absence of a matrix were evaluated and compared against H&E to identify localisation. Complex 2 displayed unspecific binding towards αβV3 integrin and little detection of ruthenium was present. This is attributed to the lack of binding and being washed off in the sample preparation stage. It was found the complex 3 displayed higher intensities over complex 2 (Figure 1.1.1.2b and Figure 1.1.1.2c) whilst the PBS treated section displayed no ruthenium mass tag. From the H&E

staining, it was found that the distribution of complex 3 to αβV3 integrin correlated well with the imaging studies. Through the use of a matrix free strategy, complex 3 displayed the uniquely identifiable isotope pattern allowing differentiation between the mass tag and background signals. The experimental peaks were compared against the theoretical patterns (Figure 1.1.1.2e) ascertaining the proof of ruthenium(II) complexes being viable in MSI.

1.2 Osmium(II) polypyridyl complexes for cellular imaging and anticancer activity

Over recent years, there have been many examples of luminescent transition metal complexes namely rhenium(I), iridium(III) and ruthenium(II), but very few in the way of osmium(II) complexes for cellular imaging applications.[48-51] Osmium(II) complexes and other transition metal complexes can tune their photophysical and electrochemical properties through substitution of their ligands.[52] Additionally, ruthenium(II) and osmium(II) metal complexes are highly inert towards ligand substitution thereby making them highly desirable in the bioimaging field.[53] Typically osmium(II) complexes display very poor photophysical properties such as short luminescence lifetimes and low quantum yields. However, they do possess some advantageous properties such as near-infrared (NIR) emission, exceptional photostability, increased tissue penetration due to long excitation wavelengths, decreased background absorption and long MLCT absorption for biological imaging applications in cells/tissues.[50,52,54-59] Additionally, osmium(II) complexes contains a high-spin orbit coupling constant that allows irradiation upon the spin forbidden direct transition from ground to ^{3}MLCT excited state. This spin forbidden absorption state is often seen with appreciable intensity in the visible spectrum between 500 – 700 nm.[60,61] Just like ruthenium(II), osmium(II) bipyridine complexes have been researched and compared to the parent compound, $[Os(bpy)_3]^{2+}$. Osmium(II) complexes have mainly been investigated for their electrochemical properties due

to the numerous oxidation states they can possess. However, conjugation of planar ligands such as dppz have been implemented for DNA staining.

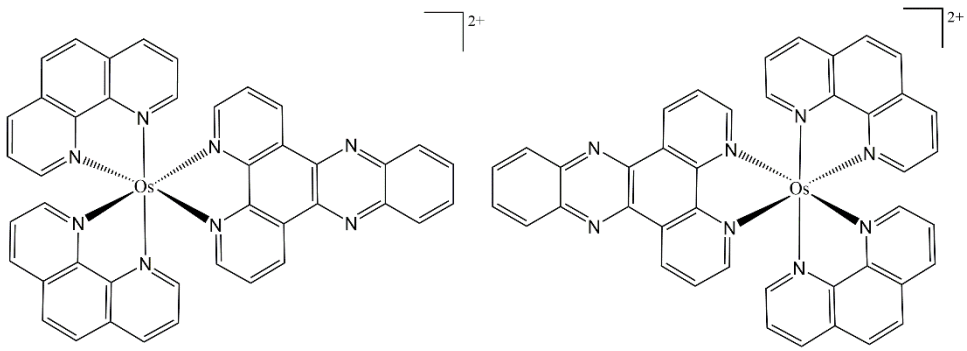

Figure 1.2.1. Chemical structures of the Λ and Δ enantiomers of osmium dppz respectively. Figure reconstructed from Huang *et al.*[8]

$[Os(phen)_2(dppz)]^{2+}$ and its two enantiomers (Λ and Δ) were synthesised for nuclear DNA imaging providing low cytotoxicity and emission deep in the visible spectrum around 750 nm (Figure 1.2.1). They were compared against the parent analogue $[Os(phen)_3]^{2+}$ as nuclear DNA imaging agents which were shown to be resistant to photobleaching in comparison to standardised organic nuclear dyes and to act as TEM contrast agents allowing for visualization of subnuclear structures. The cellular uptake and, more importantly, the nuclear uptake of these complexes were found to be enhanced through the formation of lipophilic ion pairs with chlorophenolic counteranions. It was reported that the Δ-enantiomer showed significantly higher emission in the nucleus than the Λ-enantiomer through analysis of ICP-MS due to a higher binding affinity to DNA despite similar uptake of both complexes.[9,58,62]

Alternatively to targeting DNA, RNA targeting has become of recent interest due to the lack of commercial dyes. Currently SYTO-RNA select can only stain RNA in fixed cells and its emission overlaps with auto-fluorescence. Two osmium(II) complexes with different

iminopyridine ligands were studied for cell imaging applications and their role in RNA binding (Figure 1.2.2).

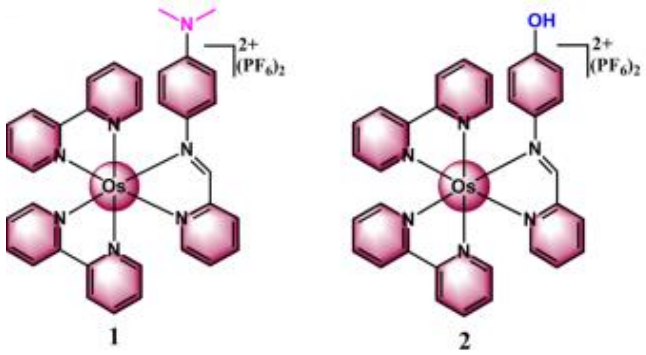

Figure 1.2.2. Chemical structures of osmium(II) complexes 1 and 2. Figure taken from Ge *et al*.[63]

These complexes were found to have dual emission peaks at 573 nm and 738 nm and exhibited preferential binding to RNA over DNA, which enabled imaging of the nucleoli and RNA in live cells. This is the first example of osmium complexes utilised for RNA-specific imaging and therefore provides a promising platform for the use of osmium complexes in cellular imaging applications. Recently, osmium pyridyltriazole complexes have been shown to be efficient imaging agents in live cells. Four osmium complexes with a variable 2,2'-bipyridine and 1-benzyl-4-(pyrid-2-yl)-1,2,3-triazole ligands as the chloride salts have been studied for the application in live cell imaging (Figure 1.2.3).[64] The emissions of these complexes range from the orange to deep red/ NIR spectrum circumventing auto-fluorescence through direct excitation into spin-forbidden direct to the ^{3}MLCT band.

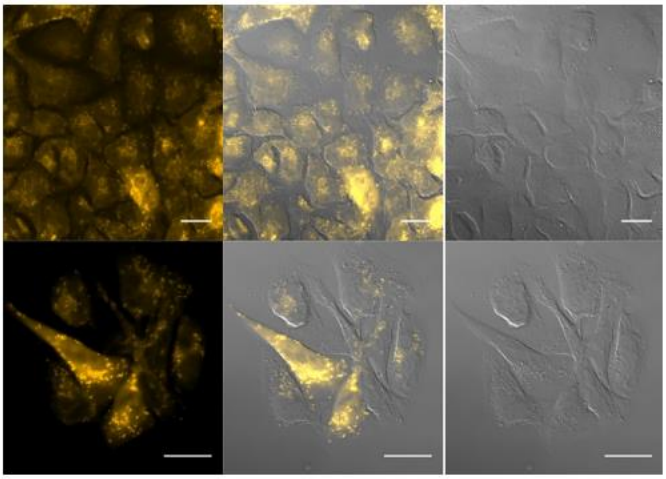

Figure 1.2.3. Confocal microscopy images of EJ bladder carcinoma cells incubated with $[Os(pytz)_3][PF_6]_2$ (20 µM, 6 h incubation, λ_{exc} = 543 nm, λ_{em} = 565−615 nm) (left), overlay of emission and brightfield (centre) and brightfield (right). Scale bars = 20 µm. Figure taken from Omar *et al*.[64]

Luminescence confocal microscopy revealed that the tris(triazole) osmium(II) complex was readily taken up by HeLa and EJ cell lines whilst localising in the lyosomal and endosomal regions with both low light and dark toxicities. Although osmium(II) complexes have received a great deal of interest as live cell imaging probes recently, they have also gained notable importance as anticancer agents.[65] Osmium complexes can exhibit multiple oxidation states of Os(II-IV) which plays a pivotal role in the redox potentials in cancerous cells. Since ruthenium(II) complexes are well-understood and widely researched, such osmium(II) complexes are designed from their ruthenium counterparts.

A pair of osmium(II) and ruthenium(II) analogues were synthesised and investigated not only for their cellular imaging capabilities, but as their potential for efficient photodynamic therapy agents (Figure 1.2.4). The osmium analogue displayed NIR emission centred at 736 nm with the ruthenium analogue at 619 nm.[66]

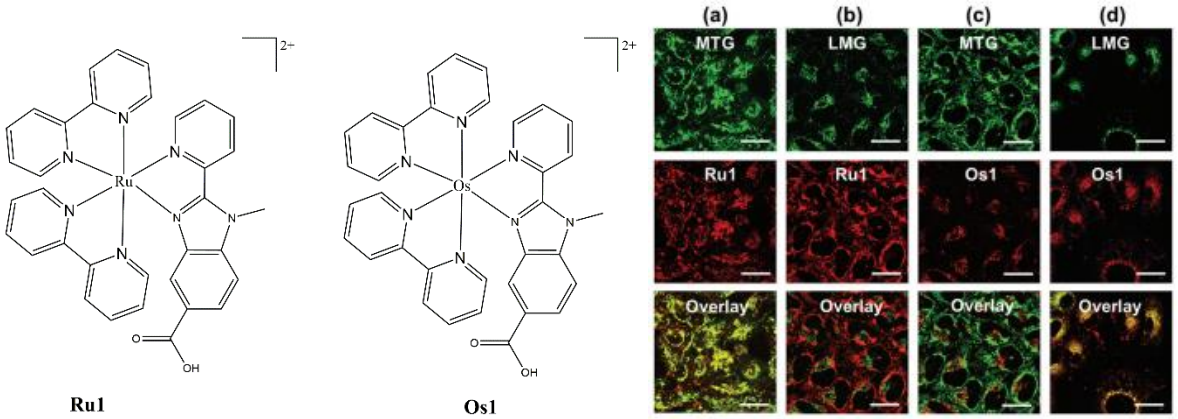

Figure 1.2.4. Chemical structures of Ru1 and Os1 and confocal images of A549 cells with Ru1 (λ_{exc} = 458 nm, λ_{em} = 600 ± 30 nm) / Os1 (λ_{exc} = 561 nm, λ_{em} = 720 ± 30 nm) (20 µM, 4 h). MitoTracker Green (MTG, 100 nM, 30 min λ_{exc} = 488 nm, λ_{em} = 520 ± 30 nm) (a) and (c). LysoTracker Green (LTG, 100 nM, 30 min, λ_{exc} = 488 nm, λ_{em} = 520 ± 30 nm) (b) and (d). Scale bar is 20 µm. Figure taken from Zhang *et al*.[66]

It was reported that the ruthenium(II) analogue accumulated seemingly in the mitochondria and the osmium(II) analogue in lysosomes. Further to this, it was shown that the osmium(II) analogue displayed strong cytotoxicity upon irradiation of 633 nm over the ruthenium(II) analogue. Despite the osmium(II) complex demonstrating weaker emission over its ruthenium(II) counterpart, the exceptional photostability, NIR emission and strong toxicity towards cancer cells when irradiated at 633 nm render it viable for imaging and photodynamic therapy.[66] It has also been well documented that osmium(II) complexes, as well as ruthenium(II), can bypass resistance mechanisms of platinum anticancer drugs making them ideal therapeutic candidates.[67, 68]

1.3 Properties and uses of ruthenium(II) decorated gold nanoparticles in imaging and cancer applications

Gold nanoparticle synthesis was first introduced by Turkevitch through the reduction of $[Au]^{3+}$ to $[Au]^{0}$ in 1951 through the use of citric acid.[69] The synthesis was then further refined through incorporation of ethylene diaminetetraacetic acid (EDTA) to control the size and shape allowing for better distribution between the sizes of 9 – 120 nm.[70,71] Gold nanoparticles in relation to bulk gold exhibit different optical properties and such have been studied for the applications as sensing probes, therapeutic agents and scaffolds for targeted delivery of drugs within the biological and pharmaceutical fields.[72-75] Gold nanoparticles are relatively easy to synthesise, non-cytotoxic, water soluble and easy to chemically modify at the surface through the addition of thiol or amine based ligands.[76-81] Their optoelectronic properties vary depending on their size, shape, aggregation state and the surface chemistry applied.[70] With this, the importance and potential of designing a tailor made gold nanoparticle system can benefit therapeutic fields. Proteins, peptides, polymers, carbohydrates, antibodies, lumophores and small molecules can be used for the functionalisation of gold nanoparticles (Figure 1.3.1).[76,77,82]

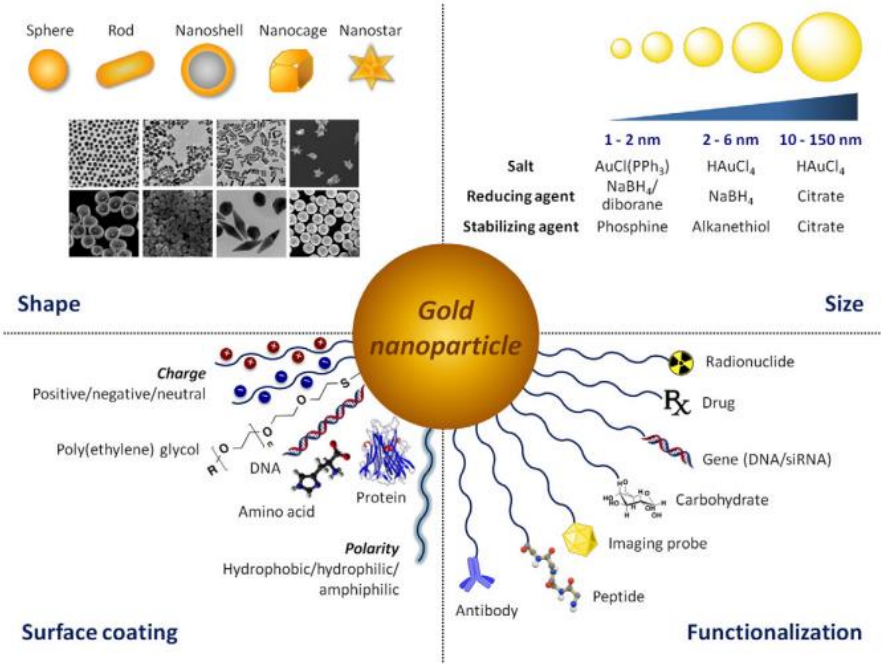

Figure 1.3.1. Representation of the versatility of gold nanoparticles. Figure taken from Her *et al.*[83]

Emissive transition metal complexes on gold nanoparticles have become an attractive area of research in recent decades for improving cellular uptake and delivery into cells, although quenching of emission has been well documented.[84-86] Three bipyridine ruthenium(II) complexes (RuS1, RuS6 and RuS12) were synthesised with different thiolated spacer units for the attachment onto gold nanoparticles and their photophysical properties were analysed.[87] It was shown that the RuS12 complex demonstrated the least quenching from the gold nanoparticle surface.

Additionally, the synthesis and photophysical properties of three different ruthenium(II) complexes for the attachment on gold through employment of a terminal alkyl thiol group was observed for their cellular uptake and DNA binding in HeLa cells (Figure 1.3.2).[88] These complexes were spatially separated from the gold nanoparticle surface to reduce quenching of the ^{3}MLCT of the ruthenium emission.[79,88-90]

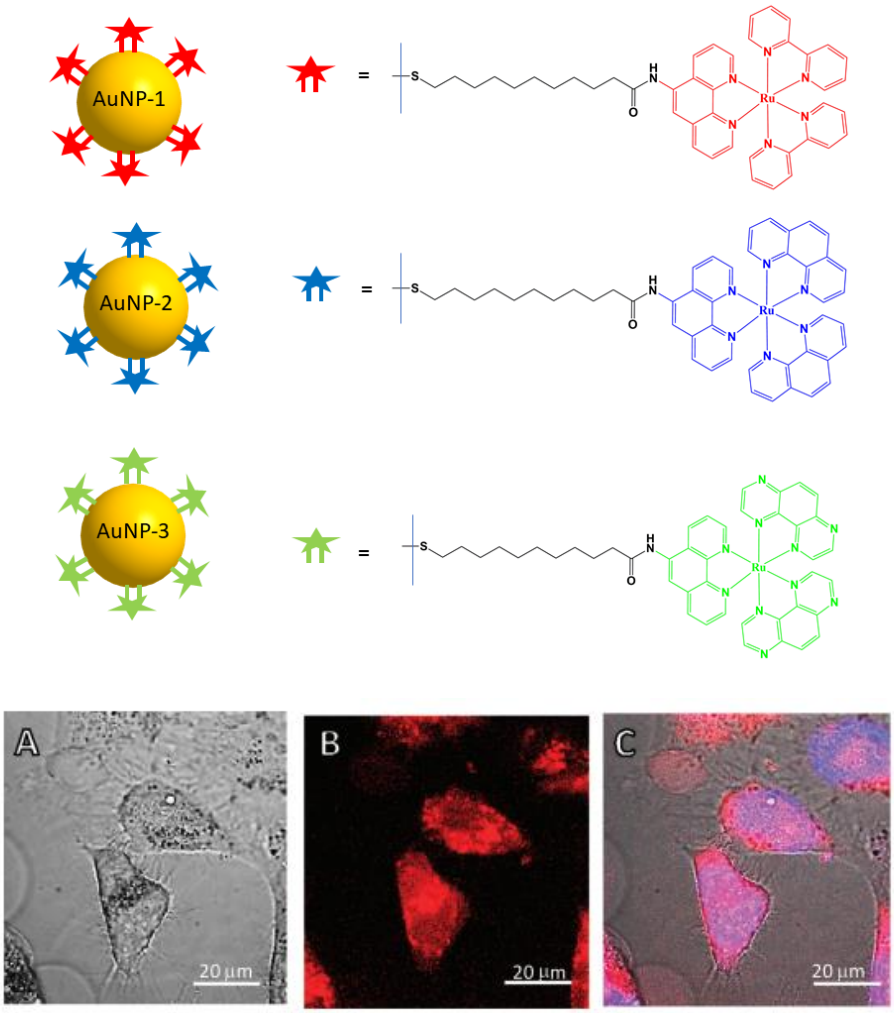

Figure 1.3.2. Reconstructed cartoon representation of ruthenium decorated gold nanoparticles (top) and confocal microscopy of live cell imaging of AuNP-1 (~16 nM, 4 hrs) in HeLa cells (bottom): Brightfield (A), Red channel: emission of ruthenium from AuNP-1 (λ_{exc} = 450 nm, λ_{em} = 600-700 nm)(B) and overlay of brightfield, emission from AuNP-1 (red) and nuclear stain DAPI (λ_{exc} = 405 nm, λ_{em} = 415-460 nm)(blue) (C). Scale bar = 20 µm. Figure taken from Elmes *et al.*[88]

Each gold nanoparticle system employed demonstrated high binding to DNA whilst claiming them to be non-toxic at high concentrations. Fluorescence and TEM studies of the dosed cells present themselves as being localised within the cytoplasm and nucleus and therefore can act as sensitive cellular imaging agents. Furthermore, a bipyridine ruthenium(II) complex (RuSH) was labelled onto two different sized gold nanoparticles (13 nm and 100 nm) providing red luminescence and prolonged lifetimes (Figure 1.3.3).[91] High loading of the complex was

ascertained through ICP-MS analysis allowing for strong detection of ruthenium emission on the nanoparticles.

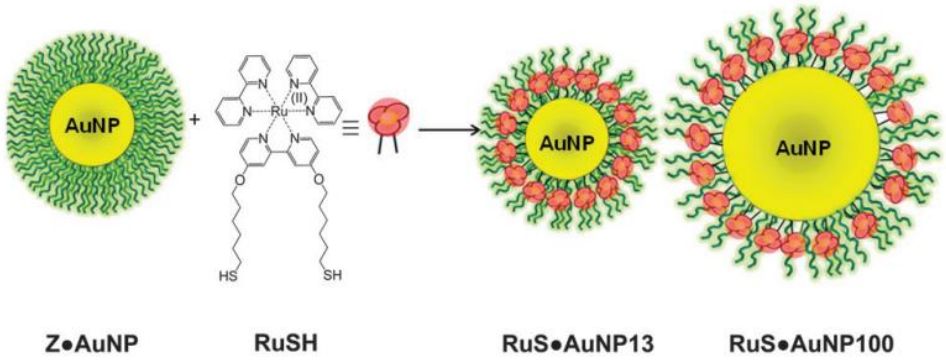

Figure 1.3.3. Schematic for coating of gold nanoparticles with RuSH. Scheme taken from Rogers *et al*.[91]

These nanoparticle systems display no significant toxicity arising in the cells and demonstrate exceptional stability. Interestingly, single 100 nm gold nanoparticles decorated with this complex were able to be visualised in cells revealing their biomolecular association with chromatin in the nucleus. Moreover, the cellular uptake and time resolved fate of a ruthenium(II) complex (RuS12) labelled on 13 nm gold nanoparticles was evaluated to demonstrate the mechanism of uptake in cells using the luminescence for quantifying the gold nanoparticles in cells (Figure 1.3.4).[92] RuS12 has been previously shown to be an ideal imaging agent leading to strong luminescence arising at 650 nm.[54]

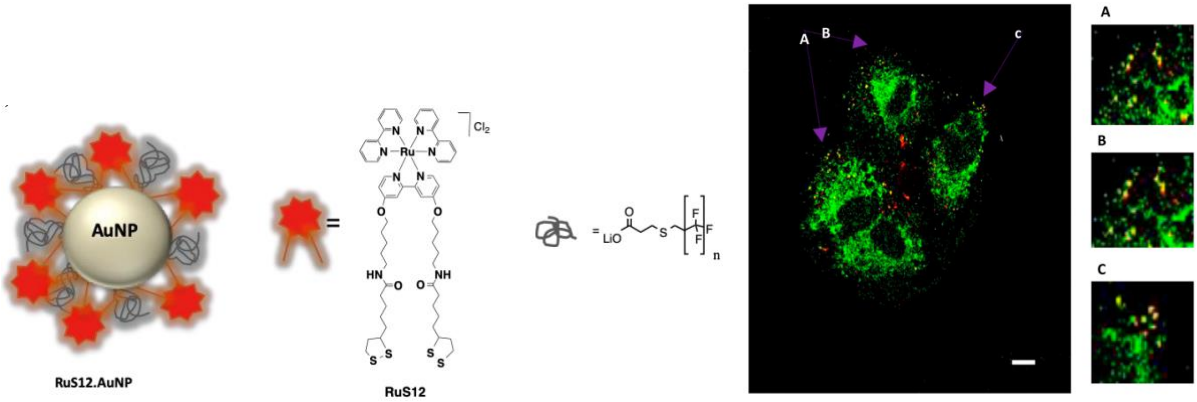

Figure 1.3.4. Schematic representation of ruthenium gold nanoparticles (left) and confocal microscopy of RuS12·AuNPs in Rab4-GFP-positive early endosomes. Confocal image of A549 transiently transfected with GFP-Rab4 and treated with 0.9 nM RuS12·AuNPs for 4 h. Red channel, RuS12·AuNP emission (λ_{exc} = 488 nm, λ_{em} 620−800 nm) and green channel, GFP emission (λ_{exc} = 488 nm, λ_{em} = 502 nm) (right) with zoomed inserts showing co-localisation (a – c). Scale bar = 10 µm. Taken from Dosumu *et al.*[92]

The ruthenium signal was used to study the uptake of particles in cells alongside TEM to identify the mechanism of uptake. The ruthenium labelled nanoparticles were tracked inside green fluorescent protein (GFP) tagged cells by following the unique luminescence signal from RuS12 at timed intervals. During the early stages of incubations, the particles were seemingly localising within the cytoplasm and mitochondria of cells whilst the main evidence of uptake was found to be micropinocytosis. However, later time points displayed accumulation within lysosomes and autophagosomes being linked with autophagy.

1.4 Gold nanoparticles in mass spectrometry imaging

Whilst gold nanoparticles have displayed uses as scaffolds for transition metal complexes for delivery and imaging applications in cells, they also have presented themselves as favourable candidates for MSI applications. Gold does not naturally occur in biological systems and thus can be used as an alternative detection method for MSI. There have been numerous reports that have previously utilised gold nanoparticles as mass probes for detection in mass spectrometry which has allowed mapping of distribution in biological samples through the use of gold ions

namely $[Au]^+$, $[Au_2]^+$ and $[Au_3]^+$.[36,93-96] Matrix assisted laser desorption ionization (MALDI) is a common technique employed for MSI of biological tissue due to the formation of intact higher molecular weight ions, high sensitivity, can detect masses up to 100 kDa and allows easy data interpretation due to the production of single charged ions. However, MALDI offers lower spatial resolution due to the probing spot (25 µm in diameter) in comparison to techniques such as secondary ion mobility mass spectrometry imaging (SIMS-MSI) (50 nm in diameter) and is therefore unable to image on a single cell level.[36,93,97] MALDI requires an energy absorbing matrix, usually a low molecular weight organic compound to absorb the bulk energy of the laser and transfer it to the analyte.[35,39,98] This is to protect the analyte of interest from fragmentation and aids in the ionisation process through electron transfer. Due to gold's natural ability for conduction of heat and electrochemical properties, it has been shown that the ionisation of gold nanoparticles is highly efficient in the absence of a matrix thus rendering them both as a matrix and detection probe.[99-105]

Gold nanoparticles have been shown to be an efficient matrix. Cationic gold nanoparticles enriched with sodium ions were employed to promote sodium adduct formation and used for the detection of low molecular weight organic compounds (Figure 1.4.1).[106] Gold nanoparticle enhanced targets (AuNPET) have been compared to their previous analogue silver nanoparticles enhanced targets (AgNPET) and are preferred for numerous reasons. They are less reactive therefore making them more stable, more efficient at ionising and possess lower intensity ion peaks therefore making trace detection of compounds easier. Additionally, by adding excess sodium ions with the AuNPET facilitates higher intensities of the analytes through adduct formation $[M+Na]^+$. Through this LDI-MSI was employed on fingerprints to allow investigation of spatial distribution of over one hundred endogenous and exogenous compounds and ridge patterns.

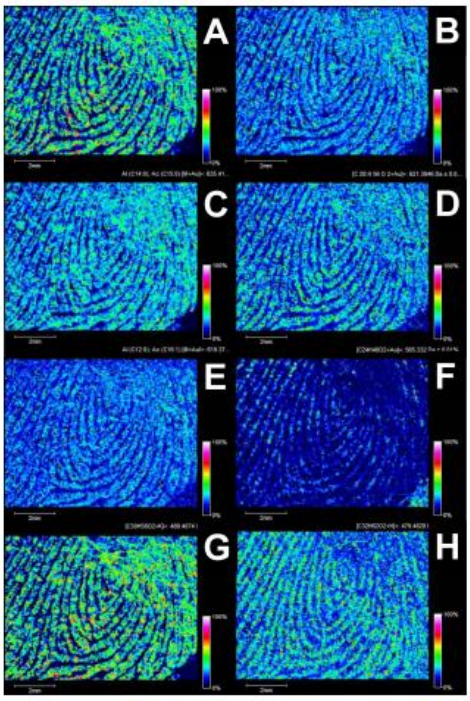

Figure 1.4.1. LDI-MSI of fingerprint on AuNPET. Imagess are TIC normalized and represent the spatial distribution of ions of m/z 635.410 (A), 621.395 (B), 619.379 (C), 565.332 (D), 489.407 (E), 479.483 (F), 459.418 (G) and 297.279 (H). Figure taken from Sekula *et al.*[106]

A variety of organic analytes was studied and detected through adduct formation with various salts such as sodium and potassium and even gold was achieved. Through the detection of these analytes, determination of their origin on the fingerprint could be ascertained through the use of AuNPET by containing a high mass accuracy. Therefore, using gold nanoparticles in the absence of a matrix has been shown to decrease ion suppression and in turn allow the determination of amino acids, saccharides, nucleosides and glycosides to a high mass accuracy.

1.5 Antibody labelled gold nanoparticles for anticancer and imaging applications

Gold nanoparticles possess many desirable and unique characteristics when employed as anticancer agents such as the ability to kill cancer cells through thermal ablation upon irradiation.[107-110] Irradiation of gold nanoparticles can occur at low energies minimising unwanted tissue damage due to the absorbance profile stretching across the visible spectrum. However, they are non-selective and non-targeting towards cancer tissue and cells. To improve selective targeting of gold nanoparticles, antibodies can be functionalised on the gold surface and following irradiation can cause highly directed cytotoxicity to cancer cells.[111] Conjugation of functionalised groups on gold nanoparticles play a critical role in their stability, biocompatibility, functionality and properties which can provide a platform for their applications in various fields.[112-115] It has been shown that gold nanoparticles conjugated with monoclonal antibodies (mAb) or other targeting moieties have been effective diagnostic and therapeutic agents.[116]

Conjugation for attachment of mAbs can occur through covalent and non-covalent strategies between the mAb and gold nanoparticles which include ionic attractions, chemisorption through thiols and adapter molecules.[96,117-119] Non-covalent binding strategies combine electrostatic and hydrophobic interactions of the mAb and the gold surface to absorb onto the surface non-specifically whilst maintaining stability.[109,116] Gold nanoparticles and gold nanorods have been synthesised making use of their intense plasmon resonance band for utilisation as contrast agents for optical imaging through the high scattering and optical absorption bands (Figure 1.5.1).[120] These nanomaterials were conjugated to a mouse mAb (HER81) that recognises human epidermal growth factor 2 (HER2) as HER2 is overexpressed by 20-40% in SKBR3 breast carcinoma cells over non-cancerous cells.[120] The conjugation

strategy employed makes use of the non-covalent binding through the electrostatic and hydrophobic interactions.

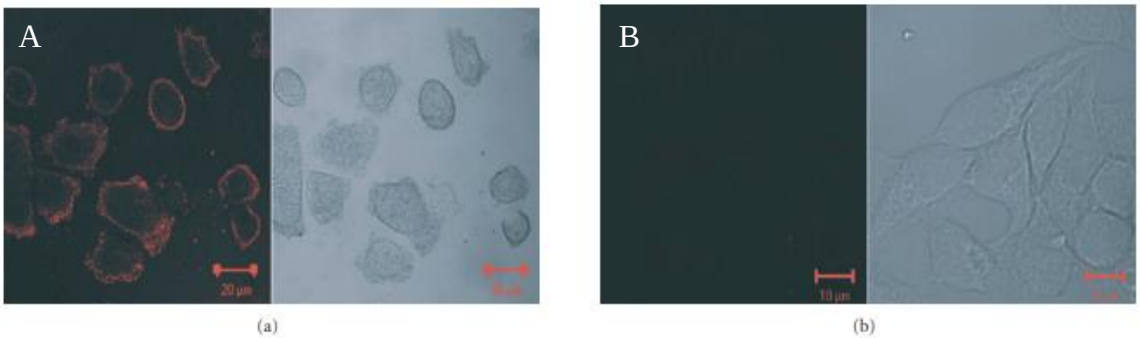

Figure 1.5.1. Confocal images of silver-stained HER81 conjugated gold nanorods incubated with SKBR3 cells (a) and CHO cells (b). Accumulation seen in SKBR3 cells where HER2 is expressed and no accumulation in HER2 negative CHO cells. Scale bar = 20µm (left) and 10 µm (right) Figure taken from Rayavarapu *et al*.[120]

The gold nanorods displayed optical properties in the far red region (675 – 850 nm) making them highly compatabible for contrast agents negating auto-fluorescence from cells. The antibody functionalised nanorods bind with high efficiency towards the HER2 receptors in SKBR3 cells for use in both live and fixed cells whilst demonstrating no binding towards CHO cells that possess no HER2 receptors.[120] In addition, other non-covalent binding strategies of anti-HER2 on gold nanoparticles has been explored for real time imaging in SiHa (ovarian cancer) cells and the diagnosis in oral cancer cells in vivo.[121-126] Conjugation of 5-aminolevulinic acid has also been shown to bind to gold nanoparticles for applications in photodyanamic therapy.[127] However, non-covalent binding strategies have limitations including random orientation, substitution from molecules present in the biological sample, pH and high antibody concentration.[96]

Direct conjugation can be achieved through covalent binding strategies such as the use of terminal thiol groups for the attachment onto the gold nanoparticle surface. However these typically require the use of spacer ligands for the ‘linking’ of the antibody to the nanoparticle

surface. In order to help stability of covalent binding strategies, coating of the nanoparticle surface with a thiolated PEG has been implemented and has also been shown to decrease non-specific interactions.[128-131] Additionally PEG has also been shown to increase the biocompatibility of the antibody-gold conjugate and provide sufficient stabilisation of gold nanoparticles.[132-134] Binding of mAbs through covalent strategies is preferred due to correct orientation and the decreased susceptibility towards substitution.[96]

Direct conjugation of trastuzumab on gold nanoparticles has been reported for its therapeutic efficacy on HER2 positive cell lines (Figure 1.5.2).[135] The cytotoxicity profile along with its mechanisms were investigated against both resistant (MKN7) and sensitive (NCI-N87) HER2 positive gastric cancer cell lines. It was found that cell death driven by autophagy played a key role in the cytotoxic mechanisms of trastuzumab bound gold nanoparticles causing internalisation of the particles. This was confirmed through western blot analysis revealing a strong LC3-II expression indicative of autophagy over unconjugated trastuzumab bound gold nanoparticles revealing direct conjugation enhances toxicity towards cancer cells. Additionally the particles displayed anti-tumour effects against both the resistant and sensitive subcutaneous tumours in mouse models in vivo.

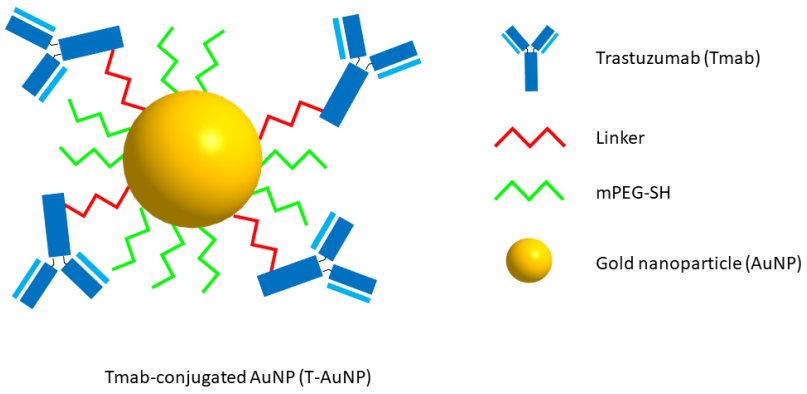

Figure 1.5.2. Schematic illustration of trastuzumab labelled gold nanoparticles. Scheme reconstructed from Kubota *et al.*[135]

These particles demonstrated the potential use for clinical applications for targeting HER2 positive cancer cells. NIR resonant gold-gold sulfide nanoparticles (GGS-NPs) have also been developed as therapeutic and contrast agents (Figure 1.5.3).[136] Such nanoparticles exhibited two photon luminescence when exposed to a NIR laser for visualisation cancer cells in vitro. An anti-HER2 antibody was covalently functionalised onto the nanoparticles for directed targeting of SKBR3 cells enabling multiphoton imaging with a low laser power. It was found that higher laser powers could be employed after treatment to induce photothermal ablation of the cells caused from the gold which in turn causes membrane blebbing and cell death within seconds.

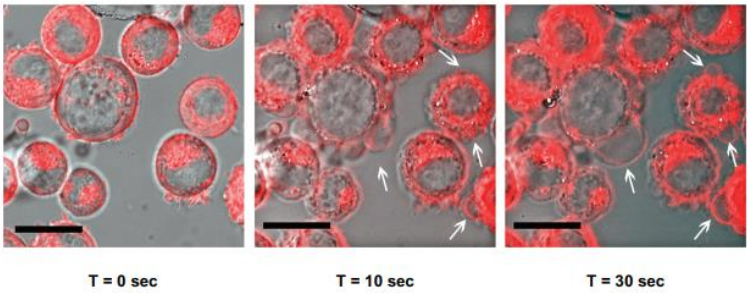

Figure 1.5.3. Time lapse images of SKBR3 cells treated with HER2 functionalised gold-gold sulphide nanoparticles. Scale bar = 20 µm. Figure taken from Day *et al.*[136]

These NIR absorbing gold-gold sulphide nanoparticles displayed suitable properties making them ideal candidates as multifunctional agents. They bound effectively towards the HER2 positive SKBR3 breast carcinoma cell lines whilst anti-IgG or mPEG-SH functionalised nanoparticles were found to be non-binding making them ideal as multifunctional agents. Although the targeting of HER2 is well documented in literature other receptors can be targeted across various cancer types including MUC-1 in breast cancer, hERG1 in pancreatic cancer, CD44 in gastric cancer and transferrin receptor in glioblastomas.[137-143]

PEGylated gold nanoparticles were synthesised and conjugated with folate, curcin (a type 1 ribosome inactivating protein),[144] and transferrin antibody (anti-transferrin) for the targeting of gliomas (human brain glioblastoma) via overexpressed folate and transferrin receptors for combined chemo and photothermal therapy. The toxicity of curcin was evaluated in vitro along with the NIR photothermal ablation properties from gold using HCN-1A (human cortical neurons) cells as a control cell line due to the lack of folate and transferrin receptors.[140]

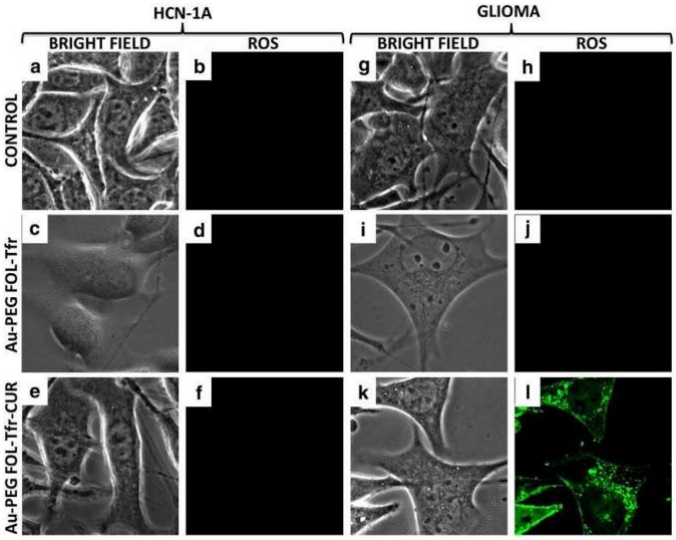

Figure 1.5.4. .Analysis of ROS generation by confocal microscopy of HCN-1A and glioma cells treated no particles (control), with PEGylated gold nanoparticles functionalised with folate and anti-transferrin (Au-PEG-FOL-Tfr) (100 µL/mL) and PEGylated gold nanoparticles functionalised with folate, curcin and anti-transferrin (Au-PEG-FOL-Tfr-CUR)(100 µL/mL) for 24 hours. Brightfield images (a, c, e, g, i, k) and ROS tracer dye (λ_{exc} = 488 nm, λ_{em} = 510-530 nm) (b, d, f, h, j and l) showing activation of ROS generation in l indicative of curcin. Figure taken from Mohamed *et al*.[140]

The nanoparticle conjugate made use of anti-transferrin and folate for increased cellular uptake to target the glioma cells to deliver the toxic drug, curcin, via a pH controlled release owing to the acidic environment of cancer cells over non-cancerous cells.[145] It was found that the delivery of curcin into glioma cells triggered ROS production specifically whilst detection of ROS was evaded in HCN-1A and the cells treated without the functionalisation of curcin (Figure 1.5.4). Moreover, excitation of the gold nanoparticles was conducted to induce photothermal ablation in the tumour site with precision. The nano-conjugate displayed high drug loading and due to

the specific targeting allowed ablation of cancer cells specifically in co-culture with normal cells.

Additionally, HeLa cells (cervical cancer) was targeted via PEGylated hollow gold nanospheres by conjugation of a mAb, anti-TROP2, to target the overexpressed trophoblast cell surface antigen 2 (TROP2) for photothermal ablation.[146] Their cellular uptake and localisation was studied through ICP-AES and TEM. In order to determine whether the hollow gold nanospheres induced double strand breaks in DNA from photothermal therapy, a γH2AX assay was performed. This assay detects phosphorylation of histone-H2AX at serine-139 through measuring nuclear foci using confocal microscopy allowing it to act as a functional and sensitive marker for double break strands in DNA (DSB) (Figure 1.5.5).[146,147]

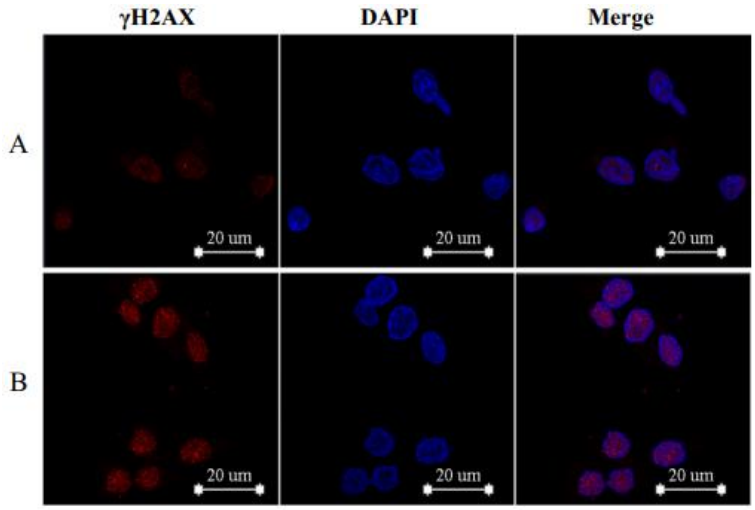

Figure 1.5.5. Confocal microscopy of HeLa cells treated with DAPI (λ_{exc} = 405 nm, λ_{em} = 415-460 nm) and γH2AX (λ_{exc} = 488 nm, λ_{em} = 515-535 nm) revealing DSB induction in cells treated with laser irradiation alone (5 Wcm^{-2}, 5 min) (A) and anti-TROP2 conjugated hollow gold nanospheres (2 $nmolL^{-1}$, 3 hrs) plus laser irradiation (5 Wcm^{-2}, 5 min) (B) revealing increased density of γH2AX foci compared to cells treated without anti-TROP2 hollow gold nanospheres. Figure taken from Liu *et al*.[146]

It was found that HeLa cells treated with NIR laser radiation (5 Wcm^{-2}) alone did not show significant expression of γH2AX therefore indicating no apparent DNA damage. However, the

hollow gold nanospheres conjugated with anti-TROP2 displayed increased expression of γH2AX under the same irradiation suggesting that these nanoparticles induce double strand breaks in DNA leading to cell death.

1.5.1 Ruthenium(II) and antibody labelled nanoparticles for imaging applications

Whilst there are many examples of antibody functionalised gold nanoparticles for guided targeting, ruthenium(II) decorated antibody functionalised gold nanoparticles have been rarely investigated. $[Ru(bpy)_3]^{2+}$ doped gold-silicon dioxide nanoparticles functionalised with an antibody have been synthesised as an electrochemiluminescence (ECL) label for multiplexed immunoassays for fast analysis of cancer markers utilising the plasmon resonance of the gold to enhance the emission of the ruthenium complex (Figure 1.5.1.1).[148]

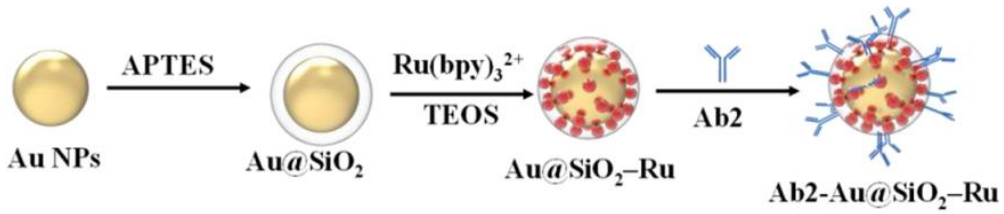

Figure 1.5.1.1. Schematic diagram of the antibody functionalised ruthenium silica gold nanoparticle. Scheme taken from Ding *et al*.[148]

These particles acted as a surface enhanced ECL immunosensor for the detection of multiple cancer markers in exhaled breath condensates based on electrode array imaging. Sensitivity and detection was enhanced through both the plasmon resonance of the gold and the increased antigens in the sample allowing for more binding of the nanoparticles thus enhancing the ruthenium emission.[148]

PEGylated hollow mesoporous ruthenium(II) nanoparticles loaded with a fluorescent ruthenium(II) anti-tumour complex ($[Ru(bpy)_2(tip)]^{2+}$) were functionalised with an Fc portion of an antibody for targeting of carcinoembryonic antigen which is overexpressed in colorectal cancer cells (Figure 1.5.1.2).[149] This Fc portion significantly improved penetration and engaged natural killer (NK) cells whilst possessing NIR sensitive cytotoxicity.

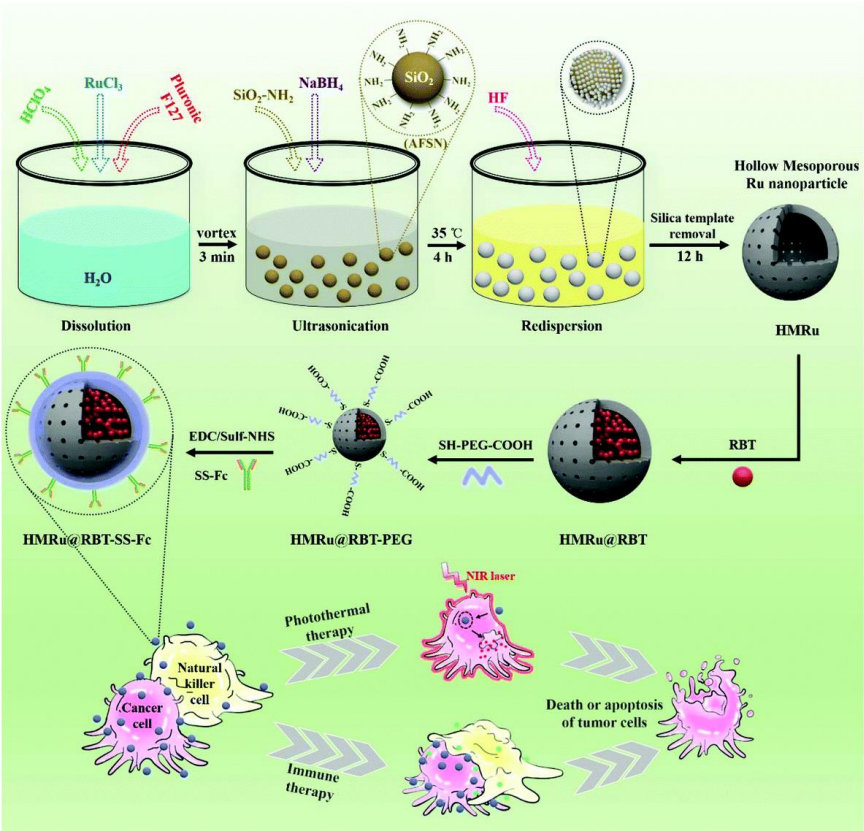

Figure 1.5.1.2. Schematic illustration of the mesoporous ruthenium antibody gold nanoparticle and the mechanism of combined treatment of cancer. Figure taken from Xu *et al*.[149]

This system acted as a multiple anticancer agent through the combined use of the hollow mesoporous ruthenium nanoparticles for photothermal therapy, $[Ru(bpy)_2(tip)]^{2+}$ for photodynamic therapy and the Fc antibody fragment for immunotherapy against colorectal cancer.

Additionally, mesoporous ruthenium nanoparticles (MRN) loaded with $[Ru(bpy)_2(tip)]^{2+}$ (RBT) was designed with anti-transferrin and single stranded DNA aptamer (AS1411) for targeting glioma cells. The aptamer has a high binding affinity for nucleolin on the surface of glioma cells and the ruthenium complex acts as a PDT agent by generating ROS species under laser irradiation.[150]

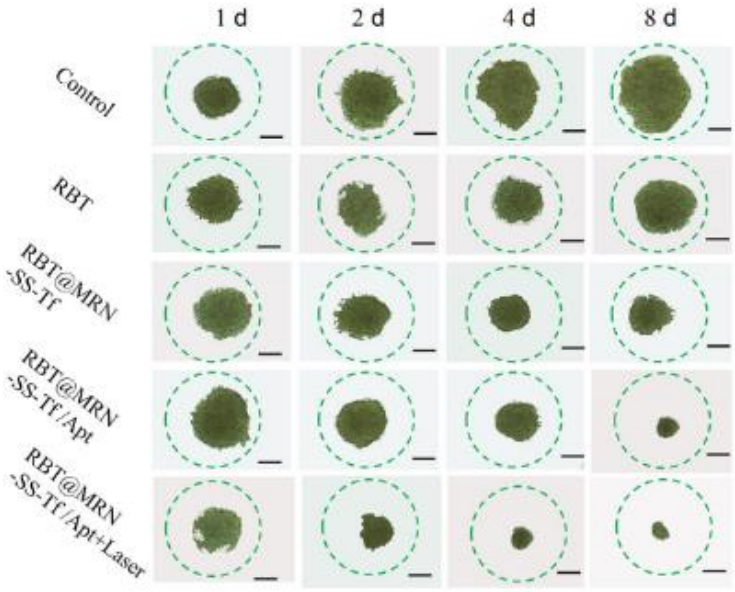

Figure 1.5.1.3. Optical images of U87 glioma spheroids after incubation in serum free media with PBS (control), RBT, RBT@MRN-SS-Tf, and RBT@MRN-SS-Tf/Apt for a variety of days. Scale bar = 200 µm. Figure taken from Zhu *et al*.[150]

It was found that the control sample (PBS) and the RBT treated samples in U87 glioma spheroids increased the tumour volume over 8 days (Figure 1.5.1.3). The nanoparticle sample containing anti-transferrin appears to start hindering tumour growth and with the addition of the aptamer significantly decreases the tumour volume. However, irradiation of the mesoporous RBT nanoparticle with the transferrin and aptamer under laser irradiation further decreased tumour volume of U87 glioma spheroids demonstrating their use as a PDT agent for gliomas.

1.5.2 Rituximab labelled gold nanoparticles for imaging applications

The first clinical use for cancer therapy using a mAb was rituximab.[151-153] Rituximab is a monoclonal antibody that is used for treatment against B-cell lymphomas that binds to the overexpressed receptor CD20.[154,155] The receptor CD20 is a non-glycosylated transmembrane glycoprotein ranging in molecular weight of 33 – 37 kDa that is expressed in both normal and malignant B-cells but is overexpressed in B-cell malignancies.[156-159] Rituximab functionalised gold nanoparticles have been utilised for delivery and release of rituximab through irradiation towards CD20 positive cells (Figure 1.5.2.1).[160] The released rituximab from the gold retains the functionality and ability for triggering cell death through complement-dependent cytotoxicity. Further cell death was triggered from the gold nanoparticles causing rupturing of the cell membranes.

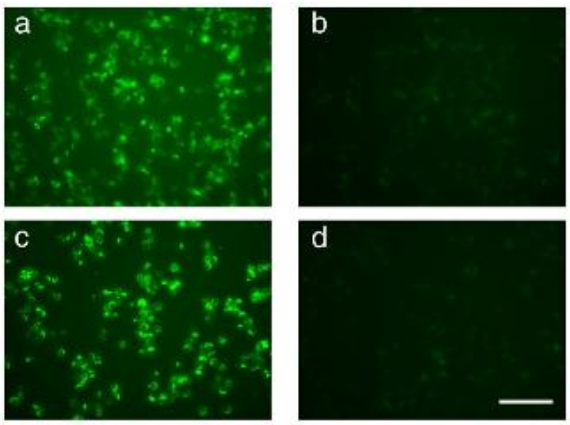

Figure 1.5.2.1. Confocal microscopy of BJAB cells incubated with released anti-CD20 from irradiated gold nanoparticles (a), supernatant form non-irradiated nanoparticles (b), free Rituximab (0.1 µg/mL) (c) and control cells with the secondary antibody (d). Scale bar is 100 µm. Figure taken from Bisker *et al.*[160]

Imaging of BJAB cells treated with the supernatant of irradiated rituximab functionalized gold nanoparticles was conducted through the use of a FITC-conjugated anti-human secondary antibody that recognises rituximab. It was found that cells incubated with the irradiated

rituximab functionalised gold nanoparticles display higher fluorescence than those without irradiation (Figure 1.5.2.1a and Figure 1.5.2.1b respectively) confirming the release of rituximab and its ability to bind efficiently. The irradiated and non-irradiated samples were compared to free rituximab at 0.1 µg/mL (Figure 1.5.2.1c) showing similar fluorescence to that of the irradiated sample whereas cells treated with the secondary antibody alone showed very low fluorescence (Figure 1.5.2.1d). Therefore it is shown that controlled release of rituximab through irradiation can be achieved by tuning the laser to the plasmonic resonance of the gold to generate cell death through complement dependent cytotoxicity from rituximab and photothermal ablation from the gold.

Additionally, different sized gold nanoparticles with varying conjugation strategies with rituximab were formed for assessing their therapeutic potential (Figure 1.5.2.2).[161]

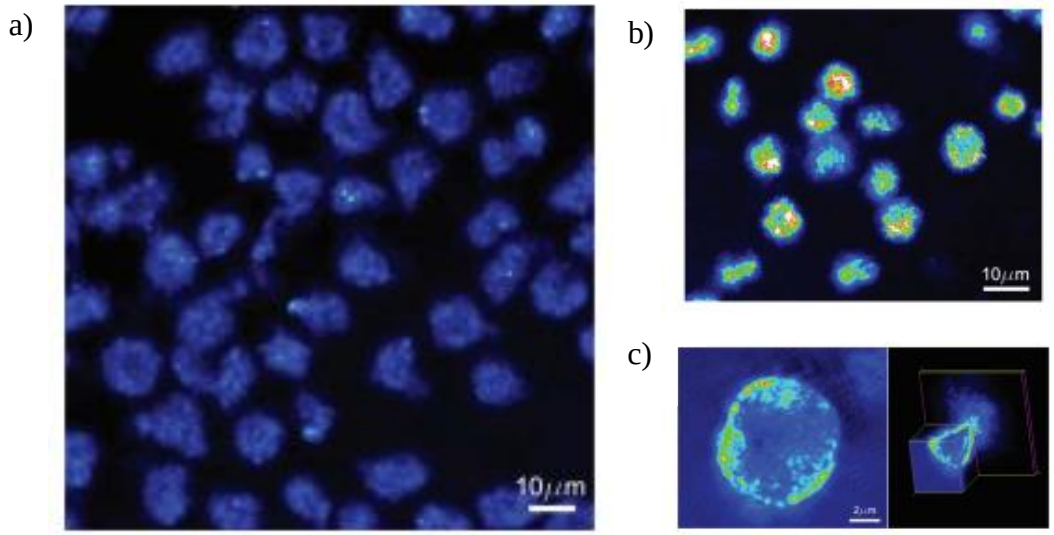

Figure 1.5.2.2. Reflectance images of Z138 cells incubated (1 hour) with PEG-NP displaying little uptake (a). Reflectance images of Z138 cells incubated (1 hour) with rituximab functionalised gold nanoparticles (b), single cell image (left) and 3D image (right) (c). Scale bar = 10 µm. Figure taken from Weiss et al.[161]

Scattering of the rituximab functionalised gold nanoparticles through confocal microscopy revealed binding to the membrane of the CD20 positive Z138 cell line whereas no binding was observed in CD20 negative cell line SKBR3 and the nanoparticles containing no rituximab.

Tumour-targeting nanoparticles have become one of the most promising anticancer and imaging strategies. Gold nanoparticles alone have been shown to be effective imaging and anticancer agents and when combined with targeting moieties overcomes the struggles of non-specific toxicity and accumulation. Although examples of metal coated gold nanoparticles and antibody guided gold nanoparticles have been studied for imaging and anticancer applications, combining the desirable imaging capabilities of ruthenium combined with the tumour specific antibody on gold nanoparticles directly for dual imaging via confocal and mass spectrometry has not been explored. It is therefore necessary to combine both the optical and MSI of ruthenium and gold for detection and imaging of cancer markers using rituximab for guided delivery.

1.6 Thesis outline

This thesis focuses on the evaluation of three ruthenium(II) complexes for their application as live cell imaging agents. Additionally, we sought to utilise the complex displaying the greatest luminescence enhancement (increased luminescence lifetimes and quantum yields) when attached onto gold nanoparticles for targeted approaches towards CD20 positive cancer cell lines allowing for combined optical and mass spectrometry imaging. Additionally, a novel osmium(II) complex attached on gold nanoparticles is described as the first example for live cell imaging capabilities. This can potentially lead to the development of osmium(II) complexes on gold nanoparticles for delivery into cells for imaging and anticancer applications and could lead to directional targeting of cancer cells through aid of an antibody.

In chapter 3, three ruthenium complexes previously used for applications in dye sensitised solar cells were evaluated for their photophysical properties is discussed in aerated water, in the presence of a fluorosurfactant and attachment onto gold nanoparticles (13 nm in size). The selected ruthenium complex displaying the greatest photophysical properties (increased luminescent lifetimes and higher quantum yield) was taken forward and tested as a live cell imaging probe and then used for later studies concerning antibody attachment.

Chapter 4 discusses the rationale behind the design of the novel osmium(II) complex (OsPhenSS) alongside the photophysical properties associated in aerated water, in the presence of a fluorosurfactant and on gold nanoparticles. Live cell imaging with dosing of the osmium(II) functionalised gold nanoparticles is presented demonstrating the first use and viability of osmium(II) functionalised gold nanoparticles for live cell imaging.

Lastly, Chapter 5 discusses the modification of the chosen monoclonal antibody, Rituximab, and its conjugation to gold nanoparticles. Flow cytometry, confocal microscopy and MSI was

performed to ascertain binding of rituximab functionalised gold nanoparticles to cancer cells and in tonsil tissue. This demonstrates the first application of dual imaging by detecting CD20 positive cells in tonsil tissue from rituximab functionalised ruthenium gold nanoparticles using the characteristic luminescence signature of ruthenium for confocal microscopy applications and the gold ions for mass spectrometry imaging applications.

1.7 References

1. J. D. Knoll and C. Turro, *Coord. Chem. Rev.*, 2015, **282-283**, 110-126.

2. L. De Cola, P. Belser, A. von Zelewsky and F. Vögtle, *Inorg. Chim. Acta*, 2007, **360**, 775-784.

3. F. E. Poynton, S. A. Bright, S. Blasco, D. C. Williams, J. M. Kelly and T. Gunnlaugsson, *Chem. Soc. Rev.*, 2017, **46**, 7706-7756.

4. A. F. Henwood and E. Zysman-Colman, *Chem. Commun.*, 2017, **53**, 807-826.

5. W. Yang, D. Wang, Q. Song, S. Zhang, Q. Wang and Y. Ding, *Organometallics*, 2013, **32**, 4130-4135.

6. P.-T. Chou and Y. Chi, *Chem. Eur. J.*, 2007, **13**, 380-395.

7. C.-P. Tan, Y.-M. Zhong, L.-N. Ji and Z.-W. Mao, *Chem. Sci.*, 2021, **12**, 2357-2367.

8. R. Huang, C.-H. Huang, J. Shao and B.-Z. Zhu, *The J. Phys. Chem. Lett.*, 2019, **10**, 5909-5916.

9. R. Huang, F.-P. Feng, C.-H. Huang, L. Mao, M. Tang, Z.-Y. Yan, B. Shao, L. Qin, T. Xu, Y.-H. Xue and B.-Z. Zhu, *ACS Appl. Mat. Inter.*, 2020, **12**, 3465-3473.

10. S. F. Mason and B. J. Norman, *J. Chem. Soc. A.*, 1969, 1442-1447.

11. K. Kalyanasundaram, *Coord. Chem. Rev.*, 1982, **46**, 159-244.

12. K. Nakamaru, *Bull. Chem. Soc. Jpn.*, 1982, **55**, 2697-2705.

13. L.-F. Tan, H. Chao, H. Li, Y.-J. Liu, B. Sun, W. Wei and L.-N. Ji, *J. Inorg. Biochem.*, 2005, **99**, 513-520.

14. C. A. Puckett and J. K. Barton, *Biochem.*, 2008, **47**, 11711-11716.

15. F. R. Svensson, M. Matson, M. Li and P. Lincoln, *Biophys. Chem.*, 2010, **149**, 102-106.

16. L. Blackmore, R. Moriarty, C. Dolan, K. Adamson, R. J. Forster, M. Devocelle and T. E. Keyes, *Chem. Commun.*, 2013, **49**, 2658-2660.

17. J. Liu, Y. Chen, G. Li, P. Zhang, C. Jin, L. Zeng, L. Ji and H. Chao, *Biomater.*, 2015, **56**, 140-153.

18. Y. Chen, T. W. Rees, L. Ji and H. Chao, *Curr. Opin. Chem. Biol.*, 2018, **43**, 51-57.

19. K. K.-W. Lo, T. K.-M. Lee and K. Y. Zhang, *Inorg. Chim. Acta*, 2006, **359**, 1845-1854.

20. K. K.-W. Lo and T. K.-M. Lee, *Inorg. Chem.*, 2004, **43**, 5275-5282.

21. U. Neugebauer, Y. Pellegrin, M. Devocelle, R. J. Forster, W. Signac, N. Moran and T. E. Keyes, *Chem. Commun.*, 2008, 5307-5309.

22. M. R. Gill and J. A. Thomas, *Chem. Soc. Rev.*, 2012, **41**, 3179-3192.

23. L. Cosgrave, M. Devocelle, R. J. Forster and T. E. Keyes, *Chem. Commun.*, 2010, **46**, 103-105.

24. A.-C. Munteanu and V. Uivarosi, *Pharmaceutics*, 2021, **13**, 874.

25. C. A. Puckett and J. K. Barton, *J.l Am. Chem. Soc.*, 2007, **129**, 46-47.

26. T. Boulikas, *J. Cell. Biochem.*, 1994, **55**, 32-58.

27. A. D. Ragin, R. A. Morgan and J. Chmielewski, *Chem. Bio.*, 2002, **9**, 943-948.

28. J. Liu, Y. Chen, G. Li, P. Zhang, C. Jin, L. Zeng, L. Ji and H. Chao, *Biomater.*, 2015, **56**, 140-153.

29. B.-Z. Zhu, X.-J. Chao, C.-H. Huang and Y. Li, *Chem. Sci.*, 2016, **7**, 4016-4023.

30. M. R. Gill, J. Garcia-Lara, S. J. Foster, C. Smythe, G. Battaglia and J. A. Thomas, *Nat Chem*, 2009, **1**, 662-667.

31. A. B. Caballero, L. Cardo, S. Claire, J. S. Craig, N. J. Hodges, A. Vladyka, T. Albrecht, L. A. Rochford, Z. Pikramenou and M. J. Hannon, *Chem. Sci.*, 2019, **10**, 9244-9256.

32. S. Dhar, W. L. Daniel, D. A. Giljohann, C. A. Mirkin and S. J. Lippard, *J. Am. Chem. Soc.*, 2009, **131**, 14652-14653.

33. H. Nohl, W. Jordan and R. J. Youngman, *Adv. Free Rad. Bio. Med.*, 1986, **2**, 211-279.

34. P. Zhang, H. Huang, Y. Chen, J. Wang, L. Ji and H. Chao, *Biomater.*, 2015, **53**, 522-531.

35. A. D. Feenstra, M. E. Dueñas and Y. J. Lee, *J. Am. Soc. Mass Spec.*, 2017, **28**, 434-442.

36. K. Chughtai and R. M. A. Heeren, *Chem. Rev.*, 2010, **110**, 3237-3277.

37. S. Theiner, A. Schoeberl, A. Schweikert, B. K. Keppler and G. Koellensperger, *Curr. Opin. Chem. Biol.*, 2021, **61**, 123-134.

38. S. Nimesh, S. Mohottalage, R. Vincent and P. Kumarathasan, *Inter. J. Mol. Sci.*, 2013, **14**, 11277-11301.

39. M. K. Andersen, S. Krossa, T. S. Høiem, R. Buchholz, B. S. R. Claes, B. Balluff, S. R. Ellis, E. Richardsen, H. Bertilsson, R. M. A. Heeren, T. F. Bathen, U. Karst, G. F. Giskeødegård and M.-B. Tessem, *Anal. Chem.*, 2020, **92**, 3171-3179.

40. H. A. Alturkistani, F. M. Tashkandi and Z. M. Mohammedsaleh, *Glob. J. Health Sci.*, 2015, **8**, 72-79.

41. L. C. Schmued, L. W. Swanson and P. E. Sawchenko, *J. Histochem. Cytochem.*, 1982, **30**, 123-128.

42. R. Catena, L. M. Montuenga and B. Bodenmiller, *J. Pathol.*, 2018, **244**, 479-484.

43. P. Mandhan, B. Q. Qi, J. I. Keenan, S. Ismail, S. W. Beasley and M. J. Sullivan, *J. Fluoresc.*, 2006, **16**, 655-658.

44. D. C. Carpenter and B. R. Nebel, *N. Y. Sci. J.*, 1931, **74**, 154-155.

45. J. Han, J. Sun, S. Song, L. Beljaars, G. M. M. Groothuis, H. Permentier, R. Bischoff, G. B. Halmos, C. J. Verhoeven, E. R. Amstalden van Hove, P. Horvatovich and A. Casini, *Chem. Commun.*, 2020, **56**, 5941-5944.

46. D. Havrylyuk, K. Stevens, S. Parkin and E. C. Glazer, *Inorg. Chem.*, 2020, **59**, 1006-1013.

47. S. Bonnet and J.-P. Collin, *Chem. Soc. Rev.*, 2008, **37**, 1207-1217.

48. R. G. Alabau, M. A. Esteruelas, M. Oliván and E. Oñate, *Organometallics*, 2017, **36**, 1848-1859.

49. W.-K. Chu, S.-M. Yiu and C.-C. Ko, *Organometallics*, 2014, **33**, 6771-6777.

50. J. Wang, S. Sun, D. Mu, J. Wang, W. Sun, X. Xiong, B. Qiao and X. Peng, *Organometallics*, 2014, **33**, 2681-2684.

51. T. Yang, A. Xia, Q. Liu, M. Shi, H. Wu, L. Xiong, C. Huang and F. Li, *J. Mater. Chem.*, 2011, **21**, 5360-5367.

52. S. Mardanya, S. Karmakar, D. Mondal and S. Baitalik, *Inorg. Chem.*, 2016, **55**, 3475-3489.

53. R. S. Lumpkin, E. M. Kober, L. A. Worl, Z. Murtaza and T. J. Meyer, *J. Phys. Chem.*, 1990, **94**, 239-243.

54. S. J. Adams, D. J. Lewis, J. A. Preece and Z. Pikramenou, *ACS Appl. Mater. Inter.*, 2014, **6**, 11598-11608.

55. S. Lazic, P. Kaspler, G. Shi, S. Monro, T. Sainuddin, S. Forward, K. Kasimova, R. Hennigar, A. Mandel, S. McFarland and L. Lilge, *Photochem. Photobio.*, 2017, **93**, 1248-1258.

56. E. C. Glazer, *Photochem. Photobio.*, 2017, **93**, 1326-1328.

57. J.-L. Liao, Y. Chi, S.-H. Liu, G.-H. Lee, P.-T. Chou, H.-X. Huang, Y.-D. Su, C.-H. Chang, J.-S. Lin and M.-R. Tseng, *Inorg. Chem.*, 2014, **53**, 9366-9374.

58. R. E. Holmlin and J. K. Barton, *Inorg. Chem.*, 1995, **34**, 7-8.

59. B. Carlson, G. D. Phelan, W. Kaminsky, L. Dalton, X. Jiang, S. Liu and A. K. Y. Jen, *J. Am. Chem. Soc.*, 2002, **124**, 14162-14172.

60. K. L. Smitten, P. A. Scattergood, C. Kiker, J. A. Thomas and P. I. P. Elliott, *Chem. Sci.*, 2020, **11**, 8928-8935.

61. F. Felix, J. Ferguson, H. U. Güdel and A. Ludi, *Chem. Phys. Lett.*, 1979, **62**, 153-157.

62. R. E. Holmlin, J. A. Yao and J. K. Barton, *Inorg. Chem.*, 1999, **38**, 174-189.

63. C. Ge, H. Huang, Y. Wang, H. Zhao, P. Zhang and Q. Zhang, *ACS Appl. Bio Mater.*, 2018, **1**, 1587-1593.

64. S. A. E. Omar, P. A. Scattergood, L. K. McKenzie, C. Jones, N. J. Patmore, A. J. H. M. Meijer, J. A. Weinstein, C. R. Rice, H. E. Bryant and P. I. P. Elliott, *Inorg. Chem.*, 2018, **57**, 13201-13212.

65. P. Zhang and H. Huang, *Dalton Trans.*, 2018, **47**, 14841-14854.

66. P. Zhang, Y. Wang, K. Qiu, Z. Zhao, R. Hu, C. He, Q. Zhang and H. Chao, *Chem. Commun.*, 2017, **53**, 12341-12344.

67. G. Berger, K. Grauwet, H. Zhang, A. M. Hussey, M. O. Nowicki, D. I. Wang, E. A. Chiocca, S. E. Lawler and S. J. Lippard, *Cancer Lett.*, 2018, **416**, 138-148.

68. C. Licona, J.-B. Delhorme, G. Riegel, V. Vidimar, R. Cerón-Camacho, B. Boff, A. Venkatasamy, C. Tomasetto, P. da Silva Figueiredo Celestino Gomes, D. Rognan, J.-N. Freund, R. Le Lagadec, M. Pfeffer, I. Gross, G. Mellitzer and C. Gaiddon, *Inorg. Chem. Front.*, 2020.

69. J. Turkevich, P. C. Stevenson and J. Hillier, *Discuss. Faraday Soc.*, 1951, **11**, 55.

70. M.-C. Daniel and D. Astruc, *Chem. Rev.*, 2004, **104**, 293-346.

71. J. Turkevich, P. C. Stevenson and J. Hillier, *Discuss. Faraday Soc.*, 1951, **11**, 55-75.

72. X. Yang, M. Yang, B. Pang, M. Vara and Y. Xia, *Chem.l Rev.*, 2015, **115**, 10410-10488.

73. J. Sun, Y. Xianyu and X. Jiang, *Chem. Soc. Rev.*, 2014, **43**, 6239-6253.

74. W. Zhou, X. Gao, D. Liu and X. Chen, *Chem. Rev.*, 2015, **115**, 10575-10636.

75. Y.-C. Yeh, B. Creran and V. M. Rotello, *Nanoscale*, 2012, **4**, 1871-1880.

76. J. Zhang, L. Mou and X. Jiang, *Chem. Sci.*, 2020, **11**, 923-936.

77. Y. Chen, Y. Xianyu and X. Jiang, *Acc. Chem. Res.*, 2017, **50**, 310-319.

78. J. Patel, L. Němcová, P. Maguire, W. G. Graham and D. Mariotti, *Nanotech.*, 2013, **24**, 245604.

79. M. Brust, M. Walker, D. Bethell, D. J. Schiffrin and R. Whyman, *J. Chem. Soc., Chem. Commun.*, 1994, 801-802.

80. R. Popovtzer, A. Agrawal, N. A. Kotov, A. Popovtzer, J. Balter, T. E. Carey and R. Kopelman, *Nano Lett.*, 2008, **8**, 4593-4596.

81. S. Eustis and M. A. El-Sayed, *Chem. Soc. Rev.*, 2006, **35**, 209-217.

82. S. Alex and A. Tiwari, *J. Nanosci. Nanotech.*, 2015, **15**, 1869-1894.

83. S. Her, D. A. Jaffray and C. Allen, *Adv. Drug Deliv. Rev.*, 2017, **109**, 84-101.

84. A. B. Chinen, C. M. Guan, J. R. Ferrer, S. N. Barnaby, T. J. Merkel and C. A. Mirkin, *Chem. Rev.*, 2015, **115**, 10530-10574.

85. J. N. Demas, D. Diemente and E. W. Harris, *J. Am. Chem. Soc.*, 1973, **95**, 6864-6865.

86. M. Martinez-Calvo, K. N. Orange, R. B. P. Elmes, B. la Cour Poulsen, D. C. Williams and T. Gunnlaugsson, *Nanoscale*, 2016, **8**, 563-574.

87. S. A. M. Osborne and Z. Pikramenou, *Faraday Discuss.*, 2015, **185**, 219-231.

88. R. B. P. Elmes, K. N. Orange, S. M. Cloonan, D. C. Williams and T. Gunnlaugsson, *J. Am. Chem. Soc.*, 2011, **133**, 15862-15865.

89. J. K. Barton, E. D. Olmon and P. A. Sontz, *Coord. Chem. Rev.*, 2011, **255**, 619-634.

90. A. M. Nonat, S. J. Quinn and T. Gunnlaugsson, *Inorg. Chem.*, 2009, **48**, 4646-4648.

91. N. J. Rogers, S. Claire, R. M. Harris, S. Farabi, G. Zikeli, I. B. Styles, N. J. Hodges and Z. Pikramenou, *Chem. Commun.*, 2014, **50**, 617-619.

92. A. N. Dosumu, S. Claire, L. S. Watson, P. M. Girio, S. A. M. Osborne, Z. Pikramenou and N. J. Hodges, *JACS Au*, 2021, **1**, 174-186.

93. S. Yang, L. Zhan, C. Liu, L. Fu, R. Chen and Z. Nie, *Microchem. J.*, 2019, **150**, 104190.

94. R.-C. Huang, W.-J. Chiu, I. Po-Jung Lai and C.-C. Huang, *Sci. Rep.*, 2015, **5**, 10292.

95. S. Giordano, V. Pifferi, L. Morosi, M. Morelli, L. Falciola, G. Cappelletti, S. Visentin, S. Licandro, R. Frapolli, M. Zucchetti, R. Pastorelli, L. Brunelli, M. D'Incalci and E. Davoli, *Nanomater.*, 2017, **7**, 71.

96. M. H. Jazayeri, H. Amani, A. A. Pourfatollah, H. Pazoki-Toroudi and B. Sedighimoghaddam, *Sens. Bio-Sens. Res.*, 2016, **9**, 17-22.

97. A. R. Buchberger, K. DeLaney, J. Johnson and L. Li, *Anal. Chem.*, 2018, **90**, 240-265.

98. A. Yoshinaga, H. Kamitakahara and K. Takabe, *Tree Physiol.*, 2016, **36**, 643-652.

99. J. L. Norris and R. M. Caprioli, *Chem. Rev.*, 2013, **113**, 2309-2342.

100. D. Wang, M. Hincapie, M. Guergova-Kuras, J. Kadas, L. Takacs and B. L. Karger, *J. Proteome Res.*, 2010, **9**, 1834-1842.

101. Q. Zhao, M. Yu, L. Shi, S. Liu, C. Li, M. Shi, Z. Zhou, C. Huang and F. Li, *Organometallics*, 2010, **29**, 1085-1091.

102. S. Liu, W. Zheng, K. Wu, Y. Lin, F. Jia, Y. Zhang, Z. Wang, Q. Luo, Y. Zhao and F. Wang, *Chem. Commun.*, 2017, **53**, 4136-4139.

103. H.-P. Wu, C.-J. Yu, C.-Y. Lin, Y.-H. Lin and W.-L. Tseng, *J. Am. Soc. Mass Spec.*, 2009, **20**, 875-882.

104. E. M. Weaver and A. B. Hummon, *Adv. Drug Deliv. Rev.*, 2013, **65**, 1039-1055.

105. H.-W. Tang, M. Y.-M. Wong, W. Lam, Y.-C. Cheng, C.-M. Che and K.-M. Ng, *Rapid Commun. Mass Spectrom.*, 2011, **25**, 3690-3696.

106. J. Sekuła, J. Nizioł, W. Rode and T. Ruman, *Anal. Chim. Acta*, 2015, **875**, 61-72.

107. L. R. Hirsch, R. J. Stafford, J. A. Bankson, S. R. Sershen, B. Rivera, R. E. Price, J. D. Hazle, N. J. Halas and J. L. West, *PNAS*, 2003, **100**, 13549-13554.

108. C. Loo, A. Lowery, N. Halas, J. West and R. Drezek, *Nano Lett.*, 2005, **5**, 709-711.

109. A. R. Lowery, A. M. Gobin, E. S. Day, N. J. Halas and J. L. West, *Inter. J. Nanomed.*, 2006, **1**, 149-154.

110. C. Loo, A. Lin, L. Hirsch, M. H. Lee, J. Barton, N. Halas, J. West and R. Drezek, *TCRT*, 2004, **3**, 33-40.

111. V. P. Zharov, E. N. Galitovskaya, C. Johnson and T. Kelly, *LSM*, 2005, **37**, 219-226.

112. X. Huang, P. K. Jain, I. H. El-Sayed and M. A. El-Sayed, *LSM*, 2008, **23**, 217-228.

113. D. P. O'Neal, L. R. Hirsch, N. J. Halas, J. D. Payne and J. L. West, *Cancer Lett*, 2004, **209**, 171-176.

114. S. Lal, S. E. Clare and N. J. Halas, *Acc. Chem. Res.*, 2008, **41**, 1842-1851.

115. D. M. Herold, I. J. Das, C. C. Stobbe, R. V. Iyer and J. D. Chapman, *Int. J. Radiat Biol.*, 2000, **76**, 1357-1364.

116. D. Kauer-Dorner, R. Pötter, A. Resch, L. Handl-Zeller, K. Kirchheiner, K. Meyer-Schell and W. Dörr, *Radiother. Oncol.*, 2012, **102**, 96-101.

117. E. L. Jones, J. R. Oleson, L. R. Prosnitz, T. V. Samulski, Z. Vujaskovic, D. Yu, L. L. Sanders and M. W. Dewhirst, *J. Clin. Oncol.*, 2005, **23**, 3079-3085.

118. T. M. Zagar, J. R. Oleson, Z. Vujaskovic, M. W. Dewhirst, O. I. Craciunescu, K. L. Blackwell, L. R. Prosnitz and E. L. Jones, *J. Inter. Hyperthermia*, 2010, **26**, 612-617.

119. J. D. Gibson, B. P. Khanal and E. R. Zubarev, *J. Am. Chem. Soc.*, 2007, **129**, 11653-11661.

120. R. G. Rayavarapu, W. Petersen, C. Ungureanu, J. N. Post, T. G. van Leeuwen and S. Manohar, *Inter. J. Biomed. Imaging*, 2007, **2007**, 29817.

121. K. Sokolov, M. Follen, J. Aaron, I. Pavlova, A. Malpica, R. Lotan and R. Richards-Kortum, *Cancer Res*, 2003, **63**, 1999-2004.

122. R. Pirker, *Target. Oncol.*, 2013, **8**, 47-53.

123. R. Pirker and M. Filipits, *Crit. Rev. Oncol. Hematol.*, 2011, **80**, 1-9.

124. I. H. El-Sayed, X. Huang and M. A. El-Sayed, *Cancer Lett.*, 2006, **239**, 129-135.

125. I. H. El-Sayed, X. Huang and M. A. El-Sayed, *Nano Lett.*, 2005, **5**, 829-834.

126. A. Mochizuki, T. Nagata, H. Kanno, M. Suzuki and T. Ohta, *Biorg. Med. Chem.*, 2011, **19**, 1623-1642.

127. M. K. Oo, X. Yang, H. Du and H. Wang, *Nanomed.*, 2008, **3**, 777-786.

128. H. Lee, *Pharmaceutics*, 2020, **12**.

129. S. Rana, A. Bajaj, R. Mout and V. M. Rotello, *Adv. Drug Deliv. Rev.*, 2012, **64**, 200-216.

130. J. V. Jokerst, T. Lobovkina, R. N. Zare and S. S. Gambhir, *Nanomed.*, 2011, **6**, 715-728.

131. J. Manson, D. Kumar, B. J. Meenan and D. Dixon, *Gold Bull.*, 2011, **44**, 99-105.

132. C. Peng, L. Zheng, Q. Chen, M. Shen, R. Guo, H. Wang, X. Cao, G. Zhang and X. Shi, *Biomater.*, 2012, **33**, 1107-1119.

133. W. Eck, G. Craig, A. Sigdel, G. Ritter, L. J. Old, L. Tang, M. F. Brennan, P. J. Allen and M. D. Mason, *ACS Nano*, 2008, **2**, 2263-2272.

134. K. Rahme, L. Chen, R. G. Hobbs, M. A. Morris, C. O'Driscoll and J. D. Holmes, *RSC Adv.*, 2013, **3**, 6085-6094.

135. T. Kubota, S. Kuroda, N. Kanaya, T. Morihiro, K. Aoyama, Y. Kakiuchi, S. Kikuchi, M. Nishizaki, S. Kagawa, H. Tazawa and T. Fujiwara, *Nanomed. Nanotech., Bio. Med.*, 2018, **14**, 1919-1929.

136. E. S. Day, L. R. Bickford, J. H. Slater, N. S. Riggall, R. A. Drezek and J. L. West, *Inter. J. Nanomed.*, 2010, **5**, 445-454.

137. D. C. Zelasko-Leon, C. M. Fuentes and P. B. Messersmith, *PloS one*, 2015, **10**, e0128756.

138. J. Spadavecchia, D. Movia, C. Moore, C. M. Maguire, H. Moustaoui, S. Casale, Y. Volkov and A. Prina-Mello, *Int J Nanomed.*, 2016, **11**, 791-822.

139. S. Liang, C. Li, C. Zhang, Y. Chen, L. Xu, C. Bao, X. Wang, G. Liu, F. Zhang and D. Cui, *Theranostics*, 2015, **5**, 970-984.

140. M. S. Mohamed, S. Veeranarayanan, A. C. Poulose, Y. Nagaoka, H. Minegishi, Y. Yoshida, T. Maekawa and D. S. Kumar, *Biochim. Biophys. Acta*, 2014, **1840**, 1657-1669.

141. O. Penon, M. J. Marín, D. A. Russell and L. Pérez-García, *J. Colloid Interface Sci.*, 2017, **496**, 100-110.

142. X. Sun, G. Zhang, R. S. Keynton, M. G. O'Toole, D. Patel and A. M. Gobin, *Nanomed. Nanotech., Bio. Med.*, 2013, **9**, 1214-1222.

143. T. Stuchinskaya, M. Moreno, M. J. Cook, D. R. Edwards and D. A. Russell, *Photochem. Photobio. Sci.*, 2011, **10**, 822-831.

144. J. Lin, F. Yan, L. Tang and F. Chen, *Acta Pharmacol. Sin.*, 2003, **24**, 241-246.

145. B. Lin, H. Chen, D. Liang, W. Lin, X. Qi, H. Liu and X. Deng, *ACS Appl. Mater. Inter.*, 2019, **11**, 11157-11166.

146. T. Liu, J. Tian, Z. Chen, Y. Liang, J. Liu, S. Liu, H. Li, J. Zhan and X. Yang, *Nanotech.*, 2014, **25**, 345103.

147. M. Podhorecka, A. Skladanowski and P. Bozko, *J. Nucleic Acids*, 2010, **2010**.

148. L. Ding, S. Xu, Y. Huang, Y. Yao, Y. Wang, L. Chen, Y. Zeng, L. Li, Z. Lin and L. Guo, *Anal. Chem.*, 2022, **94**, 7492-7499.

149. M. Xu, Y. Wen, Y. Liu, X. Tan, X. Chen, X. Zhu, C. Wei, L. Chen, Z. Wang and J. Liu, *Nanoscale*, 2019, **11**, 9661-9678.

150. K. H. Lee, J. Lee, J. S. Bae, Y. J. Kim, H. A. Kang, S. H. Kim, S. J. Lee, K. J. Lim, J. W. Lee, S. K. Jung and S. J. Chang, *MAbs*, 2018, **10**, 380-396.

151. T. M. Pierpont, C. B. Limper and K. L. Richards, *Front. Oncol.*, 2018, **8**.

152. M. R. Smith, *Oncogene*, 2003, **22**, 7359-7368.

153. T. Cerny, B. Borisch, M. Introna, P. Johnson and A. L. Rose, *Anti-Cancer Drugs*, 2002, **13**.

154. G. A. Leget and M. S. Czuczman, *Curr. Opin. Oncol.*, 1998, **10**, 548-551.

155. M. Abdollahpour-Alitappeh, S. M. Hashemi Karouei, M. Lotfinia, A. Amanzadeh and M. Habibi-Anbouhi, *Artif. Cells, Nanomed. Biotechnol.*, 2018, **46**, 1-8.

156. P. Boross and J. H. Leusen, *Am. J. Cancer Res.*, 2012, **2**, 676-690.

157. G. L. Plosker and D. P. Figgitt, *Drugs*, 2003, **63**, 803-843.

158. O. Shpilberg and C. Jackisch, *Br J Cancer*, 2013, **109**, 1556-1561.

159 X. Zhu, H. Zhou, Y. Liu, Y. Wen, C. Wei, Q. Yu and J. Liu, *Acta Biomater.*, 2018, **82**, 143-157.

160. G. Bisker, D. Yeheskely-Hayon, L. Minai and D. Yelin, *J. Controlled Release*, 2012, **162**, 303-309.

161. A. Weiss, T. C. Preston, J. Popov, Q. Li, S. Wu, K. C. Chou, H. M. Burt, M. B. Bally and R. Signorell, *J. Phys. Chem.*, 2009, **113**, 20252-20258.

2.0 General Methods

2.1 Materials

All solvents and reagents used in synthesis were purchased from Fischer Scientific, VWR Chemicals, Sigma Aldrich and Alfa Aesar without further purification and deuterated NMR solvents were purchased from Goss Scientific. Anhydrous solvents were dried over molecular sieves for 1 hour under a N_2 atmosphere (pyridine) or by PureSolv-EN solvent purification system (DCM, THF).

2.2 Synthesis techniques

All reactions were conducted under a N_2 atmosphere unless otherwise stated, using pre-dried glassware. All compounds were initially characterised by ^{1}H NMR on a Bruker AVIII300MHz spectrometer. 1D and 2D ^{1}H NMR spectroscopy, ^{13}C spectroscopy, HSQC and HMBC were carried out on a Bruker AVIII400MHz spectrometer. Electrospray ionisation mass spectra were collected on a Waters limited Xevo-G2-XS mass spectrometer attached to an Alliance e2695 LC unit and LC-MS spectra were performed on a Waters limited Synapt-G2-S mass spectrometer attached to an Alliance e2695 LC unit. Compounds prepared for MALDI analysis were performed on a Waters micromass limited MALDI Micro Mx with three different matrixes; Cobalt, gentisic acid and sinapinic acid.

2.3 Nanoparticle characterisation techniques

UV-Vis were collected by a Varian Cary 50, 60 or 5000 UV-Vis spectrometer at an acquisition rate of 300 nm min^{-1}. The aqueous solutions were prepared in 1 mL quartz cuvettes unless otherwise stated with a path length of 1 cm. Dynamic Light Scattering (DLS) measurements were carried out on a Malvern Zetasizer nano ZSP in 1 mL quartz cuvettes with a 1:1 dilution

factor. Transmission electron microscopy imaging was conducted on a JEOL1400 transmission electron microscope at ~ 1 nM on a copper 200 mesh formvar coated TEM grid.

2.4 Photophysical characterisation techniques

UV-Vis were collected by a Varian Cary 60 or 5000 UV-Vis spectrometer at an acquisition rate of 300 nm min^{-1}. The aqueous solutions were prepared in 1 mL quartz cuvettes unless otherwise stated with a path length of 1 cm. Luminscence excitation and emission spectra were conducted on an Edinburgh FLS920 spectrometer using a 450 W xenon lamp and time resolved spectroscopy was conducted on a 445 nm pulse diode laser in aerated water and analysed on the FAST software. Luminescence QY for ruthenium was measured using an integrated sphere whilst osmium was analysed using an internal reference standard, indocyanine green.

$$\Phi_x = \Phi_{ref} \left(\frac{A_r}{A_x}\right)\left(\frac{I_r}{I_x}\right)\left(\frac{n_x^2}{n_r^2}\right)\left(\frac{D_x}{D_r}\right)$$

Where Φ is the quantum yield, A is the absorbance, I is the intensity of the lamp, n is the refractive index of the solvent, D is the integral of the peak, x is the sample and r is the reference. Inductively coupled mass spectrometry was performed at the University of Warwick using an ICP-MS (Agilent LC-ICP-MS (7500cx) with an integrated auto sampler to determine gold, ruthenium and osmium concentrations. Metal concentrations were determined via PlasmCal calibration standards with R^2 values > 0.999 for ruthenium and >0.99 for gold and osmium.

2.5 Cell viability assays

Cell viability assays were conducted using MTT assay and cell titre glo assay. For MTT assays, cells were seeded at a density of 5000 cells per well in a 96 well plate. Nanoparticle concentrations were varied across the plate through a 1 in 2 dilution factor in six technical replicates. Cells were dosed with the gold nanoparticle samples and incubated for 24 hours at

37°C in a 5% CO_2 atmosphere. The cells were washed with phenol red free media and then further incubated with MTT reagent (3-(4,5-dimethylthiazol-2-yl)-2,5-diphenyltetrazolium bromide) in dulbecco's modified eagle medium (DMEM) supplemented with 10% fetal bovine serum for 4 hours and then removed completely. DMSO was added to each well and then analysed on a tecan infinite 200 probe plate reader. MTT assays were performed by Dr Garret Rochford.

For cell titre glo assay, cells were seeded at a density of $1x10^5$ cells per well in a solid bottom luminescence white 96-well plate. Cells were dosed with gold nanoparticles at varying concentrations in a 1:10 dilution (sample:complete media) for 18 hours at 37°C in a 5% CO_2 atmosphere. The cells were allowed to cool to RT before adding 25µL cell titre glo reagent and analysed on an EnVision 2105 Multimode plate reader.

All statistical analysis was performed by 1-way ANOVA followed by a Dunnetts t-test corrected for multiple comparisons.

2.6 Flow cytometry

The cells were cultured in 60 mm dishes, 1×10^5 cells per dish and the samples added in a ratio of 1:1 dilution factor and incubated for 18 hours at 37°C in a 5% CO_2 atmosphere. The samples were ran on an LSR- II flow cytometer used in the Institute of Cancer and Genomic Sciences using the FACSDiva software. Analysis was performed on FlowJo by Dr Tracey Perry (Institute of Cancer and Genomic Sciences).

2.7 Confocal microscopy and mass spectrometry imaging

Confocal microscopy of live cells was performed using a Leica TCS SP8 upright confocal laser scanning system using a 40 x ceramic H_2O immersion dip objective lens. 405 nm, 458 nm, 488 nm, 633 nm solid-state laser lines were used. Live cell images were imaged immediately after

washing. Fixing of cells was achieved through addition of 4 % paraformaldehyde (PFA) to each well (1 mL per well) for 15 minutes in the dark. PFA was removed and cells washed twice in PBS. Coverslips were removed and mounted on a droplet of hydromount media (National Diagnostics, UK) on glass slides, stored flat in the dark for at least 24 hours at 4 °C before imaging. For tissue imaging, slides were mounted with cover slips using a droplet of Hydromount media (National Diagnostics, UK) and stored flat in the dark for at least 24 hours at 4 ºC before imaging was conducted. All images were processed using ImageJ.

For mass spectrometry imaging, tissue sections on ITO slides were incubated with 3 nM RuPhen•PEG•AuNP and 3 nM RuPhen•RXB•AuNP in the presence of ammonium citrate (0.5 mM) for 18 hours in the dark in the fridge (4 ºC). Samples were then washed twice with PBS-T and baked at 60 ºC for an hour. Mass spectrometry imaging was conducted on a Bruker Ultraflextreme MALDI using an MTP-Slide adapter-II plate of treated tonsil tissues mounted on ITO slides using an automated run using FC-randomwalk in reflectron mode at 53 % laser power, 500 shots at 100 Hz between 100 to 2000 Da. Images were processed on FlexImaging 3.0.

3.0 Evaluation of Ruthenium Coated Gold Nanoparticles for Applications in Optical Microscopy and Mass Spectrometry Imaging

3.1 Introduction

Over recent years the utilisation of transition metal complexes for imaging in biological samples has received great interest due to their favourable properties over that of organic dyes.[1-3] However, despite the vast interest in the development of new transition metal complexes for bio-imaging agents, low molecular weight organic dyes are still the most commonly used imaging agents in biological studies and clinical applications.[4] Iridium(I), ruthenium(II) and osmium(II) metal complexes are just some of the few metals that have been investigated for optical imaging in biological applications.[5-12] Luminescent transition metal complexes offer many desirable properties arising from their large Stokes shift, tunable triplet metal to ligand charge transfer (^{3}MLCT) emission through substitution of their ancillary ligands and/or metal center, relatively long luminescent lifetimes and they are unsusceptible to photobleaching.[11,13-22] Additionally, transition metal complexes have excellent photostability and chemical stability compared to organic probes alongside the ability for generating high $^1O_2$ production and as such have been found to be excellent candidates for imaging probes and their utilisation in the medical field.[8,23-27] There have been many studies over the years involving luminescent transition metal complexes for biological applications and such metal complexes have also been researched as sensing agents, anticancer agents and photo-redox catalysts.[1,28-32]

The development of ruthenium(II) metal complexes employed in biological applications originated from Barton *et al*.[33] They developed a series of complexes that could act as molecular light switches for DNA and possessed the ability to be able to distinguish between DNA structures.[33,34] Additionally, they first used fluorescence microscopy to study the cellular uptake

of ruthenium(II) complexes in 2007 and since then has initiated the gradual exploration of luminescent ruthenium(II) complexes for bioimaging agents.[35] Such complexes have been found to be ideal candidates due to their singlet oxygen production ($^1O_2$) as well as their photostability and desirable photophysical properties.[36,37] Selective targeting for cellular components is of great interest for imaging and anticancer applications and more recently, ruthenium(II) complexes have been extensively studied as DNA and luminescent recognition and sensing probes.[18,38-40] This can be achieved through structural decoration such as the incorporation of planar ligands (e.g. dipyridophenazine, dppz) that can bind to DNA under physiological conditions or through the conjugation of moieties that can target specific proteins and nucleic acids.[41]

Complexes containing dppz ligands used for DNA binding are known as "lightswitches" which have desirable diagnostic and therapeutic applications but such complexes typically exhibit low cellular uptake.[34,42,43] However, enhancement of cellular uptake of $[Ru(bpy)_2(dppz)]^{2+}$ via passive diffusion was achieved through relatively stable ion-pairing allowing nuclear localisation. The complex in the absence and presence of pentachlorophenol (PCP) was incubated in human hepatocyte (QSG-7701) cells for 3 hours and then imaged through confocal luminescence microscopy correlating them to two well-known organic nuclear dyes (Hoescht 33342 and DAPI) (Figure 3.1.1).[44] Confirmation of nuclear localisation was achieved through overlay of the complex and nuclear dyes and additionally through transmission electron microscopy.[44]

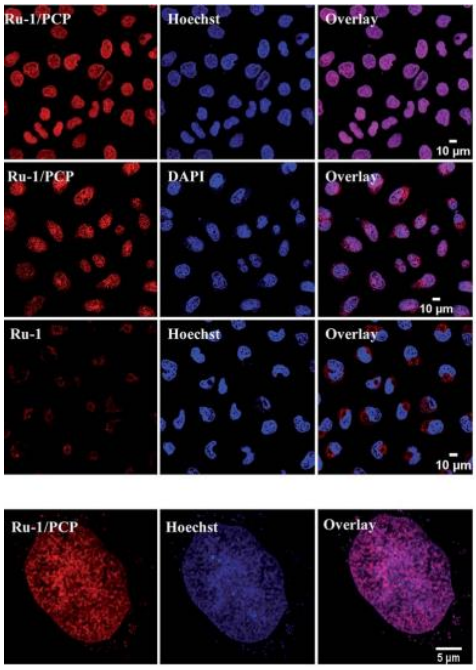

Figure 3.1.1. Luminescence confocal microscopy of $[Ru(bpy)_2(dppz)]^{2+}$ in the presence and absence of PCP with. Hoescht 3342 and DAPI staining in QSG-7701 cells for 3 hours and three dimensional structured microscopy with higher spatial resolution. Figure taken from Zhu *et al.*[44]

Alternatively, some ruthenium(II) metal complexes have been reported to accumulate in the mitochondria. Due to the membrane potential of the mitochondria, it is well known that targeting can be achieved through the development of highly lipophilic and charged metal complexes which can enter the cells primarily through passive diffusion.[30,45-47] Triphenylphosphine substituents are widely used for the targeting of mitochondria and several ruthenium(II) complexes containing this targeting moiety have been implemented.[35,48,49] Four ruthenium(II) complexes were synthesised to target mitochondria as one and two photon anti-cancer agents (Figure 3.1.2). These complexes displayed low cytotoxicity and very high $^1O_2$ quantum yields in methanol to trigger cell death with significant accumulation within the mitochondria of HeLa cells.[19]

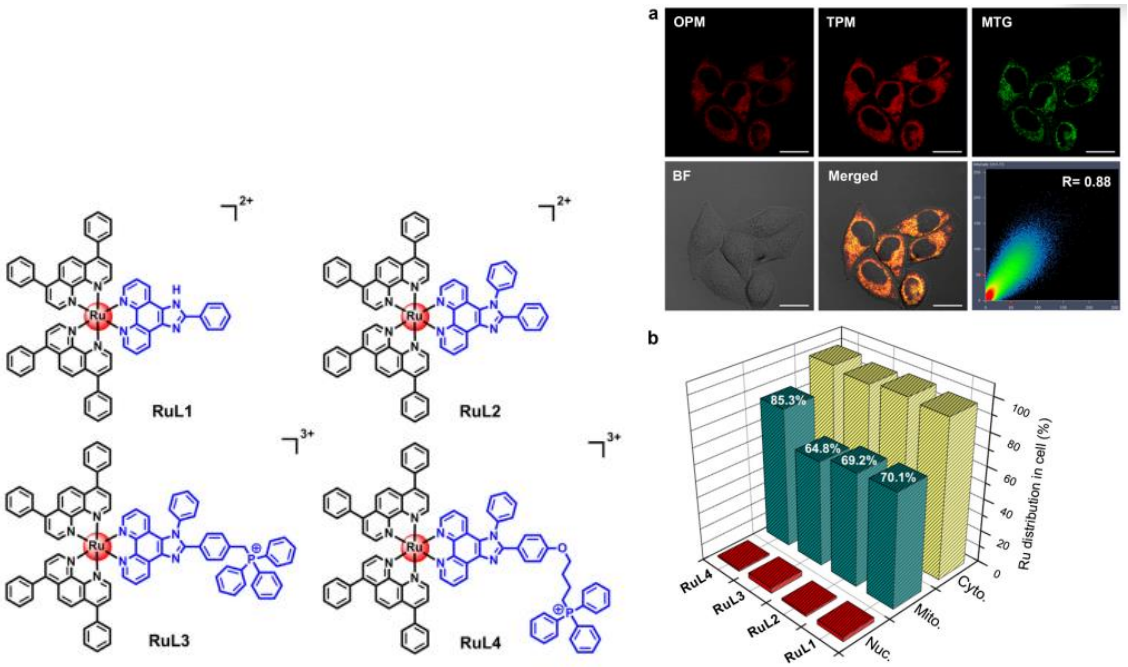

Figure 3.1.2. Chemical structures of RuL1-RuL4 (left) and one and two photon imaging of HeLa cells incubated with 10 µM RuL4 (λ_{exc} = 458 nm, λ_{em} = 610 nm) and MitoTracker green (λ_{exc} = 488 nm, λ_{em} = 510 nm) for 2 hours at 37°C. Scale bar = 20 µm (a). ICP-MS quantification ruthenium in HeLa cells treated with 10 mM RuL1 – RuL4 at 37°C for 2 hours (b). Figure taken from Liu *et al*.[19]

Correlation studies were performed through confocal luminescence microscopy involving mitotracker green which portrayed a high correlation coefficient (0.88). Inductively coupled mass spectrometry analysis of the cellular compartments was ascertained further confirming the presence of the ruthenium(II) complexes within the mitochondria.

Citrate capped gold nanoparticles display many advantageous properties ideal for imaging and biomedical purposes and have proven to have a promising future within these fields. Not only they are very easy to synthesise, but are also water soluble, non-cytotoxic, easily stabilised, can be conjugated to a variety of targeting/imaging moieties and can penetrate cells/tumours with a high retention.[50-55] Such particles are also ideal for transmission electron microscopy (TEM) due to the high electron density and they possess high light scattering for reflectance based microscopy.[56] Although gold nanoparticles can be imaged through their own unique properties

(such as photoacoustic imaging, TEM etc) they are usually conjugated with a lumophore to be observed under optical microscopy. The surface chemistry of gold nanoparticles is extremely important in absorption, distribution, metabolism, excretion and the toxicity. Surface functionalisation of gold nanoparticles is highly controllable thus the surface chemistry and hydrodynamic diameter as well as their bio-distribution can be tailored by a safe-by-design approach.[57-60] Due to this, there has been a great advancement and research for gold nanoparticle systems involving lumophores, antibodies, proteins and small molecules as delivery, detection and sensing systems.[56,61-64]

A study consisting of approximately 15 nm gold nanoparticles was reported and gold nanoparticles were conjugated to three ruthenium(II) metal complexes for studying their interaction with DNA (Figure 3.1.3). The systems displayed a low cytotoxicity profile and demonstrated their potential as live cell imaging agents.[65]

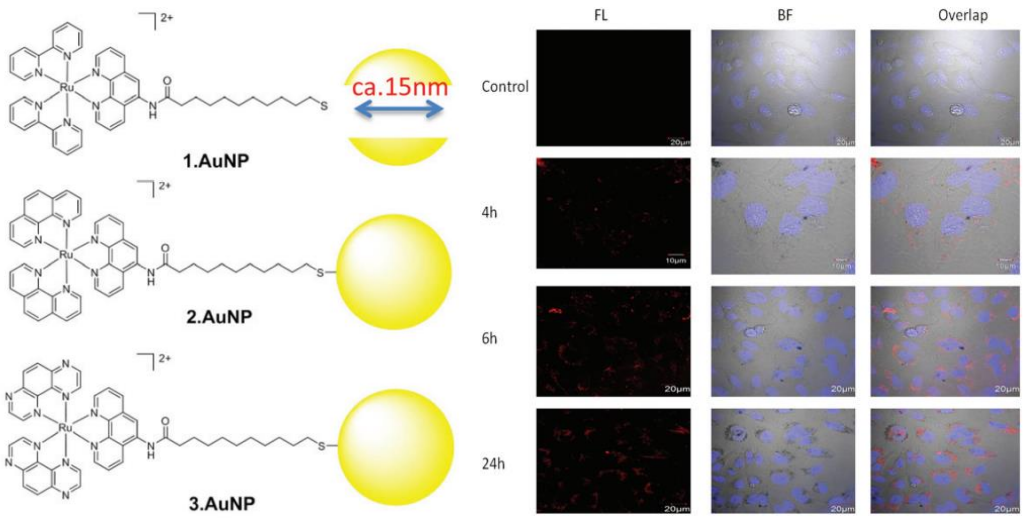

Figure 3.1.3. Representative cartoon and structures of ruthenium decorated gold nanoparticles (left) and confocal luminescence microscopy of HeLa cells treated with 3.AuNP for 2 – 24 hours (right). Figure take from Martinez-Calvo *et al.*[65]

They concluded that 3-AuNP was the most favourably stable in water and buffered solution and emission of this system within HeLa cells became stronger over time. This

suggests the nanoparticles are being readily taken in a time-dependent manner and although localisation cannot be confirmed, their potential for imaging and cellular applications remains very promising.

Although organic dyes and transition metal complexes are useful as optical microscopy agents, the use of transition metal complexes in mass spectrometry imaging is limited. Utilising mass spectrometry imaging based techniques offers unique advantages over fluorescence microscopy due to the absence of fluorescent probes or radioactive labels.[66-68] Mass spectrometry imaging (MSI) is an incredibly useful technique that offers determination of a variety of different sized biomolecules and even single atoms with their characteristic isotope patterns.[69] There are a plethora of techniques capable of imaging metals using mass spectrometry some of which include matrix assisted laser desorption ionization (MALDI), desorption electrospray ionisation (DESI), secondary ion mass spectrometry (SIMS) also including nanoscale ion microprobe SIMS (NanoSIMS) and time-of-flight SIMS (ToF-SIMS).[69] The techniques employed tend to direct towards the nature of resolution and detection such as MALDI being preferred for tissue/organ analysis due to the inability to image on a single cell level in contrast to other techniques such as SIMS. MALDI relies on the incorporation of a matrix to absorb the bulk energy of the laser resulting in the intact detection of molecules. Additionally using MSI based techniques eliminates the possibility of artifacts arising from fluorescence microscopy since emission of lumophores can be altered through the environment and through quenchers.[34,70]

Metals employed for MSI possess very unique isotopes that are not usually detectable in native biological systems allowing them to be highly distinguishable when their distributions in a biological system are analysed. Over the years there have been a handful of studies relating to the employment of ruthenium(II) metal complexes for mass spectrometry imaging. Ruthenium-arene 1,3,5-triaza-7-phosphaadamantane (RAPTA) complexes containing ^{13}C and ^{15}N

radiolabels on the arene and PTA ligands respectively was synthesised to study the mechanism of action within human ovarian cancer cells through using NanoSIMS (Figure 3.1.4).[71,72]

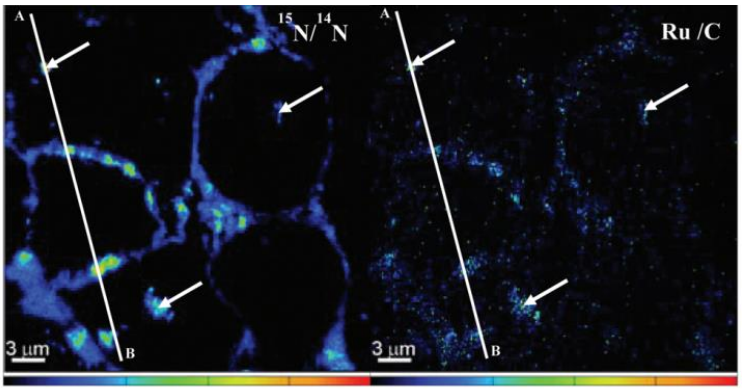

Figure 3.1.4. Secondary ion maps of $^{15}N/^{14}N$ and $^{102}Ru/^{12}C$ in A2780CR cells treated with ^{15}N and ^{13}C labelled RAPTA-T (500 µM) for 24 hours. The white line (A-B) represents the line profile. Figure taken from Lee *et al*.[71]

The radiolabeled ^{15}N and ruthenium signal was co-localised to determine the distribution of the metal complex within cells which suggested localisation on the membrane correlating the RAPTA anti-metastatic activity.[71,73] Additionally, a dual targeting ruthenium(II) anti-cancer complex was analysed under ToF-SIMS to obtain subcellular images in HeLa cancer cells.[73] Further to this, correlation of fluorescence microscopy with available cellular dyes was used with ToF-SIMS for subcellular distribution of the ruthenium(II) complex. The mapping of ruthenium signal was found to be present in the cell membrane and inside the cell demonstrating the potential for MSI on the cellular level.[73-75]

However, gold has also been shown to be effective for MSI. The incorporation of gold nanoparticles not only can act as a scaffold for delivery but also a matrix and detection marker for the employment into MSI.[76] Gold nanoparticles possess the ability to absorb energy from the laser and transfer it to its surface bound ligand which provides a highly sensitive detection technique.[66] Three gold nanoparticle systems were developed each containing a unique

detection molecule at the terminal end with a stability and biocompatibility moiety anchored onto the gold nanoparticle (Figure 3.1.5). These various detection molecules acted as mass tags viable for detection and distribution within mice after 24 hour incubation.[66]

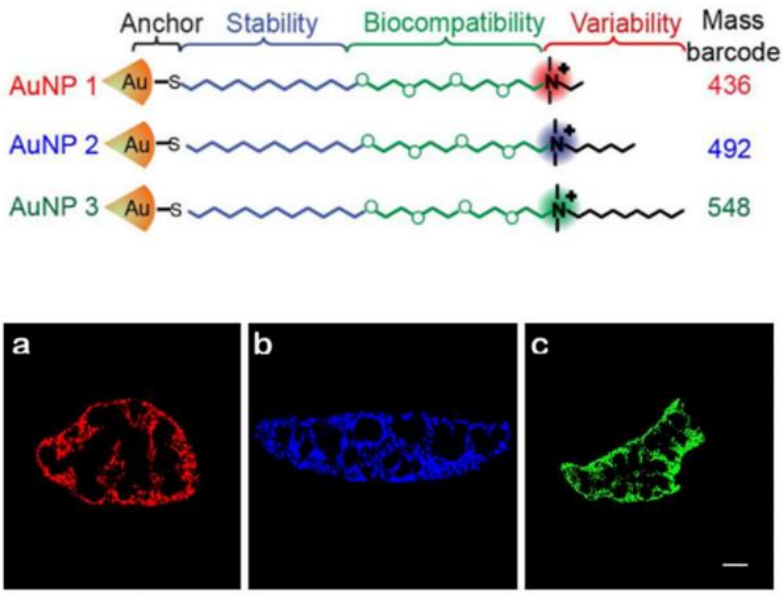

Figure 3.1.5. Structures of ruthenium mass codes labelled on gold nanoparticles (top) and LDI-MS images (bottom) of mouse spleens treated with gold nanoparticles 1-3. Ions used for detection are listed above. Scale bar = 500 µm. Figure taken from Yan *et al.*[66]

Analysis of each of the gold nanoparticle systems through detection of the unique barcodes displayed accumulation in the red pulp of splenic tissue. Alternatively to using detectable moieties anchored to gold nanoparticles, gold ions released from the nanoparticles have also been employed for detection and mapping through mass spectrometry imaging (Figure 3.1.6).[77]

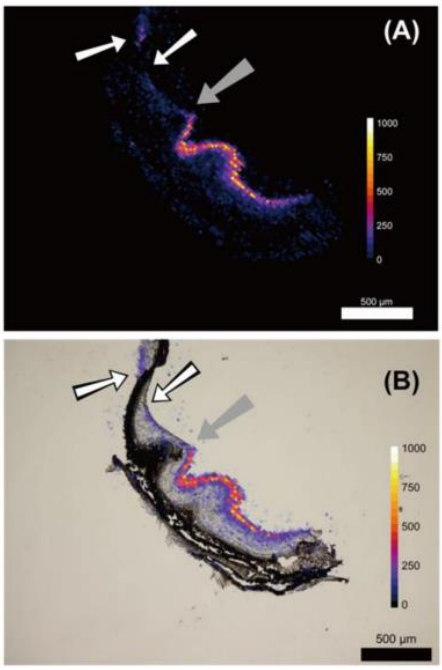

Figure 3.1.6. MSI of $[Au_2]^+$ ions (m/z 394) derived from section of eye tissue (a) and overlap of MSI and brightfield image (b). Image taken from Muko *et al*.[77]

A donkey anti-rat IgG antibody labelled with Cy3 was decorated onto the gold nanoparticle and stained on transgenic zebrafish eyeballs to target green fluorescence proteins before being imaged through fluorescence and mass spectrometry imaging. The mass spectrometry images were found to be more amenable towards $[Au_2]^+$ (394 m/z) ions through analysis of the ion heat maps. Strong intensities were observed in the outer most area of the tissue sample where it was expected the most green fluorescence proteins are produced and weaker signals observed indicated by the gray arrow. This is believed to be from tissue twisting and the white arrows indicate layering that has significantly suppressed the ion intensity signal. However, sufficient detection was achieved through analysis of $[Au_2]^+$ and has demonstrated the use of gold ions for detection and imaging in mass spectrometry.

Although there are many examples of ruthenium(II) and gold nanoparticles for optical imaging, their use for mass spectrometry imaging is even fewer. Therefore, designing a luminescent

ruthenium(II) metal complex that can be utilised for the dual imaging modalities through optical and mass spectrometry as a targeting agent towards cancer cells and tissue can provide useful information for detection, localisation and potentially tumour size.

3.2 Chapter outline

In this chapter we have evaluated and compared the photophysical properties of three ruthenium(II) complexes in aerated conditions in the absence and presence of a fluorosurfactant prior to conjugation to gold nanoparticles. These complexes have been previously studied for their applications in dye sensitised solar cells by a former group member, Shani Osborne.[53,78] We selected the ruthenium(II) complex that demonstrated the greatest enhancement when attached onto gold nanoparticles to evaluate their properties as live cell and mass spectrometry imaging agents that will accompany further studies when concerning targeted approaches towards cancer cell lines. MTT assays were ascertained to provide dosing concentrations of ruthenium(II) coated gold nanoparticles in live A549 cells. Confocal luminescence microscopy revealed localisation of the particles throughout the cytoplasm demonstrating the optical properties of RuPhenSS as a viable imaging probe. Mass spectrometry via MALDI was then conducted to detect the isotopically unique pattern of ruthenium on the gold surface. Although weak detection was observed, the gold ions generated from MALDI seemingly provides a promising detection method over ruthenium.

3.3 Results and Discussion

3.3.1 Evaluation of ruthenium(II) metal complexes

3.3.1.1 Synthesis

The ligand BpySS (also known as S12) was synthesised containing two disulphide legs for attachment onto the gold nanoparticle surface with sufficient distance between the gold surface and the metal center to reduce quenching effects. BpySS has been synthesised and fully characterised previously in our group and was selected to be the optimal ligand for limited quenching from the gold nanoparticle to the metal centre.[9,78-80]

Alternatively to BpySS, the S8 ligand that was previously synthesised and characterised within the Pikramenou group was also employed.[53,78] This is hypothesised to possess greater photophysics due to decreased quenching from $^{3}O_{2}$ when attached to the metal complex due to no adjacent oxygen on the 4,4' position of the bipyridine ring.[53] Each product in the synthetic routes of BpySS and S8 was characterised through ^{1}H NMR spectroscopy and mass spectrometry with the final products having ^{13}C NMR spectroscopy and results in good agreement with previously published data.[9,78-81] The synthesis of BpySS and S8 was confirmed through ^{1}H NMR, ^{13}C NMR and mass spectrometry (ESI^{+}) revealing a mass of 735.31 m/z indicative of $[M+H]^{+}$ for BpySS and 591.20 m/z indicative of $[M+H]^{+}$ for S8.

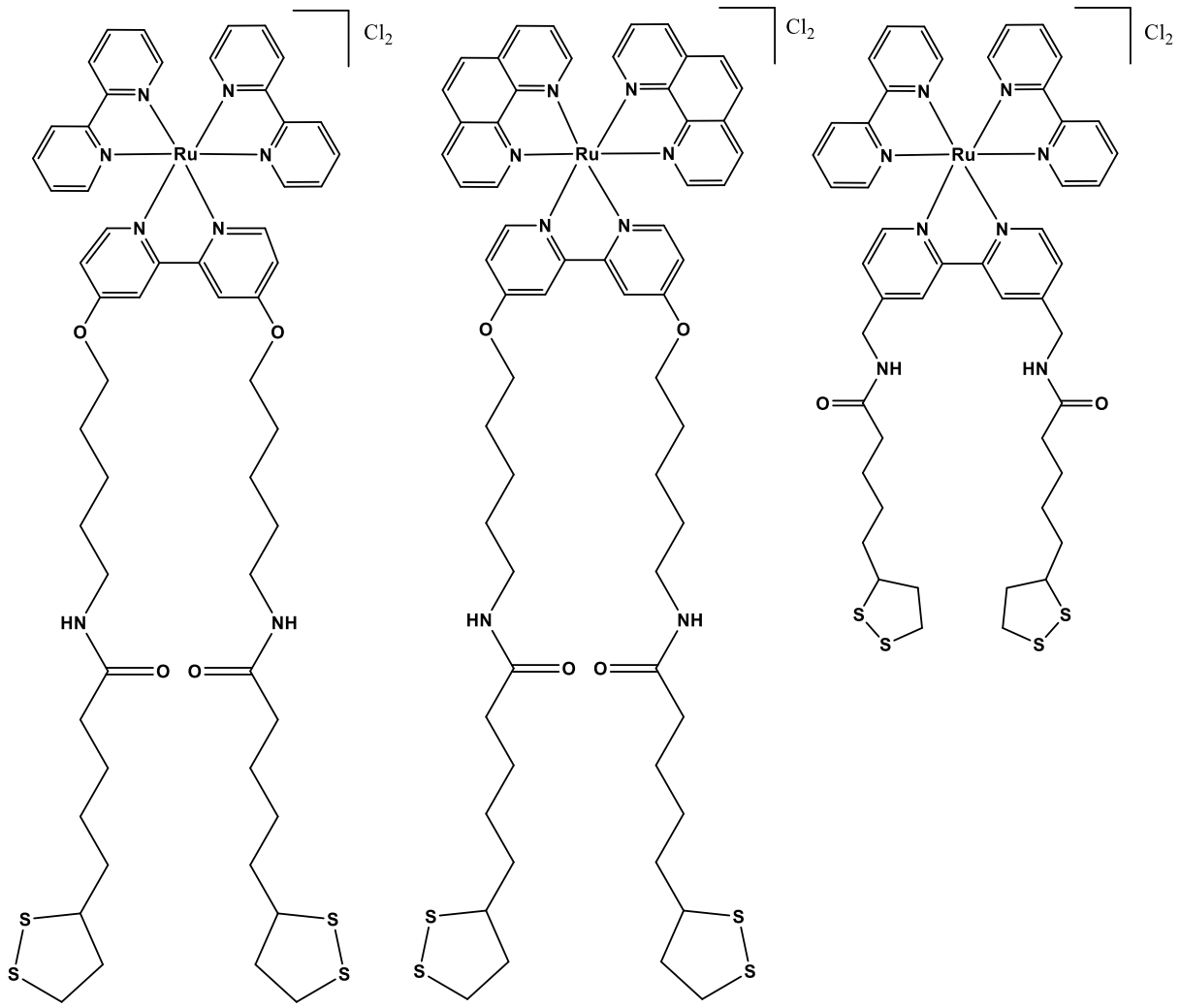

Figure 3.3.1.1.1. Structural representation of RuBpySS (left), RuPhenSS (middle) and RuS8 (right).

RuBpySS and RuPhenSS are based on the tris(bipyridine) and tris(phenanthroline) ruthenium counterparts. The metal complexes were characterised through ^{1}H NMR spectroscopy, ^{13}C NMR spectroscopy, HSQC, UV-Vis spectroscopy and mass spectrometry which is in good agreement with previously reported data.[53,78] RuPhenSS was designed for improved photophysics thereby resulting in stronger detection for optical microscopy applications. Phenanthroline ligands employed in metal complexes have been shown in literature to yield

longer luminescent lifetimes and improve the photophysics.[82] Additionally, phenanthroline ligands have also been seen to display blue shifts in emission and give rise to slightly higher molar extinction coefficients in comparison to their bipyridine analogues.[83-86]

The complex RuS8 was designed in order to improve the photophysics from that of RuBpySS through the design of removing the oxygen in the 4,4' position on the bipyridyl. This was designed in the hopes to reduce $^3O_2$ quenching of the complex and therefore increase the photophysical properties in aerated conditions. Determination of their photophysics in aerated conditions was conducted in order to evaluate and select the complex with the greatest potential for optical imaging via confocal microscopy. The three complexes evaluated in this chapter are RuBpySS, RuPhenSS and RuBpyS8 and compared to previously reported data.[53,78]

3.3.1.2 Photophysical characterisation of ruthenium(II) metal complexes

The UV-Vis, quantum yield (QY), emission, excitation and luminescence lifetimes were taken in solution in aerated water. The complexes RuBpySS, RuPhenSS and RuS8 containing the chloride counter ion were dissolved in methanol to yield stock solutions of 1 mM, 0.9 mM and 1 mM respectively and the dissolved in water to yield 20 µM, 18 µM and 20 µM solutions.

The absorption profiles of each of the three complexes are very similar to one another. Each metal complex displays a singlet metal to ligand charge transfer (^{1}MLCT) (d – π^*) centered between 400 – 500 nm. The RuPhenSS and RuS8 display an absorption maxima at 457 nm and 456 nm respectively whereas the RuBpySS complex displays a maximum centered at 460 nm in water. There is a slight blue shift in ^{1}MLCT of 3 nm between the RuPhenSS and RuBpySS complex. It has been well documented in the literature that phenanthroline metal complexes display blue shifts so this was not unexpected.[34,86-88] The same shift was also observed from

RuS8 to RuBpySS causing a 4 nm blue shift and is attributed to the lack of oxygen adjacent to the π rich ring system unlike the complex RuBpySS. All metal complexes, RuBpySS, RuPhenSS and RuS8 display a metal center (MC) absorption band (d – d) at ~430 nm. RuBpySS and RuS8 displays a sharp ligand center (LC) (π - π*) band at ~ 288 nm whereas RuPhenSS displays a sharp LC band at 265 nm. This has been blue shifted by approximately 20 nm. The molar absorptivity's of the complexes revealed a similar extinction coefficient between RuBpySS and RuS8 of 12000 M^{-1} cm^{-1}. The molar absorption of RuPhenSS was found to be 13000 M^{-1} cm^{-1}. RuPhenSS displays a slightly higher molar absorption which agrees with literature as it is known that phenanthroline ligands yield slightly higher molar absorptions when compared to bipyridine structures.[83-85]

Each emission profile of the metal complexes are very similar to each other and are very broad ranging from 550 nm to 800 nm. RuBpySS has a ^{3}MLCT maxima at 645 nm where as RuPhenSS has a ^{3}MLCT maxima at 630 nm. This is blue shifted by 15 nm in comparison to RuBpySS and is attributed to the phenanthroline character. RuS8 displays a ^{3}MLCT emission maxima at 635 nm which is 10 nm blue shifted in comparison to RuBpySS and is attributed to the S8 ligand. The excitation of each ruthenium complex mirrors the UV-Vis absorbance profile (Figure 3.3.1.2.1).

Table 3.3.1.2.1. UV-Vis, molar absorptivity, emission, lifetime and quantum yield of RuBpySS, RuPhenSS and RuS8 in aerated water.

Sample	UV-Vis λ_{max} / nm (ε / M^{-1} cm^{-1})	Emission λ_{max} / nm	τ/ ns	Φ/ %
RuBpySS	462 (12000), 430 sh, 288 (68000), 224 sh	645	285	2
RuPhenSS	457 (13000), 430 (sh), 263 (81000), 222 (84000)	630	540	2
RuS8	457 (12000), 430 (sh), 287 (72000), 244 (27000)	635	393	3

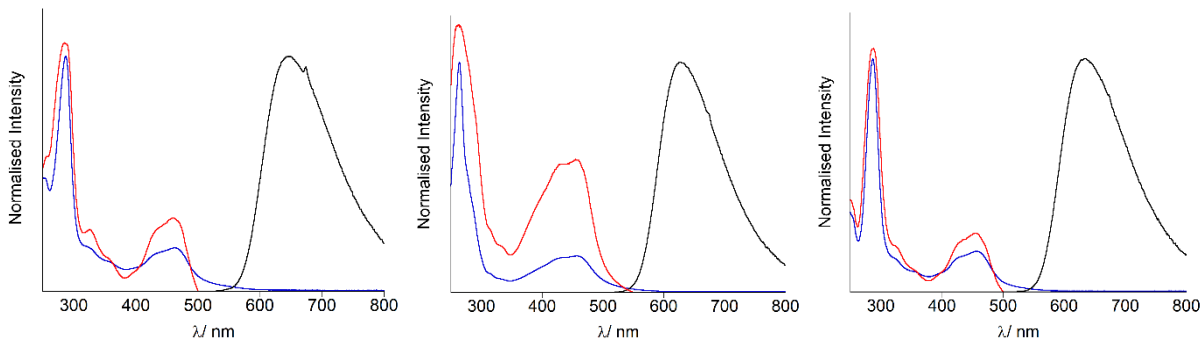

Figure 3.3.1.2.1. Normalised UV-Vis (blue), excitation (red) and emission (black) of 20 µM RuBpySS (λ_{exc} = 462 nm, λ_{em} = 645 nm) (a) 18 µM RuPhenSS (λ_{exc} = 457 nm, λ_{em} = 630 nm) (b) and 20 µM RuS8 (λ_{exc} = 457 nm, λ_{em} = 635 nm) (c) in aerated water.

The luminescent lifetimes of each complex was taken in aerated water (appendix). RuBpySS displays a lifetime of 285 ns. RuPhenSS shows a lifetime almost double that of RuBpySS of 540 ns and RuS8 displaying 393 ns owing to the phenanthroline behaviour. The QY of all the complexes was found to be around 2 – 3%. The results are in agreement with previously published data.[53,78]

3.3.1.3 Influence of fluorosurfactant for improving photophysics of ruthenium(II) metal complexes

The photophysical properties of the ruthenium(II) metal complexes were investigated in the presence of a fluorosurfactant, Zonyl FSA. Stock solutions of RuBpySS, RuPhenSS and RuS8 were dissolved in methanol yielding 1 mM, 0.9 mM and 1 mM concentrations respectively. The same concentrations of the metal complexes was maintained constant for comparing the photophysics in the presence and absence of the fluorosurfactant. To characterise the luminescence properties in the presence of the fluorosurfactant the UV-Vis, QY, emission, excitation and luminescent lifetimes was recorded.

Within the Pikramenou group, the choice of fluorosurfactant used is Zonyl FSA. Zonyl FSA has also been shown to enhance the photophysics of metal complexes in solution and provide excellent stability of coated gold nanoparticles within a biological sample.[7,65,78,79,81] Additionally, due to the layer of surfactant, this impedes adsorption of unwanted biological compounds onto the nanoparticle surface making this highly desirable for the stability of nanoparticles and less susceptible to modification which has been previously explored.[57,80,89-92] Zonyl FSA was added in excess to the solutions of the metal complexes to observe an enhancement of their luminescent properties whilst unaffecting the ^{1}MLCT and ^{3}MLCT pathways. The absorption spectra for each metal complex remains similar to that of the spectra without the presence of Zonyl FSA indicating the fluorosurfactant does not change the viability or position of the MLCT state (Figure 3.3.1.3.1).

Table 3.3.1.3.1. UV-Vis, molar absorptivities and photophysical characterisation of 20 µM RuBpySS, 18 µM RuPhenSS and 20 µM RuS8 in the presence of 164 µM Zonyl FSA in aerated water.

Sample	UV-Vis λ_{max} / nm (ε / M^{-1} cm^{-1})	Emission λ_{max} / nm	τ/ ns	Φ/ %
RuBpySS	462 (11000), 430 sh, 288 (62000), 228 sh	650	350	2
RuPhenSS	457 (13000), 430 (sh), 263 (80600), 222 (90300)	634	745	3
RuS8	457 (13000), 430 (sh), 287 (69000), 244 (27000)	635	600	4

For both RuBpySS and RuPhenSS, a very slight red shift in emission maxima is observed by 5 nm and 4 nm respectively whereas RuS8 displays no shift in emission in comparison for the emission of the complexes in the absence of Zonyl FSA. This shows that the presence of the fluorosurfactant displays a negligible effect on the ^{3}MLCT emission pathway for RuBpySS, RuPhenSS and RuS8.

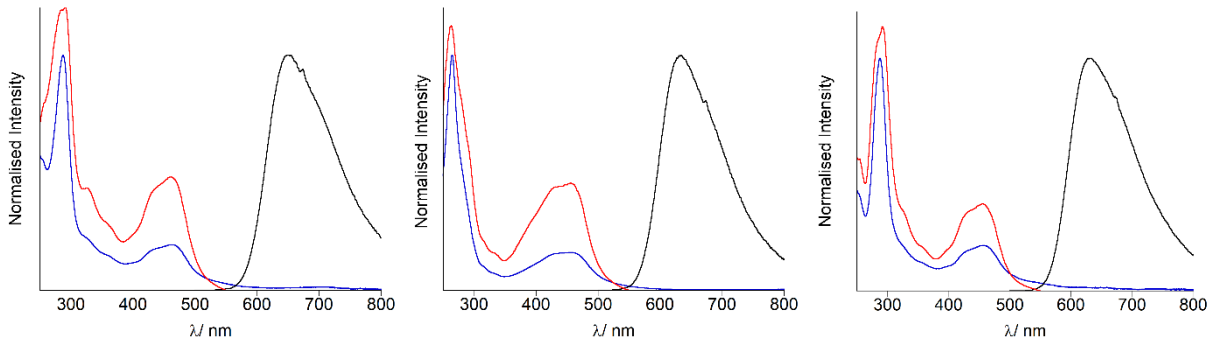

Figure 3.3.1.3.1. Normalised UV-Vis (blue), excitation (red) and emission (black) of 20 µM RuBpySS (λ_{exc} = 462 nm, λ_{em} = 645 nm) (a) 18 µM RuPhenSS (λ_{exc} = 457 nm, λ_{em} = 630 nm) (b) and 20 µM RuS8 (λ_{exc} = 457 nm, λ_{em} = 635 nm) (c) in the presence of 164 µM Zonyl FSA in aerated water.

To observe whether an increase in their luminescent lifetimes is seen, time resolved luminescence spectroscopy was performed on each of the metal complex solutions containing excess Zonyl FSA (appendix). For RuBpySS, an increase is observed from 285 ns from the free complex in solution to 350 ns; resulting in a 23% increase. For RuPhenSS, the lifetime increased from 540 ns to 750 ns, a 39% increase where as RuS8 increased from 393 ns to 600 ns resulting in a 53% increase. These increases in lifetime may be attributed to the fluorosurfactant interacting with the molecular complexes and protecting it from $^3O_2$ quenching. These increments in lifetimes is dependent on how strongly the fluorosurfactant interacts with molecular complex and suggests that the surfactant interacts more strongly in the case of RuS8 than RuPhenSS and RuBpySS. By increasing the hydrophobicity of the metal complex, this in turn increases the interaction of the fluorosurfactant and shielding from oxygen resulting in a positive change in the luminescent lifetimes. RuS8 was designed in order to enhance the luminescent capabilities by removal of the oxygen present in the 4,4' position on the bipyridine moiety to minimize $^3O_2$ quenching. It is evident that the lack of oxygen present enhances the luminescent properties of the complex over that of RuPhenSS and RuBpySS resulting in the largest increase.

Additionally, the QY for the metal complexes in the presence of Zonyl FSA displays a slight increase in quantum yield for RuPhenSS and RuS8. This is believed to be due to an increase from the LC band to the emission. The results are in agreement with previously published data.[53,78]

3.3.2 Coating of 13 nm gold nanoparticles with fluorosurfactant and metal complexes

3.3.2.1 Synthesis of 13 nm and 25 nm gold nanoparticles

The synthesis of gold nanoparticles were based on the previously published method by Vossemeyer *et al.*[55] Gold nanoparticles of larger sizes allows greater visualisation through reflectance based microscopy and possess a larger surface area allowing theoretically more complexes per nanoparticle resulting in stronger detection of the lumophores present on the surface.

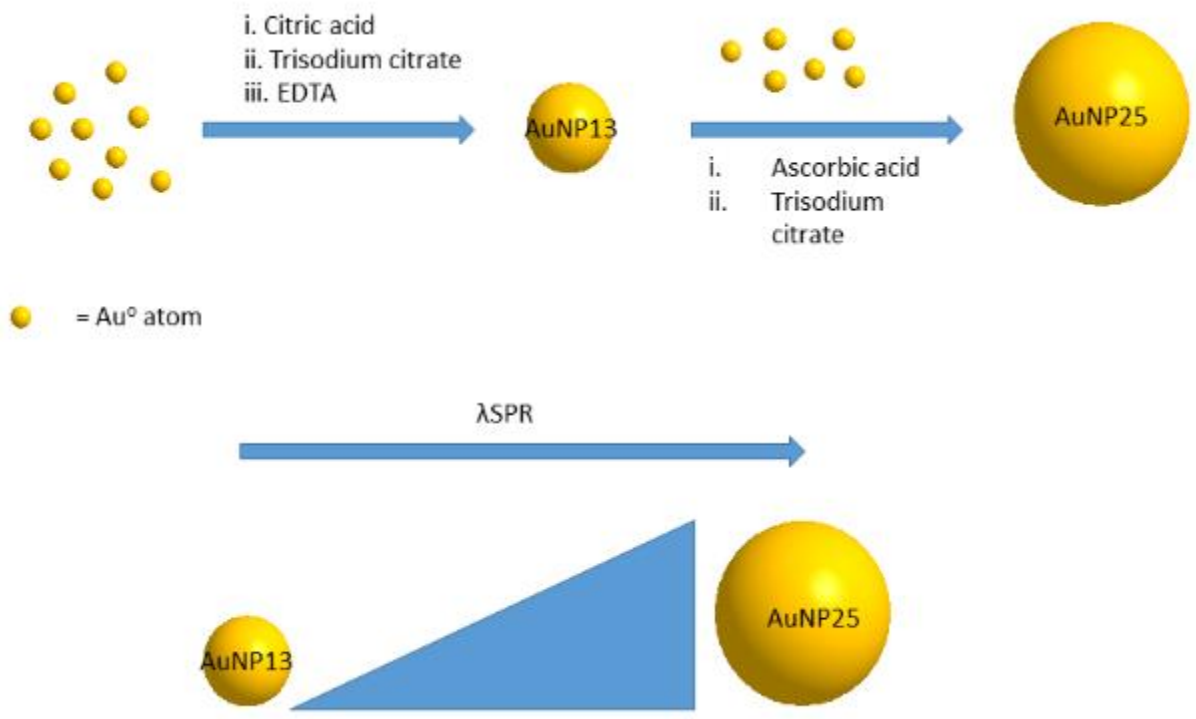

Figure 3.3.2.1.1. Cartoon representation of gold nanoparticle synthesis and seeding process.

The synthesised nanoparticles was characterised through UV-Vis spectroscopy (Figure 3.3.2.1.2), dynamic light scattering (DLS) (Table 3.3.2.1.1) and transmission electron

microscopy (TEM) techniques (Figure 3.3.2.1.3). Gold nanoparticles display a unique characteristic surface plasmon resonance (SPR) band that is seen through UV-Vis spectroscopy and can be used to estimate particle concentration through the molar extinction coefficient at 450 nm, the size of the nanoparticle, to identify any changes occurring on the nanoparticle surface and to monitor aggregation points.[93]

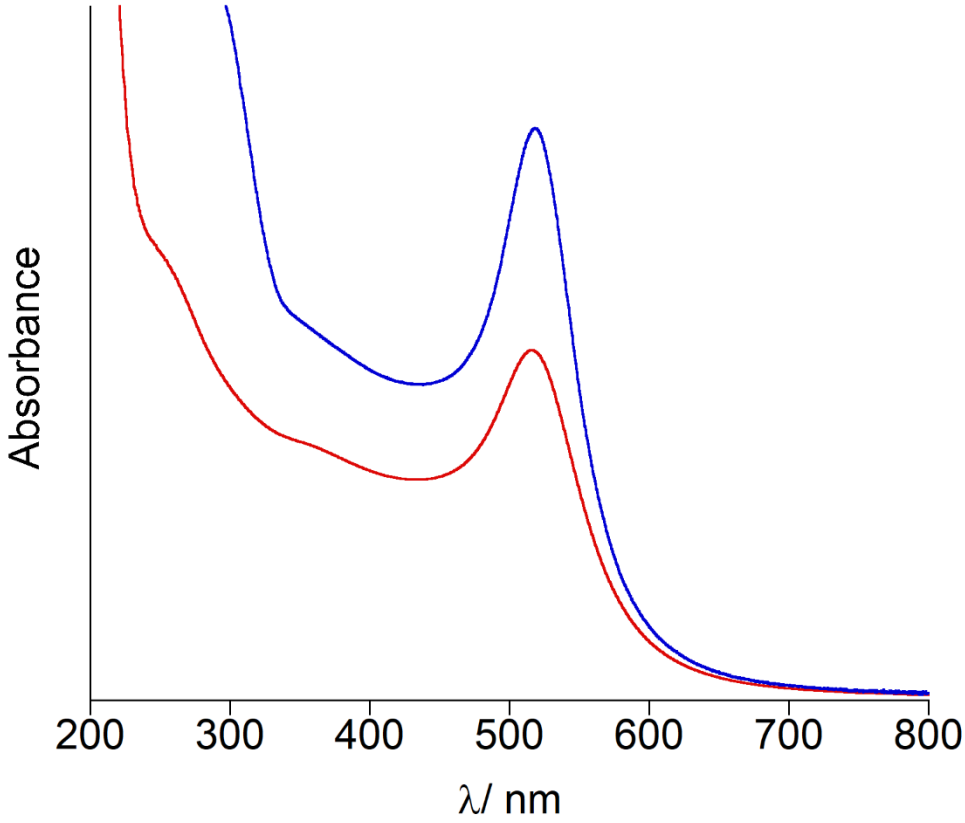

Figure 3.3.2.1.2. UV Vis of 2 nM c-AuNP13 (red) and 0.7 nM c-AuNP25 in aerated water.

The λ_{SPR} for the stock solution of 13 nm citrate capped gold nanoparticles (c-AuNP13) resulted in 516 nm and the λ_{SPR} for the stock solution of 25 nm gold nanoparticles (c-AuNP25) resulted in 518 nm, a 2 nm shift from the c-AuNP13 particles. This shift in SPR absorbance is due to the c-AuNP25 being larger in size and their ability to absorb and scatter more light thus resulting

in a higher intensity for the c-AuNP25 over c-AuNP13. In order to determine the size of the gold nanoparticles, DLS spectroscopy was performed.

Table 3.3.2.1.1. Summary of 13 nm and 25 nm c-AuNP UV-Vis and DLS data taken in 1 mL at 2 nM and 0.8 nM respectively in aerated water.

	SPR/ nm	Size by Intensity/ nm	Size by Number/ nm	PDI
c-AuNP13	517	20 ± 5	15 ± 3	0.05
c-AuNP25	518	30 ± 9	21 ± 5	0.07

DLS studies revealed sizes of 15 ± 3 nm and 21 ± 5 nm for c-AuNP13 and c-AuNP25 respectively. Both particles display very low polydispersity indexes suggesting the particles are of spherical and monodisperse nature. These values correlate well with previously published reports within the group.[7,9,56,65,78,80,94,95] TEM was further confirmed to establish the size of the nanoparticles which revealed sizes of 12 nm and 22 nm which are in good agreement with the DLS recorded data.

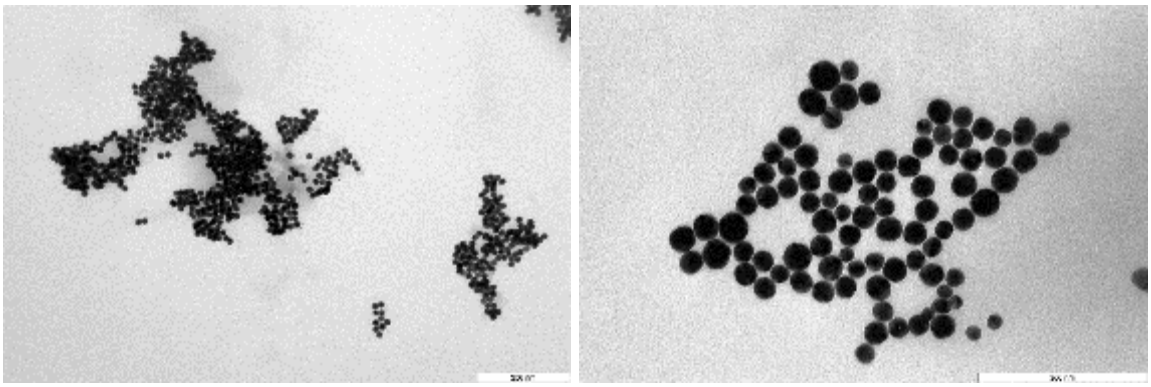

Figure 3.3.2.1.3. TEM images of c-AuNP13 (left) and c-AuNP25 (right) revealing sizes of 13 nm and 15 nm respectively. Scale bar = 200 nm.

3.3.2.2 Labelling of ruthenium(II) complexes on 13 nm gold nanoparticles

In order to determine the metal complexes efficacy for imaging capabilities on gold nanoparticles, the metal complexes were decorated on the nanoparticle surface through the formation of Au-S bonds through the thiols on the legs of the complexes. Gold has a high affinity for thiols resulting in preferential binding of the metal complexes.[51] Due to the nature of ruthenium carrying a 2+ charge, they cannot be added directly as they cause aggregation of the gold nanoparticles via electrostatic interactions between the ruthenium complex and the gold nanoparticle surface.

Monitoring of the λ_{max} through UV-Vis from the addition of Zonyl and ruthenium(II) complexes is a key indicator of binding and the aggregation point of the particles. Gold nanoparticle aggregation can be determined through significant broadening of the SPR band and the formation of new absorption bands far in the red region. In order to prevent aggregation, the fluorosurfactant Zonyl FSA was implemented for the stabilisation of the particles prior to the decoration of the metal complexes. Coating of Zonyl FSA onto c-AuNP13 was followed as per a previously published method in the Pikramenou group.[7,9,56,78,80] Upon addition of Zonyl FSA to the c-AuNP13, a 1 nm red shift is observed in the SPR band. DLS of the Z•AuNP13 indicated a size of 18 ± 5 nm and a PDI of 0.05. The slight increase in number is attributed to the layer of surfactant present on the gold nanoparticle surface and the UV-Vis and DLS confirms displacement of the citrate with the fluorosurfactant Zonyl FSA. The data agrees with previously published data within the group.[7,56,78]

Stock solutions of RuBpySS, RuPhenSS and RuS8 as the chloride counter ion were dissolved in methanol yielding 1 mM solutions. Microliter additions of the metal complexes were performed into the Z•AuNP13 solution and monitoring of the SPR band was observed to determine full saturation of the nanoparticle surface (Figure 3.3.2.2.1).

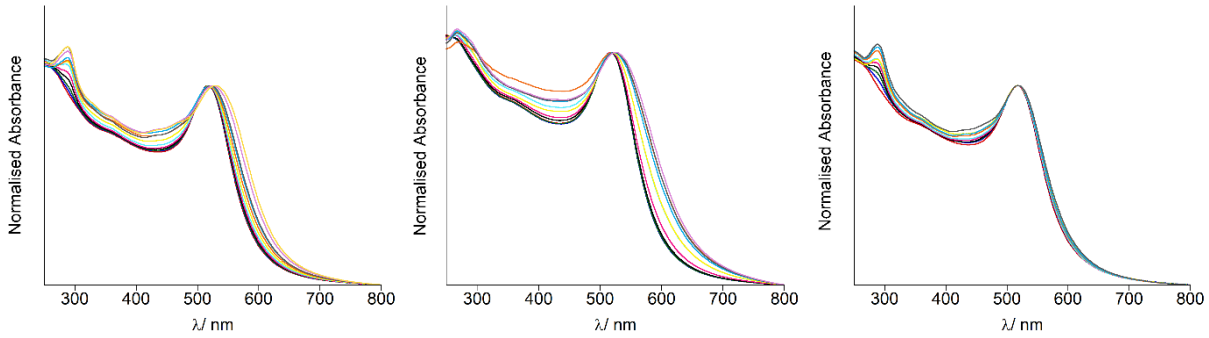

Figure 3.3.2.2.1. Microlitre additions of 1 mM RuBpySS (a) 1 mM RuPhenSS (b) and 1 mM RuS8 (c) on 2 nM Z•AuNP13 in aerated water.

Table 3.3.2.2.1. Summary of λ_{SPR} of gold nanoparticle samples and their respective shifts in λ_{SPR} in comparison to c-AuNP13.

	λ_{max} / nm	Shift/ nm
c-AuNP13	517	0
Z•AuNP13	518	1
RuBpySS•Z•AuNP13	520	3
RuPhenSS•Z•AuNP13	521	4
RuS8•Z•AuNP13	519	2

Once the particles were decorated with the ruthenium(II) metal complexes they were passed through a size exclusion column to remove any excess complex free in solution. Analysis of the particles after purification revealed the same λ_{SPR} as displayed from the titration studies suggesting the ruthenium is bound to the surface and the shift in SPR is not due to free complex in solution (Figure 3.3.2.2.2).

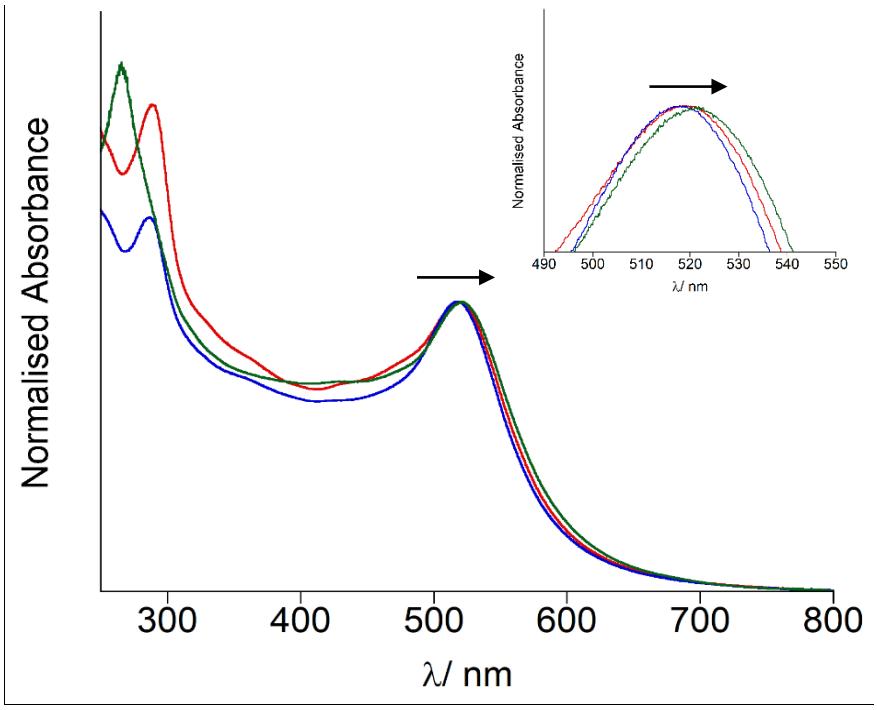

Figure 3.3.2.2.2. Normalised UV Vis of purified RuBpySS•Z•AuNP13 (red), RuPhenSS•Z•AuNP13 (green) and RuS8•Z•AuNP13 (blue) indicating their shifts in SPR and a zoom insert of the SPR bands.

The metal coated gold nanoparticle samples were then characterised through DLS and TEM techniques in order to demonstrate stability and uniformity of the particles after coating with the ruthenium(II) complexes. DLS studies of Z•AuNP13 display a slightly bigger number distribution in comparison to the stock solution of c-AuNP13. This is attributed to the presence of the surfactant on the surface and the potential to form bilayers. There have been numerous studies that have reported the use of bilayers on a gold nanoparticle surface for applications in biological specimens.[96] The small PDI of Z•AuNP13 suggests monodisperse and uniform particles. Each ruthenium(II) coated gold nanoparticle displays near identical size by number and size by intensity. RuS8•Z•AuNP13 displays a slightly lower size by intensity owing to the shorter legs in comparison to RuBpySS•Z•AuNP13 and RuPhenSS•Z•AuNP13. Each ruthenium(II) coated gold nanoparticle displays a higher PDI in comparison to c-AuNP13 and Z•AuNP13, however the low PDI of these coated particles depicts them of uniform nature.

Table 3.3.2.2.2. DLS table of gold nanoparticle samples taken in 1 mL at 1 nM in aerated water.

	SPR/ nm	Size by Intensity/ nm	Size by Number/ nm	PDI
Z•AuNP13	518	27 ± 7	20 ± 5	0.05
RuBpySS•Z•AuNP13	520	35 ± 14	18 ± 5	0.22
RuPhenSS•Z•AuNP13	521	34 ± 13	19 ± 5	0.20
RuS8•Z•AuNP13	519	31 ± 11	18 ± 5	0.17

TEM of the gold nanoparticle samples was performed in order to visualise the uniformity of the samples and determine the average size. The TEM images of RuBpySS•Z•AuNP13, RuPhenSS•Z•AuNP13 and RuS8•Z•AuNP13 display average sizes of 14 nm, 16 nm and 15 nm respectively which is in very good agreement of the DLS results.

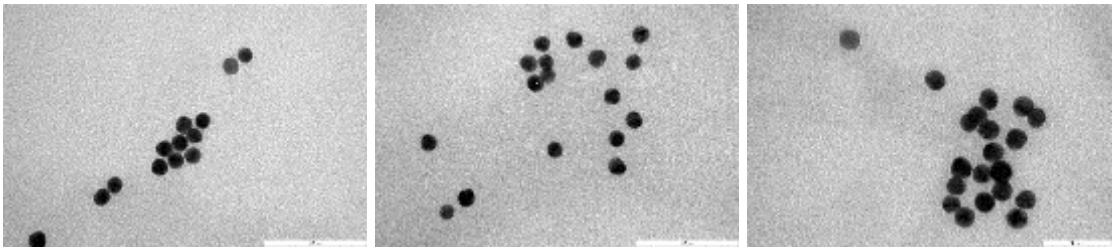

Figure 3.3.2.2.3. TEM images RuBpySS•Z•AuNP13 (a), RuPhenSS•Z•AuNP13 (b) and RuS8•Z•AuNP13 (c) displaying average sizes of 14 nm, 16 nm and 15 nm respectively. Scale bar = 100 nm for (a) and (b) and 50 nm for (c). Scale bar = 100 nm, 100 nm and 50 nm respectively.

Further to this, ICP-MS was conducted in order to determine the amount of Ru atoms to Au. It was observed for RuBpySS•Z•AuNP13 displayed 770 complexes per nanoparticle, RuPhenSS•Z•AuNP13 displayed 670 complexes per nanoparticle and RuS8•Z•AuNP13 displayed 580 complexes per nanoparticle.

3.3.2.3 Evaluation and selection of ruthenium via luminescence studies on Z•AuNP13

The steady state emission profile, excitation and UV-Vis was taken in order to prove the successful binding of ruthenium on the gold nanoparticle surface. Previous studies have found that thiol-functionalised ruthenium(II) complexes show enhancement when attached to the gold nanoparticle surface. When comparing between the three complexes in aerated water, they all display the same λ_{em} respectively when bound to the gold nanoparticle surface suggesting no change has occurred in the ^{3}MLCT pathway. The summary of the complexes on gold nanoparticles are tabulated below (Table 3.3.2.3.1). However, the lifetimes and QY of each complex has changed when attached onto the gold nanoparticle. For all lifetimes on gold nanoparticles, a short component was observed and attributed to scattering artefact so only the long component is reported. When comparing between RuBpySS•Z•AuNP13, RuPhenSS•Z•AuNP13 and RuS8•Z•AuNP13, it was found that RuPhenSS•Z•AuNP13 displays the greater enhancement in photophysical properties.

Table 3.3.2.3.1. Photophysical properties of 4.5 nM RuBpySS•Z•AuNP13, 4.5 nM RuPhenSS•Z•AuNP13 and 4.5 nM RuS8•Z•AuNP13 in aerated water.

Sample	Emission λ_{max} / nm	τ/ ns	Φ/ %
RuBpySS•Z•AuNP13	650	468	10
RuPhenSS•Z•AuNP13	635	1700	15
RuS8•Z•AuNP13	635	840	11

For RuBpySS•Z•AuNP13, an increase is observed from 285 ns from the free complex in solution to 468 ns; resulting in ~ 70% increase. For RuPhenSS•Z•AuNP13, the lifetime increased from 540 ns to 1700 ns, ~ 200% increase where as RuS8•Z•AuNP13 increased from 393 ns to 840 ns resulting in ~ 100% increase. Although RuS8 possesses no adjacent oxygen

on the 4,4' position which was believed to reduce $^3O_2$ quenching, the linker remains shorter than that of the BpySS. The lack of enhancement when compared to RuPhenSS•Z•AuNP13 suggests that RuS8•Z•AuNP13 is being quenched from the gold surface more strongly than in the case of RuPhenSS•Z•AuNP13. Generally, each complex is enhanced when decorated onto the gold nanoparticle surface and is suspected to be arising from the dipole of the complexes interacting with the electromagnetic field of the gold nanoparticle.[97]

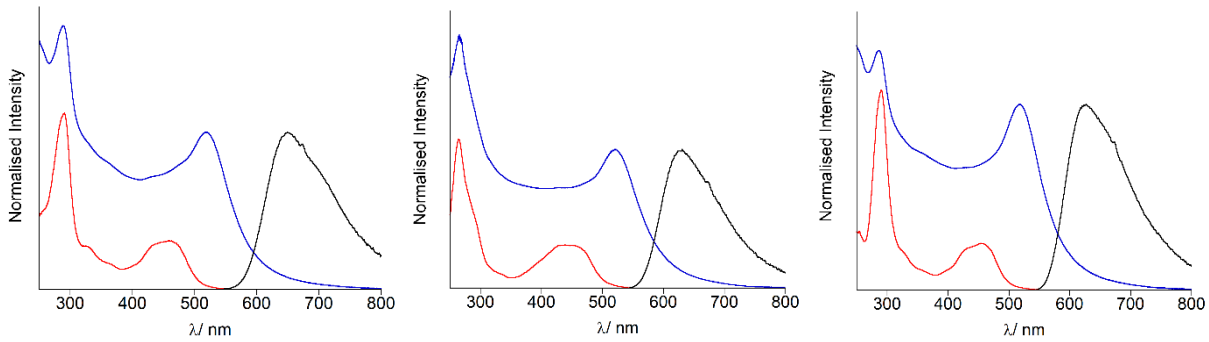

Figure 3.3.2.3.1. Normalised UV-Vis (blue), excitation (red) and emission (black) of 4.5 nM RuBpySS•Z•AuNP13 (λ_{exc} = 462 nm, λ_{em} = 645 nm) (a) 4.5 nM RuPhenSS•Z•AuNP13 (λ_{exc} = 457 nm, λ_{em} = 630 nm) (b) and 4.5 nM RuS8•Z•AuNP13 (λ_{exc} = 457 nm, λ_{em} = 635 nm) (c) in aerated water.

Additionally, the QY of RuBpySS•Z•AuNP13, RuPhenSS•Z•AuNP13 and RuS8•Z•AuNP13 increased to 10%, 15% and 11% respectively. The photophysical properties of three ruthenium(II) complexes were evaluated in aerated solution, in the presence of a fluorosurfactant and on gold nanoparticles. RuPhenSS displays the greatest enhancement of its photophysical properties in agreement with previously reported data and thus has been chosen as the ideal probe for imaging applications employed with the antibody.[78] Prior to employment of antibody functionalised gold nanoparticles, the imaging capabilities within cells of RuPhenSS•Z•AuNP13 was studied alongside RuPhenSS•Z•AuNP25 for improved reflectance properties of the gold.

3.3.3 Labelling and characterisation of RuPhenSS on 25 nm gold nanoparticles

Prior to addition of the metal complex RuPhenSS, the c-AuNP25 was coated with the fluorosurfactant Zonyl FSA for improved stability. The complex RuPhenSS was employed for the decorating of c-AuNP25 due to the photophysics exceeding the other ruthenium(II) complexes as discussed earlier in this chapter. This is key due to the reduced amount of complex expected to be added on to the gold nanoparticle surface for later studies with the antibody. The procedure for coating c-AuNP25 with Zonyl FSA mirrors the same prep for c-AuNP13 which is described in the experimental section. The particles were coated with Zonyl FSA and concentrated to form Z•AuNP25 (1 mL, 5 nM). Monitoring of the SPR band through UV-Vis spectroscopy was able to identify the maximal amount to be decorated. The SPR band resulted in a 1 nm shift from the stock particles which is identical to that of the coating procedure for Z•AuNP13.

A stock solution of RuPhenSS at 1 mM was added into 1.5 nM Z•AuNP25 through stirring for 2 minutes between each aliquot. Significant shifting of the SPR band suggests successful binding of RuPhenSS with the characteristic ligand absorption band of the phenanthroline (π – π^*) identifying at 266 nm. It was seen that after 18 µM the particles displayed signs of aggregation by the broadening of the SPR band and at 22 µM a formation of a new SPR band was apparent. It was concluded that 14 µM RuPhenSS was sufficient to coat the gold nanoparticle surface for stability (Figure 3.3.3.1).

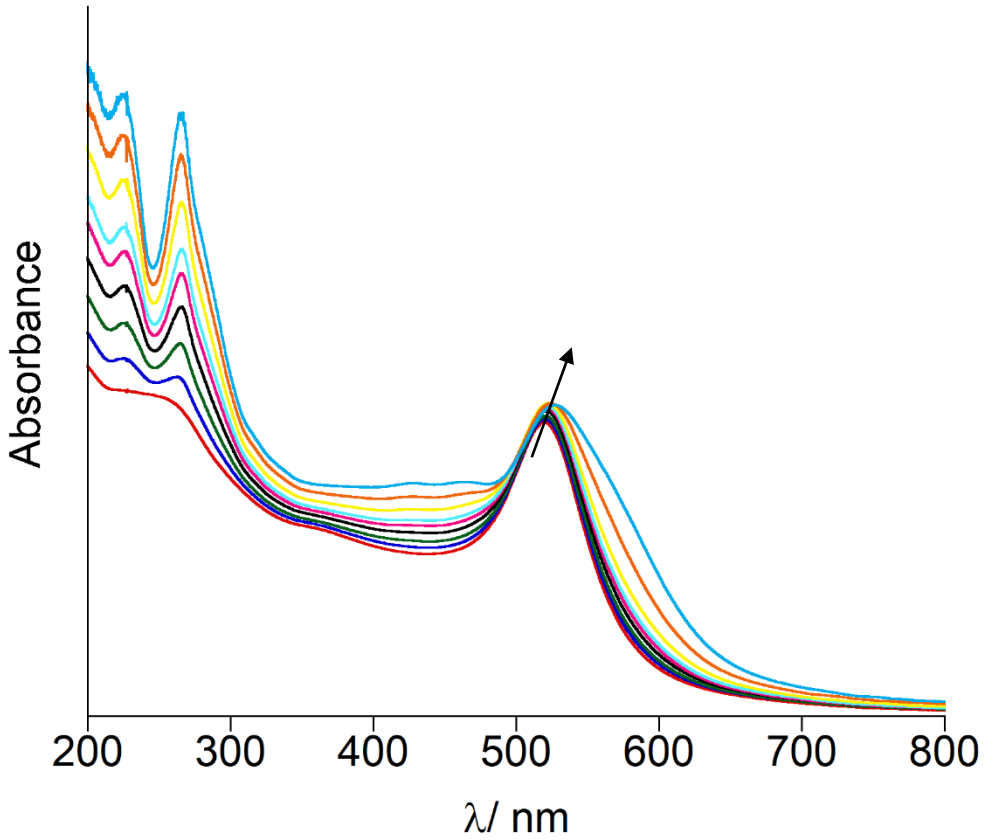

Figure 3.3.3.1. Microlitre additions of 1 mM RuPhenSS on Z•AuNP25 in aerated water.

The coating of RuPhenSS onto Z•AuNP25 displays a similar shift of 5 nm to that of the RuPhenSS•Z•AuNP13 (4 nm shift) when comparing to the λ_{SPR} of their c-AuNP counterparts. The shift in λ_{SPR} are presented in Table 3.3.3.1.

Table 3.3.3.1. Summary of λ_{SPR} from gold nanoparticle samples and their respective shifts in comparison to c-AuNP25.

	λ_{max} / nm	Shift/ nm
C-AuNP25	519	0
Z•AuNP25	520	1
RuPhenSS• Z•AuNP25	524	5

After determining the loading of RuPhenSS on Z•AuNP25, the particles RuPhenSS•Z•AuNP25 particles underwent isolation through a sephadex G25 column to remove any unbound complex from the nanoparticle solution. Confirmation of removal of free complex was determined through reduction of the LC band after isolation. The λ_{SPR} displayed the same absorption maxima displayed from the coating procedure of particles after isolation additionally confirming removal of free complex and no change of the coated particles. The isolated RuPhenSS•Z•AuNP25 was then characterized through DLS techniques and then subject to steady state emission and excitation studies. DLS studies reveal average number distributions when comparing RuPhenSS•Z•AuNP25 to Z•AuNP25.

Table 3.3.3.2. DLS summary 2 nM Z•AuNP25 and 2 nM RuPhenSS•Z•AuNP25 in aerated water.

	SPR/ nm	Size by Intensity/ nm	Size by Number/ nm	PDI
Z•AuNP25	519	48 ± 15	30 ± 8	0.22
RuPhenSS•Z•AuNP25	524	135 ± 123	28 ± 8	0.41

Steady state emission and excitation was performed for detection of the ruthenium(II) complex on RuPhenSS•Z•AuNP25 in aerated water. Upon excitation of the ^{1}MLCT band at 457 nm of the RuPhenSS•Z•AuNP25, the characteristic ^{3}MLCT band arises at 635 nm unique to the metal complex. The excitation spectrum of the RuPhenSS•Z•AuNP25 mirrors the excitation spectrum of the free complex in aerated water confirming the presence of RuPhenSS on the nanoparticle surface.

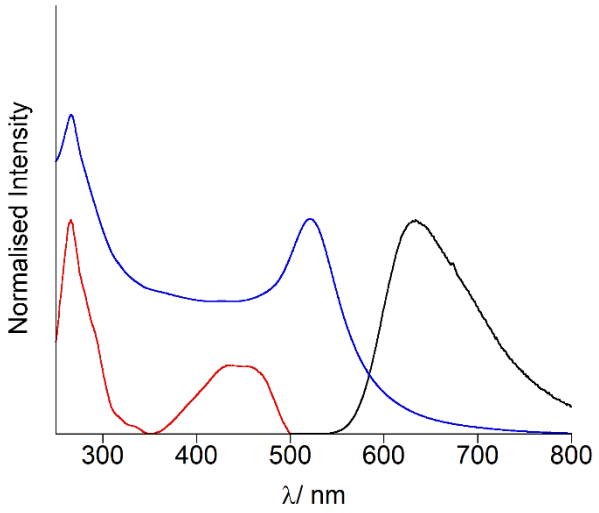

Figure 3.3.3.2. Normalised UV-Vis (blue), excitation (red) and emission (black) of 2 nM RuPhenSS•Z•AuNP25 (λ_{exc} = 457 nm, λ_{em} = 635 nm) in aerated water.

3.3.4 Biological Studies of 13 nm and 25 nm RuPhenSS coated gold nanoparticles in A549 cells

After successful coating and characterisation of both RuPhenSS•Z•AuNP13 and RuPhenSS•Z•AuNP25 biological studies were conducted. Prior to dosing of cells, a cell viability assay was conducted to establish appropriate dosing of particles and any associated toxicity. An MTT cell viability assay of A549 cells was performed with serial dilutions of RuPhenSS•Z•AuNP13 and RuPhenSS•Z•AuNP25 ranging from 9 nM – 0.14 nM and 5 nM to 0.078 nM respectively. The cells were incubated at 37ºC in a 5% CO_2 atmosphere for 24 hours in 96-well plates with the 13 nm and 25 nm RuPhenSS•Z•AuNP serial dilutions in parallel with a vehicle control (H_2O), negative control (media) and a positive control (Triton X-100). The samples were compared against the vehicle control (H_2O) in relation to the negative (media) and positive (Triton X-100, 1%) control to observe toxicity. In both cases the positive control containing 1% Triton X-100 killed the majority of the cells as expected. The negative control in both cases has no associated toxicity as determined by statistical analysis suggesting the cells

are healthy and not contaminated resulting in no cell death as expected. Interestingly, statistical analysis suggests toxicity of 13 nm and 25 nm RuPhenSS•Z•AuNP across all concentrations studied despite relatively high cell viability in the weaker concentrations. However, the results and analysis are based on one biological repeat and as such may not be representative of the true toxicity associated with these particles.

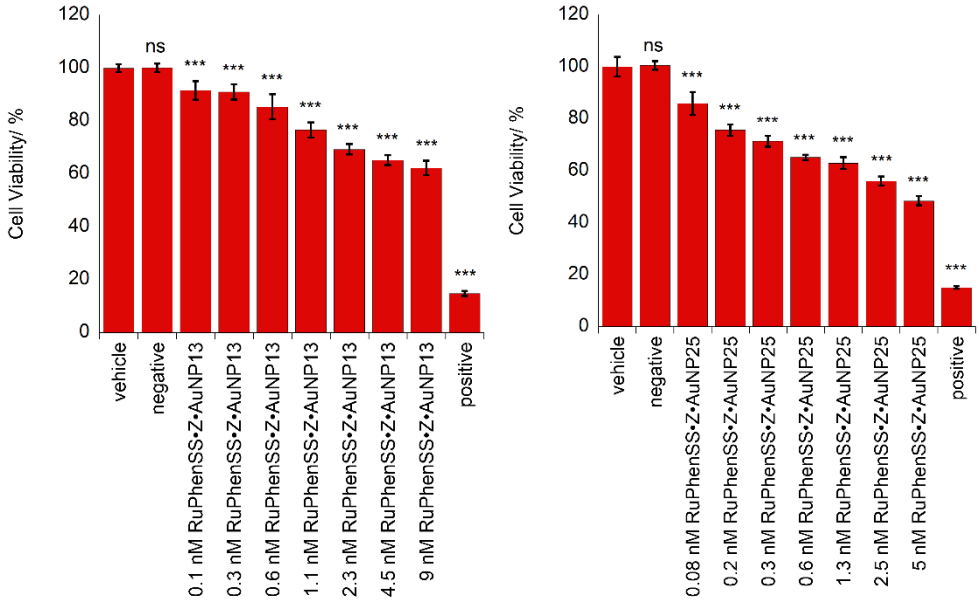

Figure 3.3.4.1. MTT assays of A549 cells treated with serial particle dilutions of RuPhenSS•Z•AuNP13 (a) and RuPhenSS•Z•AuNP25 (b) for 24 hours at 37°C 1-way ANOVA followed by a Dunnett's t-test corrected for multiple comparisons was performed. n = 1. * = P<0.01, ** = P<0.001, *** = P<0.0001.

Despite the particles being statistically toxic towards live A549 cells, 0.9 nM for RuPhenSS•Z•AuNP13 and 0.2 nM RuPhenSS•Z•AuNP25 were selected for imaging due to maintaining relativel high cell viability and to ensure sufficient uptake leading to a strong ruthenium signal.

Live cell imaging was conducted to observe their potential for imaging via detection of the luminescent signature of RuPhenSS. The cells were washed with 0.01 M PBS and imaged immediately after staining with the nuclear dye Hoescht 3368. The staining of the nucleus

through the aid of Hoescht allows the identification of where the RuPhenSS•Z•AuNP13 localise within the cell however weak staining was observed. After incubation for 18 hours, it appears that RuPhenSS•Z•AuNP13 show no preference of cellular compartments and instead accumulate within the cytoplasm. Unsurprisingly, no reflectance of the 13 nm RuPhenSS•Z•AuNP was able to be obtained due to the very small size (13 nm) of the gold nanoparticles.

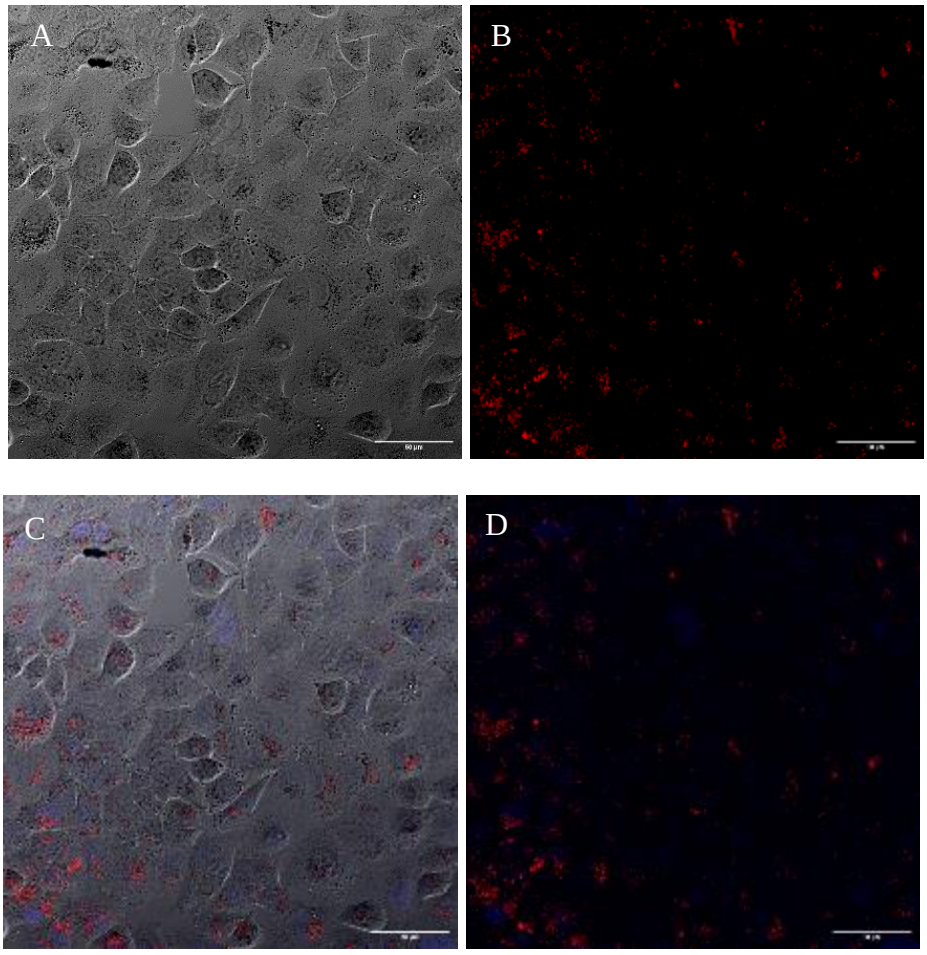

Figure 3.3.4.2. Live cell images of A549 cells treated with 0.9 nM RuPhenSS•Z•AuNP13 at 18 hours.Brightfield (a), Red channel: Ruthenium emission (λ_{exc} = 457 nm, λ_{em} = 500−800 nm) (b), overlap of Hoescht emission (λ_{exc} = 402 nm, λ_{em} = 420−470 nm), brightfield and ruthenium emission (c) and overlap of Hoescht 3368 and ruthenium emission (d). Scale bar is 50 µm.

Therefore, 25 nm RuPhenSS•Z•AuNP was employed for the benefit of increasing the reflectance properties as larger sized gold nanoparticles display greater scattering effects. The RuPhenSS•Z•AuNP25 display much brighter images over the RuPhenSS•Z•AuNP13 in A549 cells. The RuPhenSS•Z•AuNP25 appears to localise in the cytoplasm and in the perinuclear compartment of the cell similar to that of the RuPhenSS•Z•AuNP13. Confirmation of ruthenium emission arising from the RuPhenSS•Z•AuNP25 and not free complex within the cell is displayed though reflectance and ruthenium emission overlay.

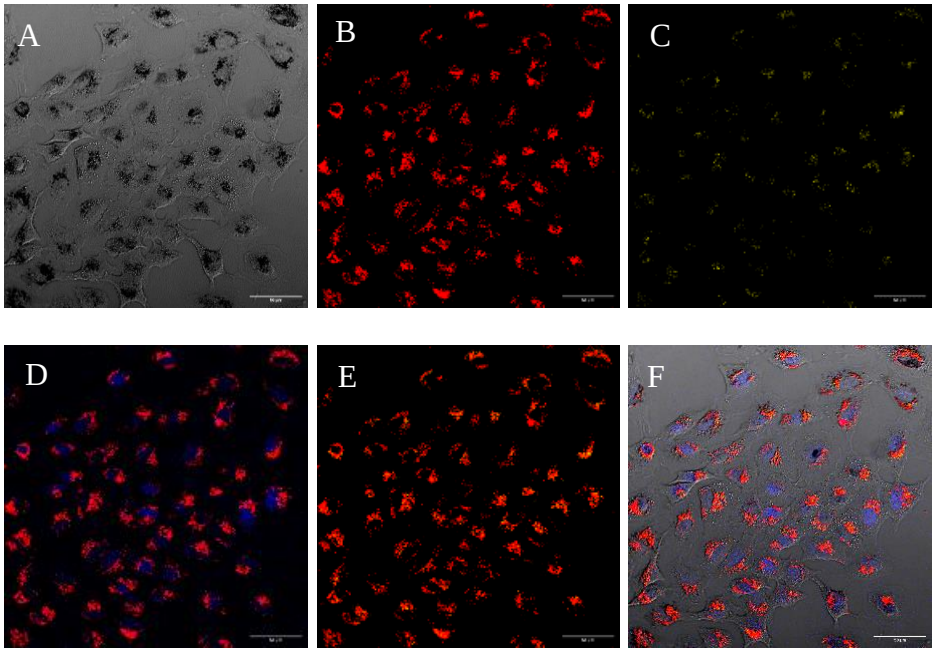

Figure 3.3.4.3. Live cell images of A549 cells treated with 0.2 nM RuPhenSS•Z•AuNP25 at 18 hours. Brightfield (a), Red channel: Ruthenium emission (λ_{exc} = 457 nm, λ_{em} 500−800 nm) (b), Yellow channel: Reflectance (λ_{exc} = 633 nm, λ_{em} 620−640 nm) (c), and overlap of Ruthenium emission and Hoescht 3368: . Blue channel, Hoescht 3368 emission (λ_{exc} = 402 nm, λ_{em} 420−470 nm)(d), overlap of Ruthenium and reflectance (e), and overlap of Hoescht 3368, brightfield, reflectance and ruthenium emission (f). Scale bar is 50 µm.

The intense emission displayed from the RuPhenSS on 13 nm and 25 nm AuNP represent their potential use as an imaging agent and its purpose for detection within a biological sample. This demonstrates the usefulness of the metal complex, RuPhenSS, in imaging which will be employed in later studies through functionalising the gold nanoparticles with a chimeric antibody (rituximab) for the detection of B-cells in tonsil tissue.

3.3.5 Mass spectrometry of RuPhenSS coated 13 nm gold nanoparticles

Mass spectrometry can serve as a dual detection method in parallel with confocal light microscopy for detection of RuPhenSS•Z•AuNP13 through identifying the unique isotope pattern of ruthenium and/or the isotope pattern of gold. There has been reports for the imaging of biological samples through mapping of the characteristic gold pattern demonstrating further uses for the employment of gold nanoparticles in imaging.[69,77,98] RuPhenSS•Z•AuNP13 was spotted onto a MTP-anchor chip 384 MALDI plate and air dried five times before analysis. Analysis of the mass spectrum was analysed under flexanalysis 3.0 and was found to detect a series of gold and ruthenium patterns arising from the sample.

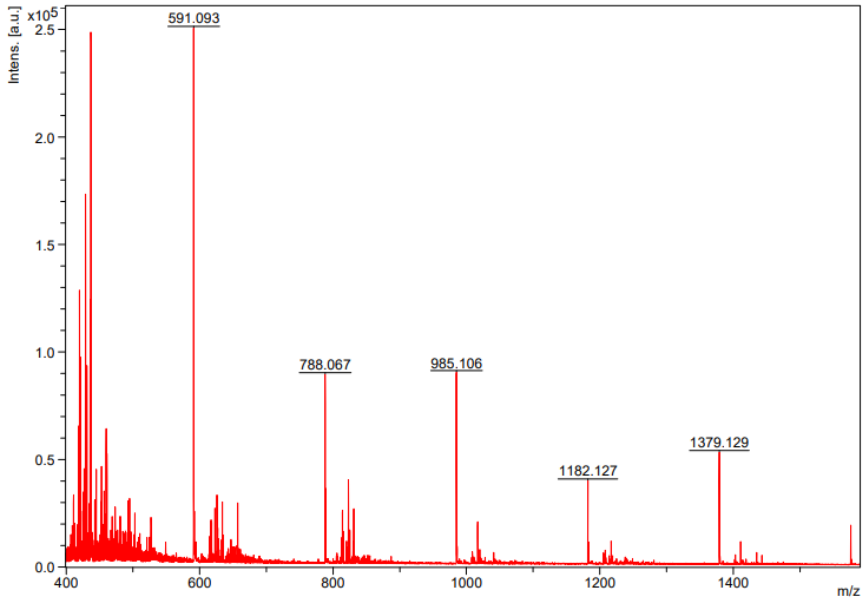

Figure 3.3.5.1. MALDI mass spectrum of RuPhenSS•Z•AuNP13 revealing characteristic gold ion peaks.

The characteristic gold ion peaks can be seen very clearly ranging from 591 m/z up to 1379 m/z relating to $[Au_3]^+$ to $[Au_7]^+$.From zooming in around the expected mass of RuPhenSS, a series

of very weak signals is present. As MALDI is a destructive technique, it is not surprising to see fragments and mixtures of RuPhenSS. However, a very weak but detectable mass arising at 1231.777 m/z suggests intact formation of $[RuPhenSS\text{-}Cl]^+$.

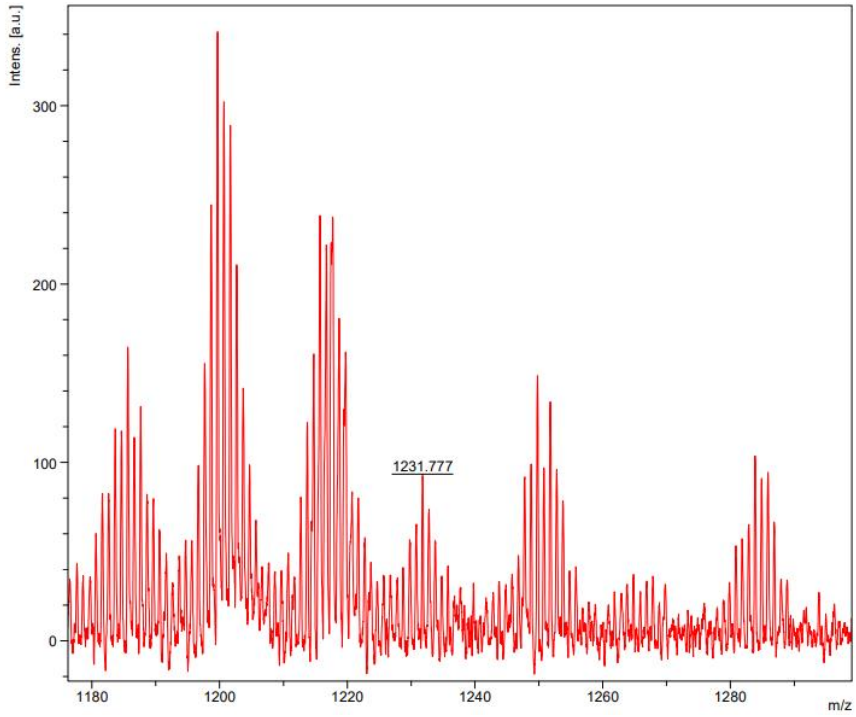

Figure 3.3.5.2. Zoom of MALDI mass spectrum of RuPhenSS•Z•AuNP13.

Although the intact mass for RuPhenSS can be detected via MALDI on the gold nanoparticle, it is very weak and dominated by the presence of more ionizing fragments. This weak detection external to a biological sample will cause issues with detection since more interference and fragments are expected when analyzing tonsil tissue. As such, it seems detection of gold ions present in MALDI is a more amenable and reliable approach for imaging when using RuPhenSS•AuNP13 which is explored further in Chapter 5.

3.4 Conclusion

In conclusion three ruthenium(II) complexes (RuBpySS, RuPhenSS and RuS8) were synthesised and characterised as per previously published methods within the group. The photophysical properties of these complexes were evaluated in aerated water in the absence and presence of a fluorosurfactant, Zonyl FSA, and then attached onto 13 nm gold nanoparticles. It was shown that the complex RuPhenSS displayed the greatest enhancement of photophysical properties when attached onto the gold nanoparticle thus rendering it an ideal complex for imaging applications. Additionally, 25 nm gold nanoparticles were synthesised for the increased scattering potential for reflectance based microscopy to correlate ruthenium emission with reflectance proving no loss of surface bound ruthenium. The cytotoxicity of the 13 nm and 25 nm RuPhenSS•Z•AuNP was then determined via MTT assays prior to cellular imaging to yield ideal dosing concentrations however all concentrations observed showed statistically significant toxicity despite high cell viability in the weaker concentrations. Imaging was performed at concentrations of 0.9 nM and 0.2 nM RuPhenSS•Z•AuNP on 13 nm and 25 nm respectively in A549 cells due to maintaining high cell viability despite being statistically toxic and demonstrated their excellent potential for cellular imaging agents showing localisation within the cytoplasm. Mass spectrometry was then conducted on the 13 nm RuPhenSS•Z•AuNP to ascertain the unique isotope pattern of ruthenium decorated on the gold surface. Although detection was very weak and dominated by fragmentation, Au ion detection remains promising in the event of total suppression of ruthenium for MSI applications.

3.5 Experimental

3.5.1 Materials

All solvents and reagents used in synthesis were purchased from Fischer Scientific, VWR Chemicals, Sigma Aldrich and Alfa Aesar without further purification and deuterated NMR solvents were purchased from Goss Scientific. Anhydrous solvents (pyridine) were dried over molecular sieves for 24 hours under a N_2 atmosphere or obtained by a PureSolv-EN solvent purification system (DCM, THF).

3.5.2 13 nm and 25 nm gold nanoparticle synthesis and coating

The synthesis of c-AuNP13 was based on a previous published method by Vossmeyer *et al.*[55] A solution of trisodium citrate (60.3 mg, 0.21 mmol), citric acid (13.6 mg, 0.07 mmol) and ethylenediaminetetraacetic acid (1.6 mg, 0.004 mmol) in filtered milli-Q water (100 mL) was stirred vigorously and brought to reflux. A preheated solution (80 °C) of Hydrogen Tetrachloroaurate ($HAuCl_4$) (8.5 mg, 0.022 mmol) in filtered milli-Q water (25 mL) was rapidly added to the centre of the vortex. After 30 mins at reflux, the heat was turned off and the solution was allowed to slowly cool to room temperature to form a ~ 2 nM solution of c-AuNP13. UV Vis (H_2O) λ_{SPR} / nm = 517 (SPR). DLS measurements: Diameter / nm = 15 ± 3, PDI = 0.05 (DLS number distribution). DLS sizing measurements were recorded with AuNP at pH 7, 2 nM in milli-Q H_2O.

For 25 nm c-AuNP, Three stock solutions were prepared: A solution of 5 mM $HAuCl_4.3H_2O$; 57 mM ascorbic acid and 34 mM trisodium citrate dihydrate in milli-Q H_2O. AuNP13 (36 mL, 2 nM) were diluted to 40 mL with milli-Q water and vigorously stirred. The solutions for addition were diluted to 1 mM, 3 mM and 0.75 mM in milli-Q water to 40 mL for

$HAuCl_4.3H_2O$, ascorbic acid and trisodium citrate dihydrate respectively. The two solutions ($HAuCl_4.3H_2O$ and ascorbic acid / trisodium citrate dihydrate) were simultaneously added dropwise over 10 minutes. The resultant solution was refluxed for 30 minutes forming a solution of ~ 0.7 nM c-AuNP25. The reaction vessel was allowed to cool to RT and stored in the dark. UV Vis (H_2O) λ_{SPR} / nm = 518 (SPR). DLS measurements: Diameter / nm = 21 ± 5, PDI = 0.07 (DLS number distribution). DLS sizing measurements were recorded with c-AuNP25 at pH 7, 0.7 nM in milli-Q H_2O.

Z•AuNP13

2 nM AuNP-13 (2 mL) was centrifuged at 13000 g for 30 mins, the supernatant was decanted and the pellet was re-suspended in filtered milli-Q water (1 mL) to form 4 nM AuNP-13. Zonyl FSA solution (2.5 % w/v) in deionised water (10 µL) was added to 4 nM AuNP-13 (1 mL), stirred for 20mins and centrifuged at 13000 g for 25 mins. The supernatant was discarded and the pellet was re-suspended in filtered milli-Q water (350 µL) to form 9 nM Z•AuNP13. λ_{max} (H_2O) / nm 518 (SPR). Diameter / nm = 20 ± 5, PDI = 0.05 (DLS number distribution). DLS sizing measurements were recorded with Z•AuNP13 at pH 7, 1 nM in milli-Q H_2O.

Z•AuNP25

0.7 nM c-AuNP25 (2 mL) was centrifuged at 13000 g for 30 mins, the supernatant was decanted and the pellet was re-suspended in filtered milli-Q water (1 mL) to form 1.4 nM c-AuNP25. Zonyl FSA solution (2.5 % w/v) in deionised water (10 µL) was added to 1.4 nM c-AuNP25 (1 mL), stirred for 20mins and centrifuged at 13000 g for 25 mins. The supernatant was discarded and the pellet was re-suspended in filtered milli-Q water (250 µL) to form 5 nM Z•AuNP25. λ_{max} (H_2O) / nm 519 (SPR). Diameter / nm = 30 ± 8, PDI = 0.22 (DLS number distribution). DLS sizing measurements were recorded with Z•AuNP25 at pH 7, 1 nM in milli-Q H_2O.

RuBpySS•Z•AuNP13

RuBpySS (36 µL, 1 mM) was titrated into a 9 nM solution of Z•AuNP13 and stirred for 2 minutes. A Sephadex G-25 size exclusion column was performed. λ_{max} (H_2O) / nm 520 (SPR). Emission λ_{max}: 650 nm.

RuPhenSS•Z•AuNP13

RuPhenSS (40 µL, 1 mM) was titrated into a 9 nM solution of Z•AuNP13 and stirred for 2 minutes. A Sephadex G-25 size exclusion column was performed. λ_{max} (H_2O) / nm 521 (SPR). Emission λ_{max}: 635 nm.

RuS8•Z•AuNP13

RuS8 (20 µL, 1 mM) was titrated into a 9 nM solution of Z•AuNP13 and stirred for 2 minutes. A Sephadex G-25 size exclusion column was performed. λ_{max} (H_2O) / nm 519 (SPR). Emission λ_{max}: 635 nm.

3.5.3 Ligand synthesis

BpySS Synthesis

<u>N-Boc-5-amino-1-pentanol (BpySS.1)</u>

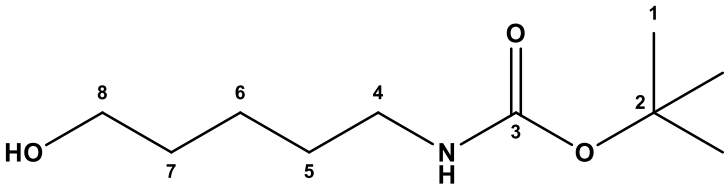

Potassium bicarbonate (28.04 g, 280.1 mmol) was suspended in a solution of 5-amino-1-pentanol (10.01 g, 97.1 mmol) in 50 mL of water. The suspension was then added to an ice bath (0-10ºC) in which di-tert-butyl dicarbonate (22.14 g, 102 mmol) in 50 mL THF was added

dropwise over 15 minutes. The resulting biphasic mixture was then heated to 50 ºC and stirred for 24 hours. The organic phase was separated and concentrated *in vacuo* resulting in a clear oil. The oil was added to H_2O:Et_2O (150 mL, 2:1) and the organic layer separated. The aqueous layer was washed with Et_2O (3 x 50 mL) and the combined extracts were dried over Na_2SO_4, filtered and reduced *in vacuo* to yield a clear oil (19.6 g, 99%). δH (300MHz; $CDCl_3$) 1.40-1.72 (6H, m, H5, 6, 7), 1.45 (9H, s, H1), 1.81 (1H, s, OH), 3.14 (2H, q, *6.6*, H4), 3.66 (2H, td, *6.4*, H8) and 4.60 (1H, s, NH). MS (ESI^+) m/z 226.14 $[M+Na]^+$. Data agreed with previously published data.[53,79]

<u>N-Boc-5-amino-1-tosylpentane (BpySS.2)</u>

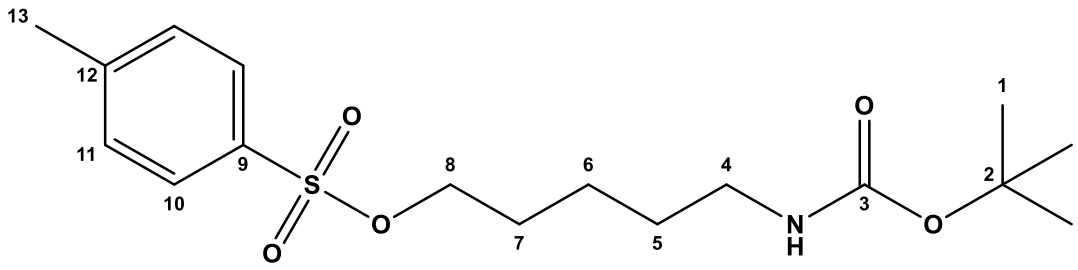

A solution of N-Boc-5-amino-1-pentanol (18.4 g, 90.5 mmol) and p-toluene sulfonyl chloride (17.94 g, 94.1 mmol) in anhydrous DCM (100 mL) was cooled to 0-5ºC. Pyridine (20 mL, 271 mmol) was added dropwise over 15 minutes maintaining the temperature at 0-5 ºC. The reaction was then allowed to warm to room temperature and stirred for 24 hours. The mixture was concentrated and the white suspension was added to H_2O:Et_2O (100 mL, 1:1) and the ether layer washed with aqueous $NaHCO_3$ and brine (50 mL) before being dried over Na_2SO_4 to yield a clear oil. The oil was triturated in hexane (50 mL) with the solid being filtered and washed with hexane to yield a white solid (32.4 g, 26 %). δH (300 MHz; $CDCl_3$) 1.32 – 1.40 (4H, m, H6, 7), 1.43 (9H, s, H1), 1.66 (2H, p, H5), 2.45 (3H, s, H13), 3.01-3.10 (2H, q, *6.6*, H4), 4.02

(2H, t, *6.4*, H8), 4.47 (1H, s, NH), 7.35 (2H, d, *7.7*, H10) and 7.79 (2H, d, *8.3*, H11). MS (ESI^+) m/z 380.1 $[M+Na]^+$. Data agreed with previously published data.[53,79]

4,4'-dihydroxy-2,2'-bipyridine (BpySS.3)

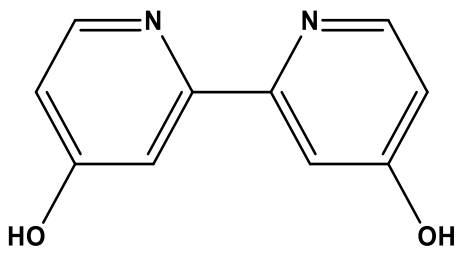

A solution of 4,4'-dimethoxy-2,2'-bipyridine (5.07 g, 23.5 mmol) in hydrobromic acid (48 % w/ v, 42 mL, 362.5 mmol) and glacial acetic acid (250 mL) was brought to reflux for 6 hours. The mixture was cooled and the solvent removed *in vacuo* affording a white/ cream solid which was dissolved in H_2O (250 mL) and neutralised with aqueous ammonia solution (31 % by weight, 20 mL). The resulting precipitate was filtered and washed with water (50 mL) and acetone (2 x 10 mL) before being baked at 60 ºC for an hour. Yielded a white solid (3.24 g, 74 %). MS (ESI^+) m/z 189.1 $[M+H]^+$. Data agreed with previously published data.[53,79]

4,4'-di-(N-(Boc)-5-amino-1-pentoxy)-2,2'-bipyridine (BpySS.4)

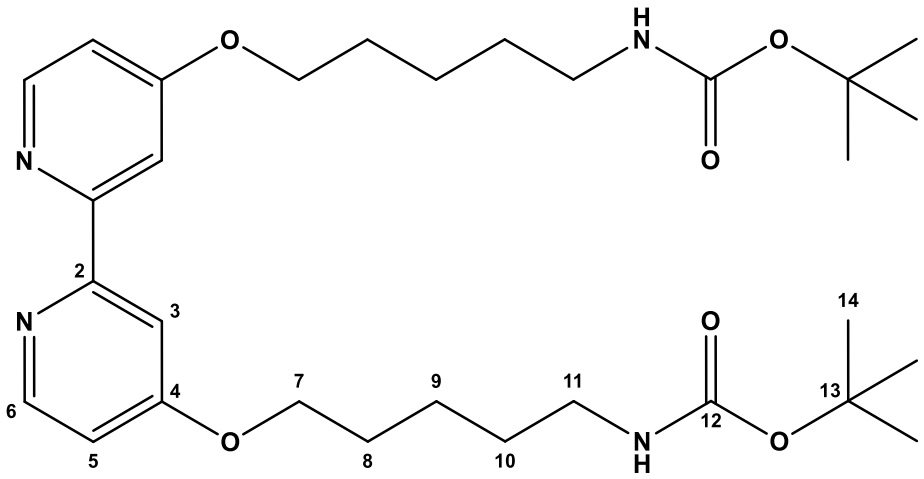

Potassium carbonate (4.4 g, 31.3 mmol) was suspended in a solution of N-Boc-5-amino-1-tosylpentane (8.45 g, 23.6 mmol), 4,4'-dihydroxy-2,2'-bipyridine (1.94 g, 10.31 mmol) and 18-crown-6 (catalytic) in acetone (200 mL) which was then stirred and heated to 60 ºC for 48 hours. The reaction mixture was hot filtered to give a yellow filtrate and place in ice to afford a white precipitate. The precipitate was filtered and washed with acetone (20 mL) with the filtrate being treated further to recover more product. A white solid was collected (5.76 g, 14 %). δH (300 MHz; $CDCl_3$) 1.42-1.56 (8H, m, H8, 9), 1.44 (18H, s, H14), 1.85 (2H, p, *6.6*, H5), 3.14 (4H, m, H11), 4.13 (4H, t, *6.3*, H7), 4.55 (2H, br s, NH), 6.82 (2H, dd, *2.5*, *5.7*, H5), 7.93 (2H, d, *2.5*, H3) and 8.45 (2H, d, *5.7*, H6). MS (ESI^+) m/z 559.4 $[M+H]^+$. Data agreed with previously published data.[53,79]

<u>4,4'-di-(5-amino-1-pentoxy)-2,2'-bipyridine (BpySS.5)</u>

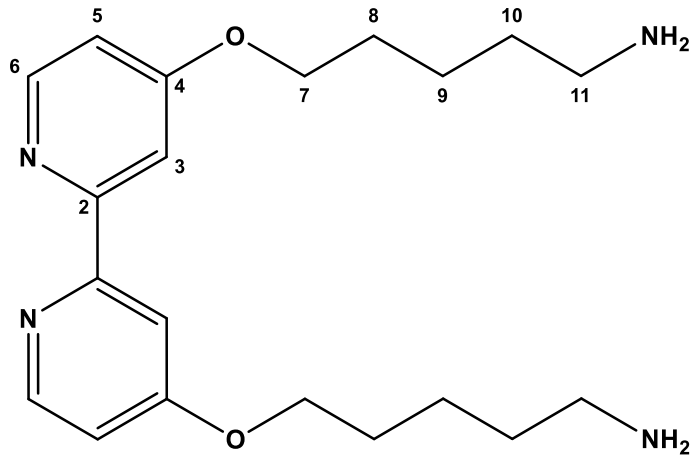

A solution of 4,4'-di-(N-Boc-5-amino-1-pentoxy)-2,2'-bipyridine (0.83 g, 1.49 mmol) in trifluoroacetic acid (7 mL) and was stirred for 2 hours. The solvent was removed *in vacuo* and the residue was separated (20 mL 1M NaOH: 20 mL $CHCl_3$). The aqueous layer was extracted with chloroform (2 x 10 mL) and combined extracts dried over Na_2SO_4 and filtered. The solvent was removed *in vacuo* to yield a white solid (0.53 g, 98 %). δH (300 MHz; $CDCl_3$) 1.19 (4H, br s, NH_2), 1.45-1.60 (8H, q, *3.7*, H8, 9), 1.85 (4H, p, *7.0*, H10), 2.73 (4H, m, H11), 4.14 (4H,

t, *6.4*, H7), 6.82 (2H, dd, *2.6, 5.7*, H5), 7.94 (2H, d, *2.5*, H3) and 8.45 (2H, d, *5.7*, H6). MS (ESI^+) m/z 359.2 $[M+H]^+$. Data agreed with previously published data.[53,79]

<u>4,4'-Di(5-lipoamido-1-pentoxy)-2,2'-bipyridine (BpySS.6)</u>

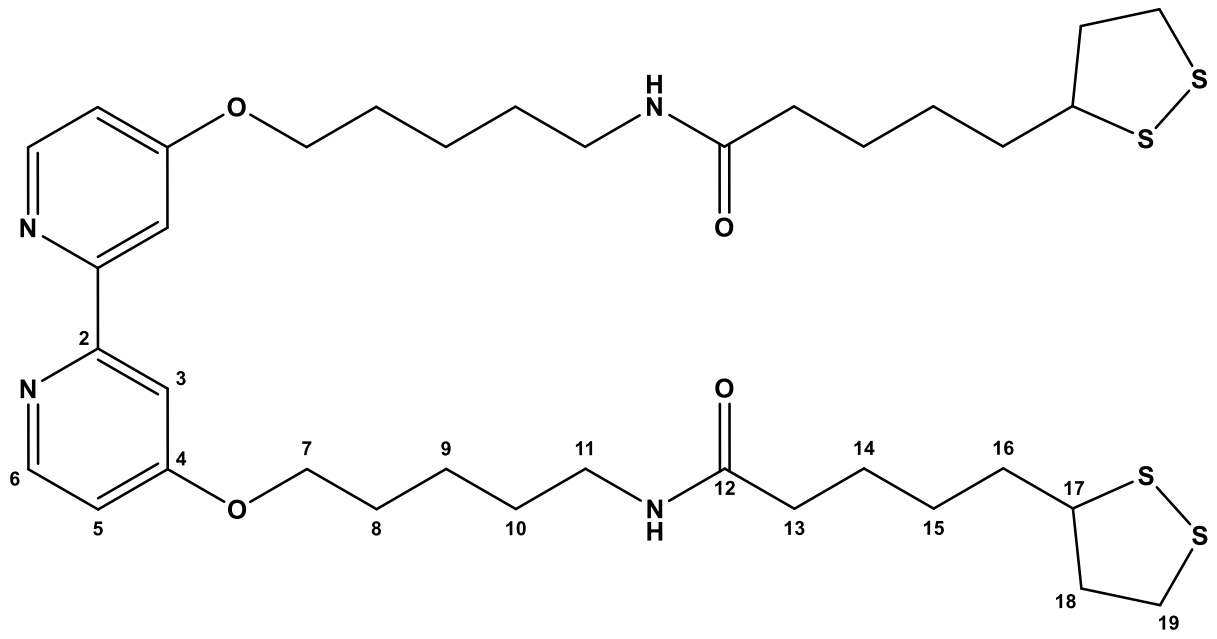

A solution of α-lipoic acid (0.72 g, 3.49 mmol) and 1-hydroxybenzotriazole hydrate (0.52 g, 3.88 mmol) in DMF (7 mL) was cooled to 0−5°C, upon which 1-ethyl-3-(3-(dimethylamino)propyl)carbodiimide (EDC) (0.61 g, 0.7 mL, 3.96 mmol) was added and stirred, maintaining this temperature. The solution was allowed to warm to room temperature and stirred for a further hour. A solution of N-ethylmorpholine (0.32 mL) and 4,4'-di-(5-amino-1-pentoxy)-2,2'-bipyridine (0.52 g, 1.45 mmol) in DMF (13 mL) was added to the reaction mixture and stirred overnight. The resulting cream precipitate was filtered and dried in air with washing of DMF. (0.80 g, 76 %). δH (400 MHz; $CDCl_3$) 1.35-1.65 (12H, m, H8, 9, 15), 1.61-1.78 (8H, m, H14, 16), 1.79-1.96 (6H, m, H10, 18'), 2.17 (4H, t, *7.4*, H13), 2.38-2.50 (2H, dq, *6.2, 12.4*, H18), 3.02-3.14 (4H, m, H19), 3.29 (4H, q, *6.4*, H11), 3.50-3.60 (2H, p, *6.7*, H17), 4.13 (4H, t, *6.3*, H7), 5.47 (2H, br s, NH), 6.82, 2H, dd, *2.5, 5.7*, H5), 7.94 (2H, d, *2.5*, H3) and

8.45 (2H, d, *5.7*, H6). δC (400 MHz; $CDCl_3$) 23.40 (C9), 25.4 (C14), 28.6 (C15), 28.9 (C8), 29.4 (C10), 34.6 (C16), 36.5 (C13), 38.5 (C19), 39.3 (C11), 40.2 (C18), 56.4 (C17), 67.7 (C7), 106.8 (C3), 111.3 (C5), 150.2 (C6), 157.8 (C2), 166.1 (C4) and 172.7 (C12). MS (ESI^+) m/z 735.3 $[M+H]^+$. Data agreed with previously published data.[53,79]

S8 Synthesis

4,4'-dimethylester-2,2'-bipyridine (S8.1)

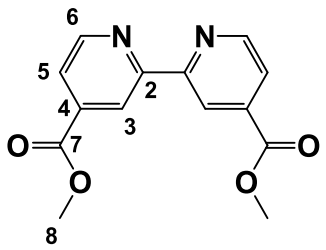

Thionyl chloride (10 mL) was slowly added to a suspension of 4,4'-dicarboxylicacid-2,2'-bipyridine (1.2 g, 4.9 mmol) in degassed MeOH (75 mL) over 5 minutes. The mixture was refluxed overnight and quenched with a saturated solution of $NaHCO_3$. The product was extracted with chloroform (3 x 100 mL), dried over $MgSO_4$ and recrystallized in chloroform/acetone (1:1) to produce a white solid (930 mg, 65%). δH (300 Hz; CDCl3): 4.00 (6H, s, H8); 7.92 (2H, dd, 5.0, 1.6, H6); 8.88 (2H, dd, 5.0, 0.7, H5); 8.97 (2H, q, 0.7, H3). Data agreed with previously published data.[53]

4,4'-dimethylalcohol-2,2'-bipyridine (S8.2)

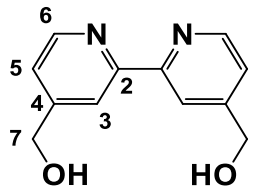

$NaBH_4$ (1.91 g, 54 mmol) was quickly added to a suspension of **S8.1** (0.90 g, 3.32 mmol) in 45 mL ethanol. The mixture was refluxed for 3 hours and quenched with saturated ammonium

chloride. The solvent was removed *in vacuo* and the solid was dissolved in 30 mL water and extracted with ethyl acetate (5 x 70 mL) and dried with Na_2SO_4 to produce a white solid (690 mg, 3.19 mmol, 96 %). δH (300 Hz; CDCl3): 4.87 (2H, d, 5.2, H7); 7.40 (2H, dquint, 4.5, 0.8, H5); 8.40 (2H, q, 0.8, H3); 8.69 (2H, d, 4.5, H6). Data agreed with previously published.[53]

4,4'-dibromomethyl-2, 2'-bipyridine (S8.3)

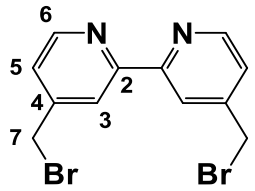

S8.2 (680 mg, 3.21 mmol) was dissolved in a solution of HBr and H_2SO_4 (25 mL 4:1) and refluxed for 6 hours. The mixture was added to 40 mL water and neutralised with 2 M NaOH. The white precipitate was filtered, washed with water and air dried. The white solid was dissolved in 40 mL chloroform, dried with $MgSO_4$ and filtered to produce a white solid (300 mg, 0.88 mmol, 28 %). δH (300 Hz; CDCl3): 4.50 (4H, s, H7); 7.38 (2H, dd, 1.5, 5.0, H5); 8.44 (2H, d, 1.5, H3); 8.68 (2H, d, 5.0, H6). Data agreed with previously published.[53]

4,4'-dimethylazide-2,2'-bipyridine (S8.4)

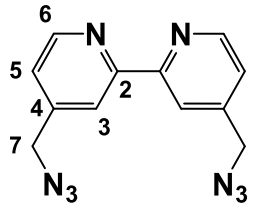

Sodium azide (890 mg, 13.7 mmol) is added to a solution of **S8.3** (470 mg, 1.37 mmol) in DMSO (5 mL). The mixture was stirred at room temperature for 24 hours. It was poured into water (40 mL) and extracted with diethyl ether (3 x 20 mL), dried with $MgSO_4$ and filtered to produce a white solid (281 mg, 1.01 mmol, 78%). δH (300 Hz; CDCl3): 4.50 (4H, s, H7); 7.32

(2H, dt, 0.8, 5.0, H5); 8.40 (2H, q, 0.8, H3); 8.71 (2H, d, 5.0, H6). m/z (TOF ES+): 267.1 (100 %), 268.1 (10 %) [M + H]+ . Data agreed with previously published.[53]

4,4'-dimethylamine-2,2'-bipyridine (S8.5)

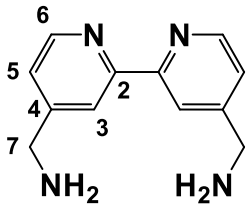

A catalytic amount of Pd/C slurried in THF was added to a solution of **S8.4** (119 mg, 0.45 mmol) and TEA (75 µL) dissolved in 20 mL THF under N_2. It was left to stir overnight in a H_2 atmosphere. The mixture was put under N_2 atmosphere and then filtered through celite. The solvent was removed *in vacuo* to produce a white solid (69 mg, 0.32 mmol, 72 %). δH (300 Hz; CDCl3): 3.88 (4H, s, H7); 7.41 (2H, dt, 1.9, 5.0, H5); 8.40 (2H, dd, 0.8, 1.8, H3); 8.58 (2H, dd, 0.8, 5.0, H6). Data agreed with previously published.[53]

4,4'-Di(5- lipoamido-1-methylene)-2,2'-bipyridine (S8.6)

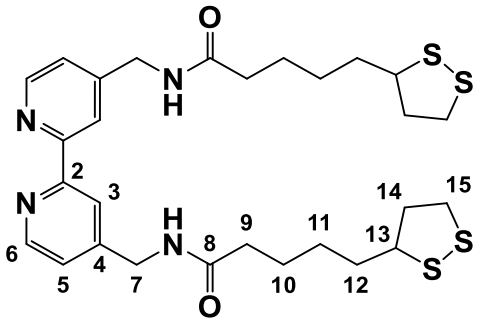

Synthesis adapted from reference. 1-Ethyl-3-(3- dimethylaminopropyl)carbodiimide (200 mg, 1.29 mmol) is added to a mixture of α-lipoic acid (281 mg, 1.36 mmol) and 1-hydroxybenzotriazol hydrate (182 mg, 1.35 mmol) in dry DMF (10 mL) at 0 °C under N_2. After 5 minutes, it was allowed to return to RT and a solution of **S8.5** (69 mg, 0.281 mmol) and N-

Ethylmaleimide (143 µL) was added and stirred overnight. Water (100 mL) was added and the product was extracted with DCM (3 x 100 mL). The organic phase was taken and the solvent was removed *in vacuo* and the off white solid was suspended in ethanol and filtered to produce a cream solid (75 mg, 0.13 mmol, 45 %). δH (300 Hz; CDCl3): 1.42 (4H, m, H11); 1.62 (8H, m, H10, H12); 1.81 (2H, m, H15); 2.23 (4H, dd, 7.5, 14.9, H9); 2.35 (2H, m, H15'); 3.07 (4H, m, H14); 3.47 (2H, tt, 6.2, 12.5, H13); 4.46 (4H, d, 6.0, H7); 6.00 (2H, t, 6.0, NH); 7.17 (2H, dd, 1.7, 5.0, H5); 8.18 (2H, t, 9.0, H3); 8.53 (2H, dd, 0.45, 5.0, H6). δC (400 Hz; CDCl3): 25.4 (C12); 28.9 (C11); 34.6 (C10); 36.3 (C9); 38.5 (C14); 40.2 (C15); 42.6 (C7); 56.4 (C13); 119.7 (C3); 122.7 (C5); 148.6 (C4); 149.5 (C6); 156.2 (C2); 172.9 (C8). Assignments by COSY and HSQC. m/z (TOF ES+): 591.2 $[M + H]^+$. Data agreed with previously published.[53]

3.5.4 Synthesis of ruthenium metal complexes

<u>*Bis*-(2,2'-bipyridine) Ruthenium Dichloride [$Ru(bpy)_2Cl_2$]</u>

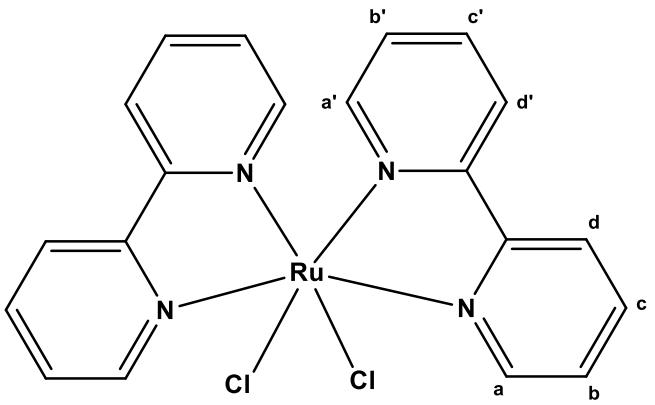

Ruthenium trichloride (0.7 g, 2.5 mmol and lithium chloride (0.20 g, 4.81 mmol) was dissolved in degassed 2-methoxyethanol (45 mL) and brought to reflux. At reflux, 2,2'-bipyridine (0.76g, 4.9mmol) in degassed 2-methoxyethanol (10 mL) was added dropwise. The mixture was allowed to reflux for a further 16 hours. It was cooled to room temperature and filtered. Acetone (20 mL) was added and it was cooled to 0 – 5 °C for 24 hours. It was filtered and washed with

water (200 mL) and diethyl ether (100 mL) to produce a black compound (0.50g, 41%). δH (300 MHz, DMSO) 7.11 (2H, t, 6.2, Hc'), 7.52 (2H, d, 5.6, Hd'), 7.69 (2H, t, 7.2, Hb'), 7.79 (2H, d, 6.7, Hb), 8.08, (2H, t, 7.4, Hc), 8.50 (2H, d, 7.9, Ha'), 8.65 (2H, d, 8.0, Hd) and 9.98 (2H, d, 5.2, Ha). MS (ESI^+) m/z 507 $[M+Na]^+$.

***Bis*-(1,10-phenanthroline) Ruthenium Dichloride [$Ru(phen)_2Cl_2$]**

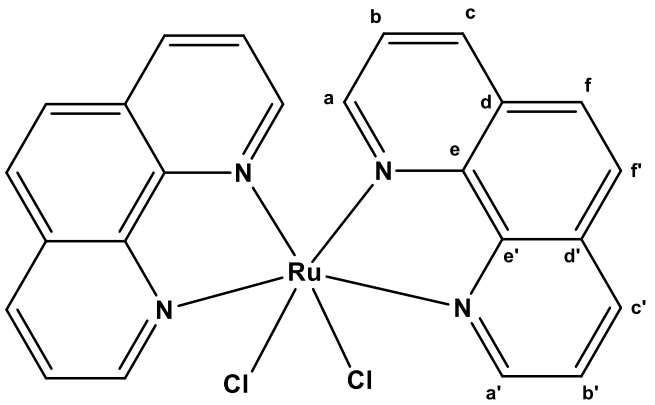

Ruthenium trichloride (0.437 g, 2.11 mmol), 1,10-phenanthroline (0.63 g, 3.49 mmol) and lithium chloride (0.20 g, 4.81 mmol) was dissolved in 5 mL degassed DMF and refluxed for 6 hours. Acetone (20 mL) was added and it was cooled to 0 – 5 °C for 24 hours. It was filtered and washed with water (200 mL) and diethyl ether (100 mL) to produce a black compound (0.513 g, 46 %). δH (300 MHz; DMSO) 7.34 (2H, dd, Hb'), 7.77 (2H, m, Ha'), 8.24 (2H, dd, Hb), 8.10-8.31 (4H, Hf, f'), 8.75 (2H, m, Hc) and 10.29 (2H, dd, Ha). MS (ESI^+) m/z 497 $[M-Cl]^+$.

RuBpySS

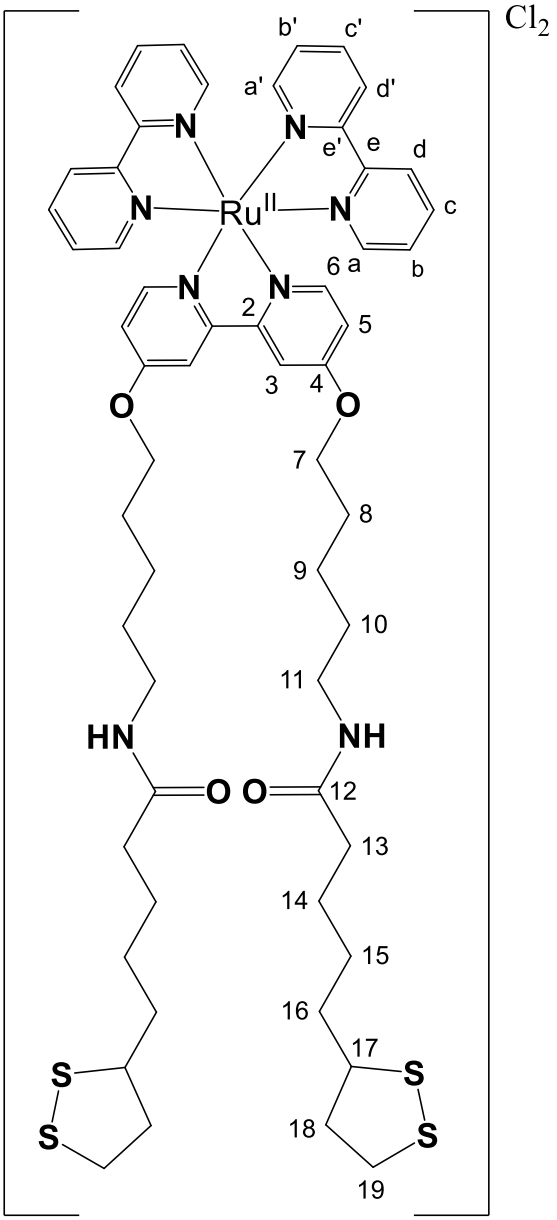

A solution of BpySS (59.3 mg, 0.081 mmol) and $Ru(bpy)_2Cl_2$ (39.5 mg, 0.082 mmol) in ethanol (40 mL) was heated under reflux for 16 hours. The red/orange solution was cooled to room temperature and concentrated *in vacuo* (~10 mL). Water (25 mL) was added, forming a fine cream precipitate, which was filtered. A saturated methanolic solution of ammonium hexafluorophosphate (150 mg in 1 mL of MeOH) was added to the filtrate to give an orange precipitate. The precipitate was filtered and washed with ice cold water and ice cold Et_2O to

give the crude product as an orange/red solid. The solid was dissolved in a minimal amount of acetonitrile and the solvent removed *in vacuo* to give a red crystalline solid. An alumina column in 5 % MeOH: DCM was performed and then reduced *in vacuo* to give the red crystalline solid (15 mg, 16 %). δH (400 MHz; CD_3CN) 1.46 (16H, m, H8, 9, 15, 16), 1.66 (4H, dddd, H14), 1.83 (6H, m, H10, 18'), 2.09 (4H, t, H13), 2.39 (2H, dtd, H18), 3.09 (8H, m, H11, 19), 3.53 (2H, m, H17), 4.20 (4H, t, H7), 6.56 (2H, t, NH), 6.90 (2H, dd, H5), 7.38 (6H, m, H6, b/ b'), 7.71 (2H, m, Ha/ a'), 7.83 (2H, dd, Ha/ a'), 8.03 (4H, dtd, Hc/ c'), 8.11 (2H, d, H3) and 8.49 (4H, dd, Hd/ d'). δC (400 MHz; CD_3CN) 23.7 (C9), 26.3 (C4), 28.9 (C15), 29.5 (C8), 30.0 (C10), 35.4 (C16), 36.7 (C13), 39.3 (C19), 39.4 (C11), 41.1 (C18), 57.5 (C17), 70.7 (C7), 112.5 (C3), 115.2 (C5), 125.1 (Cd/d'), 128.4 (Cb/b'), 138.3 (Cc/c'), 152.6 (Ca/a'), 152.8 (Ca/a'), 153.0 (C6), 158.2 (Ce/ e'), 158.3 (Ce/e'), 159.0 (C2), 167.7 (C14) and 173.5 (C12). Assignments by COSY and HSQC. MS (ESI^+) m/z 574 $[M-2PF_6]^{2+}$ .A dowex ion exchange 1 x 8 200-400 mesh was performed to convert back to the chloride salt of RuBpySS for the photophysical characterization. UV-Vis λ_{max} / nm (ε / $M^{-1}cm^{-1}$): 462 (13000), 430 (sh), 288 (70000), 224 (sh). Emission λ_{max}: 645 nm. τ -285 ns. In the presence of 164 µM Zonyl FSA surfactant. UV-Vis λ_{max} / nm (ε / $M^{-1}cm^{-1}$): 460 (13000), 430 (sh), 290 (70000), 230 (sh). Emission λ_{max}: 650 nm. τ: 350 ns. Attached to AuNP13. UV-Vis λ_{max} / nm: 520. Emission λ_{max}: 650 nm. τ: 468 ns. Φ: 10%.

RuPhenSS

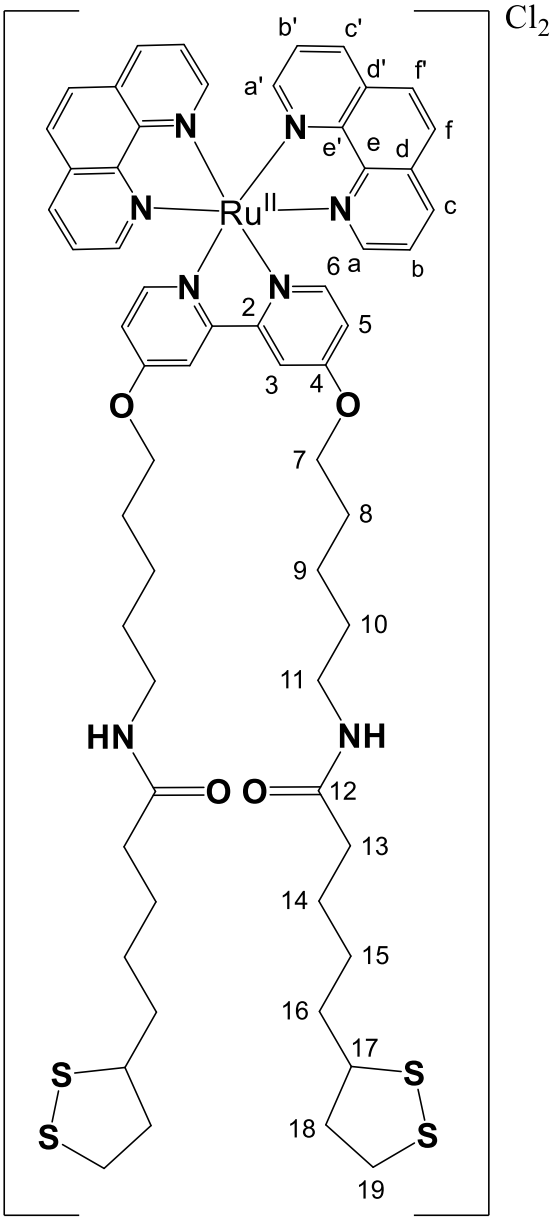

$Ru(phen)_2Cl_2$ (44.7 mg, 0.085 mmol) and BpySS (70.9 mg, 0.095 mmol) were refluxed overnight in ethanol (40 mL). The red/orange solution was cooled to room temperature and concentrated *in vacuo* (~10 mL). Water (25 mL) was added, forming a fine cream precipitate, which was filtered. A saturated methanolic solution of ammonium hexafluorophosphate (150 mg in 1 mL of MeOH) was added to the filtrate to give an orange precipitate. The precipitate was filtered and washed with ice cold water to give the crude product as an orange/red solid.

The solid was dissolved in a minimal amount of acetonitrile and the solvent removed *in vacuo* to give a red crystalline solid. An alumina column in 1 % MeOH: DCM was performed and then reduced *in vacuo* to give the red crystalline solid (85 mg, 85 %). δH (400 MHz; CD_3CN) 1.63 (16H, m, H4, 9, 14, 15, 16), 1.81 (4H, m. H10, 18'), 2.07 (4H, t, *7.2,* H13), 2.37 (2H, dtdd, *1.0, 5.4, 6.5, 12.9,* H18), 3.07 (8H, m, H11, 19), 3.52 (2H, dq, *6.3, 6.3, 8.9,* H17), 4.17 (4H, td, *2.9, 6.5, 6.6,* H7), 6.41 (2H, s, NH), 6.78 (2H, dd, *2.7, 6.6,* H5), 7.36 (2H, d, *6.5,* H6), 7.52 (2H, dd, *5.3, 8.3,* Hb'), 7.81 (2H, dd, *5.3, 8.3,* Hb), 7.87 (2H, dd, *1.3, 5.3,* Ha'), 8.09 (2H, d, *2.7,* H3), 8.23 (4H, dd, *8.9,* Hf/ f', 8.29 (2H, dd, *1.3, 5.2,* Ha), 8.51 (2H, dd, *1.3, 8.2,* Hc') and 8.64 (2H, dd, *1.3, 8.3,* Hc). δC (400 MHz; CD_3CN) 23.7 (C9), 26.3 (C15), 28.9 (C8), 29.5 (C14), 30 (C10), 35.3 (C16), 36.7 (C13), 39.2 (C19), 39.3 (C11), 41.1 (C18), H7.5 (C17), 70.7 (C7), 112.4 (C3), 115.0 (C5), 126.8 (Cb'), 129.6 (Cb), 129.0 (C4), 131.9 (Cf), 132.0 (Cf'), 137.3 (Cc'), 137.4 (Cc), 148.9 (Cd'), 149.1 (Cd), 153.5 (C6), 153.6 (Ca'), 153.7 (Ca), 159.3 (C2), 167.3 (Ce/e') and 173.4 (C12). Assignments by COSY and HSQC. MS (ESI^+) m/z 598.2 $[M-2PF_6]^{2+}$ A dowex ion exchange 1 x 8 200-400 mesh was performed to convert back to the chloride salt of RuPhenSS for the photophysical characterisation. UV-Vis λ_{max} / nm (ε / $M^{-1}cm^{-1}$): 457 (13500), 430 (sh), 263 (83700), 222 (81600). Emission λ_{max}: 630 nm. τ: 540 ns. In the presence of 164 µM Zonyl FSA surfactant. UV-Vis λ_{max} / nm (ε / $M^{-1}cm^{-1}$): 457 (13500), 430 (sh), 263 (83700), 222 (81600). Emission λ_{max}: 634 nm. τ: 745 ns. Attached to AuNP13. UV-Vis λ_{max} / nm: 521. Emission λ_{max}: 635 nm. τ: 1700 ns. Φ: 15%.

RuS8

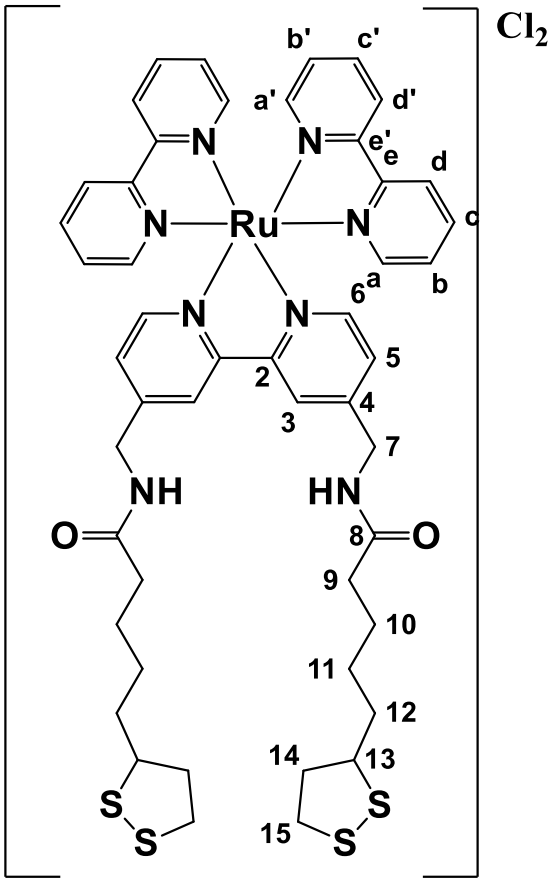

$Ru(bpy)_2Cl_2$ (23.2 mg, 0.048 mmol) and **S8.6** (35 mg, 0.059 mmol) was refluxed overnight in ethanol (30 mL). The solvent was removed *in vacuo* and the solid was dissolved in a minimal amount of methanol. A saturated methanolic solution of NH_4PF_6 was added and stirred for 2 hours. The solid was filtered and washed with water (3 x 100 mL). An neutral alumina plug was performed in 2 % methanol in DCM. The product was stirred with HCl pre-treated Dowex for 2 hours in methanol and a LH20 column in 2% methanol in DCM was performed. The solvent removed *in vacuo* to produce a red solid chloride salt (45 mg, 0.042 mmol, 94 %). δH (300 MHz; MeOD): 1.43 (4H, m, H11); 1.5-1.8 (8H, m, H10, H12); 1.88 (2H, m, H15); 2.35 (4H, t, 7.1, H9); 2.46 (2H, m, H15'); 3.11 (4H, m, H14); 3.55 (2H, m, H13); 4.61 (4H, d, 2.2, H7); 7.42 (2H, dd, 5.8, 1.5, H5); 7.51 (4H, dt, 6.4, 1.1, Hb); 7.75 (2H, d, 5.8, H6); 7.83 (4H, t,

6.4, Ha); 8.16 (4H, tt, 8.0, 1.1, Hc); 8.67 (2H, s, H3); 8.74 (4H, d, 8.0, Hd). δC (100 MHz; MeOD): 25.1 (C12); 28.5 (C11); 34.3 (C10); 35.2 (C9); 38.0 (C14); 40.0 (C15); 41.7 (C7); 56.4 (C13); 122.9 (C3); 124.3 (Cd, Cd'); 125.9 (C5); 127.6 (Cb, Cb'); 137.8 (Cc, Cc'); 151.0 (C6); 151.2 (C4); 151.3 (Ca); 151.4 (Ca'); 156.8 (C2); 157.1 (Ce, Ce'); 175.1 (C8). Assignments by COSY and HSQC. m/z (TOF MS ES+) 502.1 $[M-2Cl]^{2+}$. All photophysical characterisation is performed as a 20 µM solution in water as the chloride salt. UV-Vis λ_{max} / nm (ε / M^{-1} cm^{-1}): 456 (12000), 430 (sh), 287 (72000), 244 (27000). Emission λ_{max}: 635 nm. τ: 393 ns. In the presence of 164 µM Zonyl FSA surfactant. UV-VIS λ_{max} / nm (ε / M^{-1} cm^{-1}): 457 (13000), 430 (sh), 288 (69000). Emission λ_{max}: 635 nm. τ: 600 ns. Attached to AuNP13. UV-Vis λ_{max} / nm: 519. Emission λ_{max}: 635 nm. τ: 840 ns. Φ: 11%.

3.5.5 Cell culture

The human lung cancer A549 cell line was maintained in Dulbecco's Modified Eagle's Medium (DMEM) supplemented with 10% fetal bovine serum (FBS), L-glutamine (100 µg mL^{-1}) and 1% penicillin/streptomycin hereafter called complete media. Cells were cultured in 20 mL of complete media in vented T75 flasks at 37°C in a humidified 5% CO_2 atmosphere. Cells were routinely sub cultured from high confluency using a standard trypLE protocol.

3.5.6 MTT assays

MTT viability assays were conducted by Dr Garret Rochford. Cells were seeded at a density of 5000 cells per well in a 96 well plate. Nanoparticle concentrations were varied across the plate through a 1 in 2 dilution factor in six technical replicates containing a negative (1% triton) and positive control (cell media). Cells were dosed for 24 hours

with varying concentrations of RuPhenSS•Z•AuNP13 (9 nM – 0.14 nM) and RuPhenSS•Z•AuNP25 (5 nM – 0.078 nM) and washed with phenol red free media. The cells were then further incubated with the MTT reagent in Dulbecco's Modified Eagle Medium (DMEM) containing 10% FBS for 4 hours and then removed completely. DMSO was added to each well and then analysed on a tecan infinite 200 probe plate reader. Results were normalised against the vehicle control.

3.5.7 Confocal microscopy of live A549 cells

Dosing of A549 cells was performed in 35 mm dishes with a 10 mm glass insert. Cells were seeded at 100 000 cells per dish in 1 mL complete media. Prior to dosing with 13 nm and 25 nm RuPhenSS•Z•AuNP, cells were washed in warm PBS and cell media was replaced with 900 µL fresh media. RuPhenSS•Z•AuNP13 (100 µL, 9 nM) and RuPhenSS•Z•AuNP25 (100 µL, 2 nM) was added to the cell media for the required incubation time. For confocal microscopy of cells, cell media was removed and cells washed twice in warm PBS. For Hoechst nuclear staining 20 µM of a 20 mM stock solution of Hoechst 3328 in PBS was added for 10 minutes in the dark. The cells were washed and phenol red free cell media was added (1 mL per well) and imaged immediately. Confocal microscopy of live cells was performed using a Leica TCS SP8 upright confocal laser scanning system using a 40x ceramic H_2O immersion dip objective lens. 405 nm, 458 nm, 488 nm, 633 nm solid-state laser lines were used.

3.5.8 Mass spectrometry of RuPhenSS•AuNP13

Mass spectrometry of RuPhenSS•Z•AuNP13 was performed on a Bruker UltraFlextreme MALDI. RuPhenSS•Z•AuNP13 was dried serially (5 x) on a MTP-384 anchorchip MALDI steel target plate and analysed in Flexanalysis 3.0. Sample was conducted at 100 Hz laser frequency, 500 shots totaling 2000 shot accumulation.

3.6 References

1. P.-T. Chou and Y. Chi, *Eur. J. Chem.*, 2007, **13**, 380-395.

2. B. Ma, P. I. Djurovich and M. E. Thompson, *Coord. Chem. Rev.*, 2005, **249**, 1501-1510.

3. Y. Yang, Q. Zhao, W. Feng and F. Li, *Chem. Rev.*, 2013, **113**, 192-270.

4. Q. Zhao, M. Yu, L. Shi, S. Liu, C. Li, M. Shi, Z. Zhou, C. Huang and F. Li, *Organometallics*, 2010, **29**, 1085-1091.

5. A. Wragg, M. R. Gill, C. J. Hill, X. Su, A. J. H. M. Meijer, C. Smythe and J. A. Thomas, *Chem. Commun.*, 2014, **50**, 14494-14497.

6. R. E. Holmlin, J. A. Yao and J. K. Barton, *Inorg. Chem.*, 1999, **38**, 174-189.

7. N. J. Rogers, S. Claire, R. M. Harris, S. Farabi, G. Zikeli, I. B. Styles, N. J. Hodges and Z. Pikramenou, *Chem. Commun.*, 2014, **50**, 617-619.

8. H. Huang, B. Yu, P. Zhang, J. Huang, Y. Chen, G. Gasser, L. Ji and H. Chao, *Angew. Chem., Int. Ed.*, 2015, **54**, 14049-14052.

9. S. M. King, S. Claire, R. I. Teixeira, A. N. Dosumu, A. J. Carrod, H. Dehghani, M. J. Hannon, A. D. Ward, R. Bicknell, S. W. Botchway, N. J. Hodges and Z. Pikramenou, *J. Am. Chem. Soc.*, 2018, **140**, 10242-10249.

10. W. Wang, Z.-Z. Dong, C. Yang, G. Li, Y.-C. Tse, C.-H. Leung and D.-L. Ma, *Sens. Actuators B: Chem.*, 2017, **251**, 374-379.

11. K. K.-W. Lo and A. H.-H. Leung, *Sci. China Chem.*, 2010, **53**, 2091-2098.

12. J. Shum, P. K.-K. Leung and K. K.-W. Lo, *Inorg. Chem.*, 2019.

13. W. Zhan and A. J. Bard, *Anal. Chem.*, 2007, **79**, 459-463.

14. F. N. Castellano, J. D. Dattelbaum and J. R. Lakowicz, *Anal. Biochem.*, 1998, **255**, 165-170.

15. M. Wojdyla, J. A. Smith, S. Vasudevan, S. J. Quinn and J. M. Kelly, *Photochem. Photobiol. Sci.*, 2010, **9**, 1196-1202.

16. L.-H. Chung, K.-S. Cho, J. England, S.-C. Chan, K. Wieghardt and C.-Y. Wong, *Inorg. Chem.*, 2013, **52**, 9885-9896.

17. P. Zhang, H. Huang, Y. Chen, J. Wang, L. Ji and H. Chao, *Biomater.*, 2015, **53**, 522-531.

18. M. R. Gill, J. Garcia-Lara, S. J. Foster, C. Smythe, G. Battaglia and J. A. Thomas, *Nat Chem*, 2009, **1**, 662-667.

19. J. Liu, Y. Chen, G. Li, P. Zhang, C. Jin, L. Zeng, L. Ji and H. Chao, *Biomater.*, 2015, **56**, 140-153.

20. K. L. Smitten, P. A. Scattergood, C. Kiker, J. A. Thomas and P. I. P. Elliott, *Chem. Sci.*, 2020, **11**, 8928-8935.

21. A. F. A. Peacock, A. Habtemariam, R. Fernández, V. Walland, F. P. A. Fabbiani, S. Parsons, R. E. Aird, D. I. Jodrell and P. J. Sadler, *J. Am. Chem. Soc.*, 2006, **128**, 1739-1748.

22. M. C. Jung, N. Munro, G. Shi, A. C. Michael and S. G. Weber, *Anal. Chem.*, 2006, **78**, 1761-1768.

23. C. Mari, V. Pierroz, S. Ferrari and G. Gasser, *Chem. Sci.*, 2015, **6**, 2660-2686.

24. J. D. Knoll and C. Turro, *Coord. Chem. Rev.*, 2015, **282-283**, 110-126.

25. R. Lincoln, L. Kohler, S. Monro, H. Yin, M. Stephenson, R. Zong, A. Chouai, C. Dorsey, R. Hennigar, R. P. Thummel and S. A. McFarland, *J. Am. Chem. Soc.*, 2013, **135**, 17161-17175.

26. T. Joshi, V. Pierroz, C. Mari, L. Gemperle, S. Ferrari and G. Gasser, *Angew. Chem. Int. Ed.*, 2014, **53**, 2960-2963.

27. F. Barragán, P. López-Senín, L. Salassa, S. Betanzos-Lara, A. Habtemariam, V. Moreno, P. J. Sadler and V. Marchán, *J. Am. Chem. Soc.*, 2011, **133**, 14098-14108.

28. A. F. Henwood and E. Zysman-Colman, *Chem. Commun.*, 2017, **53**, 807-826.

29. W. Yang, D. Wang, Q. Song, S. Zhang, Q. Wang and Y. Ding, *Organometallics*, 2013, **32**, 4130-4135.

30. C.-P. Tan, Y.-M. Zhong, L.-N. Ji and Z.-W. Mao, *Chem. Sci.*, 2021, **12**, 2357-2367.

31. R. Huang, C.-H. Huang, J. Shao and B.-Z. Zhu, *J. Phys. Chem. Lett.*, 2019, **10**, 5909-5916.

32. R. Huang, F.-P. Feng, C.-H. Huang, L. Mao, M. Tang, Z.-Y. Yan, B. Shao, L. Qin, T. Xu, Y.-H. Xue and B.-Z. Zhu, *ACS Appl. Mater. Inter.*, 2020, **12**, 3465-3473.

33. K. E. Erkkila, D. T. Odom and J. K. Barton, *Chem. Rev.*, 1999, **99**, 2777-2796.

34. R. E. Holmlin, E. D. A. Stemp and J. K. Barton, *Inorg. Chem.*, 1998, **37**, 29-34.

35. C. A. Puckett and J. K. Barton, *J. Am. Chem. Soc.*, 2007, **129**, 46-47.

36. H. Huang, S. Banerjee, K. Qiu, P. Zhang, O. Blacque, T. Malcomson, M. J. Paterson, G. J. Clarkson, M. Staniforth, V. G. Stavros, G. Gasser, H. Chao and P. J. Sadler, *Nat. Chem.*, 2019, **11**, 1041-1048.

37. Q. G. Mulazzani, M. Ciano, M. D'Angelantonio, M. Venturi and M. A. J. Rodgers, *J. Am. Chem. Soc.*, 1988, **110**, 2451-2457.

38. J. Shum, P. K.-K. Leung and K. K.-W. Lo, *Inorg. Chem.*, 2019, **58**, 2231-2247.

39. A. M. Nonat, S. J. Quinn and T. Gunnlaugsson, *Inorg. Chem.*, 2009, **48**, 4646-4648.

40. B. M. Zeglis, V. C. Pierre and J. K. Barton, *Chem. Commun.*, 2007, DOI: 10.1039/B710949K, 4565-4579.

41. F. E. Poynton, S. A. Bright, S. Blasco, D. C. Williams, J. M. Kelly and T. Gunnlaugsson, *Chem. Soc. Rev.*, 2017, **46**, 7706-7756.

42. R. E. Holmlin and J. K. Barton, *Inorg. Chem.*, 1995, **34**, 7-8.

43. H. Huang, P. Zhang, B. Yu, Y. Chen, J. Wang, L. Ji and H. Chao, *J. Med. Chem.*, 2014, **57**, 8971-8983.

44. B.-Z. Zhu, X.-J. Chao, C.-H. Huang and Y. Li, *Chem. Sci.*, 2016, **7**, 4016-4023.

45. Y. Chen, T. W. Rees, L. Ji and H. Chao, *Curr. Opin. Chem. Biol.*, 2018, **43**, 51-57.

46. K. S. Gkika, A. Byrne and T. E. Keyes, *Dalton Trans.*, 2019, **48**, 17461-17471.

47. H. Singh, S. Sreedharan, E. Oyarzabal, T. S. Mahapatra, N. Green, Y.-Y. I. Shih, M. Das, J. A. Thomas, S. K. Pramanik and A. Das, *Chem. Commun.*, 2020.

48. R. Cao, J. Jia, X. Ma, M. Zhou and H. Fei, *J. Med. Chem.*, 2013, **56**, 3636-3644.

49. J. Zielonka, J. Joseph, A. Sikora, M. Hardy, O. Ouari, J. Vasquez-Vivar, G. Cheng, M. Lopez and B. Kalyanaraman, *Chem. Rev.*, 2017, **117**, 10043-10120.

50. J. Lee, D. K. Chatterjee, M. H. Lee and S. Krishnan, *Cancer Lett.*, 2014, **347**, 46-53.

51. L. Mocan, C. T. Matea, D. Bartos, O. Mosteanu, T. Pop, T. Mocan and C. Iancu, *Clujul Medical*, 2016, **89**, 199-202.

52. W. Cai, T. Gao, H. Hong and J. Sun, *Nanotechnol. Sci. Appl.*, 2008, **2008**, 10.2147/NSA.S3788.

53. S. Osborne, *PhD, University of Birmingham*, 2017.

54. J. Turkevich, P. C. Stevenson and J. Hillier, *Discuss. Faraday Soc.*, 1951, **11**, 55-75.

55. F. Schulz, T. Homolka, N. G. Bastús, V. Puntes, H. Weller and T. Vossmeyer, *Langmuir*, 2014, **30**, 10779-10784.

56. H. C. J. N. J. Rogers, S. Claire, D. J. Lewis, G. Zikeli, N. J. Hodges, S. Egginton, G. B. Nash and Z. Pikramenou *Nanomed.*, 2017.

57. J. Zhang, L. Mou and X. Jiang, *Chem. Sci.*, 2020, **11**, 923-936.

58. R. Popovtzer, A. Agrawal, N. A. Kotov, A. Popovtzer, J. Balter, T. E. Carey and R. Kopelman, *Nano Lett.*, 2008, **8**, 4593-4596.

59. J. Spadavecchia, D. Movia, C. Moore, C. M. Maguire, H. Moustaoui, S. Casale, Y. Volkov and A. Prina-Mello, *Int J Nanomed.*, 2016, **11**, 791-822.

60. C. M. Goodman, C. D. McCusker, T. Yilmaz and V. M. Rotello, *Bioconjug. Chem.*, 2004, **15**, 897-900.

61. C. Peng, L. Zheng, Q. Chen, M. Shen, R. Guo, H. Wang, X. Cao, G. Zhang and X. Shi, *Biomater.*, 2012, **33**, 1107-1119.

62. P. García Calavia, G. Bruce, L. Pérez-García and D. A. Russell, *Photochem. Photobiol. Sci.*, 2018, **17**, 1534-1552.

63. J. Manson, D. Kumar, B. J. Meenan and D. Dixon, *Gold Bull.*, 2011, **44**, 99-105.

64. C. R. Patra, R. Bhattacharya, E. Wang, A. Katarya, J. S. Lau, S. Dutta, M. Muders, S. Wang, S. A. Buhrow, S. L. Safgren, M. J. Yaszemski, J. M. Reid, M. M. Ames, P. Mukherjee and D. Mukhopadhyay, *Cancer Res.*, 2008, **68**, 1970-1978.

65. M. Martinez-Calvo, K. N. Orange, R. B. P. Elmes, B. la Cour Poulsen, D. C. Williams and T. Gunnlaugsson, *Nanoscale*, 2016, **8**, 563-574.

66. B. Yan, S. T. Kim, C. S. Kim, K. Saha, D. F. Moyano, Y. Xing, Y. Jiang, A. L. Roberts, F. S. Alfonso, V. M. Rotello and R. W. Vachet, *J. Am. Chem. Soc.*, 2013, **135**, 12564-12567.

67. N. J. Rogers, H. C. Jeffery, S. Claire, D. J. Lewis, G. Zikeli, N. J. Hodges, S. Egginton, G. B. Nash and Z. Pikramenou, *Nanomed.*, 2017, **12**, 2725-2740.

68. R.-C. Huang, W.-J. Chiu, I. Po-Jung Lai and C.-C. Huang, *Sci. Rep.*, 2015, **5**, 10292.

69. K. Chughtai and R. M. A. Heeren, *Chem. Rev.*, 2010, **110**, 3237-3277.

70. S. Liu, W. Zheng, K. Wu, Y. Lin, F. Jia, Y. Zhang, Z. Wang, Q. Luo, Y. Zhao and F. Wang, *Chem. Commun.*, 2017, **53**, 4136-4139.

71. R. F. S. Lee, S. Escrig, M. Croisier, S. Clerc-Rosset, G. W. Knott, A. Meibom, C. A. Davey, K. Johnsson and P. J. Dyson, *Chem. Commun.*, 2015, **51**, 16486-16489.

72. A. Weiss, R. H. Berndsen, M. Dubois, C. Müller, R. Schibli, A. W. Griffioen, P. J. Dyson and P. Nowak-Sliwinska, *Chem. Sci.*, 2014, **5**, 4742-4748.

73. J. Du, E. Zhang, Y. Zhao, W. Zheng, Y. Zhang, Y. Lin, Z. Wang, Q. Luo, K. Wu and F. Wang, *Metallomics*, 2015, **7**, 1573-1583.

74. K. Wu, F. Jia, W. Zheng, Q. Luo, Y. Zhao and F. Wang, *J. Biol. Inorg. Chem.*, 2017, **22**, 653-661.

75. L. Zeng, P. Gupta, Y. Chen, E. Wang, L. Ji, H. Chao and Z.-S. Chen, *Chem. Soc. Rev.*, 2017, **46**, 5771-5804.

76. S. Her, D. A. Jaffray and C. Allen, *Adv. Drug Deliv. Rev.*, 2017, **109**, 84-101.

77. D. Muko, T. Ikenaga, M. Kasai, J. B. Rabor, A. Nishitani and Y. Niidome, *J. Mass Spectrom.*, 2019, **54**, 1-6.

78. S. A. M. Osborne and Z. Pikramenou, *Faraday Discuss.*, 2015, **185**, 219-231.

79. S. J. Adams, D. J. Lewis, J. A. Preece and Z. Pikramenou, *ACS Appl. Mater. Inter.*, 2014, **6**, 11598-11608.

80. A. N. Dosumu, S. Claire, L. S. Watson, P. M. Girio, S. A. M. Osborne, Z. Pikramenou and N. J. Hodges, *JACS Au*, 2021, **1**, 174-186.

81. S. J. Adams, A. J. Carrod, L. A. Rochford, M. Walker and Z. Pikramenou, *Chem. Select*, 2018, **3**, 3251-3257.

82. S. Bernhard, J. A. Barron, P. L. Houston, H. D. Abruña, J. L. Ruglovksy, X. Gao and G. G. Malliaras, *J. Am. Chem. Soc.*, 2002, **124**, 13624-13628.

83. N. Vilvamani, R. D. Gupta and S. K. Awasthi, *RSC Adv.*, 2015, **5**, 13451-13461.

84. K. Nakamaru, *Bull. Chem. Soc. Jpn.*, 1982, **55**, 2697-2705.

85. K. Kalyanasundaram, *Coord. Chem. Rev.*, 1982, **46**, 159-244.

86. L.-F. Tan, H. Chao, H. Li, Y.-J. Liu, B. Sun, W. Wei and L.-N. Ji, *J. Inorg. Biochem.*, 2005, **99**, 513-520.

87. A. Juris, L. Prodi, A. Harriman, R. Ziessel, M. Hissler, A. El-ghayoury, F. Wu, E. C. Riesgo and R. P. Thummel, *Inorg. Chem.*, 2000, **39**, 3590-3598.

88. J. Su Park, M. Song, Y.-S. Gal, J. Wook Lee and S.-H. Jin, *Synth. Met.*, 2011, **161**, 213-218..

89. W. Eck, G. Craig, A. Sigdel, G. Ritter, L. J. Old, L. Tang, M. F. Brennan, P. J. Allen and M. D. Mason, *ACS Nano*, 2008, **2**, 2263-2272.

90. K. Rahme, L. Chen, R. G. Hobbs, M. A. Morris, C. O'Driscoll and J. D. Holmes, *RSC Adv.*, 2013, **3**, 6085-6094.

91. Z. Zhong, S. Patskovskyy, P. Bouvrette, J. H. T. Luong and A. Gedanken, *J. Phys. Chem.*, 2004, **108**, 4046-4052.

92. A. Palermo, E. M. Forsberg, B. Warth, A. E. Aisporna, E. Billings, E. Kuang, H. P. Benton, D. Berry and G. Siuzdak, *ACS Nano*, 2018, **12**, 6938-6948.

93. W. Haiss, N. T. K. Thanh, J. Aveyard and D. G. Fernig, *Anal. Chem.*, 2007, **79**, 4215-4221.

94. A. B. Caballero, L. Cardo, S. Claire, J. S. Craig, N. J. Hodges, A. Vladyka, T. Albrecht, L. A. Rochford, Z. Pikramenou and M. J. Hannon, *Chem. Sci.*, 2019, **10**, 9244-9256.

95. A. Davies, D. J. Lewis, S. P. Watson, S. G. Thomas and Z. Pikramenou, *PNAS*, 2012, **109**, 1862.

96. L. Zhang, X. Sun, Y. Song, X. Jiang, S. Dong and E. Wang, *Langmuir*, 2006, **22**, 2838-2843.

97. S. Eustis and M. A. El-Sayed, *Chem. Soc. Rev.*, 2006, **35**, 209-217.

98. J. Sekuła, J. Nizioł, W. Rode and T. Ruman, *Anal. Chim. Acta*, 2015, **875**, 61-72.

4.0 Luminescent Osmium Gold Nanoparticles for Imaging in Cells

4.1 Introduction

There have been many examples reported on luminescent transition based metal complexes employed for cellular imaging over recent years namely iridium, rhenium and ruthenium but only a very select handful concerning osmium.[1,2] Osmium(II) based metal complexes typically display poor nuclear and cellular uptake which has limited them in cell imaging applications.[3] For a transition metal complex to be employed as an imaging agent certain factors must be considered such as cell permeation, organelle specificity, chemical stability and the ability for the luminescence to be detected sufficiently within a biological environment. To address these factors, designing complexes that can permeate cells efficiently, target specific organelles, aid with chemical stability and enhance the luminescence properties can be achieved through structural ligands. For example, dipyridophenazine (dppz) can bind and target DNA and/or RNA which enhances emission intensity of the lumophore through hydrophobic pockets reducing quenching.[4-6] Additionally, conjugation of proteins including antibodies has been employed for permeating and targeting specific cells however the antibody guided conjugation typically rely on a scaffold for delivery.[7-13] Ruthenium(II), iridium(I), osmium(II) metal complexes typically already possess high chemical and photostability compared to organic fluorophores making them inert towards ligand substitution rendering them extremely desirable for imaging applications.[14]

Although osmium(II) metal complexes have highly desirable characteristics ideal for imaging such as excitation at lower wavelengths reducing cell damage, possess emission profiles deep into the red region and NIR region and can significantly decrease background absorption, they are notoriously known for displaying poor photophysical properties such as very small

luminescent lifetimes and weak emission.[15-17] Those that have been reported as imaging agents consist of a variety of ligands ranging from triazoles to dppz ligands.[16,18-22]

A series of $[Os(bpy)_{3-n}(pytz)_n](PF_6)_2$, where bpy = 2,2'-bipyridine, pytz = 1-benzyl-4-(pyrid-2-yl)-1,2,3-triazole, were synthesised and characterised for their luminescence properties as cellular imaging agents.[23] The variance in pytz and bpy ligands for the four complexes are denonted by n and the complexes utilised were as their chloride salts which remained emissive in aerated solutions at room temperature. These complexes utilised osmium's rare feature for being able to access the usually spin forbidden direct ground state into the triplet metal to ligand charge transfer band at the red region negating auto-fluorescence from cells (Figure 4.1.1). The potential imaging agents were employed in cancer cell lines where they were readily taken up in HeLa (cervical cancer cells) and EJ (bladder carcinoma) cancer cells displaying apparent lysosomal and endosomal localisation whilst the cell viability was maintained in both light and dark conditions.[23]

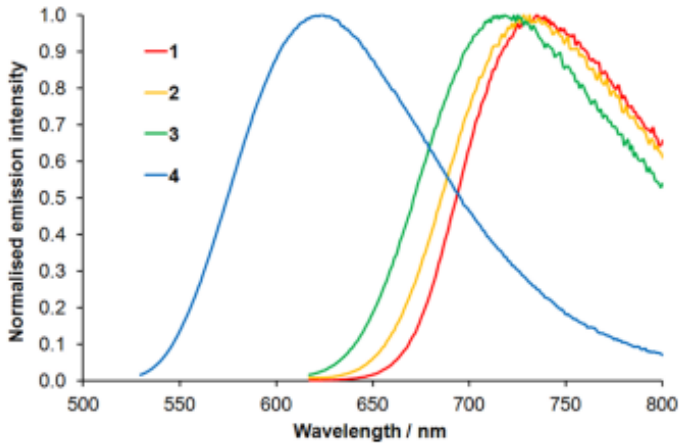

Figure 4.1.1. Emission profiles of $[Os(bpy)_{3-n}(pytz)_n](PF_6)_2$ where 1, n = 0, 2, n = 1, 3, n = 2 and 4 n = 3 in aerated water at room temperature. Figure taken from Omar *et al.*[23]

The complexes display identical absorption properties to their "PF_6" counterparts from aerated acetonitrile to aerated water. Additionally, the emission profiles of the chloride ion complexes

show very little change in comparison to the "PF_6" counter ions in aerated acetonitrile which is due to the solvent interactions. They also range from orange to NIR emission allowing a plethora of applications through tuning of different ligands.

Alternatively to triazole based osmium complexes, conjugating targeting proteins for efficient cellular uptake can be employed. Cancer cells differentiate to normal cells through their cellular function. Normal cells rely on oxidative phosphorylation for the generation of adenosine triphosphate (ATP).[24] However, cancer cells have increased glucose uptake and rely on aerobic glycolysis (fermentation of glucose to lactate in the presence of oxygen) even in the presence of completely functioning mitochondria to generate ATP.[25,26] This is known as the Warburg effect.

Targeting mitochondria within cancer cells has become an increasingly researched field over the last few decades. It is well known that osmium can exhibit multiple oxidation states ranging from +2 to +4 and have been extensively and primarily researched as electrochemical agents.[27-30] Osmium(II) [bis-(4'-(4-carboxyphenyl)-2,2':6',2''-terpyridine)] was synthesised and conjugated to mitochondrial targeting peptides (Figure 4.1.2).[18] The conjugate complexes and the parent complex each display strong NIR emission centred deep into the red and NIR region of the spectrum at 750 nm. To observe the potential as mitochondrial targeting agents, they were dosed in live HeLa and MCF-7 cancer cells which revealed the parent complex unable to permeate the cell membrane. However, the osmium(II) complex conjugated with the targeting peptides was readily taken up and distributed in a concentration dependent manner. It was found that under concentrations of 50 µM the conjugated osmium(II) complex localised in the mitochondria and concentrations exceeding 50 µM displayed localisation throughout the cell and caused apoptosis following activation of caspase-3.[18]

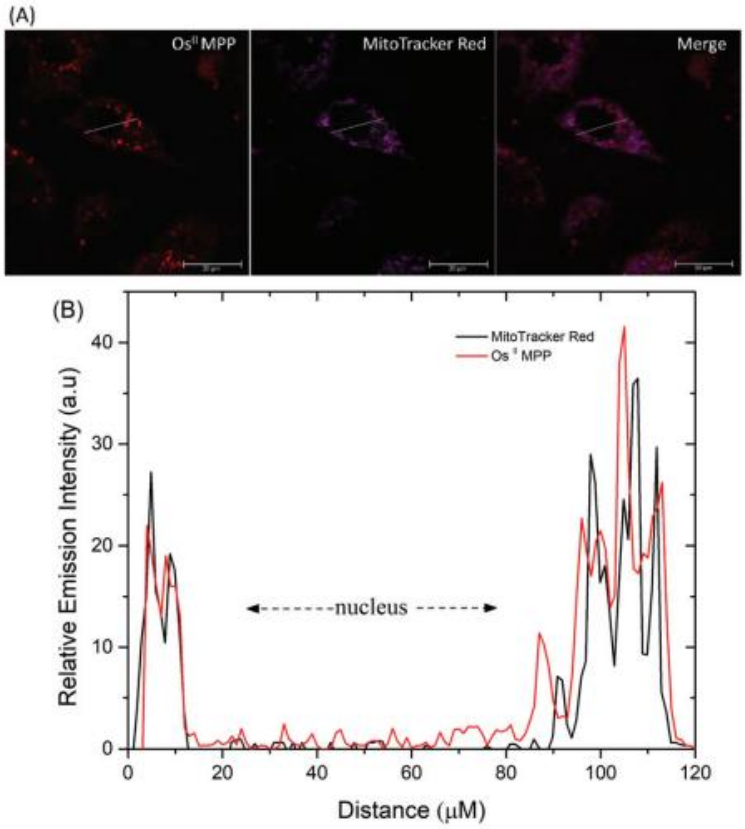

Figure 4.1.2. Co-localisation of osmium(II) conjugated mitochondrial targeting protein where (A) osmium emission (red), MitoTracker (purple) and merged and (B) fluorescence intensity profiles obtained from line profiles across the cell. Figure taken from Gkika *et al.*[18]

These conjugated osmium complexes displayed excellent photostability and reasonably good quantum yields making them attractive cell imaging agents regardless of displaying moderately lower emission lifetimes and quantum yields relative to the parent complex. To observe localisation, co-localisation with MitoTracker deep red was performed which demonstrated strong overlap of the complex to the mitochondrial stain (Figure 4.1.2).

Alternatively, octarginine, a cell penetrating peptide has also been studied when conjugated to a osmium(II) (bis-2,2-bipyridyl)-2(4-carboxylphenyl) imidazo[4,5f][1,10]phenanthroline complex for live cell imaging whilst comparing to its ruthenium analogue (Figure 4.1.3).[31] The cellular uptake and distribution was observed and compared against the ruthenium(II) analogue

which revealed similar uptakes and distribution. The osmium(II) complex displayed far red emission centred at 726 nm and exhibited very low cytotoxicity under both dark and light conditions however it displayed short lived luminescence in water.[31]

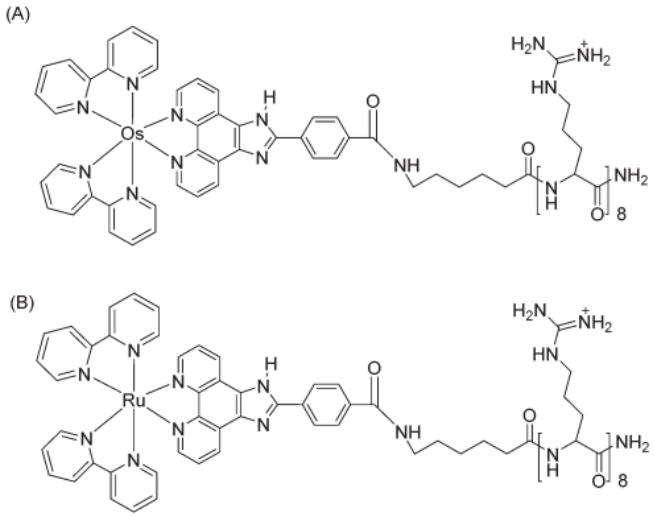

Figure 4.1.3. Chemical structures of $[Os(bpy)_2(pic\text{-}arg8)]^{10+}$ and $[Ru(bpy)_2(pic\text{-}arg8)]^{10+}$. Figure taken from Byrne *et al.*[31]

The parent analogue, $[Os(bpy)_2(pic)]^{2+}$ was impermeable to cells whereas the conjugated osmium complex, $[Os(bpy)_2(pic\text{-}arg8)]^{10+}$ was rapidly taken up and internalised within cells distributing it throughout the cell. This highlights the importance of designing such osmium(II) complexes for rapid cellular uptake for the employment as cellular imaging agents.

Alternatively to targeting mitochondria, the targeting of DNA and RNA has become of interest over recent decades.[3,32] RNA can be imaged through fluorescence imaging such as fluorescence in situ hybridisation (FISH), fluorophore tagged RNA binding proteins or aptamers, through use of a tripeptide (Lys-Cys-Lys) on gold nanoclusters and organic molecules.[33-38] However, currently there is only one commercially available RNA dye, Syto RNA-select, which has

emission properties in the green region and can only stain RNA in fixed cells. Two osmium(II) complexes $[Osbpy)_2(IP\text{-}NMe_2)]^{2+}$ and $[Os(bpy)_2(IP\text{-}OH)]^{2+}$, where IP = iminopyridine and Me = methyl, were synthesised for their NIR luminescence imaging capabilities in cells and their binding ability to RNA through use of their iminopydridine ligands (Figure 4.1.4). Imines and amines can bind to DNA and RNA through amino acids and as such make them ideal candidates as targeting agents.[39,40]

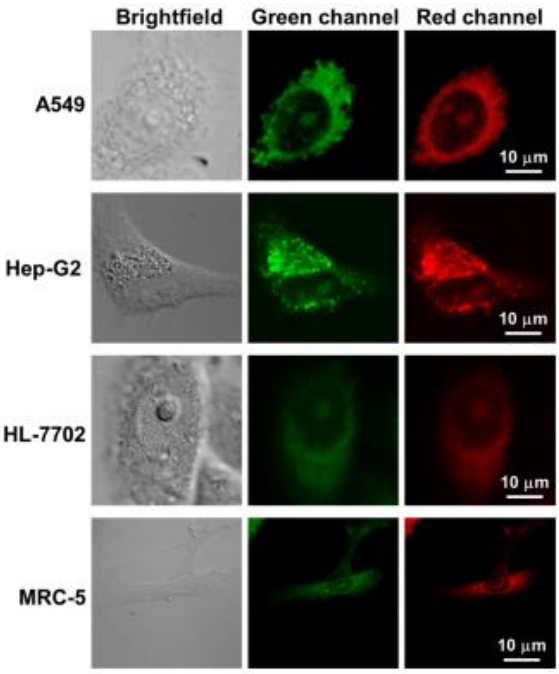

Figure 4.1.4. Confocal microscopy images of live cells incubated with $[Os(bpy)_2(IP\text{-}OH)]^{2+}$ (10 µM, 2 hours) showing dual emission in green (λ_{exc} = 488 nm, λ_{em} = 540 – 600 nm) and in red channel (λ_{exc} = 488 nm, λ_{em} = 710 – 780 nm). Scale bar = 10 µm. Figure taken from Ge *et al.*[22]

It was found the two osmium(II) complexes designed exhibited dual emission properties in both the green region centred at 573 nm and NIR luminescence centred at 738 nm. It is noteworthy that these complexes display enhanced luminescence when binding to RNA and can simultaneously image the nucleoli of both fixed and live cells. Additionally, they display low

cytotoxicity and good photostability allowing their development as potential RNA and nucleoli imaging probes.

Dinuclear metal complexes have started emerging over recent years for their potential as imaging agents. A dinuclear osmium complex, $[Os(TAP)_2tpphz]^{4+}$ where tpphz = tetrapyrido[3,2- a:2′,3′-c:3″,2″-h:2‴,3‴-j]phenazine and TAP = 1,4,5,8- tetraazaphenanthrene) was employed for imaging nuclear DNA (Figure 4.1.5).[41] Studies revealed the dinuclear complex to have a NIR centred emission at 780 nm and was shown to be both non cytotoxic or photocytotoxic when comparing to its ruthenium analogue. Additionally this complex is highly photostable and can permeate live cell membranes making it attractive for cellular imaging applications.

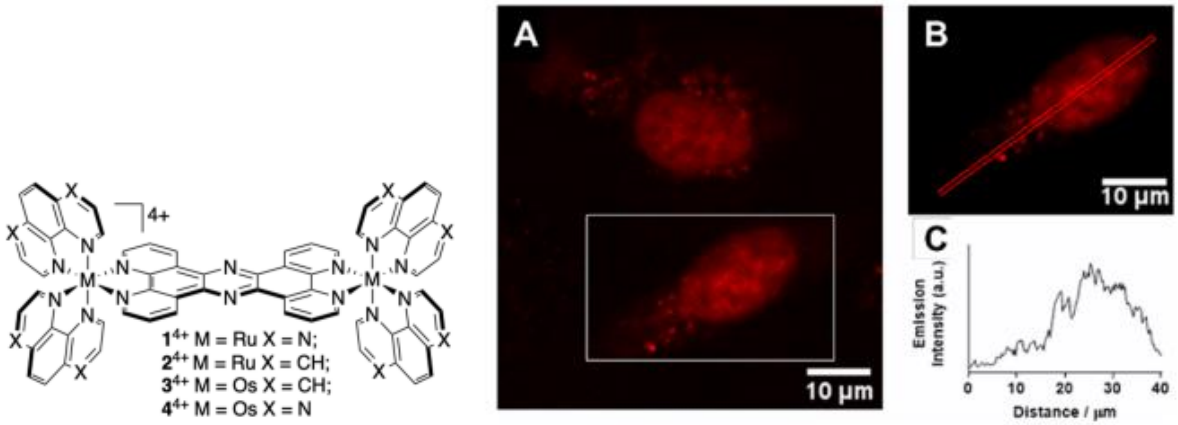

Figure 4.1.5. Chemical structures of osmium complexes (left) and live cell imaging (right) of MCF7 cells treated with 150 µM complex 4 for 24 hours (A) single MCF7 cell (B) and distance vs emission profile of the single cell in B. Figure taken from Droge *et al*.[41]

Despite the four complexes synthesised being structurally similar and all binding to DNA, their photophysical properties vary massively. This is observed between complex 3 and 4 whereby complex 3 being non-emissive and complex 4 being emissive. Complex 4 also displayed excellent stability when constantly irradiated by displaying no changes in its optical properties.

However, in addition to imaging transition metal complexes via confocal light microscopy, TEM is another alternative. Transition metal complexes are electron dense and can therefore be visualised under TEM. Two dinuclear osmium complexes have been synthesised to act as a TEM contrast agents allowing high resolution visualisation of the intracellular structures (Figure 4.1.6).[42]

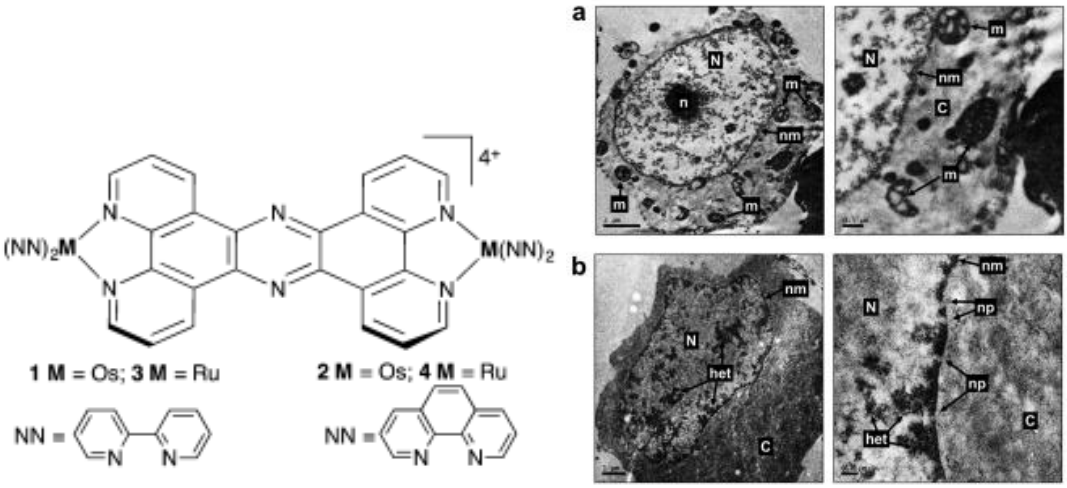

Figure 4.1.6. Chemical structures of osmium and ruthenium complexes (left) and TEM (right) of necrotic MCF7 cells visualised by complex 1 (500 µM, 1 hour)(a), successful nuclear internalisation of complex 2 in MCF cell in the nucleus through dense heterochromatin staining(500 µM, 1 hour) (b). Key: pm = plasma membrane, nm = nuclear membrane, N = nucleus, C = cytosol, n = nucleolus, m = mitochondria, het = heterochromatin, np = nuclear pore complex. Figure taken from Wragg *et al.*[42]

These complexes were found to be chemically stable, water soluble and non-volatile allowing them to function as contrast agents for TEM. They display excellent sub nuclear resolution and have been shown to be inert and easy to handle allowing them to pave a way as TEM contrast agents.

Although there are a handful of osmium complexes utilised as imaging agents, currently to our knowledge there is no such examples of osmium decorated onto a gold nanoparticle surface for

imaging applications. In addition to imaging, osmium has been studied for its anti-cancer activity and detection of molecules.[12,20,28,43-48]

Gold nanoparticles have received immense interest over the years for its multipurpose properties ranging from delivery of drugs to its anticancer activity and to its imaging properties utilising the unique surface plasmon resonance associated with them.[15,49-58] Since osmium typically exhibits poor photophysical properties and generally has poor cellular and nuclear uptake within cells, designing an luminescent osmium complex that can bind to gold nanoparticles is of paramount interest. This overcomes the shortcomings of related uptake issues associated with osmium through utilisation of the gold nanoparticles and allows a new pathway for the development of imaging and anticancer agents of osmium complexes to be delivered.

4.2 Chapter outline

In this chapter we have designed a novel luminescent osmium(II) complex with strong emission bridging the visible and NIR region for the attachment onto gold nanoparticles for imaging purposes. We present the justification of synthesising the novel osmium(II) complex (OsPhenSS) and the luminescent properties associated in aerated conditions and in the presence of a fluorosurfactant. Gold nanoparticles were synthesised and characterised through standard techniques of DLS and TEM. Upon coating of OsPhenSS onto the gold nanoparticles, the luminescent signature was obtained demonstrating the use of these particles as imaging agents in live A549 cells. Cell viability assays ascertained to the particles display non-cytotoxicity at all concentrations as determined statistically using a one-way ANOVA followed by a Dunnett's t-test towards live A549 cells making them ideal candidates for imaging.

4.3 Results and Discussion

4.3.1 Synthesis and luminescence characterisation of OsPhenSS

4.3.1.1 Synthesis of OsPhenSS

The complex OsPhenSS was synthesised based on the previously studied analogue, OsBpySS which was fully characterised by a previous group member, Sam Adams.[15] OsPhenSS was designed in the hope for greater photophysical properties in solution and to be employed onto gold nanoparticles for imaging capabilities despite the current limitations that osmium(II) complexes possess.[15,57,59,60] The bipyridine linker used (BpySS) has been previously examined and discussed in the previous chapter.[57]

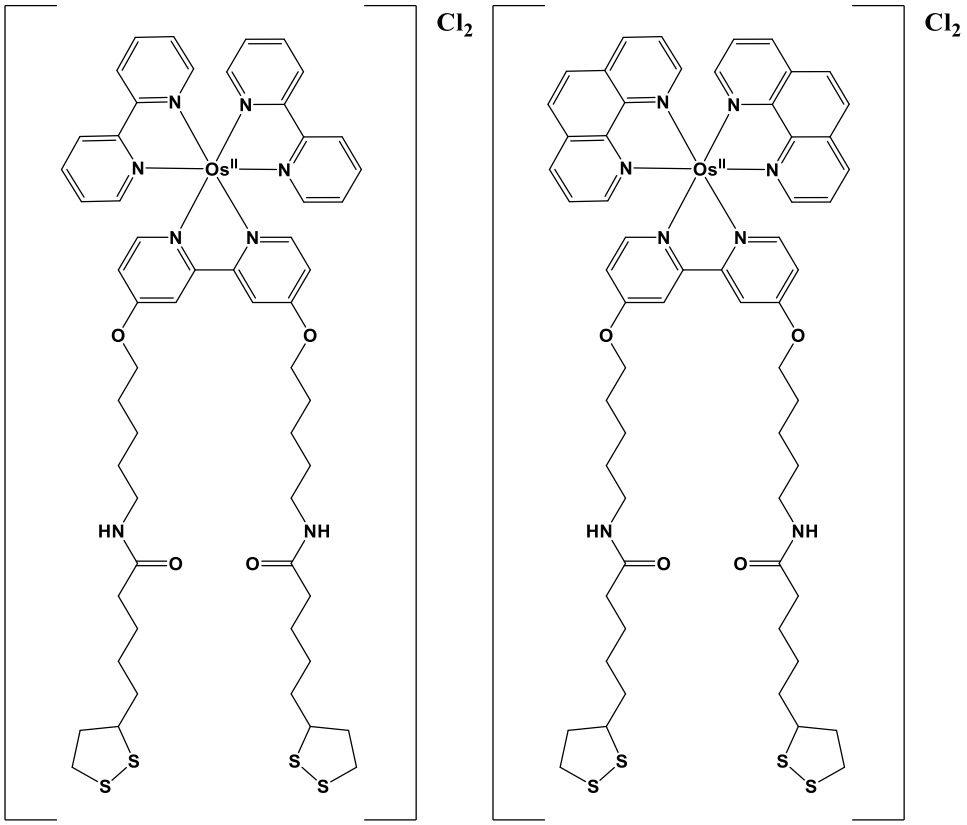

Figure 4.3.1.1.1. Chemical structures of OsBpySS (left) and OsPhenSS (right).

OsPhenSS was synthesised based on previously established methods for osmium(II) complexes and fully characterised by ^{1}H NMR, ^{13}C NMR, ESI MS, HSQC and HMBC which is in good agreement with similar complexes.[15,57,59,60] Confirmation of successful synthesis of OsPhenSS was indicated through ^{1}H NMR shifts from H5 at 6.82ppm on BpySS upfield to 6.74ppm on OsPhenSS whereas H3 shifts downfield from 7.94ppm to 8.04ppm. H6 shifts upfield from 8.45ppm to 7.26ppm due to being close to the nitrogen binding site and experiencing a change in environment. Ha and Hb cannot be used due to the $[Os(phen)_2Cl_2]$ being paramagnetic and unable to be characterised through ^{1}H NMR. ESI^+ MS further confirmed the successful synthesis of OsPhenSS from changing 622.07 m/z of $[Os(phen)_2Cl_2]^+$ to 643.2 m/z for $[OsPhenSS\text{-}2Cl]^{2+}$ resulting in a mass difference of 0.5 m/z between the isotope peaks indicating the presence of a +2 species.

Following isolation as the hexafluorophosphate salt, the complex underwent an ion exchange back to the chloride salt for solubility purposes. The exchange was confirmed through infra-red spectroscopy (Figure 4.3.1.1.2) revealing no bands associated at~540 cm^{-1} and ~860 cm^{-1} associated with the PF_6^- stretching frequencies.

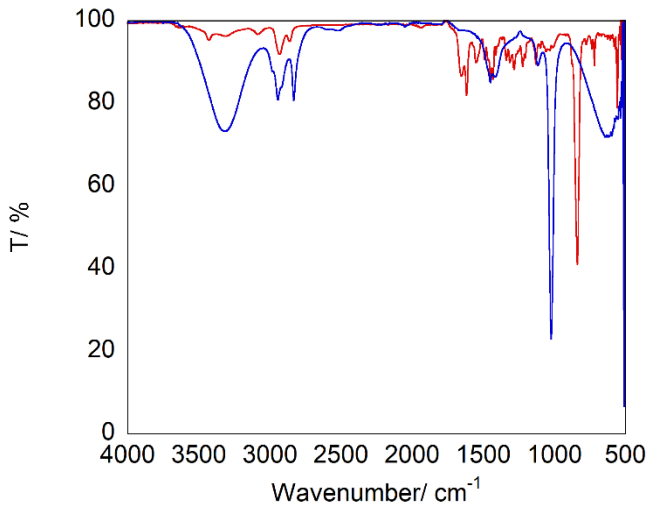

Figure 4.3.1.1.2. IR spectrum of OsPhenSS as the PF_6 counter ion (red) and the Cl_2 counter ion (blue) showing successful ion exchange.

4.3.1.2 Luminescence studies of OsPhenSS

The UV-Vis, emission, excitation, luminescent lifetimes and the luminescence quantum yield was taken in aerated water. The complex OsPhenSS was dissolved in methanol to yield a stock solution (1 mL, 1 mM) and then dissolved in water to form a 10 µM solution as the chloride salt.

The absorption profile, excitation and emission is displayed in Figure 4.3.1.2.1. The absorption profile of OsPhenSS displays the characteristic phenanthroline ^{1}LC (π - π^*) band arising at 266 nm. There is a small ILCT band and approximately 340 nm and a mix of MC (d-d) and the spin allowed ^{1}MLCT (d – π^*) states arising at 400 – 500 nm. Additionally, osmium complexes display the absorption of the spin forbidden direct ground state to ^{3}MLCT due to the high spin orbit coupling constant associated with the metal center which is visible in appreciable intensity from 500 – 700 nm.[61-63] In comparison to the parent analogue $[Os(phen)_3]^{2+}$, the ^{1}MLCT is red shifted by 10 nm.[64] The absorption wavelengths and their corresponding molar extinction coefficients, emission maxima and QY is tabulated below (Table 4.3.1.2.1). In comparison to

OsBpySS, OsPhenSS displays greater enhancement of the ^{1}MLCT extinction coefficient (13500 to 17600 M^{-1} cm^{-1}) whilst displaying minor blue shifts in emission and absorption wavelengths which is attributed to the presence of phenanthroline. It has been well documented that complexes employed with bis phenanthroline ligands display greater molar extinction coefficients, increased lifetimes and luminescence QY.[5,65] The absorption profile displayed by OsPhenSS is in good agreement with other bis phenanthroline osmium complexes.[60,64,66,67]

Table 4.3.1.2.1. Molar extinction coefficients, absorbance peaks and emission intensity of 10 µM OsPhenSS as the chloride salt in aerated water.

	UV-Vis λ_{max} / nm (ε / M^{-1} cm^{-1})	**Emission λ_{max} / nm**
OsPhenSS	225 (61000), 266 (63400), 343sh (9200), and 485 (17600)	770

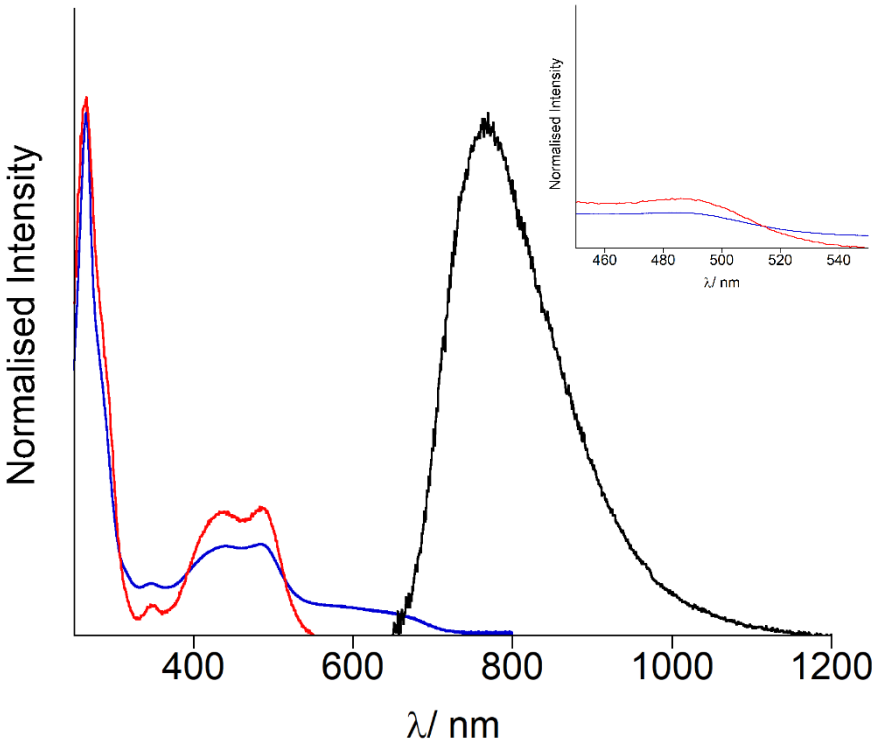

Figure 4.3.1.2.1. Normalised emission (black), excitation (red) and UV Vis (blue) of 10 µM OsPhenSS in 1mL aerated water (λ_{ex} = 485nm, λ_{em} = 770nm). Insert is magnification of excitation spectra 450 – 550 nm showing tail off.

Upon excitation at 485 nm, a broad based emission attributed to the ^{3}MLCT centred at 770 nm is observed in aerated water. In comparison to the bipyridine analogue, OsBpySS, this is 10 nm blue shifted. This is expected due to the phenanthroline behaviour causing blue shifts observed in literature. Additionally, this is significantly red shifted by 62 nm when compared to the tris phenanthroline osmium complex.[14,68] This far red broad emission centred at 770 nm exceeds other bis phenanthroline, the majority of bis bipyridine and bis terpyridine osmium(II) complexes although there are a few that demonstrate emission profiles exceeding far into the NIR (>800 nm).[3,12,16,18,19,21-23,41,69-73] The luminescence lifetime was taken in aerated water which revealed a very weak detection of a single component of 36 ns. This shows enhancement of 80% when compared to OsBpySS but is markedly decreased when comparing to

$[Os(Phen)_3]^{2+}$ which reveal lifetimes of 210 ns in acetonitrile.[15,64,74,75] Despite the significantly lower lifetime to its parent analogue, the lifetime matches well with other reported osmium(II) complexes ranging in the low nanosecond scale (10 – 50 ns) however much longer lifetimes have been reported.[5,41,71,73,75,76] The luminescence QY of OsPhenSS was taken in DMSO and compared to a standard (indocyanine green, ICG) with a known QY in the same solvent.[77] The QY of OsPhenSS was calculated to be 1.3% in aerated DMSO.

4.3.1.3 Luminescence studies of OsPhenSS in the presence of Zonyl FSA

In order to determine enhancement of the photophysical properties of OsPhenSS, the UV-Vis, emission, excitation and the luminescent lifetimes was taken in aerated water in the presence of 485 µM Zonyl FSA. The complex OsPhenSS was dissolved in methanol to yield a stock solution (1 mL, 1 mM) and then dissolved in water to form a 10 µM solution as the chloride salt in the presence of the fluorsurfactant.

Just like the ruthenium(II) complexes, no significant change is present in the absorption profile indicating no changes to the ^{1}MLCT or LC states. This suggests any enhancement of emission or through the luminescence lifetimes is due to shielding from $^1O_2$ thereby making the process more efficient. Upon excitation at 485 nm, a broad based emission attributed to the ^{3}MLCT centred at 770 nm is observed in aerated water in the presence of the fluorosurfactant. In comparison to OsPhenSS in aerated water, no shift in λ_{max} is seen.

Table 4.3.1.3.1. Molar extinction coefficients, absorbance peaks and emission intensity of 10 µM OsPhenSS as the chloride salt in the presence of 485 µM Zonyl FSA in aerated water

	UV-Vis λ_{max} / nm (ε / M^{-1} cm^{-1})	Emission λ_{max} / nm
OsPhenSS	225 (61000), 266 (63400), 343sh (9200), and 485 (17600)	770

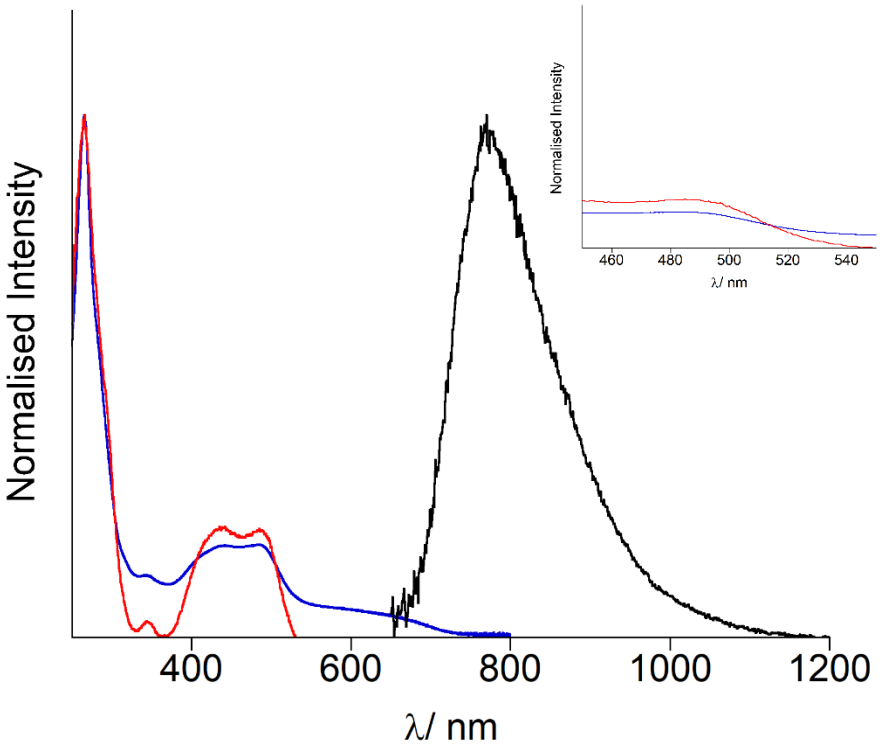

Figure 4.3.1.3.1. Normalised emission (black), excitation (red) and UV Vis (blue) of 10 µM OsPhenSS in the presence of 485 µM Zonyl FSA in 1mL aerated water (λ_{ex} = 485nm, λ_{em} = 770nm). Insert is magnification of excitation spectra 450 – 55 nm showing tail off.

The luminescence lifetimes however displayed an increase to 46 ns, a 27% increase from the free complex in solution. Despite again a weak signal of detection, it was clear this enhancement in lifetime is attributed to the interaction of Zonyl FSA with OsPhenSS due to protection of $^3O_2$ quenching.[78-80] Additionally, solvent interactions have been shown to lower the rate of diffusion of $^3O_2$ which results in stronger emission and lifetimes. This suggests the surfactant shields the metal complex from $^3O_2$ thereby enhancing the lifetimes and emission of OsPhenSS in aerated water.[32,57]

4.3.2 Coating of OsPhenSS on 13 nm and 25 nm gold nanoparticles

Synthesis and characterisation of 13 nm and 25 nm c-AuNP is described in the previous chapter. The coating of Zonyl FSA onto 13 nm and 25 nm c-AuNP was followed as per the previous chapter and published methods within the Pikramenou group.[56,57,81-83]

Upon addition of Zonyl FSA, a 1 nm red shift is observed in the SPR band for both 13 nm and 25 nm AuNP yielding a λ_{max} at 518 nm and 520 nm respectively. DLS of the Z•AuNP13 indicated a size of 20 ± 5 nm and a PDI of 0.05 whereas the Z•AuNP25 indicated an average size of 29 ± 8 nm with a PDI 0.22. The small PDI from the Z•AuNP13 suggests uniform and spherical sizes whereas the Z•AuNP25 displayed a larger PDI suggesting a slight variance in sizes or shape of the gold nanoparticles. Additionally, there is a slight increase in size for both the 13 nm and 25 nm Z•AuNP when compared to the c-AuNP counterparts which is attributed to the surfactant layer present on the surface however the PDI for the 13 nm gold nanoparticles stay constant whereas the Z•AuNP25 PDI increase from the c-AuNP25.[84]

For coating of Z•AuNP13 and Z•AuNP25, the complex OsPhenSS was dissolved in methanol to yield a stock solution of 1 mM as the chloride salt. OsPhenSS, just like the ruthenium(II) complexes discussed in chapter 3, can bind through the disulphide legs present on the legs of the linker.[85] Microlitre additions of OsPhenSS were mixed with Z•AuNP13 and Z•AuNP25 to observe maximum decoration on the surface of the gold nanoparticles through monitoring the SPR band via UV-Vis spectroscopy (Figure 4.3.2.1).

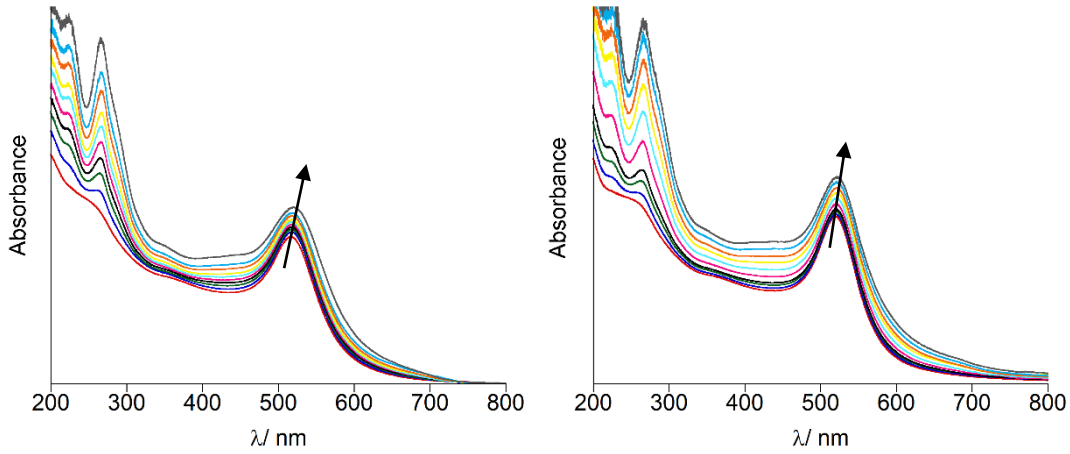

Figure 4.3.2.1. Titration of 5 µL quantities of 1 mM OsPhenSS into 4.5 nM Z•AuNP13 in aerated water (28 µL added) (left) and titration of 5 µL quantities of 1 mM OsPhenSS into 2 nM Z•AuNP25 in aerated water (35 µL added) (right).

It was found that 28 µM was sufficient to coat the surface of Z•AuNP13 whereas for the coating of Z•AuNP25, 35 µM was sufficient to provide coated and stable nanoparticles. It was also seen that a similar shift is observed for the OsPhenSS•AuNP13 and OsPhenSS•AuNP25 when comparing to the previously characterised RuPhenSS•AuNP13 and RuPhenSS•AuNP25 whereby a 4 nm and 6 nm shift is observed from the 13 nm and 25 nm c-AuNP to the coated particles. The shifts in SPR are summarised below in Table 4.3.2.1.

Table 4.3.2.1. Table summarising SPR and their respective shifts in comparison to their citrate counterparts.

	λmax / nm	Shift/ nm
c-AuNP13	517	0
Z•AuNP13	518	1
OsPhenSS•AuNP13	521	4
c-AuNP25	518	0
Z•AuNP25	519	1
OsPhenSS•AuNP25	524	6

The fully coated osmium(II) decorated 13 nm and 25 nm gold nanoparticles were then purified through a G25 sephadex size exclusion column and the UV-Vis was conducted. No shift in SPR was observed from either of the nanoparticle samples from the SPR on the titrations indicating no free complex in solution and the OsPhenSS has successfully bound to the gold surface.

The 13 nm and 25 nm purified osmium coated gold nanoparticles were then characterised through DLS and TEM techniques. The number distribution of the OsPhenSS•AuNP13 reveal sizes of 18 ± 5 nm which remain constant with that of the c-AuNP13 and Z•AuNP13 particles. However, upon coating and purifying the PDI increases. OsPhenSS•AuNP25 reveal number distributions of 27 ± 8 nm and a slightly larger PDI than that of the Z•AuNP25. The DLS characterisation and λ_{SPR} are summarised in Table 4.3.2.2. In order to determine whether the osmium(II) coated gold nanoparticles are of spherical nature, TEM was conducted (Figure 4.3.2.2).

Table 4.3.2.2. DLS summary of gold nanoparticle samples

	SPR	Number	PDI
AuNP13	516	14 ± 3	0.06
Z-AuNP13	517	20 ± 5	0.05
OsPhen•AuNP13	521	18 ± 5	0.27
AuNP25	519	21 ± 5	0.07
Z-AuNP25	520	29 ± 8	0.22
OsPhen•AuNP25	524	27 ± 8	0.32

The TEM images of OsPhenSS•AuNP13 and OsPhenSS•AuNP25 display average sizes of 13 nm (n = 30) and 22 nm (n = 20) respectively which is in good agreement of the DLS results. Additionally, ICP-MS revealed approximately 1800 complexes per AuNP for OsPhenSS•AuNP13 demonstrating high loading of the complex on the gold nanoparticle ideal for imaging applications.

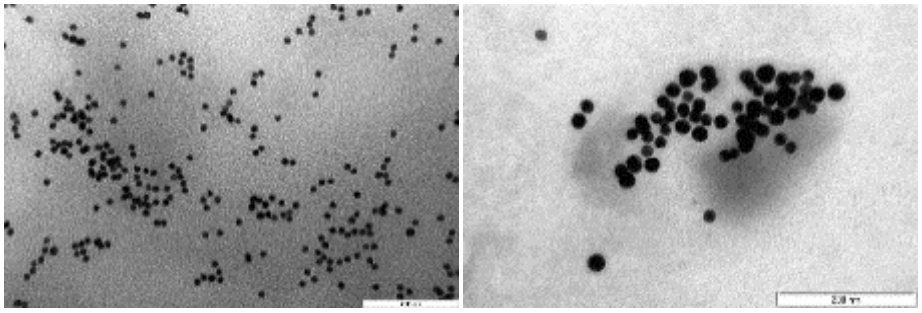

Figure 4.3.2.2. TEM images of OsPhenSS•AuNP13 (left) and OsPhenSS•AuNP25 (right) revealing average sizes of 13 nm (n = 30) and 22 nm (n = 20) respectively. Scale bar = 200 nm.

In order to determine whether the osmium(II) functionalised gold nanoparticles have enhanced photophysical properties and are ideal for imaging applications, the steady state emission profile, excitation and lifetimes was taken in aerated water. Upon excitation at 485 nm a weak but broad based ^{3}MLCT emission centred at 785 nm is observed for both the OsPhenSS•AuNP13 and OsPhenSS•AuNP25.

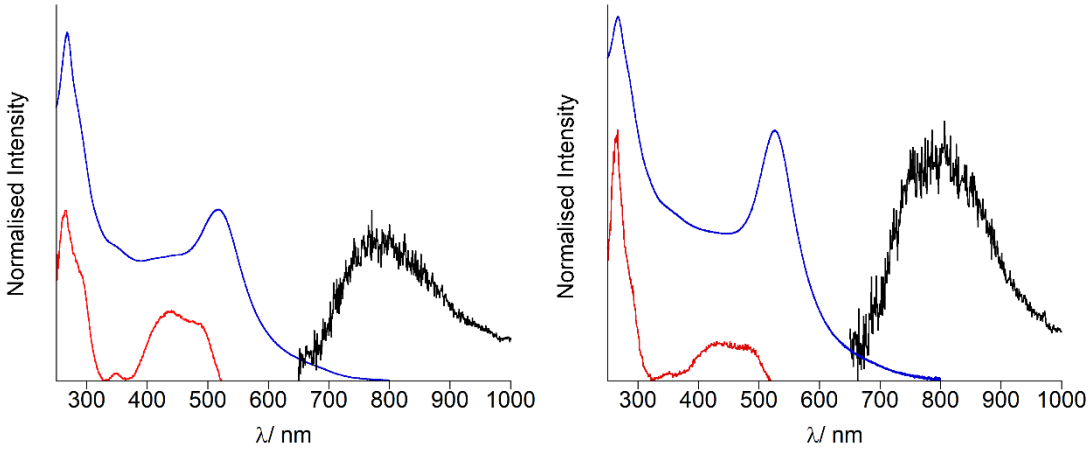

Figure 4.3.2.3. Normalised emission (black), excitation (red) and UV Vis (blue) of 4.5nM OsPhenSS.AuNP13 in 1mL aerated water (λ_{ex} = 485nm, λ_{em} = 785nm) (left) and normalised emission (black), excitation (red) and UV Vis (blue) of 2 nM OsPhenSS.AuNP25 in 1mL aerated water (λ_{ex} = 485nm, λ_{em} = 785nm) (right).

The luminescence lifetime of OsPhenSS•AuNP13 revealed a lifetime of 55 ns; a 19 ns increase in comparison to the free complex in aerated water. This enhancement is suspected to be from the electric field from gold nanoparticle interacting with the complex.

4.3.3 Biological studies of 13 nm and 25 nm gold nanoparticles

4.3.3.1 Cell viability assays of OsPhenSSAuNP in A549 cells

Prior to cell imaging, cell survival assays were conducted to obtain cell viability through a standard MTT assay technique. Cell viability assays were conducted at ranging concentrations of OsPhenSS•AuNP13 (4.5 nM – 0.14 nM) and OsPhenSS•AuNP25 (1 nM – 0.0306 nM) via a dilution series across six technical repeats. The cells were incubated at 37ºC in a 5% CO_2 atmosphere for 24 hours in 96-well plates with the 13 nm and 25 nm OsPhenSS•AuNP in parallel with a vehicle control (H_2O), negative control (media) and a positive control (Triton X-100). The samples were compared against the vehicle control (H_2O) in relation to the negative (media) and positive (Triton X-100, 1%) control to observe toxicity. In both cases the positive control containing 1% Triton X-100 killed the majority of the cells as expected. The negative control in both cases has no associated toxicity suggesting the cells are healthy and not contaminated resulting in no cell death as expected.

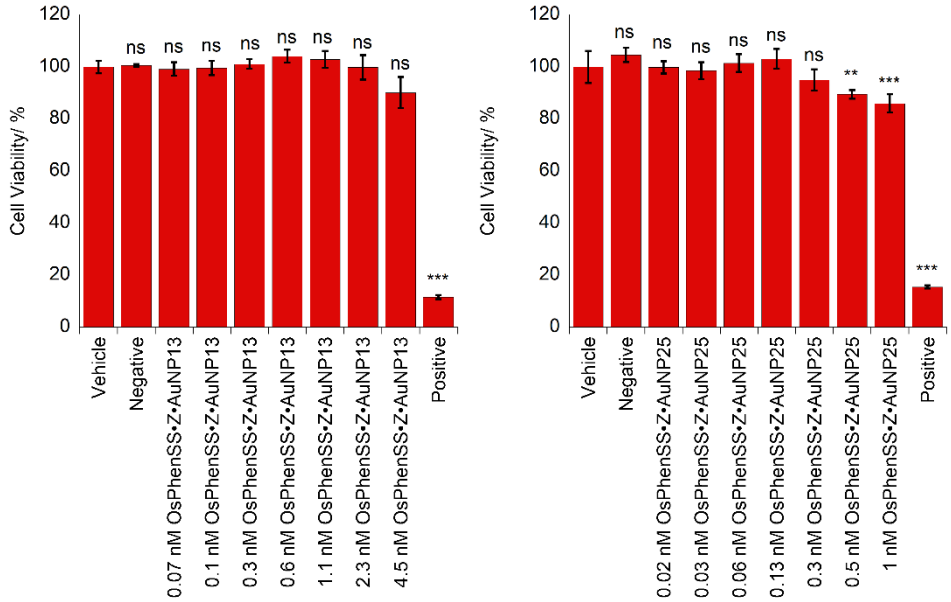

Figure 4.3.3.1.1. . MTT assays of A549 cells treated with serial particle dilutions of OsPhenSS•AuNP13 (a) and OsPhenSS•AuNP25 (b) for 24 hours at 37°C 1-way ANOVA followed by a Dunnett's t-test corrected for multiple comparisons. *=P<0.01, **=P<0.001, ***=P<0.0001.

For OsPhenSS•AuNP13 there is no significant change in viability between the dilution series suggesting concentrations up to 4.5 nM were non-cytotoxic with OsPhenSS. For OsPhenSS•AuNP25 toxicity towards the upper concentrations is starting to appear (0.5 nM and 1 nM). The viability assays concluded that dosing of cells could be achieved with 0.9 nM OsPhenSS•AuNP13 and 0.2 nM OsPhenSS•AuNP25 resulting in no toxicity towards A549 cells leading them as viable imaging agents.

4.3.3.2 Luminescence imaging of 13 nm and 25 nm OsPhenSS•AuNP in live A549 cells

Upon dosing of the A549 cells, the treated samples were incubated for 18 hours and then imaged immediately. Staining of the nucleus through the aid of Hoescht allows the identification of where the OsPhenSS•AuNP13 localize within the cell. Analysis reveals that the OsPhenSS•AuNP13 seemingly localise in the cytoplasm and perninuclear regions of the cell.

Unsurprisingly, very little reflectance of the 13 nm OsPhenSS•AuNP was able to be obtained due to the very small size (13 nm) of the gold nanoparticle. Therefore, 25 nm OsPhenSS•AuNP was employed for the benefit of increasing the reflectance properties as larger sized gold nanoparticles display greater scattering effects.

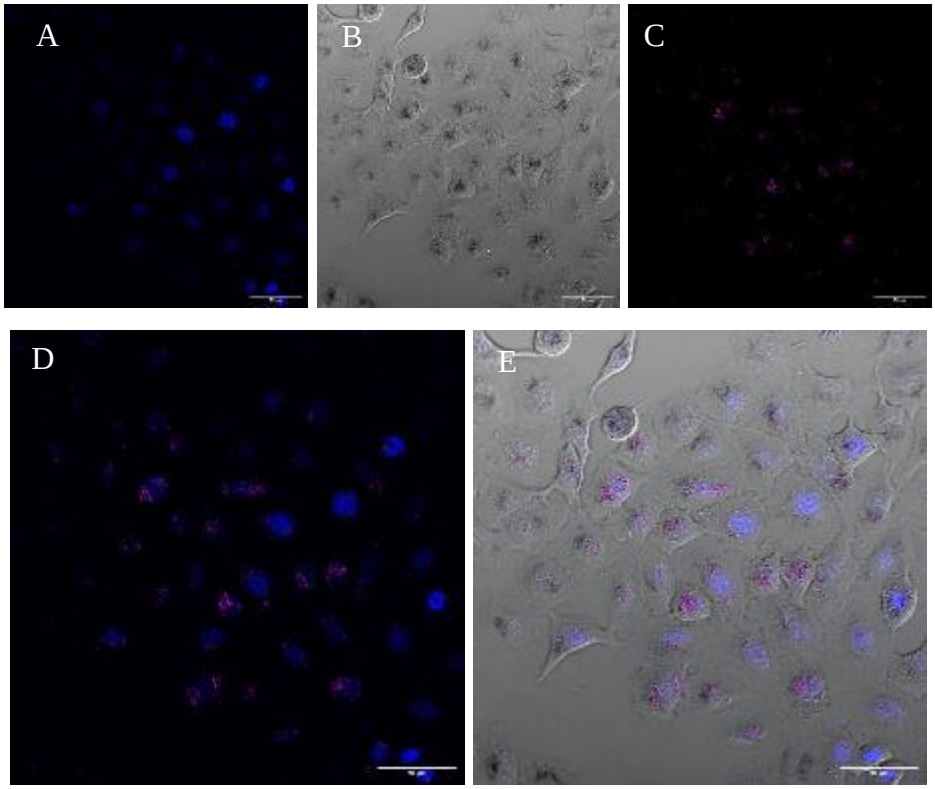

Figure 4.3.3.2.1. Live cell images of A549 cells treated with 0.9 nM OsPhenSS•AuNP13 at 18 hours. Hoescht 3368, Blue channel, Hoescht emission (λ_{exc} = 402 nm, λ_{em} 420−470 nm)(A), Brightfield (B), Purple channel, Osmium emission (λ_{exc} = 488 nm, λ_{em} 650−800 nm) (C), Hoescht 3368 overlapped with osmium emission (D) and overlay of all (E). Scale bar is 50 µm.

The OsPhenSS•AuNP25 demonstrates brighter emission from the osmium(II) complex on the gold nanoparticle surface inside live A549 cells. In comparison to OsPhenSS•AuNP13, the similar trend of localisation is seen. The indication of no free complex within the cell is supported through overlapping the characteristic emission profile of the osmium with the reflectance of the gold nanoparticle.

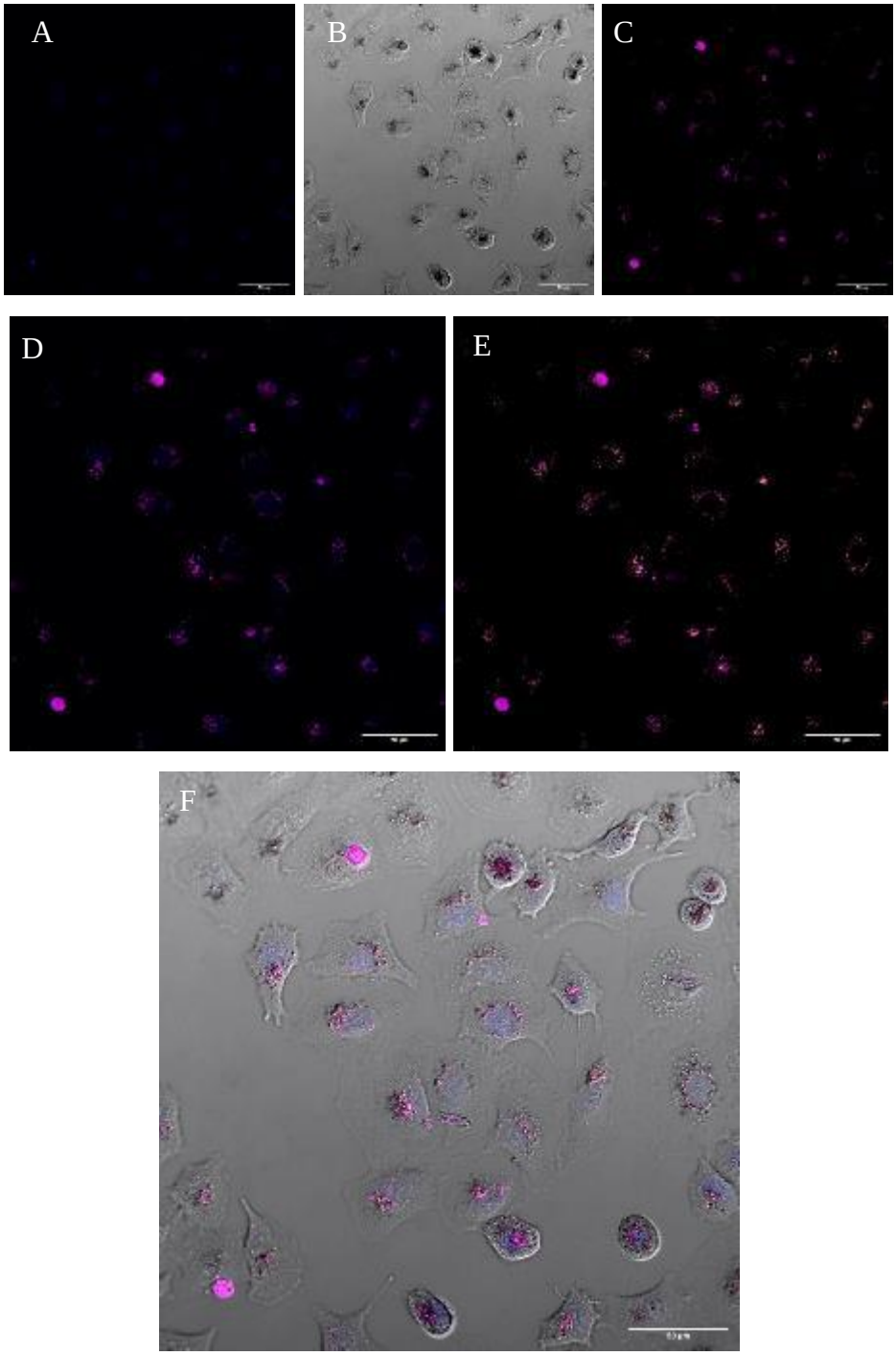

Figure 4.3.3.2.2. Live cell images of A549 cells treated with 0.2 nM OsPhen•AuNP25 at 18 hours. Hoescht 3368, Blue channel, Hoescht emission (λ_{exc} = 402 nm, λ_{em} 420−470 nm)(A), Brightfield (B), Purple channel, Osmium emission (λ_{exc} = 488 nm, λ_{em} 650−800 nm) (C), Hoescht 3368 overlapped with osmium emission (D), overlap of reflectance (λ_{exc} = 633 nm, λ_{em} 623−643 nm) and osmium emission (E) and overlay of all (F). Scale bar is 50 µm.

Interestingly, the electron dense gold and osmium can be visualised in both OsPhenSS•AuNP13 and OsPhenSS•AuNP25 brightfield images allowing additional confirmation of gold nanoparticles present in the cell. Overlays of osmium emission and the reflectance with the brightfield were ascertained to prove luminescent osmium gold nanoparticles.

4.4 Conclusion

In conclusion we have successfully synthesised and characterised a novel osmium(II) complex derived from its bipyridine counterpart for the attachment onto gold nanoparticles for luminescence imaging. OsPhenSS displayed minor blue shifts in its photophysical properties attributed to the phenanthroline character. Upon irradiation at 485 nm, the complex displays strong emission centred at 770 nm in aerated water. The complex was serially added into a known concentration of gold nanoparticles and was monitored through change in the SPR resonance of the particles to achieve full coating. Both OsPhenSS•AuNP13 and OsPhenSS•AuNP25 display no signs of cytotoxicity at varying concentrations except at 0.5 nM and 1 nM via statistical analysis in OsPhenSS•AuNP25 in A549 cells. These nanoparticles were able to be imaged via confocal microscopy seemingly displaying localisation in the cytoplasm and perinuclear regions. These osmium(II) functionalised gold nanoparticles allow a promising future for the development of osmium(II) complexes as imaging agents negating the concerns of cellular uptake through use of a gold nanoparticle scaffold and potentially the development for delivering anticancer osmium(II) complexes to cancer cells.

4.5 Experimental

4.5.1 Synthesis of BpySS

See section **3.5.2**.

4.5.2 Synthesis of *Bis*-(1,10-phenanthroline)-Osmium dichloride

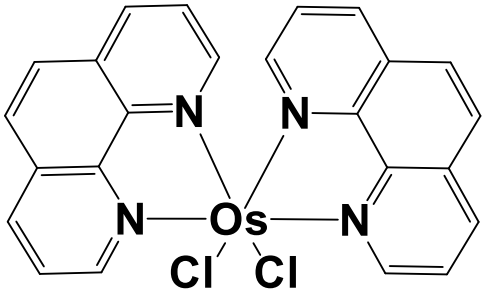

$OsPhen_2Cl_2$ was synthesised with modification as according to Chao *et al.*[71] A ethylene glycol solution of $OsCl_3.xH_2O$ (210 mg, 0.57 mmol) and 1, 10- phenanthroline (210 mg, 1.16 mmol) was refluxed under an N_2 atmosphere for 1 h. After cooling to room temperature, the solution was added to an aqueous solution containing $Na_2S_2O_4$ (4.55 g, 25 mL) and then kept in a refrigerator overnight. The dark precipitate was collected by vacuum filtration, washed with water and diethyl ether, and directly used in the following reactions without further purification. MS [ESI^+] m/z 622.0 $[M]^+$.

4.5.3 Synthesis of OsPhenSS

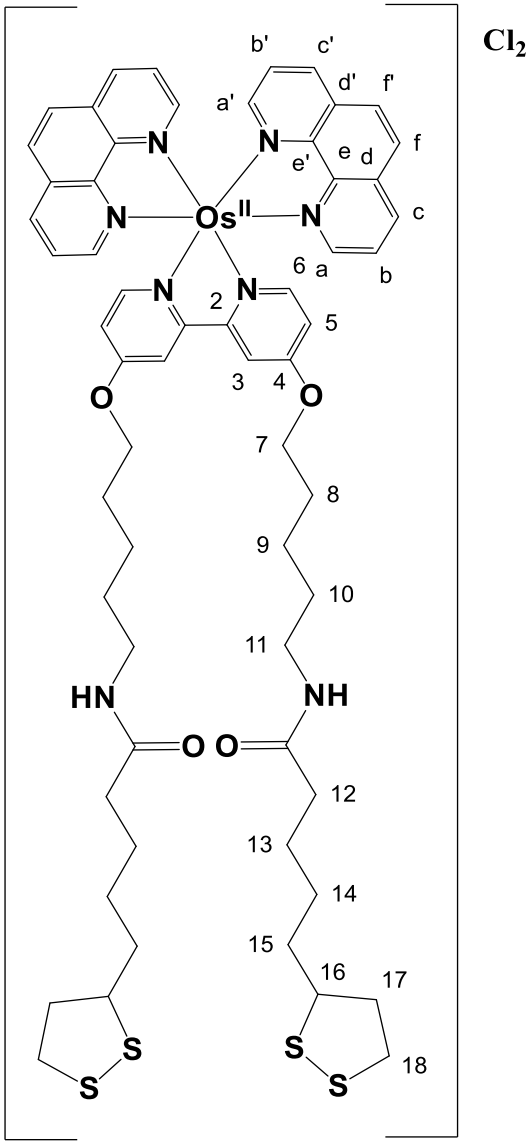

$Os(phen)_2Cl_2$ (39.5 mg, 0.0635 mmol) and BpySS (46.23 mg, 0.0629 mmol) was suspended in ethylene glycol (20 mL) and heated to 120 °C overnight. The black/ brown solution was cooled to room temperature and 20 mL deionised water was added. Saturated NH_4PF_6 in water (1 mL) was added and stirred for 20 mins at RT and filtrated to give a black precipitate. The precipitate was washed with copious amounts of ice cold water and followed by washes of diethyl ether (3

x 20 mL). The solid was dissolved in a minimal amount of acetonitrile and the solvent removed in vacuo to give a black powder. An alumina column in MeCN was performed and then reduced in vacuo to yield OsPhenSS (23 mg, 72 %). MS [ESI$^+$] m/z 643.2 [M-2 PF_6]$^{2+}$.λ_{max} (MeCN)/nm (ε/dm^3 mol^{-1} cm^{-1}) 225 (61000), 266 (63400), 343sh (9200), and 485 (17600) δH (400MHz; CD3CN) 1.48 (20H, m, H8, 9, 14, 15, 16), 1.80 (6H, m, H10, 18'), 2.07 (4H, td, *2.5, 7.2*, H13), 2.37 (2H, dtdd, *1.3, 5.6, 6.9, 13.3,* H18), 3.08 (8H, m, H11, 19), 3.53 (2H, ddd, *2.3, 4.4, 8.5*, H17), 4.18 (4H, td, *1.9, 6.5*, H7), 6.39 (2H, s, NH), 6.74 (2H, dd, *2.6, 6.6*, H5), 7.26 (2H, dd, *1.0, 6.5*, H6), 7.43 (2H, dd, *5.4, 8.2*, Hb'), 7.74 (2H, dd, *5.4, 8.2*, Hb), 7.77 (2H, dd, *1.2, 5.4*, Ha'), 8.04 (2H, d, *2.5*, H3), 8.22 (6H, m, Hf/f'/ a), 8.27 (2H, dd, *1.2, 8.2*, Hc), 8.37 (2H, dd, *1.2, 8.2*, Hc'). δC (400MHz; CD3CN) 23.6 (C9), 26.3 (C15), 28.9 (C8), 29.5 (C14), 29.9 (C10), 35.3 (C16), 36.7 (C13), 39.2 (C19), 39.3 (C11), 41.1 (C18), 57.5 (C17), 70.7 (C7), 112.4 (C3), 115.3 (C5), 126.9 (Cb'), 127.1 (Cb), 129.2 (Cf/f'), 132.2 (C4), 136.9 (Cc/c'), 151.4 (Cd/d'), 152.8 (C6), 153.0 (Ca'), 153.2 (Ca), 161.0 (C2), 167.2 (Ce/e') and 173.5 (C12). NMR assignments were confirmed by COSY, HSQC and HMBC.

4.5.4 Synthesis of 13 nm and 25 nm c-AuNP

See section **3.5.3**.

4.5.5 Coating of 13 nm and 25 nm OsPhenSS•AuNP13

OsPhenSSAuNP13

A suspension of AuNP-13 (2 mL, 2 nM) was centrifuged at 13000 g for 25 mins, the supernatant was decanted and the pellet was re-suspended in filtered MILLI-Q® water (1 mL) to form 4 nM AuNP-13. Zonyl FSA solution (2.5% w/v) in deionised water (10 µL, 0.05 M) was added to 4 nM AuNP-13 (1 mL), stirred for 20 mins and centrifuged at 13000 g for 20 mins. The

supernatant was discarded and the pellet was re-suspended in filtered MILLI-Q® water (350 µL) and combined to form Z•AuNP-13 (1 mL, 9 nM). λ_{max} (H_2O) / nm 517 (SPR). Diameter / nm = 20 ± 5, PDI = 0.05 DLS sizing measurements were recorded with AuNP at pH 7, 1 nM in MILLI-Q® H_2O. OsPhenSS (70 µL, 1 mM) was titrated into a 9 nM solution of Z·AuNP-13 in 5 µL aliquots with continuous stirring. A Sephadex G-25 size exclusion column was performed to isolate the OsPhenSS·AuNP13. λ_{max} (H_2O) / nm 521 (SPR). DLS measurements: Diameter / nm = 18 ± 5, PDI = 0.27. DLS sizing measurements were recorded with AuNP at pH 7, 1 nM in MILLI-Q® H_2O). Diameter / nm = 13 (Transmission Electron Microscopy). Molar concentration = 9 nM.

OsPhenSSAuNP25

A suspension of AuNP-25 (2 mL, 0.7 nM) was centrifuged at 13000 g for 25 mins, the supernatant was decanted and the pellet was re-suspended in filtered MILLI-Q® water (1 mL) to form 1.4 nM AuNP-25. Zonyl FSA solution (2.5% w/v) in deionised water (10 µL, 0.05 M) was added to 1.4 nM AuNP-25 (1 mL), stirred for 20 mins and centrifuged at 13000 g for 20 mins. The supernatant was discarded and the pellet was re-suspended in filtered MILLI-Q® water (250 µL) and combined to form Z-AuNP-25 (1 mL, 5 nM). λ_{max} (H_2O) / nm 520 (SPR). Diameter / nm = 29 ± 8, PDI = 0.22, DLS sizing measurements were recorded with AuNP at pH 7, 1 nM in MILLI-Q® H_2O. OsPhenSS (75 µL, 1 mM) was titrated into a 5 nM solution of Z·AuNP-25 in 5 µL aliquots with continuous stirring. A Sephadex G-25 size exclusion column was performed for the isolation of OsPhenSS·AuNP25. λ_{max} (H_2O) / nm 524 (SPR). DLS measurements: Diameter / nm = 27 ± 8, PDI = 0.32. DLS sizing measurements were recorded with AuNP at pH 7, 1 nM in MILLI-Q® H_2O). Diameter / nm = 22 (Transmission Electron Microscopy). Molar concentration = 5 nM

4.5.6 Cell culture of A549 cells

The human lung cancer A549 cell line was maintained in Dulbecco's Modified Eagle's Medium (DMEM) supplemented with 10% fetal bovine serum (FBS), L-glutamine (100 µg mL^{-1}) and 1 % penicillin/ streptomycin hereafter called complete media. Cells were cultured in 20 mL of complete media in vented T75 flasks at 37°C in a humidified 5% CO_2 atmosphere. Cells were routinely sub cultured from high confluency using a standard trypLE protocol. Dosing of A549 cells was performed in 35 mm dishes with a 10 mm glass insert. Cells were seeded at 100 000 cells per dish in 1 mL complete media. Prior to dosing with AuNP cells were washed in warm PBS and cell media was replaced with 900 µL fresh media. OsPhen•AuNP13 (100 µL, 9 nM) and OsPhen•AuNP25 (100 µL, 5 nM) was added to the cell media for the required incubation time. For confocal microscopy of cells, cell media was removed and cells washed twice in warm PBS. For Hoechst nuclear staining 20 µM of a 20 mM stock solution of Hoechst 3328 in PBS was added for 10 minutes in the dark. The cells were washed and phenol red free cell media was added (1 mL per well).

4.5.7 MTT assays

MTT viability assays were conducted by Dr Garret Rochford. Cells were seeded at a density of 5000 cells per well in a 96 well plate. Nanoparticle concentrations were varied across the plate through a 1 in 2 dilution factor in six technical replicates containing a negative (1% triton) and positive control (cell media). Cells were dosed for 24 hours with varying concentrations of OsPhen•AuNP13 (4.5 nM – 0.07 nM) and OsPhen•AuNP25 (1 nM – 0.0305 nM) and washed with phenol red free media. The cells

were then further incubated with (3-[4,5-dimethylthiazol-2yl]-2,5-diphenyl-tetrazolium bromide) (MTT) in Dulbecco's Modified Eagle Medium (DMEM) containing 10% FBS for 4 hours and then removed completely. DMSO was added to each well and then analysed on a tecan infinite 200 probe plate reader. Results were normalised against the vehicle control. Statistical analysis was performed by 1-way ANOVA followed by Dunnett's t-test corrected for multiple comparisons.

4.5.8 Confocal microscopy

Confocal microscopy of fixed cells was performed using a Leica TCS SP8 upright confocal laser scanning system using a 64x oil immersion objective lens. 405 nm, 458 nm, 488 nm, 633 nm solid-state laser lines were used. Confocal microscopy of live cells was performed using a Leica TCS SP8 upright confocal laser scanning system using a 40x ceramic H_2O immersion dip objective lens. 405 nm, 458 nm, 488 nm, 633 nm solid-state laser lines were used. Fixing of cells was achieved through addition of 4% paraformaldehyde (PFA) to each well (1 mL per well) for 15 minutes in the dark. PFA was removed and cells washed twice in PBS. Coverslips were removed and mounted on a droplet of hydromount media (National Diagnostics, UK) on glass slides, stored flat in the dark for at least 24 hours at 4°C before imaging. Live cells were imaged immediately after the washing procedure as described in section 2.4.

4.5.9 Transmission electron microscopy

TEM analysis was carried out for OsPhen•AuNP13 and OsPhen•AuNP25 from 9 nM and 5 nM stock solutions respectively. For all metal coated nanoparticle samples, a 1 in

1 dilution was performed in Milli-Q H_2O yielding 4.5 nM and 2.5 nM respectively. From this, a 1 in 5 dilution was carried out on all nanoparticle samples in Milli-Q H_2O and a 20 µL aliquot was dropped on to a 200 mesh formvar coated TEM grid and left to dry in the dark overnight. Imaging took place on a JEOL1400 transmission electron microscope by Theresa Morris and Ludwig Schneider (Materials and Metallurgy, University of Birmingham).

4.5.10 Inductively coupled mass spectrometry

Nanoparticle samples were analysed at the University of Warwick using an ICP-MS (Agilent LC-ICP-MS (7500cx).To prepare the samples, the coated samples were diluted to 4.5 nM. A 20 µL aliquot was added to 80 µL Milli-Q H_2O yielding a concentration of ~ 1 nM. Samples were digested with ultra pure aqua regia (~ 300 µL). The samples were then diluted to 5 mL to reduce the aqua regia content to < 4% with a 4% HNO_3 solution containing ascorbic acid (50 mM), EDTA (50 mM) and thiourea (50 mM) in order to stop the production of the volatile osmium tetraoxide species. A series of gold and osmium standards were used for calibration.

4.6 References

1. J. Wang, S. Sun, D. Mu, J. Wang, W. Sun, X. Xiong, B. Qiao and X. Peng, *Organometallics*, 2014, **33**, 2681-2684.

2. T. Yang, A. Xia, Q. Liu, M. Shi, H. Wu, L. Xiong, C. Huang and F. Li, *J. Mater. Chem.*, 2011, **21**, 5360-5367.

3. R. Huang, F.-P. Feng, C.-H. Huang, L. Mao, M. Tang, Z.-Y. Yan, B. Shao, L. Qin, T. Xu, Y.-H. Xue and B.-Z. Zhu, *ACS Appl. Mater. Inter.*, 2020, **12**, 3465-3473.

4. R. E. Holmlin, J. A. Yao and J. K. Barton, *Inorg. Chem.*, 1999, **38**, 174-189.

5. R. E. Holmlin and J. K. Barton, *Inorg. Chem.*, 1995, **34**, 7-8.

6. R. E. Holmlin, E. D. A. Stemp and J. K. Barton, *Inorg. Chem.*, 1998, **37**, 29-34.

7. M. Arruebo, M. Valladares and Á. González-Fernández, *J. Nanomater.*, 2009, 439389.

8. S. F. M. van Dongen, H.-P. M. de Hoog, R. J. R. W. Peters, M. Nallani, R. J. M. Nolte and J. C. M. van Hest, *Chem. Rev.*, 2009, **109**, 6212-6274.

9. E. J. Simpson, P. Gobbo, F. C. Bononi, E. Murrell, M. S. Workentin and L. G. Luyt, *J. Interdiscip. Nanomed.*, 2017, **2**, 174-187.

10. R. Cao, J. Jia, X. Ma, M. Zhou and H. Fei, *J. Med. Chem.*, 2013, **56**, 3636-3644.

11. C. K. C. Chiu, Y. P. Y. Lam, C. A. Wootton, M. P. Barrow, P. J. Sadler and P. B. O'Connor, *J. Am. Soc. Mass Spec.*, 2020, **31**, 594-601.

12. P. Zhang and H. Huang, *Dalton Trans.*, 2018, **47**, 14841-14854.

13. L.-H. Chung, K.-S. Cho, J. England, S.-C. Chan, K. Wieghardt and C.-Y. Wong, *Inorg. Chem.*, 2013, **52**, 9885-9896.

14. R. S. Lumpkin, E. M. Kober, L. A. Worl, Z. Murtaza and T. J. Meyer, *J. Phys. Chem.*, 1990, **94**, 239-243.

15. S. J. Adams, D. J. Lewis, J. A. Preece and Z. Pikramenou, *ACS Appl. Mater. Inter.*, 2014, **6**, 11598-11608.

16. S. Lazic, P. Kaspler, G. Shi, S. Monro, T. Sainuddin, S. Forward, K. Kasimova, R. Hennigar, A. Mandel, S. McFarland and L. Lilge, *Photochem. Photobiol.*, 2017, **93**, 1248-1258.

17. E. C. Glazer, *Photochem. Photobiol.*, 2017, **93**, 1326-1328.

18. K. S. Gkika, A. Byrne and T. E. Keyes, *Dalton Trans.*, 2019, **48**, 17461-17471.

19. C. Ge, J. Zhu, A. Ouyang, N. Lu, Y. Wang, Q. Zhang and P. Zhang, *Inorg. Chem. Frontiers*, 2020, **7**, 4020-4027.

20. G. Berger, K. Grauwet, H. Zhang, A. M. Hussey, M. O. Nowicki, D. I. Wang, E. A. Chiocca, S. E. Lawler and S. J. Lippard, *Cancer Lett.*, 2018, **416**, 138-148.

21. S. Mardanya, S. Karmakar, D. Mondal and S. Baitalik, *Inorg. Chem.*, 2016, **55**, 3475-3489.

22. C. Ge, H. Huang, Y. Wang, H. Zhao, P. Zhang and Q. Zhang, *ACS Appl. Bio Mater.*, 2018, **1**, 1587-1593.

23. S. A. E. Omar, P. A. Scattergood, L. K. McKenzie, C. Jones, N. J. Patmore, A. J. H. M. Meijer, J. A. Weinstein, C. R. Rice, H. E. Bryant and P. I. P. Elliott, *Inorg. Chem.*, 2018, **57**, 13201-13212.

24. O. Bergman and D. Ben-Shachar, *Can. J. Psychiatry.*, 2016, **61**, 457-469.

25. M. V. Liberti and J. W. Locasale, *Trends Biochem. Sci*, 2016, **41**, 211-218.

26. O. Warburg, *J. Cancer Res.*, 1925, **9**, 148-163.

27. D. van der Westhuizen, J. Conradie and K. G. von Eschwege, *Electroanal.*, 2020, **32**, 2838-2851.

28. A. Dorcier, W. H. Ang, S. Bolaño, L. Gonsalvi, L. Juillerat-Jeannerat, G. Laurenczy, M. Peruzzini, A. D. Phillips, F. Zanobini and P. J. Dyson, *Organometallics*, 2006, **25**, 4090-4096.

29. N. Lu, Z. Deng, J. Gao, C. Liang, H. Xia and P. Zhang, *Nature Commun.*, 2022, **13**, 2245.

30. A. A. Abdel-Shafi, D. R. Worrall and A. Y. Ershov, *Dalton Trans.*, 2004, 30-36.

31. A. Byrne, C. Dolan, R. D. Moriarty, A. Martin, U. Neugebauer, R. J. Forster, A. Davies, Y. Volkov and T. E. Keyes, *Dalton Trans.*, 2015, **44**, 14323-14332.

32. R. Huang, C.-H. Huang, J. Shao and B.-Z. Zhu, *J. Phys. Chem. Lett.*, 2019, **10**, 5909-5916.

33. L. V. Mannack, S. Eising and A. Rentmeister, *F1000 Res.*, 2016, **5**.

34. X. Wang, Y. Wang, H. He, X. Ma, Q. Chen, S. Zhang, B. Ge, S. Wang, W. M. Nau and F. Huang, *ACS Appl. Mater. Inter.*, 2017, **9**, 17799-17806.

35. W. Liu, B. Zhou, G. Niu, J. Ge, J. Wu, H. Zhang, H. Xu and P. Wang, *ACS Appl. Mater. Inter.*, 2015, **7**, 7421-7427.

36. Y.-J. Lu, Q. Deng, D.-P. Hu, Z.-Y. Wang, B.-H. Huang, Z.-Y. Du, Y.-X. Fang, W.-L. Wong, K. Zhang and C.-F. Chow, *Chem. Commun.*, 2015, **51**, 15241-15244.

37. S. Kummer, A. Knoll, E. Socher, L. Bethge, A. Herrmann and O. Seitz, *Bioconjug. Chem.*, 2012, **23**, 2051-2060.

38. C. Y. Y. Yu, W. Zhang, R. T. K. Kwok, C. W. T. Leung, J. W. Y. Lam and B. Z. Tang, *J. Mater. Chem. B*, 2016, **4**, 2614-2619.

39. A. Umuhire Juru, Z. Cai, A. Jan and A. E. Hargrove, *Chem. Commun.*, 2020, **56**, 3555-3558.

40. M. Roitzsch and B. Lippert, *J. Am. Chem. Soc.*, 2004, **126**, 2421-2424.

41. F. Dröge, F. F. Noakes, S. A. Archer, S. Sreedharan, A. Raza, C. C. Robertson, S. MacNeil, J. W. Haycock, H. Carson, A. J. H. M. Meijer, C. G. W. Smythe, J. Bernardino de la Serna, B. Dietzek-Ivanšić and J. A. Thomas, *J. Am. Chem. Soc.*, 2021, **143**, 20442-20453.

42. A. Wragg, M. R. Gill, C. J. Hill, X. Su, A. J. H. M. Meijer, C. Smythe and J. A. Thomas, *Chem. Commun.*, 2014, **50**, 14494-14497.

43. Y. Xie, Y. Lei, S. Shah, H. Wu, J. Wu, E. Megehee and E. Wang, *Int J Anal Chem*, 2013, **2013**, 419716-419716.

44. C. Licona, J.-B. Delhorme, G. Riegel, V. Vidimar, R. Cerón-Camacho, B. Boff, A. Venkatasamy, C. Tomasetto, P. da Silva Figueiredo Celestino Gomes, D. Rognan, J.-N. Freund, R. Le Lagadec, M. Pfeffer, I. Gross, G. Mellitzer and C. Gaiddon, *Inorg Chem. Frontiers*, 2020.

45. T. Joshi, V. Pierroz, C. Mari, L. Gemperle, S. Ferrari and G. Gasser, *Angew. Chemie Int. Ed.*, 2014, **53**, 2960-2963.

46. J. P. C. Coverdale, H. E. Bridgewater, J.-I. Song, N. A. Smith, N. P. E. Barry, I. Bagley, P. J. Sadler and I. Romero-Canelón, *J. Med. Chem.*, 2018, **61**, 9246-9255.

47. R. J. Needham, C. Sanchez-Cano, X. Zhang, I. Romero-Canelón, A. Habtemariam, M. S. Cooper, L. Meszaros, G. J. Clarkson, P. J. Blower and P. J. Sadler, *Angew. Chemie Int. Ed.*, 2017, **56**, 1017-1020.

48. T. M. Allen, *Nat. Rev. Cancer*, 2002, **2**, 750-763.

49. R. A. Sperling, P. Rivera Gil, F. Zhang, M. Zanella and W. J. Parak, *Chem. Soc. Rev.*, 2008, **37**, 1896-1908.

50. X. Huang, I. H. El-Sayed, W. Qian and M. A. El-Sayed, *J. Am. Chem. Soc.*, 2006, **128**, 2115-2120.

51. C.-Z. Li, K. B. Male, S. Hrapovic and J. H. T. Luong, *Chem. Commun.*, 2005, 3924-3926.

52. A. Portugués, L. González, D. Bautista and J. Gil-Rubio, *Angew. Chemie Int. Ed.*, 2020, **132**, 15332-15337.

53. H.-P. Wu, C.-J. Yu, C.-Y. Lin, Y.-H. Lin and W.-L. Tseng, *J. Am. Soc. Mass Spec.*, 2009, **20**, 875-882.

54. J. Lee, D. K. Chatterjee, M. H. Lee and S. Krishnan, *Cancer Lett.*, 2014, **347**, 46-53.

55. E. Boisselier and D. Astruc, *Chem. Soc. Rev.*, 2009, **38**, 1759-1782.

56. N. J. Rogers, S. Claire, R. M. Harris, S. Farabi, G. Zikeli, I. B. Styles, N. J. Hodges and Z. Pikramenou, *Chem. Commun.*, 2014, **50**, 617-619.

57. S. A. M. Osborne and Z. Pikramenou, *Faraday Discuss.*, 2015, **185**, 219-231.

58. X. Ge, Q. Fu, L. Su, Z. Li, W. Zhang, T. Chen, H. Yang and J. Song, *Theranostics*, 2020, **10**, 4809-4821.

59. E. M. Kober, B. P. Sullivan, W. J. Dressick, J. V. Caspar and T. J. Meyer, *J. Am. Chem. Soc.*, 1980, **102**, 7383-7385.

60. E. M. Kober, J. V. Caspar, B. P. Sullivan and T. J. Meyer, *Inorg. Chem.*, 1988, **27**, 4587-4598.

61. D. Zych, A. Slodek, D. Matuszczyk and S. Golba, *Eur. J. Inorg. Chem.*, 2018, **2018**, 5117-5128.

62. A. Ito, T. E. Knight, D. J. Stewart, M. K. Brennaman and T. J. Meyer, *J. Phys. Chem. A*, 2014, **118**, 10326-10332.

63. E. M. Kober and T. J. Meyer, *Inorg. Chem.*, 1982, **21**, 3967-3977.

64. J. A. Roque, P. C. Barrett, H. D. Cole, Liubov M. Lifshits, G. Shi, S. Monro, D. von Dohlen, S. Kim, N. Russo, G. Deep, C. G. Cameron, M. E. Alberto and S. A. McFarland, *Chem.l Sci.*, 2020, **11**, 9784-9806.

65. K. Maruyama, Y. Mishima, K. Minagawa and J. Motonaka, *Anal. Chem.*, 2002, **74**, 3698-3703.

66. B. J. Pankuch, D. E. Lacky and G. A. Crosby, *J. Phys. Chem.*, 1980, **84**, 2061-2067.

67. S. A. E. Omar, P. A. Scattergood, L. K. McKenzie, H. E. Bryant, J. A. Weinstein and P. I. P. Elliott, *Molecules*, 2016, **21**.

68. E. M. Kober, J. V. Caspar, R. S. Lumpkin and T. J. Meyer, *J. Phys. Chem.*, 1986, **90**, 3722-3734.

69. K.-C. Hwang, J.-L. Chen, Y. Chi, C.-W. Lin, Y.-M. Cheng, G.-H. Lee, P.-T. Chou, S.-Y. Lin and C.-F. Shu, *Inorg. Chem.*, 2008, **47**, 3307-3317.

70. W.-K. Chu, S.-M. Yiu and C.-C. Ko, *Organometallics*, 2014, **33**, 6771-6777.

71. P. Zhang, Y. Wang, K. Qiu, Z. Zhao, R. Hu, C. He, Q. Zhang and H. Chao, *Chem. Commun.*, 2017, **53**, 12341-12344.

72. P. A. Scattergood, A. Sinopoli and P. I. P. Elliott, *Coord. Chem. Rev.*, 2017, **350**, 136-154.

73. B. Carlson, G. D. Phelan, W. Kaminsky, L. Dalton, X. Jiang, S. Liu and A. K. Y. Jen, *J. Am. Chem. Soc.*, 2002, **124**, 14162-14172.

74. W. J. Vining, J. V. Caspar and T. J. Meyer, *J. Phys. Chem.*, 1985, **89**, 1095-1099.

75. A. Juris, L. Prodi, A. Harriman, R. Ziessel, M. Hissler, A. El-ghayoury, F. Wu, E. C. Riesgo and R. P. Thummel, *Inorg. Chem.*, 2000, **39**, 3590-3598.

76. B. Boff, C. Gaiddon and M. Pfeffer, *Inorg. Chem.*, 2013, **52**, 2705-2715.

77. T. Kurahashi, K. Iwatsuki, T. Onishi, T. Arai, K. Teranishi and H. Hirata, *J. Biomed. Optics*, 2016, **21**, 86009.

78. M. El Garah, N. Marets, M. Mauro, A. Aliprandi, S. Bonacchi, L. De Cola, A. Ciesielski, V. Bulach, M. W. Hosseini and P. Samorì, *J. Am. Chem. Soc.*, 2015, **137**, 8450-8459.

79. J.-L. Liu, J.-Q. Zhang, Z.-L. Tang, Y. Zhuo, Y.-Q. Chai and R. Yuan, *Chem. Sci.*, 2019, **10**, 4497-4501.

80. S. Zanarini, E. Rampazzo, L. D. Ciana, M. Marcaccio, E. Marzocchi, M. Montalti, F. Paolucci and L. Prodi, *J. Am. Chem. Soc.*, 2009, **131**, 2260-2267.

81. S. M. King, S. Claire, R. I. Teixeira, A. N. Dosumu, A. J. Carrod, H. Dehghani, M. J. Hannon, A. D. Ward, R. Bicknell, S. W. Botchway, N. J. Hodges and Z. Pikramenou, *J. Am. Chem. Soc.*, 2018, **140**, 10242-10249.

82. A. N. Dosumu, S. Claire, L. S. Watson, P. M. Girio, S. A. M. Osborne, Z. Pikramenou and N. J. Hodges, *JACS Au*, 2021, **1**, 174-186.

83. H. C. J. N. J. Rogers, S. Claire, D. J. Lewis, G. Zikeli, N. J. Hodges, S. Egginton, G. B. Nash and Z. Pikramenou *Nanomed.*, 2017.

84. L. Zhang, X. Sun, Y. Song, X. Jiang, S. Dong and E. Wang, *Langmuir*, 2006, **22**, 2838-2843.

85. L. Mocan, C. T. Matea, D. Bartos, O. Mosteanu, T. Pop, T. Mocan and C. Iancu, *Clujul Med.*, 2016, **89**, 199-202.

5.0 Luminescent Rituximab Labelled Gold Nanoparticles for Detection and Imaging

5.1 Introduction

The use of immunotherapies in medicine consists of a very broad and expanding collection of therapies that are having an important role on cancer outcomes. Immunotherapies rely on their potential to activate the immune system to specifically target the cancer cells and initiate apoptosis without the severely toxic side effects that current anticancer treatments produce.[1,2] The first initial types of immunotherapy approved for anticancer treatments involved the utilisation of monoclonal antibodies (mAbs) which continue to pave the way in the growing field of current anti-cancer treatment regimens.[3] Monoclonal antibodies were first produced in mice using a hybridoma technique. This is achieved through immunising a certain species against a specific epitope on an antigen and obtaining the B-lymphocytes from the spleen. These are then fused with an immortal myeloma cell line to produce hybridoma cells which do not contain any other immunoglobulin producing cells and are then cultured in selective medium.[4] The culturing of the hybridomas contains a mixture of antibodies derived from different primary B-lympocyte clones which each secrete is own individual specific antibody into the culture medium.[4,5]

In oncology, the first mAb to be used for treatment is the CD20 targeting antibody Rituximab, which is still the most widely used therapeutic agent for treatment of B-cell malignancies. Rituximab (MabThera) is a chimeric (made up of domains from different species, i.e mouse and human) monoclonal antibody and is used to treat nearly all B-cell non-Hodgkin lymphomas (NHLs). It is most commonly given with other anticancer agents such as doxorubicin and prednisone.[2,6,7] The use of mAbs in therapy has resulted in successful targeting of receptors such as CD20 in the case of Rituximab, however many other methods for targeted therapy

include the inhibition of various growth factors. For instance, trastuzumab (Herceptin), is used in breast cancer therapy to target the human epidermal growth factor receptor 2 (HER2).[8] Although chemotherapy is one of the most popular approaches in cancer treatment, it is non-specific, possesses low efficacy and toxicity to the host.[9]

The demand for personalised medicine (tailored to an individual patient) in cancer treatment is therefore becoming of great interest which addresses the importance of specifically delivering drugs to a tumour site.[10] This can be achieved through the design of targeted nanosystems which has already began to revolutionize the medical and therapeutic fields. Attachment of such targeted moieties to an imaging agent on nanomaterials can aid the progression of diagnosis of pathological conditions.[11-14] It has become increasingly evident that the use of nanoparticles employed in drug delivery reduce the toxicity of the anticancer drug whilst increasing its therapeutic efficacy.[15-18] Gold nanoparticles are among the most widely explored nanomaterials due to the relative ease of synthesis, biocompatibility, water solubility and they are relatively non-toxic.[19-27] Gold nanoparticles can be synthesised in various sizes and shapes which allow them to permeate tumour vasculature easily and remain in the tumour due to the enhanced permeability and retention (EPR) effect. Additionally, gold nanoparticles are able to stay inside the tumour site due to the lack of lymphatic clearance and due to a disordered extracellular matrix.[17,28]

The use of polyethylene glycol (PEG) for the stabilisation of gold nanoparticles has become a widely used method for particle stability.[29] PEG has many desirable properties such as being a neutral, water soluble polymer that has a flexible backbone. PEG is additionally biocompatible and plays a key role in protecting the gold nanoparticle from aggregation in vitro and in vivo as well as protection from the immune system.[30,31] It is well known that citrate stabilises gold nanoparticles and aggregate in the presence of high salt concentrations and particular solvents.

However, PEG coated gold nanoparticles has been shown to be stable in a series of solvents and salt concentrations (0.15 M – 1 M) whereas citrate capped gold nanoparticles aggregated immediately under identical conditions. Additionally, stability of PEG coated gold nanoparticles was enhanced through lower loading levels.[32] Despite the many advantages of PEG, it has been reported that 13 nm gold nanoparticles coated with PEG induce acute apoptosis in the liver thereby having clinical concerns for safety.[33] However it is well known that toxicity of gold nanoparticles is associated with surface modifications and the results for this are most likely due to the large molecular weight of PEG.[33] The enhanced stability at low levels of PEG loading allows further modification with other agents such as molecular and targeting probes on gold nanoparticles.

5.1.1 Optical detection of gold nanoparticles for targeting tumour cells

The use of targeting proteins and mAbs functionalised onto gold nanoparticles for delivery have demonstrated high cellular binding and accumulation in tissue.[34-38] DNA coated gold nanoparticles have been studied for their cellular uptake and ability in targeting cancer cells. Dual imaging was conducted from utilising a fluorescent Cy3 on DNA and the plasmonic resonance band from the gold nanoparticles to examine the clustering state and intracellular transport. It was found that Cy3-DNA coated gold nanoparticle followed endocytosis using fluorescence imaging (Figure 5.1.1.1).[39]

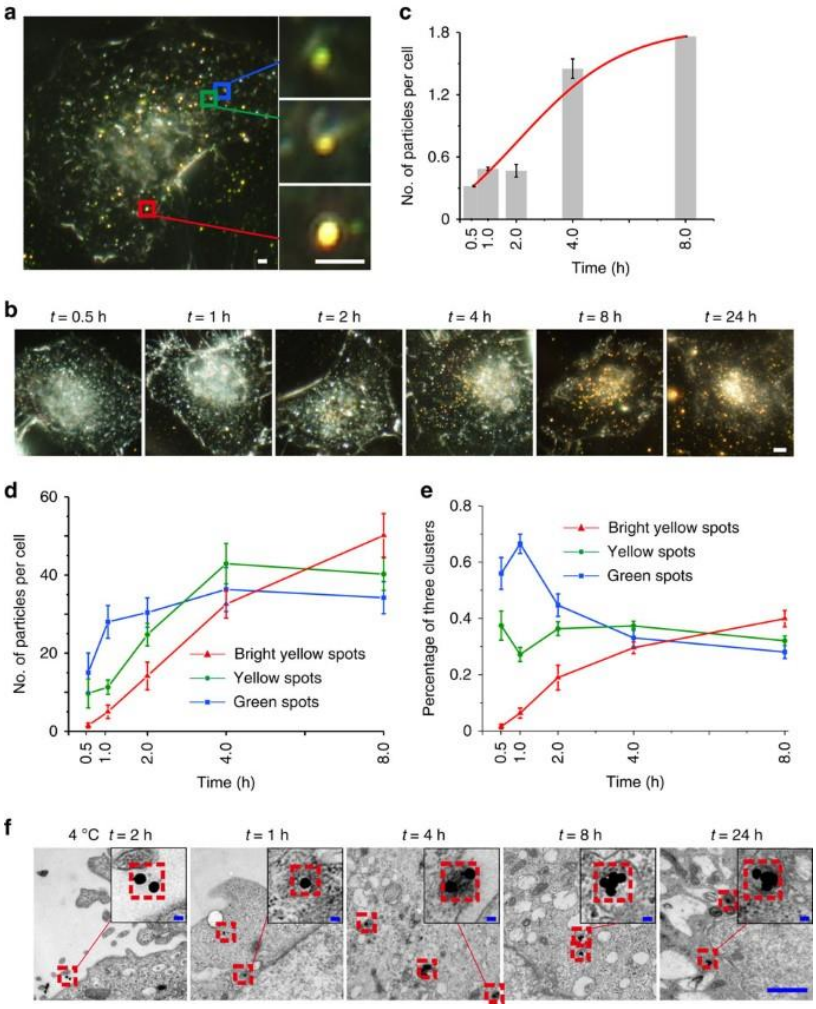

Figure 5.1.1.1. Dark field microscopy images of single particles, small clusters, and large clusters (blue, green and red rectangles respectively). Scale bar = 2 µm (a), Dark field microscopy over time points (scale bar = 5 µm) (b), ICP-AES analysis of gold in cells over time points (c), average particle counts (d), percentages of different clustering states in cells over time (e) and TEM images of gold nanoparticles incubated in HeLa cells (scale bar = 50 nm) (f). Figure taken from Liu *et al*.[39]

Alternatively to DNA, mAbs have been employed however limitations of mAbs is their structural stability upon immobilisation on gold nanoparticles and the high cost of production.[40,41] Antibodies are among the most widely used targeting moiety in medicine due to their ability for high affinity and availability for proteins.[14] A key and critical step in synthesis of these functionalised antibody gold nanoparticles is the conjugation of the antibody to the surface. Conjugation of the antibody onto the gold nanoparticle can be conducted in a variety

of ways consisting of electrostatic interactions, indirect conjugation forming a random orientated system or direct conjugation forming a directed system. Conjugation of mAbs onto gold nanoparticles has been reported since 2008 whereby a cetuximab and gemcitabine functionalised gold nanoparticle was able to inhibit tumour growth in vivo and tumour cell proliferation in three separate pancreatic cancer cell lines.[42] Adsorption of the antibody can occur through the isoelectrical point of the gold nanoparticle through electrostatic interactions however this method has been proven to display severe shortcomings.[43] This method typically relies on a high concentration of antibody which is not cost effective, random orientation thereby limiting its specificity and has the potential to be substituted by other biological complexes in the samples.[16,44]

Non covalent conjugation of antibodies onto the gold nanoparticle surface can be utilised however the limitation of this approach is the antibodies can be replaced by other molecules when they are introduced into a biological environment. Covalent binding strategies, namely non directional binding, can overcome this effect but they are still disadvantageous due to the random orientation of the antibodies which negates its ability to target specifically. Therefore directional covalent attachment of antibodies onto the gold nanoparticle surface is preferable as it affords optimal targeting specificity.[45,46]

There have been numerous reports of covalently attached antibodies onto gold nanoparticles. A covalently attached anti-FAP (fibroblast activation protein, termed F19) antibody on PEGylated gold nanoparticles for the detection of pancreatic cancer tissue was conducted which exhibited exceptional stability through particle characterisation using transmission electron microscopy (TEM) and DLS techniques (Figure 5.1.1.2).[47] Stroma was labelled with anti-F19 gold nanoparticles and imaged through dark field microscopy near to the SPR band in 5 µm sections

of pancreatic adenocarcinoma cancer tissue displaying its functionality as an imaging agent for the identification of cancer tissue.[47]

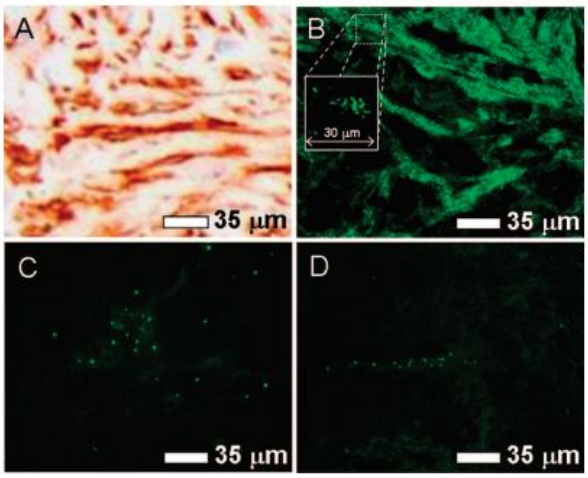

Figure 5.1.1.2. Pancreatic cancer tissue stained with secondary antibody (red regions) (a), darkfield scattering images of F19 labelled gold nanoparticles in pancreatic tissue (b), F19 labelled gold nanoparticles in healthy tissue (c) and monoclonal IgG labelled gold nanoparticles in pancreatic tissue (d). Scale bar = 35 µm. Figure taken from Eck *et al.*[47]

Cancer tissue labelled by immunohistochemical (IHC) staining using a secondary antibody to FAP was used as comparison (Figure 5.1.1.2a) revealing the presence of cancer stroma in red. The anti-F19 labelled gold nanoparticles was imaged using darkfield scattering of the gold revealing stromal structure as indicated by IHC staining (Figure 5.1.1.2b) whereas the cancer control sample using non-specific conjugated mIgG gold nanoparticles in cancer tissue (Figure 5.1.1.2c) and anti-F19 labelled gold nanoparticles in healthy issue (Figure 5.1.1.2d) reveal minimal contrast.

Additionally, a gold nanoparticle system consisting of a functionalised HER2 antibody on the nanoparticle surface was evaluated for the targeting of MCF7 and SKOV3 cells for cancer electrotherapy. It was suspected that an enhanced electric field strength induced from the application of the functionalised gold nanoparticles could lead to cell death of the cancerous

cells whilst keeping the non-cancerous cells unharmed. It was reported that different cancer cells react differently upon the optical frequency of the electric field. The cell viability was measured through an Annexin V/EthD-III assay and observed a decrease in proliferation from the addition of the HER2-AuNP system without affecting the non-cancerous HUVEC (human umbilical vein endothelial cells) and MCF10a (human mammary epithelial cell line) cells.[48]

Furthermore, an epidermal growth factor receptor (EGFR) antibody, termed (EGFRmAb) was conjugated onto gold nanoparticles for NIR photo-thermal treatment and the cell viability was assessed in 293T (human embryonic kidney) and FaDu (hypopharyngeal carcinoma) cells. The functionalised gold nanoparticle system displayed specific targeting towards the FaDu cell line and reduced cytotoxicity towards the non-expressing EGFR cell line, 293T. Interestingly enough, they also show nuclear localisation and consequently increased cellular damage through the functionalised gold nanoparticle system through DNA damage.[49]

5.1.2 Mass spectrometry imaging in cancer

Although there have been many reports for optical imaging through use of organic fluorophores or through the scattering of gold nanoparticles, mass spectrometry imaging has rarely been reported for these systems. MSI has attracted a great deal of interest for the purpose of real time identification of tissues in biological and clinical applications.[50] MSI offers a highly sensitive and rapid detection method that allows simultaneous identification from a very broad range of biomolecules present in cells and tissue and can be utilised without the need of fluorescent probes.[50,51]

An aptamer coated gold nanoparticle immobilised on graphene oxide was studied for the targeting of mucin 1 (MUC1) in adenocarcinomas through laser desorption ionisation (LDI) MS. They utilised an MUC1 binding aptamer bound to the nanoparticle for detection of gold

ions, namely $[Au]^+$, $[Au_2]^+$ and $[Au_3]^+$ for detection in MCF7 cells as well as four other MUC1 expressing cell lines and imaged through laser desorption mass spectrometry (LDI-MS).[52] Additionally, a poly(catechin) capped gold nanoparticle and nucleolin-binding aptamer gold nanoparticles was developed for simple, rapid and high-throughput cancer diagnosis (Figure 5.1.2.1).[53] These were used as targeting agents making use of the gold cluster peaks in LDI-MS tumor imaging. These nanoparticles bound effectively on nucleolin molecules present on MCF-7 breast cancer cell membranes.[53]

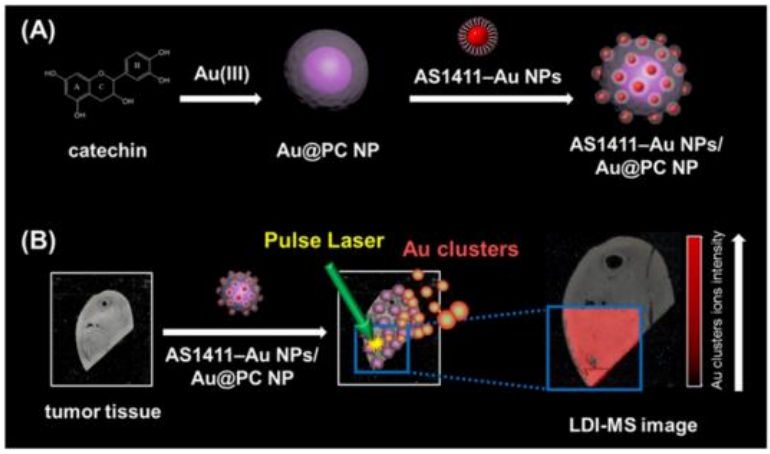

Figure 5.1.2.1. Schematic representation of the preparation of gold nanoparticles (A) tumor tissue imaging through monitoring Au cluster ions by LDI-MSI (B). Figure taken from Tseng *et al.*[53]

The use of poly(catechin) demonstrated excellent use as a matrix for the gold nanoparticle conjugates and was observed to act efficiently as a pulse light energy transducer. These nanoparticle systems also demonstrated higher specificity towards nucleolin over the previously studied aptamer gold nanoparticles modified on graphene oxide for protein targeting.[52]

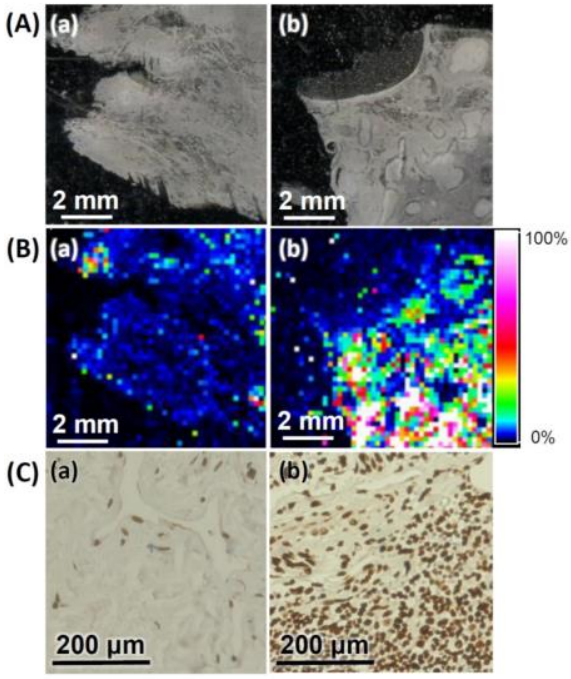

Figure 5.1.2.2. Healthy breast tissue (a) and breast tumour tissue (b). Optical images of (a) and (b) (A). LDI-MSI of $[Au]^+$ intensity of (a) and (b) after labelling with functionalised gold nanoparticles (B) and Immunostaining of nucleolin of (a) and (b) (C). Figure taken from Tseng *et al*.[53]

It was found that the gold nanoparticle conjugates displayed high signal output for gold cluster ions, namely $[Au]^+$, $[Au_2]^+$ and $[Au_3]^+$ for LDI-MSI demonstrating the usefulness of gold as targeting agents in mass spectrometry (Figure 5.1.2.2).

There have been many examples seen in literature consisting of imaging antibody labelled gold nanoparticles via confocal microscopy through the scattering of gold and/or organic fluorophores but only a handful of reports concerning the combination of dual imaging using light and mass spectrometry imaging. It is therefore important to design both an optically active and mass spectrometry imaging agent using the advantageous properties of luminescent metals combined with golds affinity for MSI detection, anticancer properties and imaging properties for the specific detection of cancer markers..

5.2 Chapter Outline

In this chapter, red luminescent gold nanoparticles functionalised with the chimeric monoclonal antibody, Rituximab, were developed in order to determine efficacy of binding and detection through the optical signature of RuPhenSS via flow cytometry and confocal microscopy whilst utilising the characteristic gold ion peaks for detection via MSI in tonsil tissue. Gold nanoparticles were synthesised and characterised using standard techniques such as UV-Vis, DLS and TEM. We employed a directional conjugation method through use of the glycosylation site for linking Rituximab to the gold nanoparticle surface via a PEG intermediary. The Rituximab functionalised gold nanoparticles were examined in three cell lines two of which containing the binding receptor for Rituximab and evaluation of the ruthenium intensity was measured to compare binding to those without Rituximab. Cell viability assays were measured to observe any cell death arising from the Rituximab. Confocal microscopy imaging measuring the luminescent signature of RuPhenSS and mass spectrometry imaging measuring $[Au_2]^+$ and $[Au_3]^+$ ions was conducted on tonsil tissue revealing higher intensities from the Rituximab functionalised nanoparticles. The results described in this chapter represent a promising nanoprobe that can be used for dual imaging applications that provide a highly specific and targeted approach to B-cell malignancies.

5.3 Results and Discussion

5.3.1 Modification of Rituximab for attachment onto gold nanoparticles

Rituximab was modified through the N-linked glycosylation site at asparagine 297 which is located in the Fc portion of the antibody.[54] An indication of successful oxidation of this site can be verified using the purpald test (Figure 5.3.1.1). The hydroxy group present in the Fc region of Rituximab was oxidised via the use of sodium perodiate ($NaIO_4$) to allow the hydrazide-PEG-dithiol linker to be attached.[55] The formation of PEG-linker with Rituximab was formed through the Schmidt reaction whereby an azide reacts with a carbonyl derivative, in this case an aldehyde, to form an amide.[56] This rapid test is efficient and a colour change from clear to purple suggests successful oxidation of the hydroxy group to an aldehyde. The PEG-linker-Rituximab will hereby be called modified Rituximab.

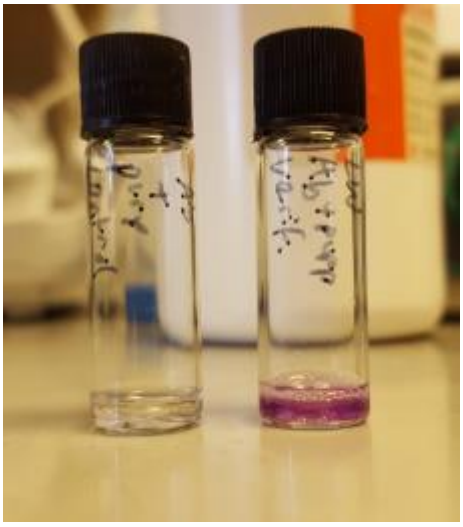

Figure 5.3.1.1. Picture of Rituximab without being oxidised (left) vs oxidation of Rituximab (right) using the purpald test. Visible colour change to purple indicating successful oxidation.

UV-Vis spectroscopy was performed at a known concentration of Rituximab before any modification and compared with the modified Rituximab to assess the concentration. Rituximab has a known absorbance molar extinction coefficient value at 280 nm and 204 nm.[57-59]

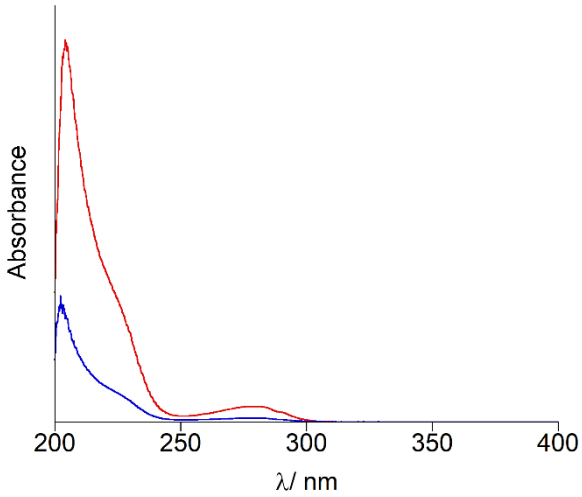

Figure 5.3.1.2. UV-Vis of unmodified Rituximab (40 µg/ mL) in aerated PBS (red) and modified Rituximab (11 µg/ mL) in aerated PBS (blue).

The concentration of unmodified Rituximab was estimated by UV-Vis at 40 µg/mL. By knowing a known concentration and volume added, a calculation based off the OD280 value was able to be performed. The concentration of modified Rituximab by UV-Vis was calculated to be 11 µg/mL. However, the sensitivity of a nanodrop is more accurate and concentrations were calculated based on the values recorded in Table 5.3.1.1.

Table 5.3.1.1. Optical density values (OD280) of unmodified and modified Rituximab.

sample	OD280 1	OD280 2	OD280 3	Avg OD280
1 mg/mL RXB	1.521	1.703	1.593	1.605667
RXB PEG-linker	0.544	0.424	0	0.484

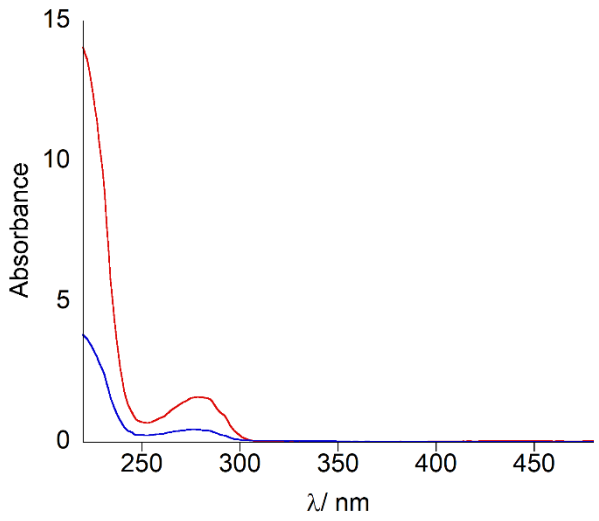

Figure 5.3.1.3. Average OD280 values of 1 mg/ mL unmodified Rituximab (red) and unknown concentration of modified Rituximab (blue).

Three absorbance values were taken of a known concentration of unmodified Rituximab and the unknown concentration of modified Rituximab. Through use of the Beer-Lambert law, an epsilon value was calculated which was in good agreement with literature values and yielded a stock concentration of modified Rituximab at 2.1 µM in 0.01 M PBS.[60]

5.3.2 Coating of Rituximab and RuPhenSS onto gold nanoparticles

5.3.2.1 Synthesis of gold nanoparticles

Monodispersed gold nanoparticles were synthesised using the Turkevich method with slight modification as according to Kumar *et al.*[27,61] Gold nanoparticles were fully characterised through UV-Vis, DLS and TEM techniques.[62,63] Determination of the gold nanoparticle size and concentration can be achieved through the SPR band and the epsilon value at 450 nm and was found to be approximately 15 nm and ~ 3 nM respectively.[64] The calculation for gold nanoparticles concentration can be found in the appendix.

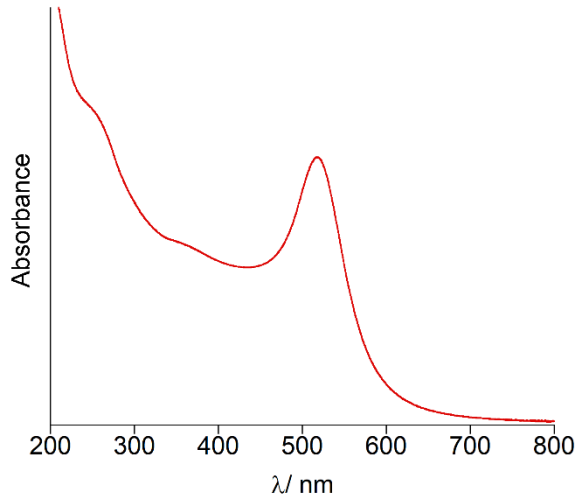

Figure 5.3.2.1.1. UV-Vis of 3 nM c-AuNP in aerated water.

The synthesised citrate capped gold nanoparticles (c-AuNP) displayed an absorption maxima at λ_{max} 518 nm which is in agreement with previously published data.[26,61-63,65-68]

Table 5.3.2.1.1. DLS size, PDI, Intensity and SPR of c-AuNP in aerated water.

	SPR/λ_{max}	**Intensity/nm**	**Number/nm**	**PDI**
Citrate-AuNP	518	23 ± 6	16 ± 4	0.06

DLS studies of c-AuNP revealed an average number of 16 ± 4 nm as shown in Table 5.3.2.1.1. The small polydispersity index indicates particles of a monodisperse nature indicating majority of the particles being of similar size. To further correlate the gold nanoparticle uniformity, TEM images were acquired. TEM suggested sizes of 16 nm (n = 30) which is in very good agreement with the UV-Vis and DLS data.

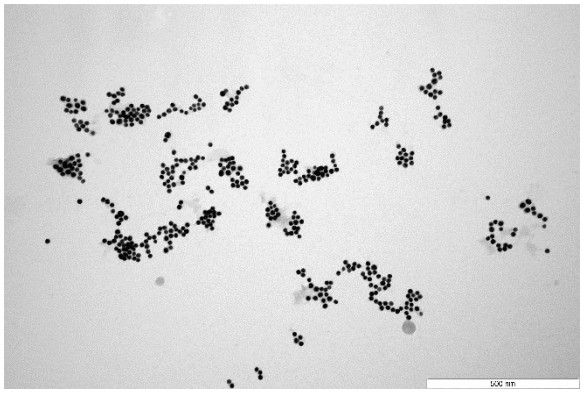

Figure 5.3.2.1.2. Transmission electron microscopy of c-AuNP revealing average sizes of 16 nm. Scale bar = 500 nm.

5.3.2.2 Attachment of Rituximab and RuPhenSS onto gold nanoparticles

The complex RuPhenSS was selected for the labelling due to displaying higher QYand longer lifetimes amongst the other ruthenium(II) complexes synthesised as discussed in Chapter 3.[63] Following the published protocol as described by Kumar *et al*, direct additions of modified Rituximab to the gold nanoparticle solution in 2 µL aliquots resulted in aggregation of the particles (Figure 5.3.2.2.1). This is indicative of significant broadening and shifting of the SPR band. This could be due to the larger size of Rituximab in comparison to the smaller targeting moieties used by Kumar *et al* or it could be due to electrostatic interactions between the particles and the antibody. The attachment of larger molecules to the gold nanoparticles could compromise the nanoparticle stability.[69,70]

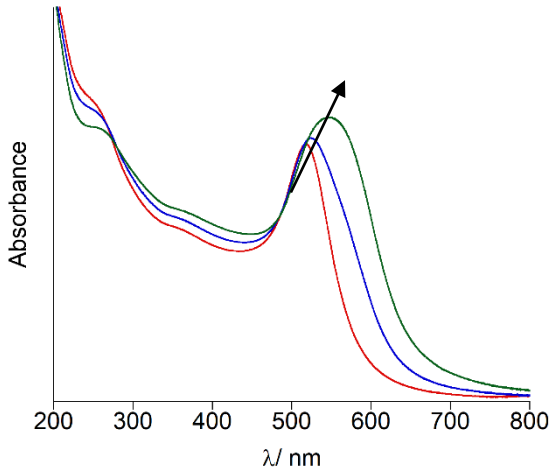

Figure 5.3.2.2.1. Addition of 2 µL quantities of 2.1 µM modified Rituximab (4 µL total added) to 3 nM c-AuNP in aerated water displaying immediate aggregation.

Therefore, prior to adding of the modified Rituximab to the gold nanoparticle surface, additions of polyethylene glycol (PEG) to partially coat the gold nanoparticle surface were conducted to stabilise them. PEG has been used for coating the surface of nanoparticles due to it being water soluble and biocompatible.[71-74]

A stock solution of PEG (1 mL, 1 mM) was titrated in 2 µL aliquots to 3 nM c-AuNP. Partial coverage was achieved by monitoring the SPR shift and generating an SPR curve. It was found that the addition of 4 µM PEG partially coated the gold nanoparticles before addition of the modified Rituximab took place. This partial coverage of PEG shifted the characteristic SPR band from 518 nm to 519 nm suggesting binding of the PEG to the gold nanoparticle surface. After the addition of 8 µM of PEG the SPR band failed to shift further indicating saturation. Partial coverage of the gold nanoparticles with PEG (denoted PEG•AuNP here on) was achieved to allow binding of modified Rituximab and RuPhenSS. Modified Rituximab at a stock concentration of 2.1 µM was added in 2 µL aliquots to partially coat PEG•AuNP.

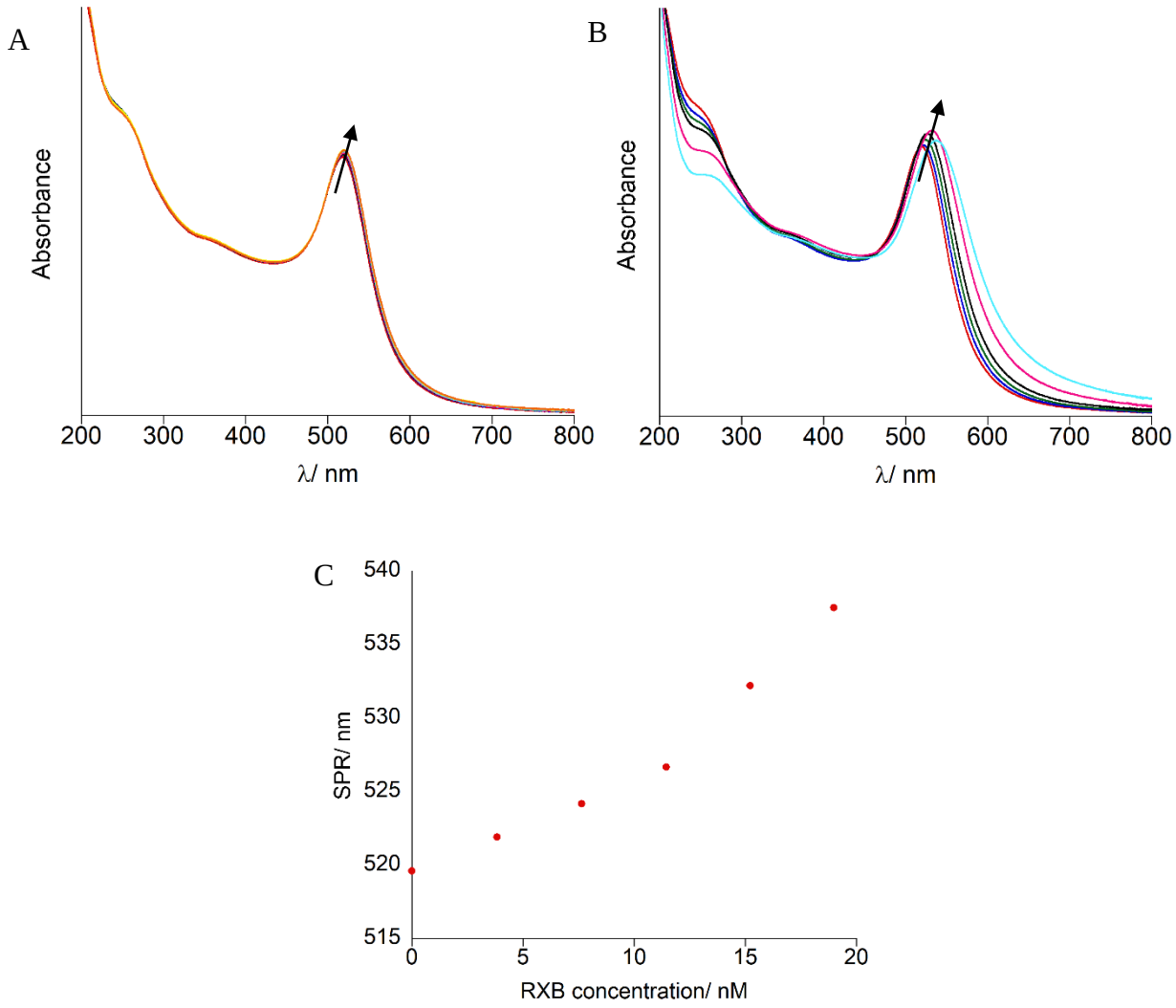

Figure 5.3.2.2.2. Titration of 2 µL quantities of 1 mM PEG into 3 nM c-AuNP in aerated water (4 µL added) (A), titration of 2 µL quantities of 2.1 µM modified Rituximab (RXB) into partially coated 3 nM PEG•AuNP in aerated water (5 µL added) (B) and an SPR curve from generated from B (C).

It is seen after 12 nM of modified Rituximab has been added the particles start displaying aggregation. This is seen by a drop in intensity of the SPR band and broadening. Partial coverage of Rituximab on PEG•AuNP was determined by monitoring the SPR band until aggregation started occurring. From the SPR shifts, it was seen that appropriate coverage of Rituximab was 10 nM. Partial coverage of both PEG and Rituximab on gold nanoparticles (denoted PEG•RXB•AuNP here on) allows the binding of the lumophore, RuPhenSS.

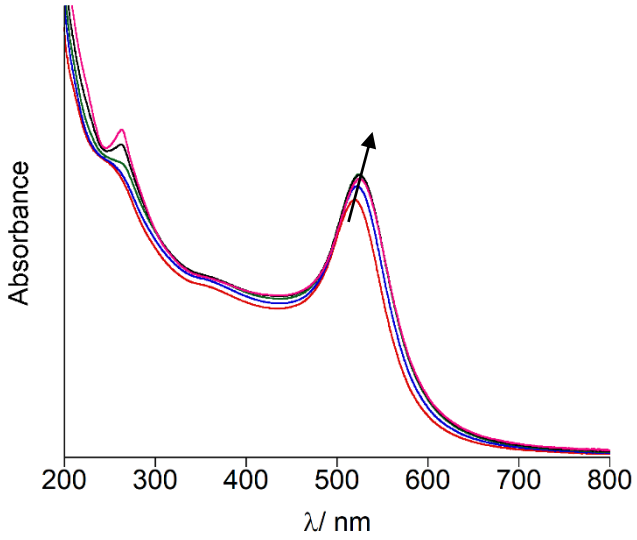

Figure 5.3.2.2.3. Titration of 1 µL quantities of 1mM RuPhenSS on PEG•RXB•AuNP in aerated water (2 µL added).

A stock solution of RuPhenSS in methanol (1 mM, 1 mL) was titrated into PEG•RXB•AuNP via 1 µL aliquots with stirring and the SPR shift was monitored to determine saturation of the gold nanoparticle. It was observed after 2 µM the intensity of the SPR band began to drop suggesting partial instability. The stock particles were concentrated up to 6 nM allowing additions of 8 µM PEG, 20 nM modified Rituximab and 4 µM RuPhenSS (denoted RuPhenSS•RXB•AuNP here on) which resulted in a shift of 1 nm, 3 nm and 7 nm respectively to c-AuNP (Table 5.3.2.2.1). Gold nanoparticles without the antibody were synthesised as control particles (RuPhenSS•PEG•AuNP) and were made in the same concentrations with those of the antibody for comparison in luminescence for flow cytometry and optical microscopy experiments with tonsil tissue.

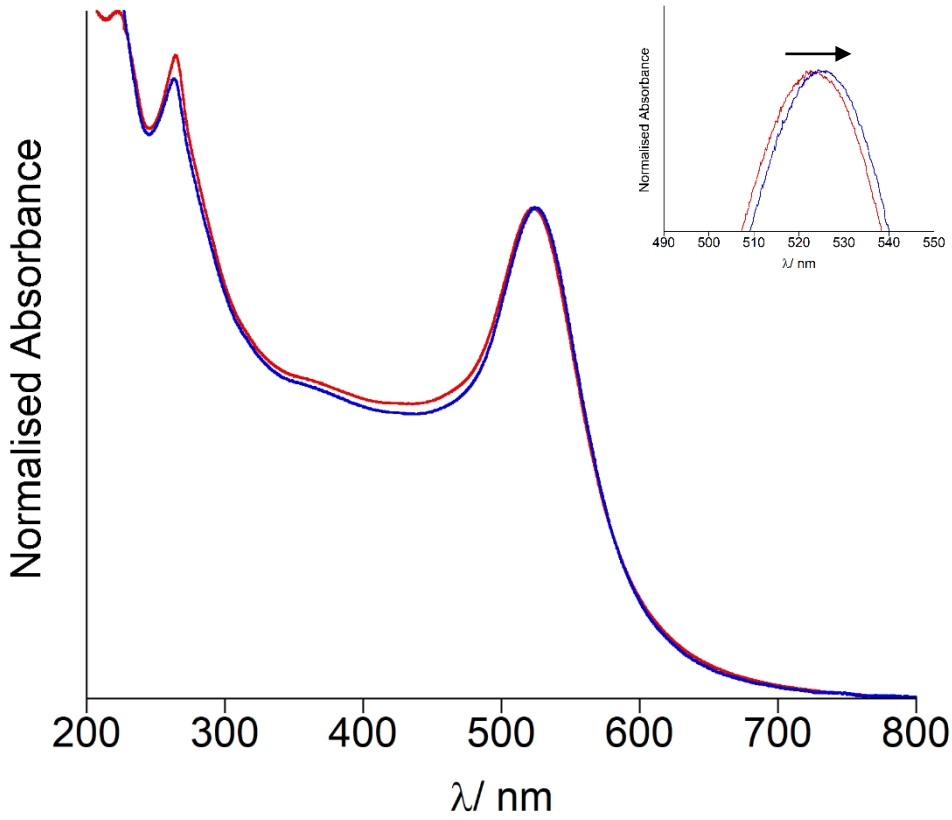

Figure 5.3.2.2.4. Normalised UV-Vis of purified 3 nM RuPhenSS•PEG•AuNP (red) and 3 nM RuPhenSS•RXB•AuNP (blue) in aerated water and a zoom in indicating shift in wavelength from attachment of Rituximab.

After coating was achieved, the particles were isolated through 10 kDa molecular weight cut off centrifugation filters to purify them from any excess PEG, Rituximab and RuPhenSS. The isolated particles displayed the same λmax as the particles saturated with the Rituximab and ruthenium complex formed during the titrations. This confirms that the surface coating of the particles has not been altered through the isolation process.

Table 5.3.2.2.1. Summary of SPR absorption maximas and shifts relative to c-AuNP

	λmax / nm	Shift/ nm
c-AuNP	518	0
PEG•AuNP	519	1
PEG•RXB•AuNP	522	4
RuPhen•AuNP	523	5
RuPhen•RXB•AuNP	525	7

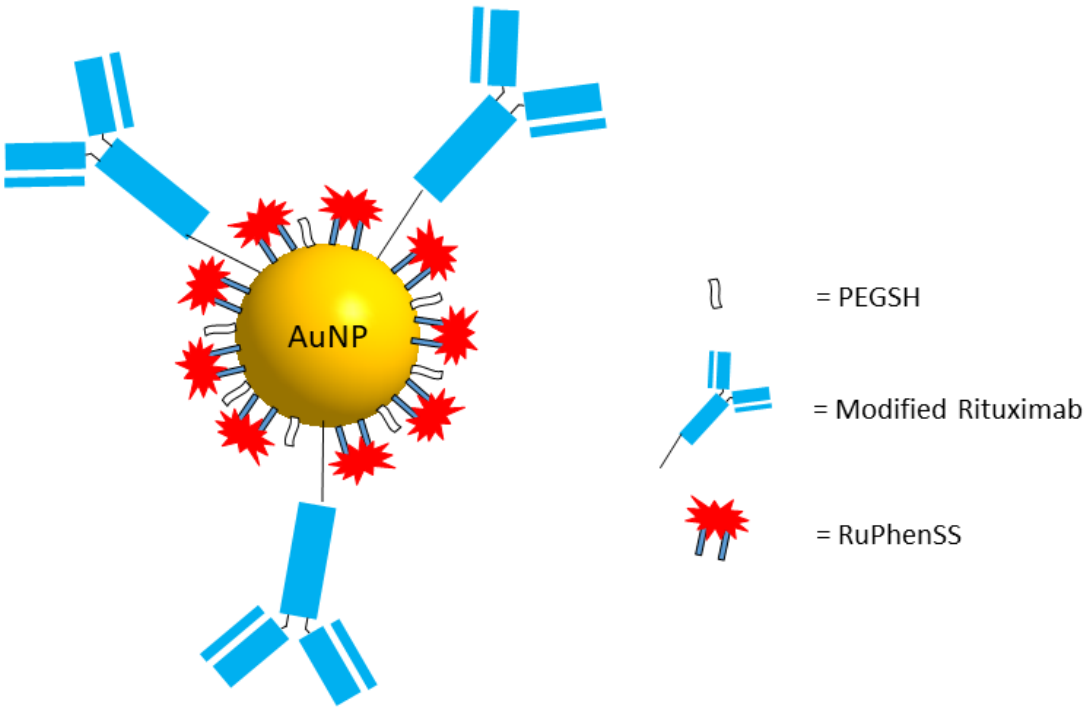

Figure 5.3.2.2.5. Cartoon representation of directional conjugation of Rituximab to luminescent AuNP estimating ~3 Rituximab per AuNP based on concentration.

5.3.2.3 Characterisation of gold nanoparticles in the absence and presence of Rituximab

The coated particles were characterised using DLS size and TEM techniques. The hydrodynamic diameter and intensity was measured via DLS in order to evaluate the dispersity of the functionalised particles. In comparison to PEG•AuNP, the DLS measurements showed higher intensity distributions for PEG•RXB•AuNP and RuPhenSS•RXB•AuNP which suggests the presence of Rituximab of the surface of the gold nanoparticle. During the coating procedure of the particles, all particles display relatively low PDI's suggesting that when modified with PEG, Rituximab and RuPhenSS they maintain their monodispersity.

Table 5.3.2.3.1. Summary DLS size of AuNP samples

	Size by Intensity/ nm	Size by Number/ nm	PDI
C-AuNP	23 ± 6	16 ± 4	0.06
PEG•AuNP	38 ± 11	26 ± 6	0.13
PEG•RXB•AuNP	45 ± 15	27 ± 7	0.16
RuPhenSS•PEG•AuNP	46 ± 16	26 ± 7	0.19
RuPhenSS•RXB•AuNP	52 ± 20	28 ± 8	0.20

Attachment of the RuPhenSS complex onto the PEG•AuNP resulted in an increase in the intensity distribution. This confirms the presence of the complex on the gold surface via DLS whilst maintaining the same number distribution indicating stability of the particles. Aggregation upon addition of the complex to the particle would result in a large PDI, intensity and number distribution. However, there was no significant change on the intensity distribution

when the complex was added onto PEG•RXB•AuNP. This could be attributed to the fact that an antibody is much larger than the metal complex. The metal complex size is about 2 nm in size whilst Rituximab is estimated about 10 nm in size.[75,76] Due to this, it is seen that no significant increase is observed in the intensity distribution when the metal complex is added onto the functionalised surface of the PEG•RXB•AuNP. Uniformity and polydispersity of the particles was further confirmed through TEM. TEM imaging of PEG•AuNP, RuPhenSS•PEG•AuNP and RuPhenSS•RXB•AuNP showed highly monodisperse and uniformly sized gold nanoparticles of about 15 nm (n = 18), 13 nm (n = 20) and 15 nm (n = 15) respectively (Figure 5.3.2.3.1).

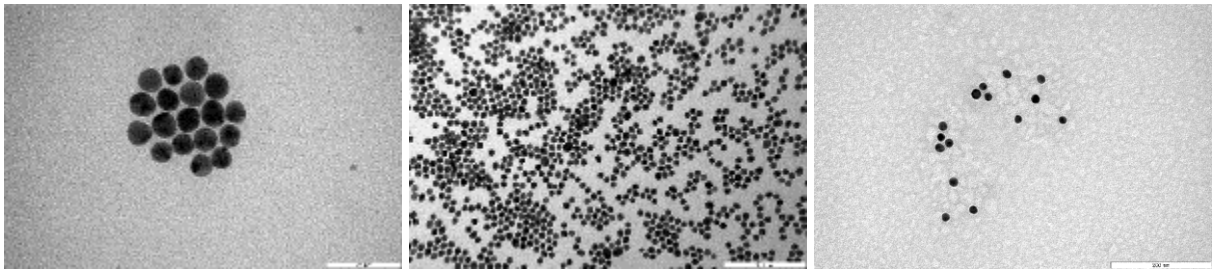

Figure 5.3.2.3.1. Transmission electron microscopy of PEG•AuNP (Scale bar = 50 nm) (A), RuPhenSS•PEG•AuNP (B) and RuPhenSS•RXB•AuNP (Scale bar = 200 nm) (C) indicating monodisperse and spherical particles (Scale bar = 200 nm) revealing sizes of 15 nm, 13 nm and 15 nm respectively.

5.3.2.4 Determining the presence of Rituximab on gold nanoparticles

Confirmation of Rituximab attachment onto the gold nanoparticle was further obtained by testing the antibody content using a conjugate strip test from Expedeon based on binding affinities to proteins A and G. These half strips are suitable for gold nanoparticle conjugates and provide rapid confirmation of antibody attachment. The strips contain a nitrocellulose membrane immobilised with protein A and protein G on the test line. Both of these have high affinities to the Fc region of various IgG antibodies. Rituximab contains human IgG1 in the Fc portion of the antibody which has high binding affinities to proteins A and G on the strip test.[77]

The control sample was provided from the supplier which contained a lyophilized gold nanoparticle antibody conjugate. The nanoparticles in this instance acts as a coloured label to verify binding of the antibody on the concentrated test line indicating successful conjugation of the antibody on the particle (Figure 5.3.2.4.1).

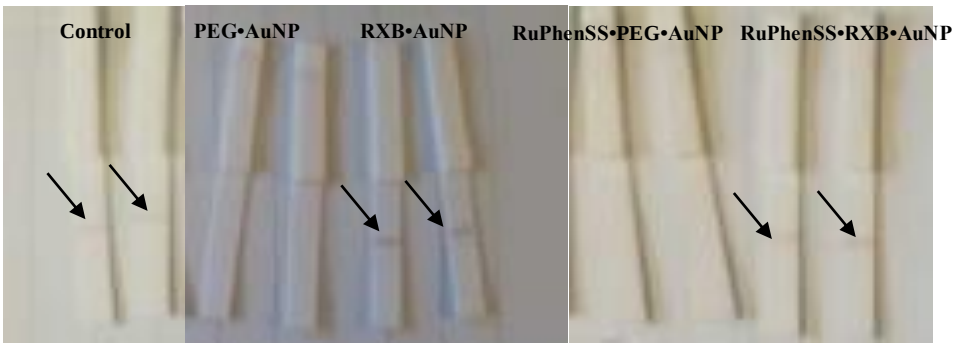

Figure 5.3.2.4.1. Check and go strip test of control sample, PEG•AuNP and RXB•AuNP (B) and RuPhenSS•PEG•AuNP and RuPhenSS•RXB•AuNP (C) in duplicates for detection of Rituximab presence. Indication of binding is represented through the arrows.

Figure 5.3.2.4.1 depicts successful conjugation of Rituximab on the particles in the samples tested by visualisation of the coloured band on the "test strip". The samples with no Rituximab were ran parallel to the those with Rituximab and these show no evidence of binding on the "test strip" suggesting there is no non-specific binding occurring within our nanoparticle system. This confirms successful attachment of Rituximab onto the gold nanoparticle surface.

5.3.3 Luminescent and biological studies of functionalised gold nanoparticles

5.3.3.1 Detection of ruthenium emission on RuPhenSS•PEG•AuNP and RuPhenSS•RXB•AuNP

Before starting experimental studies in a biological environment, photophysical characterisation of RuPhenSS•AuNP and RuPhenSS•RXB•AuNP was performed in order to confirm and evaluate any differences in the unique luminescent properties of the RuPhenSS. The luminescence excitation and emission was conducted in aerated water.

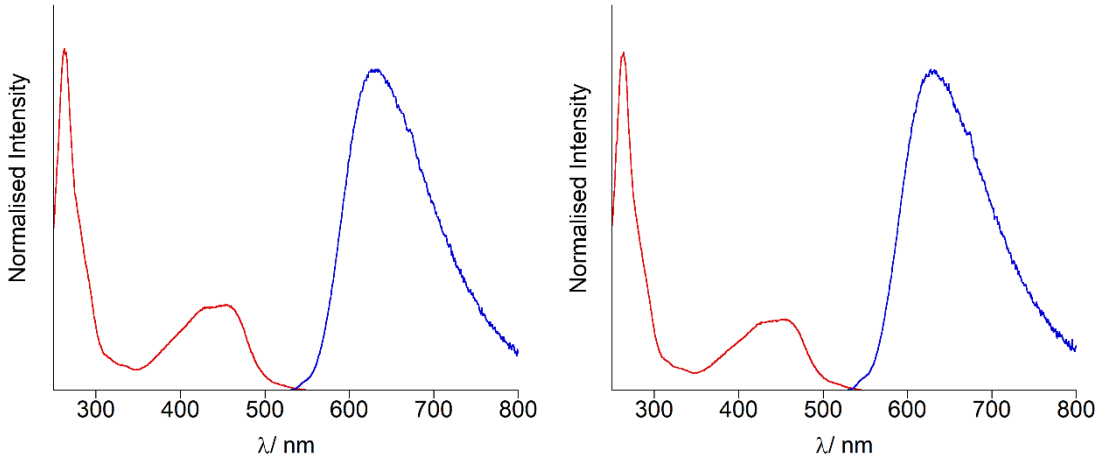

Figure 5.3.3.1.1. Excitation (red) and emission (blue) of 3 nM RuPhenSS•PEG•AuNP (λ_{exc} = 457 nm, λ_{em} = 635 nm) in aerated water (A) and RuPhenSS•RXB•AuNP (λ_{exc} = 457 nm, λ_{em} = 635 nm) in aerated water.

The excitation bands of the RuPhenSS•PEG•AuNP and RuPhenSS•RXB•AuNP display identical spectra to that of the complex in water suggesting that the complex has retained its photophysical properties at 457 nm and 266 nm. Upon excitation of the RuPhenSS•PEG•AuNP and RuPhenSS•RXB•AuNP at 457 nm, the functionalised gold nanoparticles show emission at λ_{max} at 635 nm. This displays a 5 nm shift from the free metal complex in aerated water. Interestingly there is no shift seen between RuPhenSS•PEG•AuNP and

RuPhenSS•RXB•AuNP. The emission observed on RuPhenSS•PEG•AuNP and RuPhenSS•RXB•AuNP when excited at 457 nm demonstrates the gold nanoparticles have retained its luminescence properties viable for confocal luminescence microscopy.

5.3.3.2 Cell viability assays of Rituximab labelled gold nanoparticles

To determine toxicity of the functionalised gold nanoparticles on cancer cell lines, cell survival assays were performed using Cell Titre-Glo™. Toxicity of gold nanoparticles derives from the surface modification and has been well documented.[78] Cell Titre-Glo™ determines cell viability by the quantitation of adenosine triphosphate (ATP) present which is a key indicator of metabolically active cells.[79] There are other cell viability assays available that are widely used, namely MTT assay which relies on the ability of mitochondrial dehydrogenase enzymes to convert the 3,-4,5 dimethyithiazol-2,5 diphenyl tetrazolium bromide (MTT) to a purple formazan precipitate.[80] However, in comparison to Cell Titre-Glo™ it takes significantly longer for incubation.[81] Rituximab's mechanism of action for inducing cell death includes complement-mediated cytotoxicity (CDC) and antibody dependant cell mediated cytotoxictity (ADCC).[82, 83] However, ADCC requires high concentrations of antibody and relies on other immunological responses such as natural killer (NK) cells.

Toxicity of the functionalised gold nanoparticles was investigated using serial dilutions and measured using Cell Titre-Glo™ and comparing to the untreated control (cells in complete media). RuPhenSS•PEG•AuNP and RuPhenSS•RXB•AuNP were evaluated in Jurkat, a T lymphocyte cell line, Raji, a B-cell Burkitt lymphoma (BL) cell line and Karpas 422, a B-cell non-Hodgkin lymphoma (NHL) cell line. Jurkat is a CD3 positive cell line and does not express CD20 whereas both RAJI and Karpas 422 are CD20 positive expressing cell lines. The cell viability assays of RuPhenSS•PEG•AuNP and RuPhenSS•RXB•AuNP in Jurkat display toxicity at 0.11 nM for RuPhenSS•PEG•AuNP whereas toxicity arises at 0.23 nM for

RuPhenSS•RXB•AuNP. This is most likely due to the inability for RuPhenSS•RXB•AuNP to bind to Jurkat since CD20 is not presented where as RuPhenSS•PEG•AuNP are readily taken up. It is therefore likely that toxicity in concentrations exceeding 0.23 nM is due to the increased concentration of gold. For Raji, all concentrations observed display toxicity showing no preference in cell death between the Rituximab labelled and Rituximab free gold nanoparticles. For Karpas-422 a different trend is observed. Concentrations below 0.11 nM are non-toxic towards the cell line but at 0.23 nM, toxicity is starting to appear for RuPhenSS•RXB•AuNP. This could be due to Karpas-422 being more sensitive to Rituximab over the Raji cell line

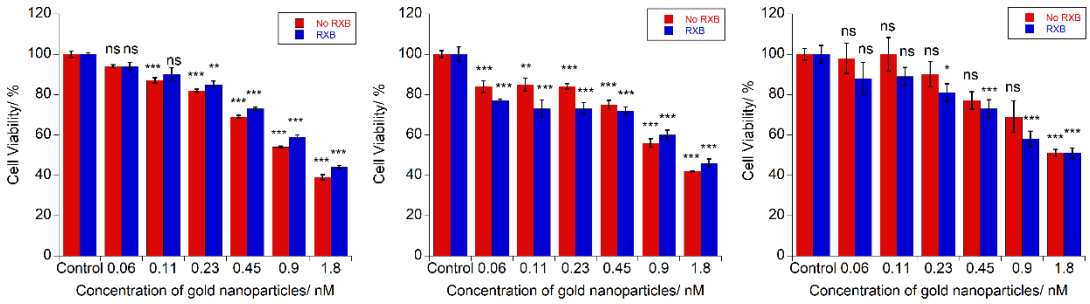

Figure 5.3.3.2.1. Cell viability assays of control (media) and varying concentrations of RuPhenSS•PEG•AuNP (red) and RuPhenSS•RXB•AuNP (blue) in Jurkat (left), Raji (middle) and Karpas 422 (right) using Cell-Titre-Glo by 1-way ANOVA followed by a Dunnett's t-test corrected for multiple comparisons. *=P<0.01, **=P<0.001, ***=P<0.0001. n = 2.

5.3.3.3 Flow cytometry of Rituximab labelled gold nanoparticles

To determine whether the luminescent nanoparticles could serve as a nanoparticle-based imaging and detection delivery system, the cellular uptake of RuPhenSS•PEG•AuNP and RuPhenSS•RXB•AuNP was evaluated in cells that express CD20. The cellular uptake of these particles was evaluated through flow cytometry analysis using the PerCP-Cy5-5-A filter, a blue laser that excites at 482 nm and has an emission maxima at 695 nm.

Cellular uptake of RuPhenSS•PEG•AuNP and RuPhenSS•RXB•AuNP was evaluated in Jurkat, Raji and Karpas 422. For each cell line, the cellular uptake efficacy of the

RuPhenSS•PEG•AuNP and RuPhenSS•RXB•AuNP was analysed through comparing the increase in fluorescence intensity of the ruthenium in treated cells against the cells treated with negative control (control – H_2O). Initially, to confirm expression of CD20 in the cell lines, the cells were treated with 0.25 mg/ mL anti-CD20 antibody labelled with an APC-Cy7-A lumophore alongside controls (control = H_2O) and incubated for 30 minutes. They were monitored by flow cytometry using the APC-Cy7-A channel exciting at 650 nm and has an emission maxima of 785 nm. Since Jurkat is a CD3 positive expressing cell line, it is expected no fluorescence from APC-Cy7 would be detected. Confirmation of CD20 was detected in both the CD20 positive cell lines through the APC-Cy7 fluorescence channel, RAJI and Karpas 422 which both show 88% and 79% respectively via histogram analysis.

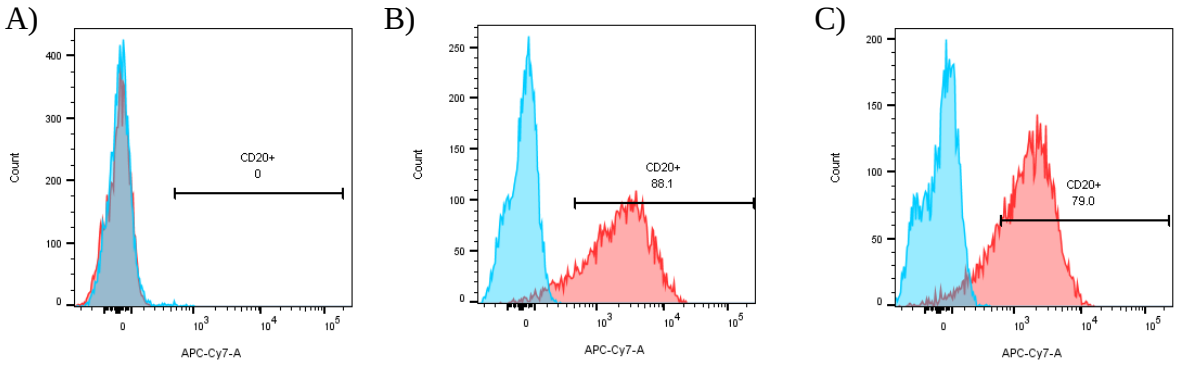

Figure 5.3.3.3.1. Flow cytometry of CD20 expression in untreated cells (blue) and through staining of an anti-CD20 antibody labelled with APC-Cy7-A fluorophore (red) (λ_{exc} = 457 nm, λ_{em} = 635 nm) in Jurkat (A), Raji (B) and Karpas 422 (C). n=1.

Once confirmation of the CD20 was conducted, the cells were treated with 1.5 nM RuPhenSS•PEG•AuNP and RuPhenSS•RXB•AuNP respectively for 18 hours. This time point was found to be optimal through previous work with 13 nm gold nanoparticles and previous studies exhibited low to none ruthenium signal at 4 hours.[26,67,84,85] Histogram analysis and MFI plots was plotted by Dr Tracey Perry (Institute of Cancer and Genomic Sciences, University of

Birmingham) using FlowJo. Histogram analysis (Figure 5.3.3.3.2) revealed that treatment of the RuPhenSS•PEG•AuNP in Jurkat cells showed a small increase in ruthenium fluorescence. The RuPhenSS•RXB•AuNP interestingly shows a small percentage of fluorescence and is most likely due to a few nanoparticles without an antibody on being taken up by the cells. The RuPhenSS•PEG•AuNP shows a higher increase in fluorescence when compared to the RuPhenSS•RXB•AuNP since Jurkat do not express CD20 and thus shows low fluorescence. Histogram analysis of Karpas 422 show an increase in fluorescence between RuPhenSS•PEG•AuNP and RuPhenSS•RXB•AuNP from the control cells showing increases of 5% and 10% respectively. This difference in fluorescence suggests the RuPhenSS•RXB•AuNP has a higher affinity for Karpas 422 over the particles with no antibody. Finally, histogram analysis of RAJI shows similar trends in fluorescence intensity as with the Karpas 422 cell line. As mentioned earlier, it is not surprising to see a higher intensity increase for that of the RuPhenSS•RXB•AuNP over the RuPhenSS•PEG•AuNP since the antibody, Rituximab, is specific for CD20 positive cells.

When comparing between the cell lines for RuPhenSS•PEG•AuNP and RuPhenSS•RXB•AuNP, a steady increase in fluorescence is observed from Karpas 422 and Raji. According to literature, different B cell lymphomas have significantly different levels of sensitivity to CD20 targeting antibodies.[7] This in part, is due to the level of expression which varies across different B-cell lines. This trend of expression is seen when confirming the presence of CD20 across the three cell lines investigated (Figure 5.3.3.3.1). It has been reported that Karpas 422 and Raji cells in comparison to other lymphoma lines exhibit lower levels of CD20.[6, 7] This could explain the low fluorescence intensity of the RuPhen•RXB•AuNP across Karpas 422 and Raji resulting in minimal binding or uptake of the gold nanoparticles.[4, 7,86]

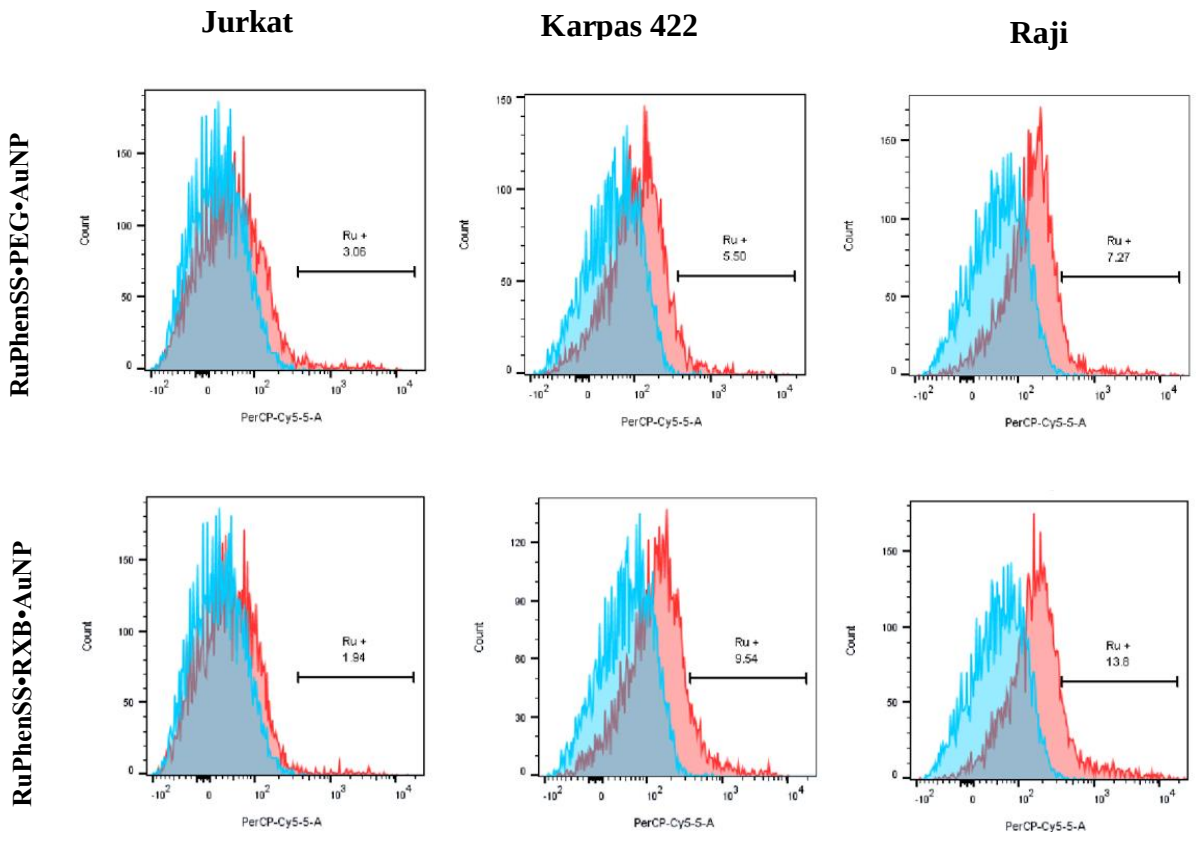

Figure 5.3.3.3.2. Histogram analysis of untreated cells (blue) and 1.5 nM RuPhenSS•PEG•AuNP and 1.5 nM RuPhenSS•RXB•AuNP (red) in Jurkat, Raji and Karpas 422 cell lines. n=1.

The higher expression of CD20 on the Raji cells as seen through histogram analysis from staining with an anti CD20 labelled with an APC-Cy7-A fluorescent lumophore would suggest higher uptake in the cells for RuPhenSS•RXB•AuNP. This is seen through uptake of the RuPhenSS•PEG•AuNP and RuPhenSS•RXB•AuNP in Raji cells when compared to Karpas 422. However, Figure 5.3.3.3.2 is representative of one biological repeat so the differences between fluorescence of RuPhenSS•PEG•AuNP and RuPhenSS•RXB•AuNP cannot be determined statistically. Median fluorescence intensity plots are another way to visualise expression of CD20 across the nanoparticle samples and controls in the different cell lines. In

the Jurkat cell line, there appears to be little difference between the control (H_2O) and the two nanoparticle samples RuPhenSS•PEG•AuNP and RuPhenSS•RXB•AuNP abbreviated Ru-Au and RXB-Au respectively (Figure 5.3.3.3.3). Jurkat do not express the cell surface antigen of interest, and thus little fluorescence is detected.

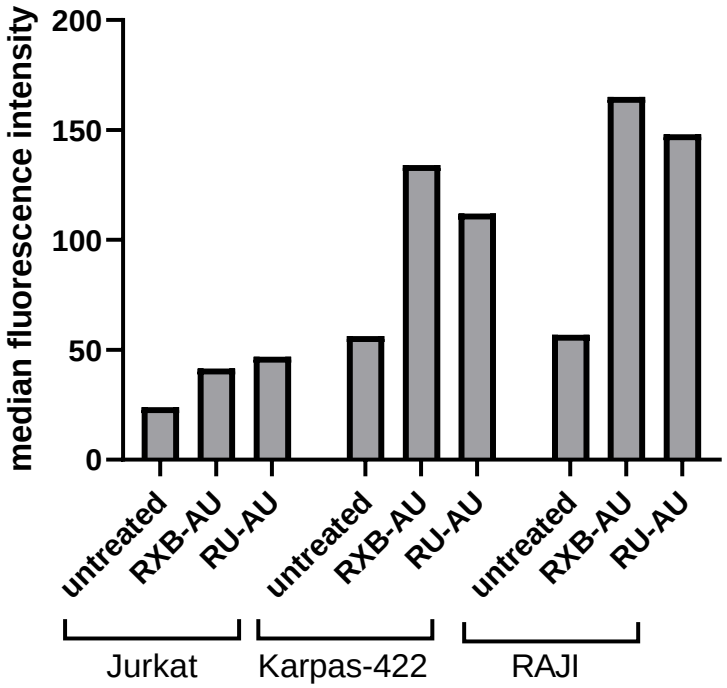

Figure 5.3.3.3.3. Median Fluorescence Intensity plot of gold nanoparticles in Jurkat, Raji and Karpas 422 cells. n=1.

Comparing to the control (H_2O) in Karpas 422 displays a significant increase in MFI for both RuPhenSS•PEG•AuNP and RuPhenSS•RXB•AuNP. There appears to be an increase between the RuPhenSS•PEG•AuNP and RuPhenSS•RXB•AuNP which suggests preferential uptake of those with the antibody on the functionalised gold nanoparticle system. However, the difference is very small and cannot be determined statistically as this is representative of one biological repeat. A similar trend is observed in the Raji cell line of the RuPhenSS•PEG•AuNP and RuPhenSS•RXB•AuNP when compared to the control. The small increase in MFI of the

RuPhenSS•RXB•AuNP between Karpas 422 and Raji is most likely due to the expression of CD20. It was seen that Raji express higher levels of CD20 through staining (14%) by flow cytometry which would account for the increase in MFI between the two cell lines. This could also be due to Rituximab on the functionalised gold nanoparticles having a greater affinity to the CD20 antigen expressed on the cell surface of Raji over Karpas 422.

Histogram analysis and MFI plots of the RuPhenSS•PEG•AuNP and RuPhenSS•RXB•AuNP in the cell lines Jurakt, Raji and Karpas 422 have demonstrated higher uptake in the CD20 positive expressing cell lines with RuPhenSS•RXB•AuNP over RuPhenSS•PEG•AuNP. This demonstrates the ability for targeting, detection and imaging capabilities via fluorescence of the RuPhenSS•RXB•AuNP against B-cell lymphomas. Confocal microscopy of RuPhenSS•RXB•AuNP over RuPhenSS•PEG•AuNP was conducted on OCI-LY3 (B-cell NHL cell line) cytospins (appendix). Cytospins were used due to the similar staining preparations as fixed tissue samples (antigen retrieval). It was found that the RuPhenSS•PEG•AuNP displayed little to no fluorescence whereas RuPhenSS•RXB•AuNP displayed greater ruthenium intensity likely owing to the presence of Rituximab however the signal was weak.

5.3.4 Detection of functionalised gold nanoparticles in tonsil tissue

The binding, detection and imaging via optical microscopy and mass spectrometry of the Rituximab coated functionalised gold nanoparticles was studied in tonsil tissue. Rituximab in combination with cyclophosphamide, doxorubicin (hydroxydaunorubicin), vincristine (Oncovin), and prednisone (CHOP) has been used for the treatment of tonsillar lymphoma (primary tonsil diffuse large B-cell lymphoma) due to the high expression of CD20 expressed in tonsillar tissue, thus making it an ideal target for Rituximab based therapies.[87-91] The tonsil

samples were treated under the same conditions to that of the cells in flow cytometry. Gold nanoparticle concentration on the tissue samples was increased to maximise the ratio of Rituximab functionalised gold nanoparticles to CD20 receptors. The tonsil tissue was sectioned to 5 µm on glass slides and Indium Tin Oxide (ITO) slides and baked for two hours. Antigen retrieval was conducted on the tonsil slides and the tonsil samples were treated with 3 nM RuPhenSS•PEG•AuNP and 3 nM RuPhenSS•RXB•AuNP for 18 hours in the dark and imaging was performed using confocal luminescence microscopy. Treatment of the sectioned tonsil tissue with RuPhenSS•PEG•AuNP resulted in low to no luminescence intensity signal from the RuPhenSS complex during imaging (Figure 5.3.4.1). This suggests low to no particles are present on the tonsil tissue slide. This is not unexpected because the tissue is not live and fixed in paraformaldehyde and the RuPhenSS•PEG•AuNP major uptake mechanism in cells is via pinocytosis and endocytosis, thus impeding the mechanism for uptake.[67] Another contributing factor for low detection could be the quantity of ruthenium present surrounding the particle surface.

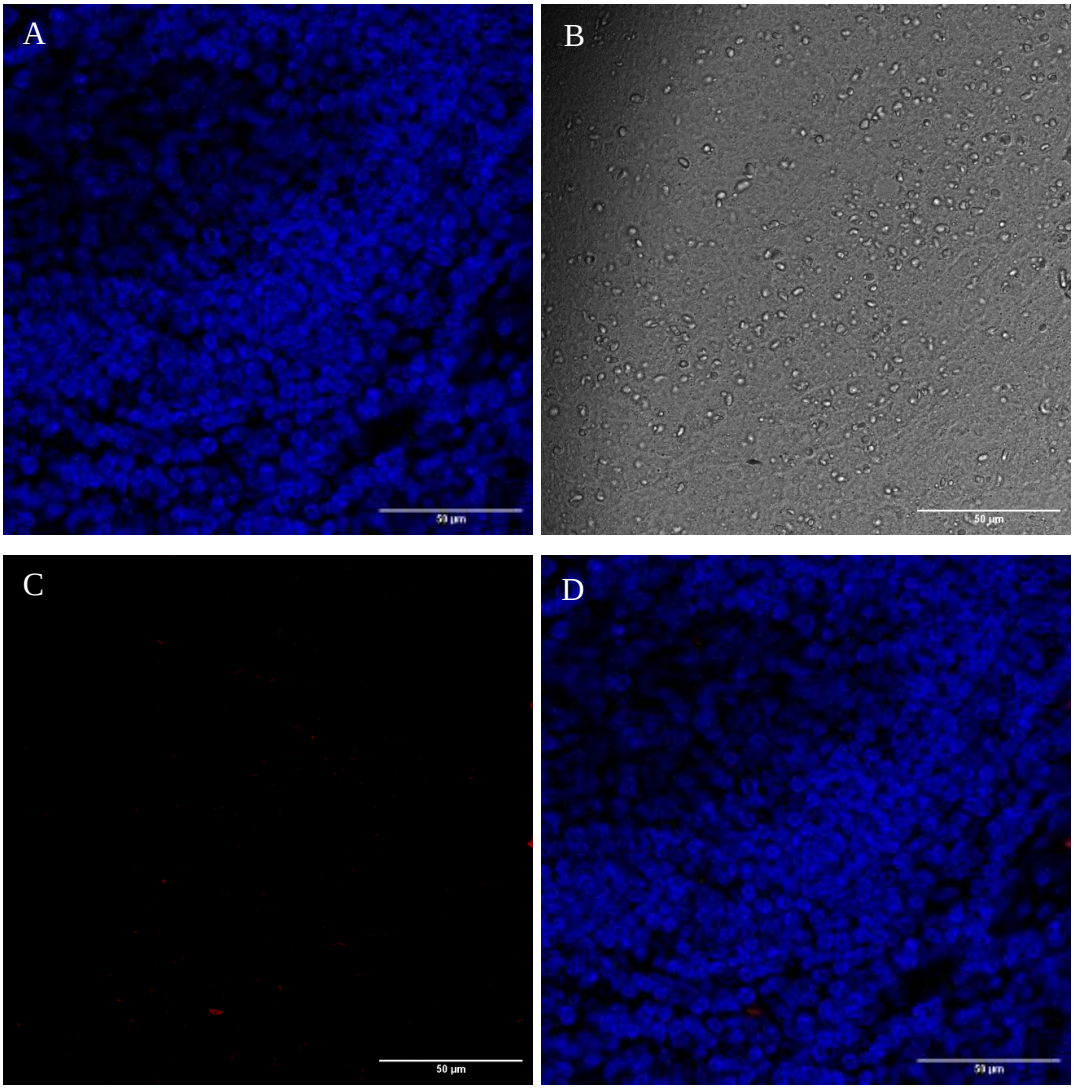

Figure 5.3.4.1. Confocal microscopy of Tonsil Tissue treated with 3 nM RuPhenSS•PEG•AuNP 16 hours. Blue channel, DAPI emission (λ_{exc} = 405 nm, λ_{em} 415−460 nm) (A), Brightfield (B); Red channel, Ruthenium emission (λ_{exc} = 488 nm, λ_{em} 580−780 nm) (C), and overlap of A and C (D). Scale bar = 50 µm.

The RuPhenSS•RXB•AuNP shows enhanced luminescence intensity (Figure 5.3.4.2) over that of the RuPhenSS•PEG•AuNP confirming specificity of Rituximab to CD20 cells in the tonsil tissue. Both tonsil tissue samples were co-stained with a nuclear dye, DAPI, to visualise the nuclei of cells and observe the localisation of the Rituximab functionalised gold nanoparticles. However detection of ruthenium surrounding the cells is seen suggesting that the antibody coated ruthenium gold nanoparticles can display selective and specific targeting of CD20 and

the increase in luminescence when compared to RuPhenSS•PEG•AuNP is attributed to the addition of Rituximab. This has the capabilities of providing novel theranostic opportunities in being able to detect and map tumour biomarkers in vivo.

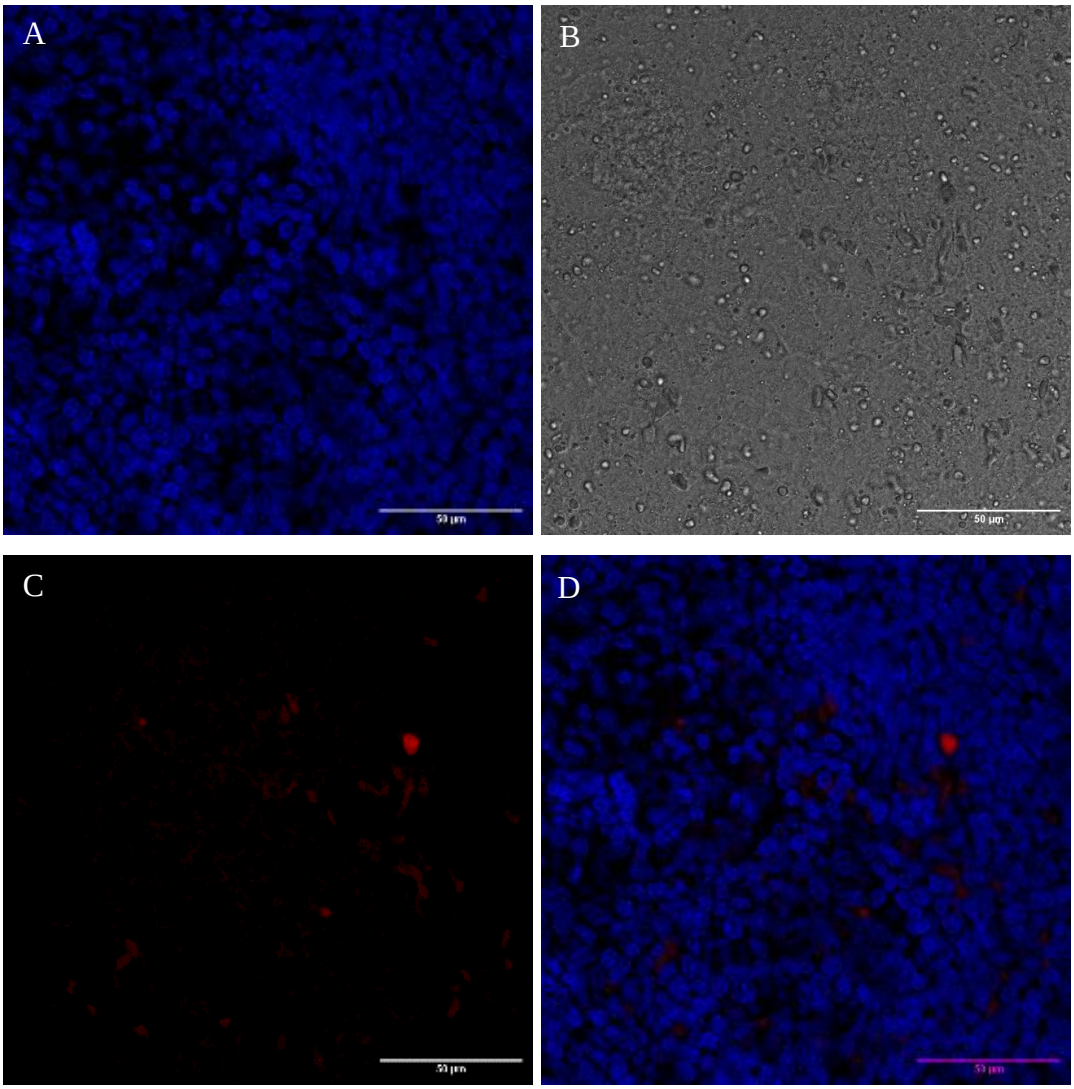

Figure 5.3.4.2. Confocal microscopy of tonsil tissue treated with 3 nM RuPhenSS•RXB•AuNP 16 hours. Blue channel, DAPI emission (λ_{exc} = 405 nm, λ_{em} 415−460 nm) (A), Brightfield (B); Red channel, Ruthenium emission (λ_{exc} = 488 nm, λ_{em} 580−780 nm) (C), and overlap of A and C (D). Scale bar = 50 µm.

To further support the efficacy of binding of the Rituximab functionalised gold nanoparticle over that of the ruthenium coated gold nanoparticles, mass spectrometry imaging (MSI) was performed. Antigen retrieval on 5 µm thick tonsil tissue was conducted and treated with 3 nM

RuPhenSS•PEG•AuNP and 3 nM RuPhenSS•RXB•AuNP for 18 hours in the dark in the presence of 0.5 mM ammonium citrate. The samples were washed and baked for an hour prior to MSI. MSI was performed on a Bruker Ultraflex MALDI in reflective mode from 100 – 2000 Da. Microscope images were taken after the experiment to observe the tissue morphology (appendix). Due to the high abundance of gold in relation to ruthenium, detection of the characteristic isotope pattern for ruthenium was not observed. A unique advantage for using gold nanoparticles and a metal complex allows dual analysis of detection via MS since these do not exist naturally in a biological system. Literature studies have shown MSI using gold nanoparticles to image tissue samples using their unique isotope pattern.[92-94]

The addition of ammonium citrate has been used to improve signal-noise ratio in biological specimens.[95] Due to the abundance of gold ions relative to ruthenium, mapping using $[Au]^+$, $[Au_2]^+$ and $[Au_3]^+$ ions was possible in the tonsil tissue and compared to a negative control (H_2O). The control sample displayed no ions relating to that of gold and thus suggesting that the peaks detected across the RuPhenSS•PEG•AuNP and RuPhenSS•RXB•AuNP samples are real and not from the surrounding environment in the tissue (Figure 5.3.4.3).

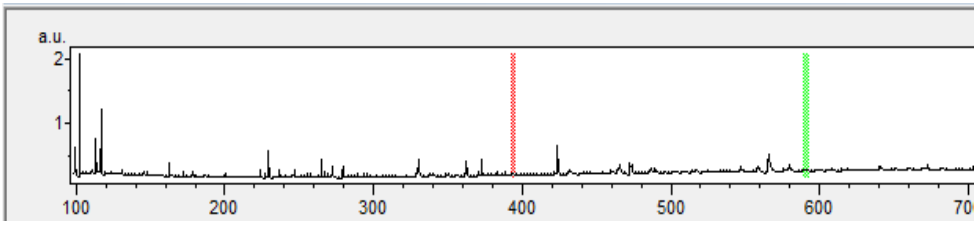

Figure 5.3.4.3. Screenshot of control tonsil tissue sample mass spectrum indicating no presence of Au ions in the tonsil prior to imaging of treated samples.

Two intensity maps were plotted using the dominant $[Au_2]^+$ and $[Au_3]^+$ species. According to literature, $[Au_2]^+$ and Au_3^+ are the most amenable for detection since $[Au]^+$ typically overlapped and was supressed with fragmented ions from the tissue.[94,96] The dominance of the $[Au_2]^+$ and

$[Au_3]^+$ species can be observed from the MS spectrum of RuPhenSS•PEG•AuNP and RuPhenSS•RXB•AuNP. Due to the nature of dominance, these ions were selected for detection of the functionalised gold nanoparticles in the tonsil tissue. The control, RuPhenSS•PEG•AuNP and RuPhenSS•RXB•AuNP was ran under the same conditions so comparison between the samples could be performed.

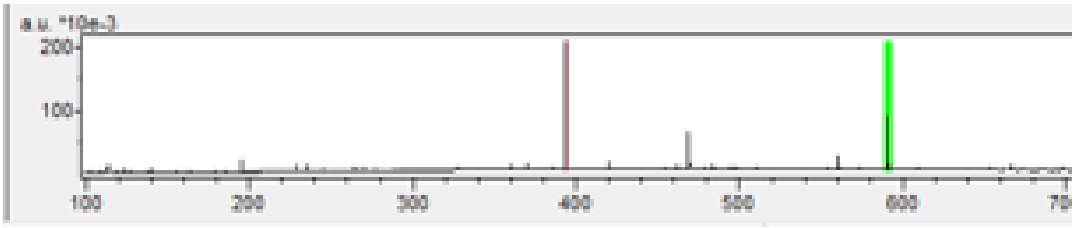

Figure 5.3.4.4. Screenshot MS spectrum RuPhenSS•PEG•AuNP displaying the dominance of the $[Au_2]^+$ and $[Au_3]^+$ species present from the AuNP.

From the MS images, RuPhenSS•PEG•AuNP shows little presence of the gold nanoparticles on the tissue sample. This supports the confocal microscopy imaging by revealing low detection of the gold nanoparticles. Interestingly, it seems the particles of the RuPhenSS•PEG•AuNP localise on the surrounding edges of the tissue. This is most likely due to the particles being trapped in folds on the edge of the tissue rather than uptake and giving rise to detection. Cellular uptake of the RuPhenSS•PEG•AuNP is not to be expected due to the tissue being fixed. Both heat maps of the $[Au_2]^+$ and $[Au_3]^+$ species display identical images with low intensity of the gold nanoparticles suggesting low cellular uptake.

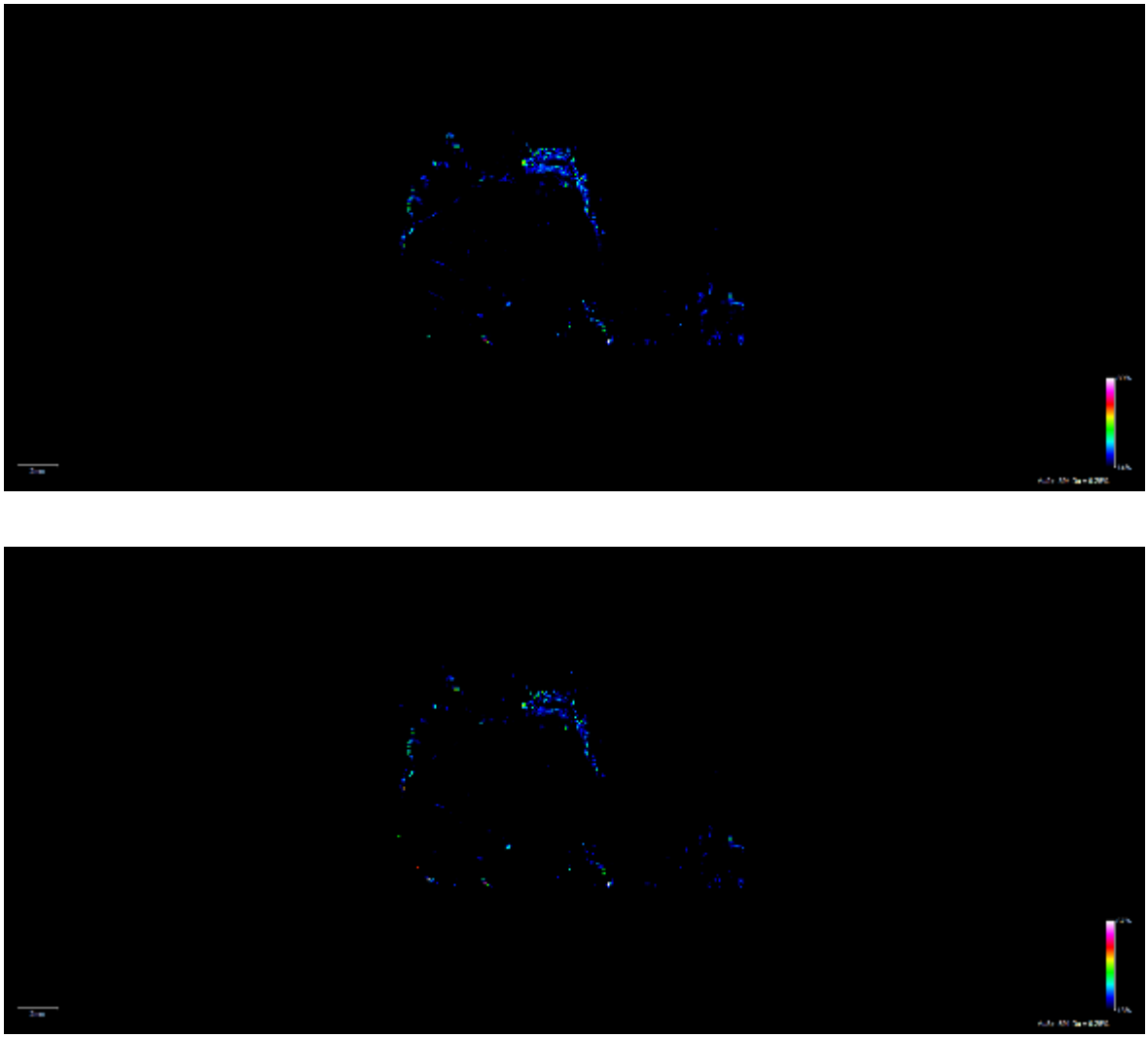

Figure 5.3.4.5. Relative ion intensity heat maps using $[Au_2]^+$ (top) and $[Au_3]^+$ (bottom) for the detection of RuPhenSS•PEG•AuNP in tonsil tissue. Scale bar = 2 mm.

Heat maps of the $[Au_2]^+$ and $[Au_3]^+$ species for RuPhenSS•RXB•AuNP display significantly higher intensity in detection. Interestingly, the particles of RuPhenSS•RXB•AuNP show significant increase in the central part of the tissue. Tonsil tissue contains germinal centres which are rich in B-cells. Since Rituximab binds to CD20 positive expressing B-cells, the high intensity of gold nanoparticle detection via the $[Au_2]^+$ and $[Au_3]^+$ species could suggest specific targeting of the Rituximab functionalised gold nanoparticles. Interestingly, the nanoparticles also display detection of the surrounding edges of the tissue as is the case for

RuPhenSS•PEG•AuNP. As mentioned earlier, this could be due to the particles being trapped in folds of the tissue which is the most likely cause or it could be due to an abundance of B-cells on the edge of the tissue.

In comparison of RuPhenSS•PEG•AuNP to RuPhenSS•RXB•AuNP, there is significantly higher increase in detection via the gold species. This significant increase in detection could be attributed to the presence of the Rituximab on the gold nanoparticle surface. This suggests the efficacy of detection through a modified Rituximab functionalised gold nanoparticles for the detection and imaging of B-cell lymphomas.

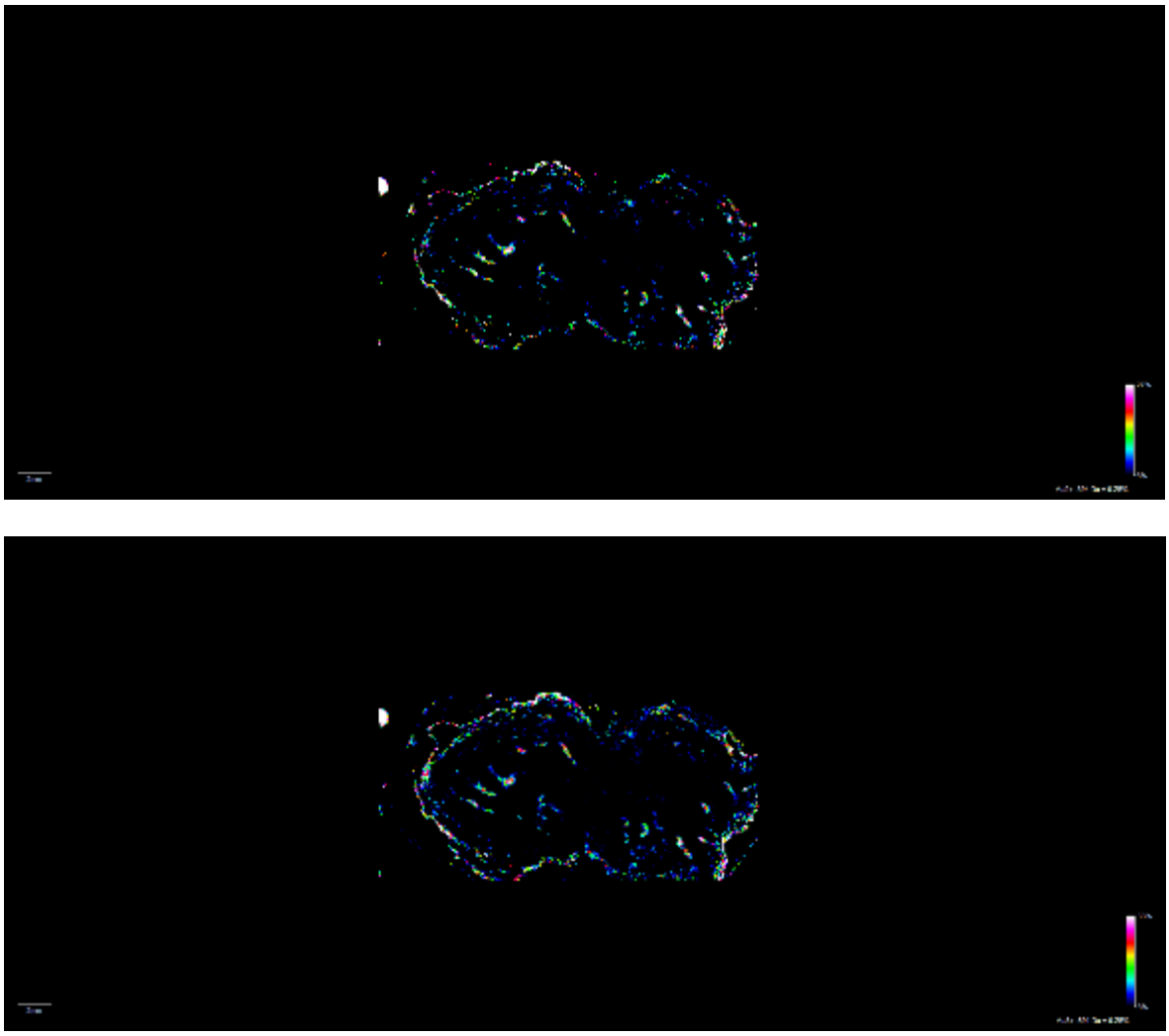

Figure 5.3.4.6. Relative ion intensity heat maps using $[Au_2]^+$ (top) and $[Au_3]^+$ (bottom) for the detection of RuPhenSS•RXB•AuNP in tonsil tissue. Scale bar = 2 mm.

Confocal luminescence microscopy of RuPhenSS•PEG•AuNP in comparison with the mass spectrometry image displays minimal luminescence and gold detection respectively. The MS image agrees with the confocal luminescence that non-selective targeting occurs and as a result, the most likely cause for detection is due to particles being trapped in craters and folds in the tissue perimeter. However, confocal microscopy of RuPhenSS•RXB•AuNP shows increased luminescence and gold detection via MS. This increase in luminescence and detection is attributed to the presence of the directionally conjugated Rituximab on the gold nanoparticle surface. This functionalised antibody gold nanoparticle displays dual detection in being able to track tumours *in vivo* via optical microscopy and successfully image and detect lymphomas via MSI.

5.4 Conclusion

In this chapter we present red luminescent gold nanoparticles functionalised with a chimeric monoclonal antibody (Rituximab) via direct conjugation strategies to afford optimal targeting in B-cell lines for confocal and mass spectrometry imaging applications. Gold nanoparticles were synthesised and characterised by UV-Vis, DLS and TEM techniques and partially coated with PEG and Rituximab before additions of RuPhenSS. RuPhenSS was selected to be the lumophore presented in this work due to the findings in Chapter 3. Rituximab and ruthenium functionalised gold nanoparticles displayed higher luminescence intensity in flow cytometry, confocal microscopy and mass spectrometry imaging over ruthenium functionalised gold nanoparticles. This displays the appropriateness of using targeted approaches for imaging capabilities.

5.5 Experimental

5.5.1 Materials

All reagents for AuNP synthesis and characterisation was purchased from Alfa-Aesar. Honeywell and Sigma-Aldrich. Rituximab (monoclonal antibody to CD20, 10 mg mL^{-1} in PBS, assumed MW = 150 kDa) was provided by Margaret Goodall (Institute of Immunology and Immunotherapy) and Tonsil tissue (S296244) was provided by Dr Tracey Perry (Institute of Cancer and Genomic Sciences) and sectioned by Miss Ciara Leahy (Institute of Cancer and Genomic Sciences). Reagents for modification of Rituximab was purchased from Fisher Scientific, Sigma-Aldrich and Sensopath Technologies. Conjugate Check&Go assay was purchased from Expedeon and Hydromount mounting medium was purchased from National Diagnostics.

5.5.2 Modification of Rituximab

Rituximab (monoclonal antibody to CD20, 10 mg mL^{-1} in PBS) was provided by Margaret Goodall (Institute of Immunology and Immunotherapy) was diluted to 1 mg mL^{-1} in PBS and buffer exchanged with 100 mM Na_2HPO_4, pH 7.5 using 10k MWCO centrifuge concentrators. To 100 µL of 1 mg mL^{-1} Rituximab, 10 µL of 100 mM $NaIO_4$ was added and the solution incubated in the dark at RT for 30 minutes. PBS (500 µL, 0.1 mM) was added to quench the reaction. Verification of the oxidation of the antibody was performed using the Purpald test. Fresh Purpald solution (60 µL, 10 mg mL^{-1} in 1 M NaOH, PBS, 0.01 M) was mixed with the antibody solution (20 µL) in a sealed glass vial and left at RT for 2 minutes. The resulting solution turned from colourless to purple indicating the presence of aldehydes and successful oxidation. PEG linker solution (2 µL, 46.5 mM) was added to the original antibody solution

and incubated in the dark for 1 hour at RT. Purification by centrifugation (x3) was performed in 10k MWCO, 0.5 mL filter tubes and resuspended in PBS (500 µL, 0.01 M). Concentration and presence of Rituximab was checked by UV-Vis spectrometry and Nanodrop. The solution was stored at 4°C in the dark.

5.5.3 Metal complex synthesis

The synthesis of RuPhenSS was described in Chapter 3.

5.5.4 Synthesis of AuNPs

AuNP

Citrate stabilised AuNP were synthesised as according to Kumar *et al*.[61] All glassware used was cleaned in freshly prepared aqua regia (3:1 v/v HCl/HNO_3), rinsed thoroughly with dH_2O and dried at 120°C overnight. A 100 mL solution of $HAuCl_4$ (12.7 mM) in Milli-Q H_2O was brought to reflux at stirred vigorously at 150°C. Trisodium citrate (1.88 mL, 38.8 mM) was added to this preheated solution rapidly. Heating via reflux was continued for 5 minutes during which time a colour change from pale yellow to blue and then red was observed. The reaction vessel was wrapped with foil and allowed to cool to RT. The AuNP was sealed and stored in darkness at RT in the vessel. UV-Vis (H2O) λ_{SPR} [nm] = 518. Number diameter = 16 ± 4 nm, PDI = 0.06 (DLS number distribution). Zeta potential = -37 ± 7 mV. UV-Vis, DLS sizing and zeta potential measurements were recorded with AuNP in 1 mL Milli-Q H_2O at 3.2 nM. Diameter = 16 nm (Transmission Electron Microscopy). Molar concentration = 3.2 nM.

PEG•AuNP

3 nM AuNP (2 mL) was centrifuged at 13000 g for 30 mins, the supernatant was decanted and the pellet was re-suspended in filtered Milli-Q water (1 mL) to form 6 nM AuNP. PEG-SH (1 mM, 4 µL) was added to 6 nM AuNP (1 mL), stirred for 20 mins and centrifuged at 13000 g for 25 mins. The supernatant was discarded and the pellet was re-suspended in filtered Milli-Q water (1 mL) to form 6 nM PEG•AuNP. UV-Vis (H_2O) λ_{SPR} [nm] = 519. Number diameter = 26 ± 6 nm, PDI = 0.13 (DLS number distribution). Zeta potential = -22 ± 10 mV. UV-Vis, DLS sizing and zeta potential measurements were recorded with AuNP in 1 mL Milli-Q H_2O at 3.2 nM. Diameter = 15 nm (Transmission Electron Microscopy).

PEG•RXB•AuNP

Modified Rituximab (2.1 µM, 20 µL) was added to 6 nM AuNP (1 mL) in 2 µL aliquots and stirred for 2 min between each addition. The solution was centrifuged at 10000 g for 5 mins using 10 MWCO filter tubes, the supernatant was discarded and the pellet was re-suspended in filtered Milli-Q water (1 mL) to form 6 nM PEG•RXB•AuNP. UV-Vis (H_2O) λ_{SPR} [nm] = 522. Number diameter = 27 ± 7 nm, PDI = 0.16 (DLS number distribution). Zeta potential = -41 ± 7 mV. UV-Vis, DLS sizing and zeta potential measurements were recorded with AuNP in 1 mL Milli-Q H_2O at 3.2 nM.

RuPhen•PEG•AuNP

RuPhenSS (1 mM, 8 µL) was added to to 6 nM PEG•AuNP (1 mL) in 2 µL aliquots and stirred for 2 min between each addition. The solution was centrifuged at 10000 g for 5 mins using 10 MWCO filter tubes, the supernatant was discarded and the pellet was re-

suspended in filtered Milli-Q water (1 mL) to form 6 nM RuPhen•PEG•AuNP. UV-Vis (H_2O) λ_{SPR} [nm] = 523. Number diameter = 26 ± 7 nm, PDI = 0.19 (DLS number distribution). Zeta potential = -35 ± 8 mV. UV-Vis, DLS sizing and zeta potential measurements were recorded with AuNP in 1 mL Milli-Q H_2O at 3.2 nM. Diameter = 13 nm (Transmission Electron Microscopy).

RuPhen•RXB•AuNP

RuPhenSS (1 mM, 8 µL) was added to to 6 nM PEG•RXB•AuNP (1 mL) in 2 µL aliquots and stirred for 2 min between each addition. The solution was centrifuged at 10000 g for 5 mins using 10 MWCO filter tubes, the supernatant was discarded and the pellet was re-suspended in filtered Milli-Q water (1 mL) to form 6 nM RuPhen•RXB•AuNP. UV-Vis (H_2O) λ_{SPR} [nm] = 525. Number diameter = 28 ± 8 nm, PDI = 0.20 (DLS number distribution). Zeta potential = -41 ± 9 mV. UV-Vis, DLS sizing and zeta potential measurements were recorded with AuNP in 1 mL Milli-Q H_2O at 3.2 nM. Diameter = 15 nm (Transmission Electron Microscopy).

5.5.5 Transmission electron microscopy

TEM imaging was carried out on citrate capped AuNP, PEG•AuNP, RuPhen•PEG•AuNP and RuPhen•RXB•AuNP from 3 nM stock solutions. For all nanoparticle samples, a 1 in 3 dilution was performed in Milli-Q H_2O yielding ~ 1 nM and 20 µL aliquot was dropped on to a 200 mesh formvar coated TEM grid and left to dry in the dark over night. Imaging took place on a JEOL1400 transmission electron microscope by Theresa Morris and Ludwig Schneider (Materials and Metallurgy, University of Birmingham).

5.5.6 Check&Go strip test

The running buffer (10 x, 100 µL) was diluted with 900 µL DI H_2O and a blocking agent consisting of 1 % BSA, (10 mg, final concentration = 1 %) to obtain the 1 x running buffer + BSA. The positive control containing a lyophilised antibody gold conjugate was suspended in 800 µL of 1x running buffer + BSA. The nanoparticle samples tested (3 nM) was diluted 1:1 with 1 x running buffer + BSA to yield 1.5 nM. The positive control and all nanoparticle samples were ran in duplicate with 40 µL loading per well on a 96 well plate. One strip per well was inserted and ran for 10 minutes. Confirmation of successful antibody presence and conjugation was observed through visual confirmation of a red line on the test strip.

5.5.7 Cell culture

The Jurkat, Raji and Karpas 422 cell lines was maintained in RPMI media supplemented with 10 % fetal bovine serum (FBS), hereafter called complete media. Cells were cultured in 20 mL complete media in vented T75 flasks and kept at 37°C in a humidified 5% CO_2 atmosphere.

5.5.8 Cell viability assay

The cells was cultured in solid bottom luminescence white 96-well assay plate, 1 x 10^5 cells per well and the sample was added in a 1:10 (sample:complete media) dilution and incubated at 37 °C in a humidified 5 % CO_2 atmosphere for 18 hours. The survival of the cells from varying concentrations of RuPhen•PEG•AuNP and RuPhen•RXB•AuNP was determined using Cell-Titre Glo. After incubation, the cells were allowed to cool to RT to avoid rapid degradation of Cell-Titre Glo. Once at RT, 25 µL Cell-Titre Glo was added and then the cells luminescence was recorded on an EnVision 2105 Multimode plate reader.

5.5.9 Flow cytometry

The cells were cultured in 60 mm dishes, 1 x 10^5 per dish and the samples added in a ratio of 1:1 (sample:complete media). Uptake of the particles was evaluated after dosing of the cells with 1.5 nM RuPhen•PEG•AuNP and 1.5 nM RuPhen•RXB•AuNP for 18 hours. After the incubation time, the cells were collected into 15 mL falcon tubes and centrifuged at 1000 rpm for 5 minutes. The supernatant was discarded and the cells were washed twice with sterile PBS. The pelleted cells were then re-suspended in sterile PBS supplemented with 1 % FBS and transferred into FACS tubes for analysis. The samples were ran on an LSR- II flow cytometer in the Institute of Cancer and Genomic Sciences using the FACSDiva software. Analysis was performed on FlowJo by Dr Tracey Perry (Institute of Cancer and Genomic Sciences).

5.5.10 Cytospins

Cytospins of fixed OCI-LY3 cells in formalin-fixed paraffin embedded (FFPE) on glass slides were provided by Dr Tracey Perry. The slides were immersed in xylene for 10 minutes, rehydrated in 100 % IMS for 10 minutes and then rinsed under tap water for 5 minutes. Citrate buffer pH 6 was made using 1.26 g sodium citrate, 0.25 g citric acid in 800 mL DI H_2O and adjusted to pH 6 using 2 M NaOH. It was then brought up to make 1 L. The slides were immersed in the buffer and covered partially with cling film and boiled on high for 10 minutes and medium for 10 minutes in a 1000W microwave. The slides were allowed to cool to RT in the buffer and washed with tap water for a further 5 minutes. A hydrophobic barrier was drawn around the tissue sample using a hydrophobic pen and washed with PBS-T. The tissue was then blocked using 5x Casein for 10 minutes and washed. 3 nM RuPhenSS•PEG•AuNP and 3 nM RuPhenSS•RXB•AuNP was then added onto the tissue allowing full coverage and stored in the dark in the fridge (4 ºC) for 18 hours. The samples were then washed with PBS-T and DAPI

(100 µL, 300 nM) was added and incubated in the dark for 10 minutes. The tonsil tissue was washed twice with PBS-T and then the slides covered using cover slips. Cover slips were mounted using a droplet of Hydromount media (National Diagnostics, UK) on the glass slides and stored flat in the dark for at least 24 hours at 4 ºC before imaging was conducted.

5.5.11 Tonsil staining

Sectioning of the tonsil tissue block (S296244) was carried out by Ciara Leahy (Institute of Cancer and Genomic Sciences) using a rotary microtome machine. Sections of 5 µm tissue was performed and dried on glass and ITO slides and baked for 3 hours. The slides was immersed in xylene for 10 minutes, rehydrated in 100 % IMS for 10 minutes and then rinsed under tap water for 5 minutes. Citrate buffer pH 6 was made using 1.26 g sodium citrate, 0.25 g citric acid in 800 mL DI H_2O and adjusted to pH 6 using 2 M NaOH. It was then brought up to make 1 L. The slides were immersed in the buffer and covered partially with cling film and boiled on high for 10 minutes and medium for 10 minutes in a 1000W microwave. The slides were allowed to cool to RT in the buffer and washed with tap water for a further 5 minutes. A hydrophobic barrier was drawn around the tissue sample using a hydrophobic pen and washed with PBS-T. The tissue was then blocked using 5 x Casein for 10 minutes and washed. 3 nM RuPhen•PEG•AuNP and 3 nM RuPhen•RXB•AuNP was then added onto the tissue allowing full coverage and stored in the dark in the fridge (4 ºC) for 18 hours. The samples were then washed with PBS-T and DAPI (100 µL, 300 nM) was added and incubated in the dark for 10 minutes. The tonsil tissue was washed twice with PBS-T and then the slides covered using cover slips. Cover slips were mounted using a droplet of Hydromount media (National Diagnostics, UK) on the glass slides and stored flat in the dark for at least 24 hours at 4 ºC before imaging was conducted.

5.5.12 Confocal microscopy

Preparation of tonsil tissue is described in section 5.5.11. The tonsil tissue slides were imaged via confocal microscopy using a Leica TCS SP8 upright confocal laser scanning system using a 64x oil immersion objective lens. The solid state laser lines used was 405 nm, 458 nm and 633 nm.

5.5.13 Mass Spectrometry Imaging

Tonsil tissue preparation is identical to that described in section 5.5.10 up to the point of incubation of the samples. Tissue sections on ITO slides were incubated with 3 nM RuPhen•PEG•AuNP and 3 nM RuPhen•RXB•AuNP in the presence of ammonium citrate (0.5 mM) for 18 hours in the dark in the fridge (4 ºC). Samples were then washed twice with PBS-T and baked at 60 ºC for an hour. Teach points were marked on the slide and a picture taken. The slides were inserted into an MTP-Slide adapter-II plate and MSI recorded on a bruker UltraFlexteme MALDI. A JPEG image of the slides were uploaded into FlexImaging 3.0 and the teach points marked. A raster box was drawn between the teach points over the entire tonsil tissue and an automated run using FC-randomwalk in reflectron mode at 53 % laser power, 500 shots at 100 Hz between 100 to 2000 Da. Analysis was performed using FlexImaging 3.0.

5.6 References

1. D. N. Khalil, E. L. Smith, R. J. Brentjens and J. D. Wolchok, *Nat. Rev. Clin. Oncol.*, 2016, **13**, 273-290.

2. L. Milling, Y. Zhang and D. J. Irvine, *Adv. Drug Deliv. Rev.*, 2017, **114**, 79-101.

3. T. M. Pierpont, C. B. Limper and K. L. Richards, *Frontiers Oncol.*, 2018, **8**.

4. M. Arruebo, M. Valladares and Á. González-Fernández, *J. Nanomater.*, 2009, **2009**, 439389.

5. J. K. Liu, *Ann. Med. Surg.*, 2014, **3**, 113-116.

6. J. Golay, L. Zaffaroni, T. Vaccari, M. Lazzari, G.-M. Borleri, S. Bernasconi, F. Tedesco, A. Rambaldi and M. Introna, *Blood*, 2000, **95**, 3900-3908.

7. J. L. Teeling, R. R. French, M. S. Cragg, J. van den Brakel, M. Pluyter, H. Huang, C. Chan, P. W. H. I. Parren, C. E. Hack, M. Dechant, T. Valerius, J. G. J. van de Winkel and M. J. Glennie, *Blood*, 2004, **104**, 1793-1800.

8. O. Shpilberg and C. Jackisch, *Br J Cancer*, 2013, **109**, 1556-1561.

9. C. R. Patra, R. Bhattacharya, D. Mukhopadhyay and P. Mukherjee, *Adv. Drug Deliv. reviews*, 2010, **62**, 346-361.

10. L. Mocan, C. T. Matea, D. Bartos, O. Mosteanu, T. Pop, T. Mocan and C. Iancu, *Clujul Med.*, 2016, **89**, 199-202.

11. M. Srinivasarao and P. S. Low, *Chem. Rev.*, 2017, **117**, 12133-12164.

12. M. Srinivasarao, C. V. Galliford and P. S. Low, *Nat. Rev. Drug Disc.*, 2015, **14**, 203-219.

13. T. M. Allen, *Nat. Rev. Cancer*, 2002, **2**, 750-763.

14. G. Farahavar, S. S. Abolmaali, N. Gholijani and F. Nejatollahi, *Biomater. Sci.* 2019, **7**, 4000-4016.

15. E. S. Day, L. R. Bickford, J. H. Slater, N. S. Riggall, R. A. Drezek and J. L. West, *Int. J. Nanomed.*, 2010, **5**, 445-454.

16. X. Huang, I. H. El-Sayed, W. Qian and M. A. El-Sayed, *J. Am. Chem. Soc.*, 2006, **128**, 2115-2120.

17. S. Her, D. A. Jaffray and C. Allen, *Adv. Drug Deliv. Rev.*, 2017, **109**, 84-101.

18. R. Kotcherlakota, D. J. Srinivasan, S. Mukherjee, M. M. Haroon, G. H. Dar, U. Venkatraman, C. R. Patra and V. Gopal, *J. Mater. Chem. B*, 2017, **5**, 7082-7098.

19. A. R. Fernandes, J. Jesus, P. Martins, S. Figueiredo, D. Rosa, L. M. R. D. R. S. Martins, M. L. Corvo, M. C. Carvalheiro, P. M. Costa and P. V. Baptista, *J. Controlled Release*, 2017, **245**, 52-61.

20. M. J. Mathers, S. Roth, M. Klinkhammer-Schalke, M. Gerken, F. Hofstaedter, S. Wilm and T. Klotz, *J Cancer*, 2011, **2**, 76-80.

21. M.-C. Daniel and D. Astruc, *Chem. Rev.*, 2004, **104**, 293-346.

22. D. A. Giljohann, D. S. Seferos, W. L. Daniel, M. D. Massich, P. C. Patel and C. A. Mirkin, *Angew. Chem. Int. Ed. Engl.*, 2010, **49**, 3280-3294.

23. F. Wang, J. Pang, L. Huang, R. Wang, Q. Jiang, L. Zhang and K. Sun, *Nano Res.*, 2018, **11**, 3886-3898.

24. C. Yang, K. K. Chan, W.-J. Lin, A. M. Soehartono, G. Lin, H. Toh, H. S. Yoon, C.-K. Chen and K.-T. Yong, *Nano Res.*, 2017, **10**, 3049-3067.

25. C. J. Murphy, A. M. Gole, J. W. Stone, P. N. Sisco, A. M. Alkilany, E. C. Goldsmith and S. C. Baxter, *Acc. Chem. Res.*, 2008, **41**, 1721.

26. N. J. Rogers, S. Claire, R. M. Harris, S. Farabi, G. Zikeli, I. B. Styles, N. J. Hodges and Z. Pikramenou, *Chem. Commun.*, 2014, **50**, 617-619.

27. J. Turkevich, P. C. Stevenson and J. Hillier, *Discuss. Faraday Soc.*, 1951, **11**, 55.

28. J. Lee, D. K. Chatterjee, M. H. Lee and S. Krishnan, *Cancer Lett.*, 2014, **347**, 46-53.

29. G. Zhang, Z. Yang, W. Lu, R. Zhang, Q. Huang, M. Tian, L. Li, D. Liang and C. Li, *Biomater.*, 2009, **30**, 1928-1936.

30. Y. Wang, J. E. Q. Quinsaat, T. Ono, M. Maeki, M. Tokeshi, T. Isono, K. Tajima, T. Satoh, S.-i. Sato, Y. Miura and T. Yamamoto, *Nat. Commun.*, 2020, **11**, 6089.

31. E. Boisselier and D. Astruc, *Chem. Soc. Rev.*, 2009, **38**, 1759-1782.

32. J. Manson, D. Kumar, B. J. Meenan and D. Dixon, *Gold Bull.*, 2011, **44**, 99-105.

33. W.-S. Cho, M. Cho, J. Jeong, M. Choi, H.-Y. Cho, B. S. Han, S. H. Kim, H. O. Kim, Y. T. Lim, B. H. Chung and J. Jeong, *Toxicol. Appl. Pharmacol.*, 2009, **236**, 16-24.

34. S. De Koker, L. J. De Cock, P. Rivera-Gil, W. J. Parak, R. Auzély Velty, C. Vervaet, J. P. Remon, J. Grooten and B. G. De Geest, *Adv. Drug Deliv. Rev.*, 2011, **63**, 748-761.

35. S. F. M. van Dongen, H.-P. M. de Hoog, R. J. R. W. Peters, M. Nallani, R. J. M. Nolte and J. C. M. van Hest, *Chem. Rev.*, 2009, **109**, 6212-6274.

36. A. K. Pearce and R. K. O'Reilly, *Bioconjug. Chem.*, 2019, **30**, 2300-2311.

37. P. Schmid, S. Adams, H. S. Rugo, A. Schneeweiss, C. H. Barrios, H. Iwata, V. Diéras, R. Hegg, S.-A. Im, G. Shaw Wright, V. Henschel, L. Molinero, S. Y. Chui, R. Funke, A. Husain, E. P. Winer, S. Loi and L. A. Emens, *NEJM*, 2018, **379**, 2108-2121.

38. S. Wilhelm, A. J. Tavares, Q. Dai, S. Ohta, J. Audet, H. F. Dvorak and W. C. W. Chan, *Nat. Rev. Mater.*, 2016, **1**, 16014.

39. M. Liu, Q. Li, L. Liang, J. Li, K. Wang, J. Li, M. Lv, N. Chen, H. Song, J. Lee, J. Shi, L. Wang, R. Lal and C. Fan, *Nat. Commun.*, 2017, **8**, 15646.

40. P. Holliger and P. J. Hudson, *Nat. Biotechnol.*, 2005, **23**, 1126-1136.

41. K. Yong, D. Yuen, M. Z. Chen and A. P. R. Johnston, *ACS Appl. Mater. Inter.*, 2020.

42. C. R. Patra, R. Bhattacharya, E. Wang, A. Katarya, J. S. Lau, S. Dutta, M. Muders, S. Wang, S. A. Buhrow, S. L. Safgren, M. J. Yaszemski, J. M. Reid, M. M. Ames, P. Mukherjee and D. Mukhopadhyay, *Cancer Res.*, 2008, **68**, 1970-1978.

43. K. Sokolov, M. Follen, J. Aaron, I. Pavlova, A. Malpica, R. Lotan and R. Richards-Kortum, *Cancer Res*, 2003, **63**, 1999-2004.

44. I. H. El-Sayed, X. Huang and M. A. El-Sayed, *Nano Lett.*, 2005, **5**, 829-834.

45. C. Loo, L. Hirsch, M. H. Lee, E. Chang, J. West, N. Halas and R. Drezek, *Opt. Lett.*, 2005, **30**, 1012-1014.

46. S. Pathak, M. C. Davidson and G. A. Silva, *Nano Lett.*, 2007, **7**, 1839-1845.

47. W. Eck, G. Craig, A. Sigdel, G. Ritter, L. J. Old, L. Tang, M. F. Brennan, P. J. Allen and M. D. Mason, *ACS Nano*, 2008, **2**, 2263-2272.

48. E. Hondroulis, R. Zhang, C. Zhang, C. Chen, K. Ino, T. Matsue and C.-Z. Li, *Theranostics*, 2014, **4**, 919-930.

49. Y. Zhang, L. Cong, J. He, Y. Wang, Y. Zou, Z. Yang, Y. Hu, S. Zhang and X. He, *Acta Biochim. Biophys. Sin.*, 2018, **50**, 567-578.

50. J. L. Norris and R. M. Caprioli, *Chem. Rev.*, 2013, **113**, 2309-2342.

51. E. M. Weaver and A. B. Hummon, *Adv. Drug Deliv. Rev.*, 2013, **65**, 1039-1055.

52. R.-C. Huang, W.-J. Chiu, I. Po-Jung Lai and C.-C. Huang, *Sci. Rep.*, 2015, **5**, 10292.

53. Y.-T. Tseng, S. G. Harroun, C.-W. Wu, J.-Y. Mao, H.-T. Chang and C.-C. Huang, *Nanotheranostics*, 2017, **1**, 141-153.

54. M. R. Smith, *Oncogene*, 2003, **22**, 7359-7368.

55. V. C. Tsang, R. M. Greene and J. B. Pilcher, *J. Immunoassay*, 1995, **16**, 395-418.

56. P. A. S. Smith, *J. Am. Chem. Soc.*, 1948, **70**, 320-323.

57. F. Johari Doha, S. Rahmani, P. Rikhtechi, S. Rasaneh, Z. Sheikholislam and S. Shahhosseini, *Iran J Pharm Res*, 2017, **16**, 619-629.

58. K. H. Lee, J. Lee, J. S. Bae, Y. J. Kim, H. A. Kang, S. H. Kim, S. J. Lee, K. J. Lim, J. W. Lee, S. K. Jung and S. J. Chang, *MAbs*, 2018, **10**, 380-396.

59. M. Abdollahpour-Alitappeh, S. M. Hashemi Karouei, M. Lotfinia, A. Amanzadeh and M. Habibi-Anbouhi, *Artif. Cells, Nanomed. Biotechnol.*, 2018, **46**, 1-8.

60. M. E. Pedersen, J. Østergaard and H. Jensen, *ACS Omega*, 2020, **5**, 10519-10524.

61. S. Kumar, J. Aaron and K. Sokolov, *Nat. Protocols*, 2008, **3**, 314-320.

62. S. A. M. Osborne and Z. Pikramenou, *Faraday Discuss.*, 2015, **185**, 219-231.

63. S. Osborne, *PhD, University of Birmingham*, 2017.

64. W. Haiss, N. T. K. Thanh, J. Aveyard and D. G. Fernig, *Anal. Chem.*, 2007, **79**, 4215-4221.

65. A. Davies, D. J. Lewis, S. P. Watson, S. G. Thomas and Z. Pikramenou, *PNAS*, 2012, **109**, 1862.

66. S. Farabi, *University of Birmingham*, 2012.

67. A. N. Dosumu, S. Claire, L. S. Watson, P. M. Girio, S. A. M. Osborne, Z. Pikramenou and N. J. Hodges, *JACS Au*, 2021, **1**, 174-186.

68. N. J. Rogers, H. C. Jeffery, S. Claire, D. J. Lewis, G. Zikeli, N. J. Hodges, S. Egginton, G. B. Nash and Z. Pikramenou, *Nanomed.*, 2017, **12**, 2725-2740.

69. R. T. Busch, F. Karim, J. Weis, Y. Sun, C. Zhao and E. S. Vasquez, *ACS Omega*, 2019, **4**, 15269-15279.

70. M. P. Miranda-Hernández, C. A. López-Morales, N. D. Ramírez-Ibáñez, N. Piña-Lara, N. O. Pérez, A. Molina-Pérez, J. Revilla-Beltri, L. F. Flores-Ortiz and E. Medina-Rivero, *J. Immunol. Res.*, 2015, **2015**, 910763.

71. K. Rahme, L. Chen, R. G. Hobbs, M. A. Morris, C. O'Driscoll and J. D. Holmes, *RSC Adv.*, 2013, **3**, 6085-6094.

72. J. V. Jokerst, T. Lobovkina, R. N. Zare and S. S. Gambhir, *Nanomed.*, 2011, **6**, 715-728.

73. J. Zhang, L. Mou and X. Jiang, *Chem. Sci.*, 2020, **11**, 923-936.

74. J. Spadavecchia, D. Movia, C. Moore, C. M. Maguire, H. Moustaoui, S. Casale, Y. Volkov and A. Prina-Mello, *Int J Nanomed.*, 2016, **11**, 791-822.

75. S. J. Adams, D. J. Lewis, J. A. Preece and Z. Pikramenou, *ACS Appl. Mater. Inter.*, 2014, **6**, 11598-11608.

76. M. Reth, *Nat. Immunol.*, 2013, **14**, 765-767.

77. L. Rougé, N. Chiang, M. Steffek, C. Kugel, T. I. Croll, C. Tam, A. Estevez, C. P. Arthur, C. M. Koth, C. Ciferri, E. Kraft, J. Payandeh, G. Nakamura, J. T. Koerber and A. Rohou, *NY Sci. J.*, 2020, **367**, 1224-1230.

78. C. M. Goodman, C. D. McCusker, T. Yilmaz and V. M. Rotello, *Bioconjug. Chem.*, 2004, **15**, 897-900.

79. X.-D. Zhang, M.-L. Guo, H.-Y. Wu, Y.-M. Sun, Y.-Q. Ding, X. Feng and L.-A. Zhang, *Int. J. Nanomed.*, 2009, **4**, 165-173.

80. D. C. Marks, L. Belov, M. W. Davey, R. A. Davey and A. D. Kidman, *Leukemia Res.*, 1992, **16**, 1165-1173.

81. M. Ghasemi, T. Turnbull, S. Sebastian and I. Kempson, *Int. J. Mol. Sci.*, 2021, **22**, 12827.

82. G. J. Weiner, *Semin. Hematol.*, 2010, **47**, 115-123.

83. T. Cerny, B. Borisch, M. Introna, P. Johnson and A. L. Rose, *Anti-Cancer Drugs*, 2002, **13**.

84. S. M. King, S. Claire, R. I. Teixeira, A. N. Dosumu, A. J. Carrod, H. Dehghani, M. J. Hannon, A. D. Ward, R. Bicknell, S. W. Botchway, N. J. Hodges and Z. Pikramenou, *J. Am. Chem. Soc.*, 2018, **140**, 10242-10249.

85. H. C. J. N. J. Rogers, S. Claire, D. J. Lewis, G. Zikeli, N. J. Hodges, S. Egginton, G. B. Nash and Z. Pikramenou *Nanomed.*, 2017.

86. L. Zhang, Y. Mazouzi, M. Salmain, B. Liedberg and S. Boujday, *Biosens. Bioelectron.*, 2020, **165**, 112370.

87. D. R. Withers, C. Fiorini, R. T. Fischer, R. Ettinger, P. E. Lipsky and A. C. Grammer, *Blood*, 2007, **109**, 4856-4864.

88. J. Jia and W. Chen, *Radiat. Oncol.*, 2021, **16**, 193.

89. B. Coiffier, E. Lepage, J. Brière, R. Herbrecht, H. Tilly, R. Bouabdallah, P. Morel, E. Van Den Neste, G. Salles, P. Gaulard, F. Reyes, P. Lederlin and C. Gisselbrecht, *NE J. Med.*, 2002, **346**, 235-242.

90. D. O. Persky, J. M. Unger, C. M. Spier, B. Stea, M. LeBlanc, M. J. McCarty, L. M. Rimsza, R. I. Fisher and T. P. Miller, *J. Clin. Oncol.*, 2008, **26**, 2258-2263.

91. Y. H. Lee, S. G. Cho, S. E. Jung, S. H. Kim, J. H. O, G. S. Park, S. W. Yang, I. S. Lee, C. K. Rhee and B. O. Choi, *Radiat. Oncol. J.*, 2016, **34**, 273-279.

92. J. Sekuła, J. Nizioł, W. Rode and T. Ruman, *Anal. Chim. Acta*, 2015, **875**, 61-72.

93. K. Chughtai and R. M. A. Heeren, *Chem. Rev.*, 2010, **110**, 3237-3277.

94. D. Muko, T. Ikenaga, M. Kasai, J. B. Rabor, A. Nishitani and Y. Niidome, *J. Mass Spectrom.*, 2019, **54**, 1-6.

95. A. R. Buchberger, K. DeLaney, J. Johnson and L. Li, *Anal. Chem.*, 2018, **90**, 240-265.

96. S. Yang, L. Zhan, C. Liu, L. Fu, R. Chen and Z. Nie, *Microchem. J.*, 2019, **150**, 104190.

6.0 General conclusions and future Work

In this thesis the evaluation of three previously synthesised ruthenium(II) complexes that have had previous applications in dye sensitised solar cells was studied in aerated conditions and on gold nanoparticles for selection as live cell imaging agents and as mass spectrometry imaging probes. It has been well documented that phenanthroline ligands enhance the photophysical properties making them desirable for imaging applications. Additionally, a novel osmium(II) complex was synthesised, inspired by its previously studied bipyridine analogue, in the hopes to enhance the poor photophysical properties attributed to osmium complexes. The design of the novel osmium complex is presented displaying emission bridging the visible and the NIR region making it highly desirable for luminescence imaging applications. Additionally, to our knowledge, this is the first example of a luminescent osmium(II) complex attached on a gold nanoparticle for imaging. Rituximab was directly conjugated to the gold nanoparticles via a PEG linker intermediary to enhance selective targeting within cells. Binding was confirmed through flow cytometry and confocal microscopy using the luminescence signature of the ruthenium metal complex whilst combining gold ion heat maps from the gold nanoparticles in mass spectrometry imaging to generate a dual imaging nanosystem. The results generated in this thesis demonstrate the first use of a dual imaging nanosystem combining luminescence and mass spectrometry for imaging applications for selective targeting of cancer using the nanosystem described.

In the first study (Chapter 3) the photophysical evaluation of three ruthenium(II) metal complexes was performed in the absence and presence of a fluorosurfactant, Zonyl FSA, in aerated conditions. These complexes were explored for their potential as live cell and fixed cell imaging probes. It was determined that the presence of the phenanthroline ligands enhanced the photophysical properties in aerated conditions over that of its bipyridine counterpart and a

complex designed to reduce quenching. Other ruthenium complexes could be synthesised and employed such as a longer linker chain based on S8 to observe the photophysical properties given RuS8 displaying a higher QY (3 %) in aerated water over RuBpySS and RuPhenSS (2 %) respectively. Gold nanoparticles were synthesised and decorated with each of the aforementioned ruthenium(II) metal complexes to observe any enhancement or reduction in photophysical properties. It was determined, and in good agreement from previous studies, that RuPhenSS displayed the greatest potential as an imaging probe by having desirable photophysical properties. Additionally, utilising larger gold nanoparticles afforded brighter images through luminescence and scattering of the gold highlighting the properties desired for optical imaging. These particles could have future potential for targeting cellular components and through generation of ROS to induce programmed cell death.

In addition to the ruthenium(II) complexes, studies to improve the photophysical properties of osmium(II) complexes was conducted (Chapter 4). OsBpySS was previously studied on gold chips for its interaction with BSA however the luminescent signature eluded detection. It was suspected that signal could be obtained on a gold nanoparticle given the higher surface area presented and the novel complex, OsPhenSS, was designed to improve the already well known weak photophysical properties owing to osmium(II) complexes. To our surprise, OsPhenSS displayed strong detection in aerated water bridging the visible and NIR optical windows. Osmium complexes are more favoured for imaging applications due to the exceedingly far red emission, safer excitation wavelengths in comparison to ruthenium or iridium metal complexes and for generating singlet oxygen due to the heavy atom effect for anticancer applications. Despite weak detection presented on the gold nanoparticles, live cell imaging was conducted which displayed seemingly nuclear and subnuclear localisation. Singlet oxygen generation of this complex and on gold nanoparticles is currently being tested and would provide excellent

information for the potential of a luminescent and anticancer agent. To our knowledge, this is the first example of a luminescent osmium(II) complex on a gold nanoparticle to be employed for imaging applications. This example of a luminescent osmium(II) gold nanoparticle can pave the way into the exploration of further osmium(II) imaging agents and anticancer agents to specifically target cancer given osmium(II) complexes have received great interest as anticancer agents recently and possess good therapeutic effects. It would also be of benefit to further explore the nuclear localisation tendencies of OsPhenSS and generate a library to improve osmium's QY such as the incorporation of different linker units or incorporating alkylated phenanthroline ligands in the 5' position to shield from $^3O_2$ or by substitution of the phenanthroline for 4,7-diphenyl-1,10-phenanthroline.

In the final study (Chapter 5) we compile the findings from Chapter 3 to be utilised in this work. We modify a well-known current drug, rituximab, for the treatment of B-cell malignancies to be directly covalently attached onto our gold nanoparticle following a PEG linker. Partial coverage of PEG and rituximab was performed before saturating the surface with the luminescent metal complex, RuPhenSS. These particles displayed higher affinity towards B-cell malignancies in two cancer cell lines expressing the antigen of interest, CD20 through flow cytometry and demonstrated their use in confocal microscopy and mass spectrometry imaging on tonsil tissue. As mentioned earlier, osmium(II) complexes are more favoured for tissue and cell imaging due to their photophysical properties and can penetrate tissue deeper than ruthenium(II) complexes. It would therefore be interesting to see if the luminescent signature of osmium could be detected on the rituximab functionalised nanoparticles for specific delivery to B- cell malignancies and if so, whether the osmium could play a key role in generating cell death from ROS. Additionally, exploring various monoclonal glycosylated antibodies for more specific recognition and detection of other cancer cell lines would be advantageous.

7.0 Appendix

7.1 Synthesis characterisation: NMR and MS

7.1.1 BpySS ligand

BpySS.1

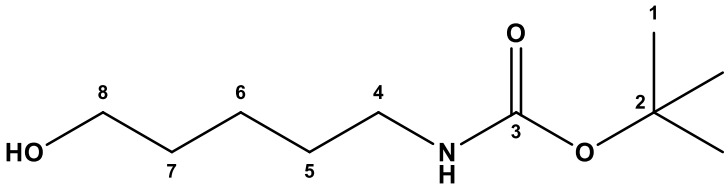

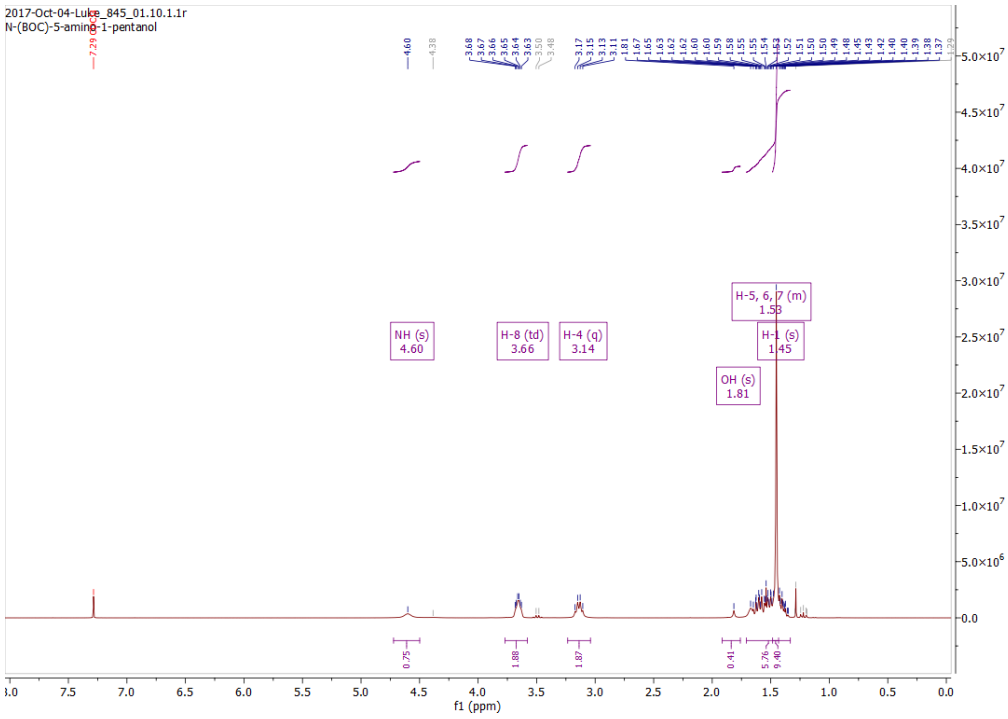

Figure 7.1.1.1. ^{1}H NMR of BpySS.1 in aerated $CDCl_3$. (δ- $CDCl_3$).

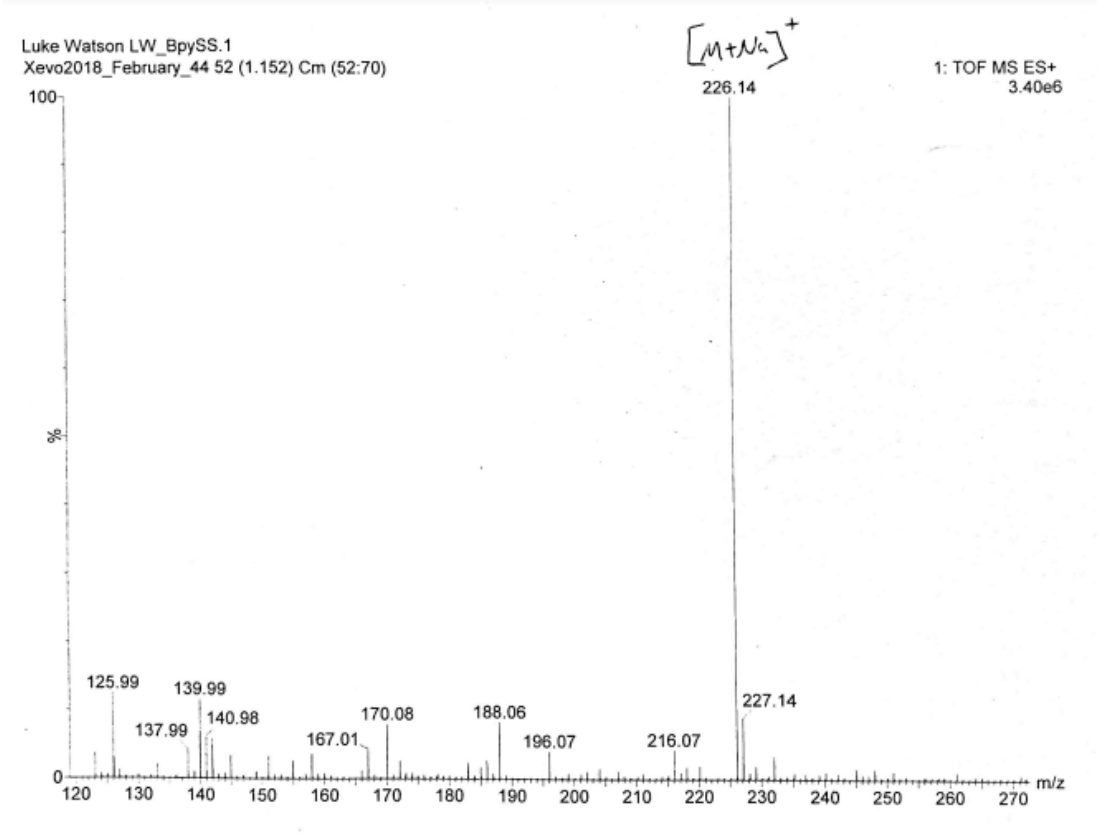

Figure 7.1.1.2. MS spectrum of BpySS.1.

BpySS.2

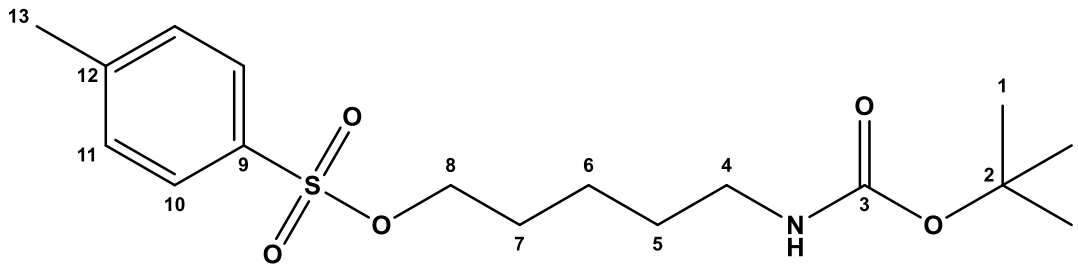

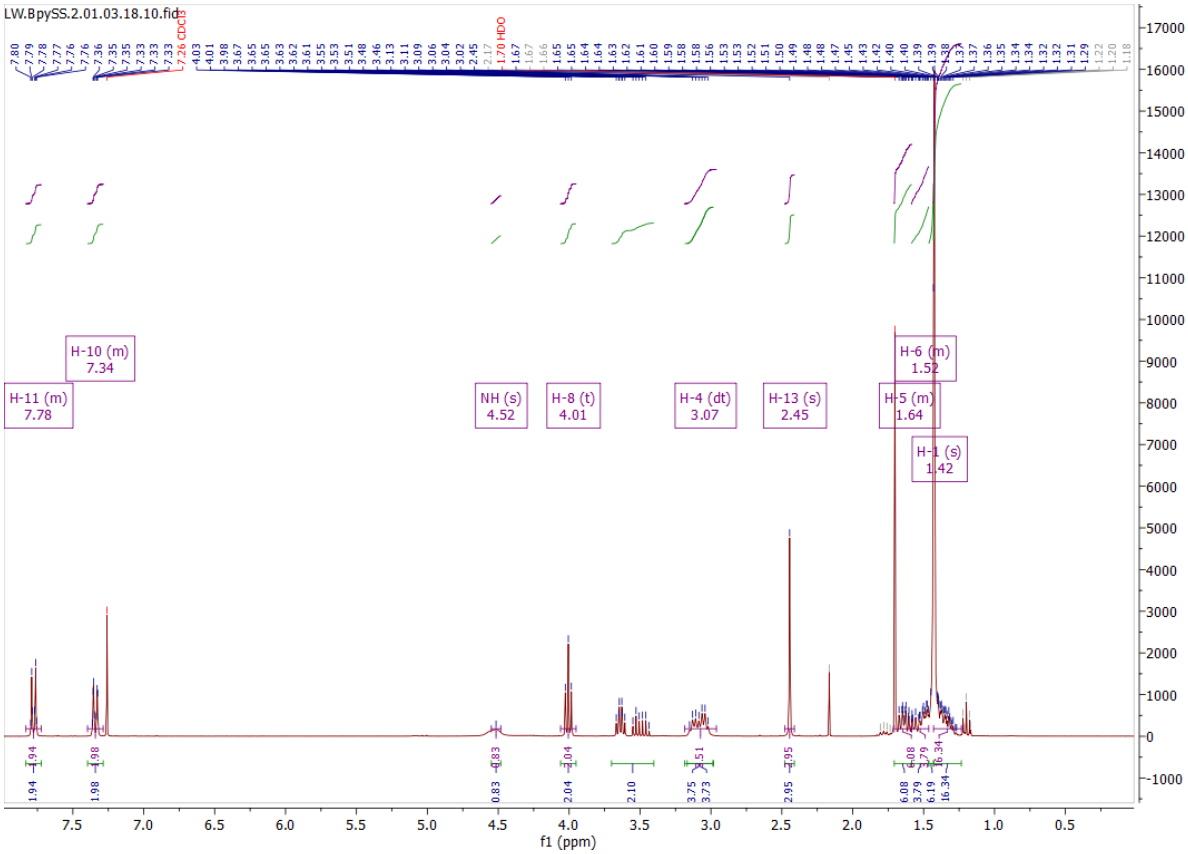

Figure 7.1.1.3. ^{1}H NMR of BpySS.2 in aerated $CDCl_3$. (δ- $CDCl_3$).

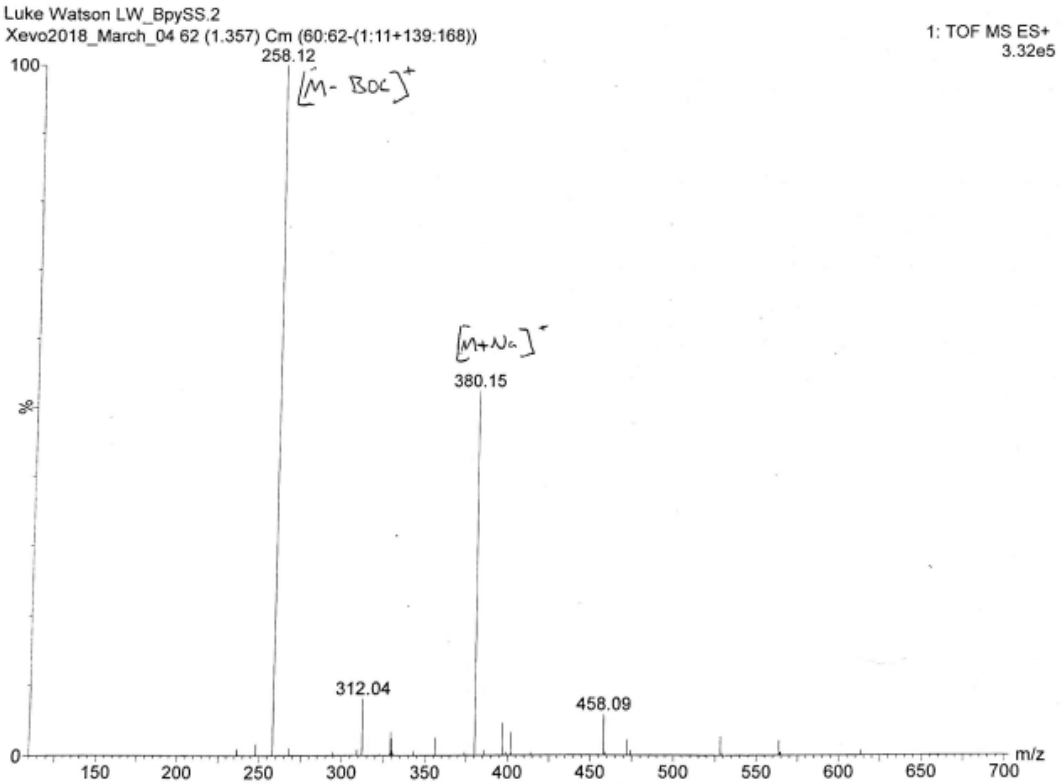

Figure 7.1.1.4. MS spectrum of BpySS.2.

BpySS.3

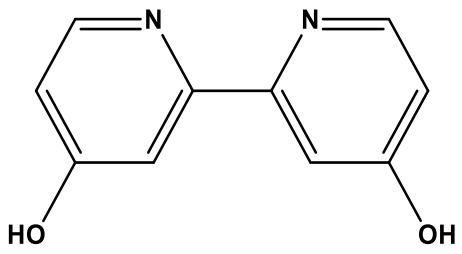

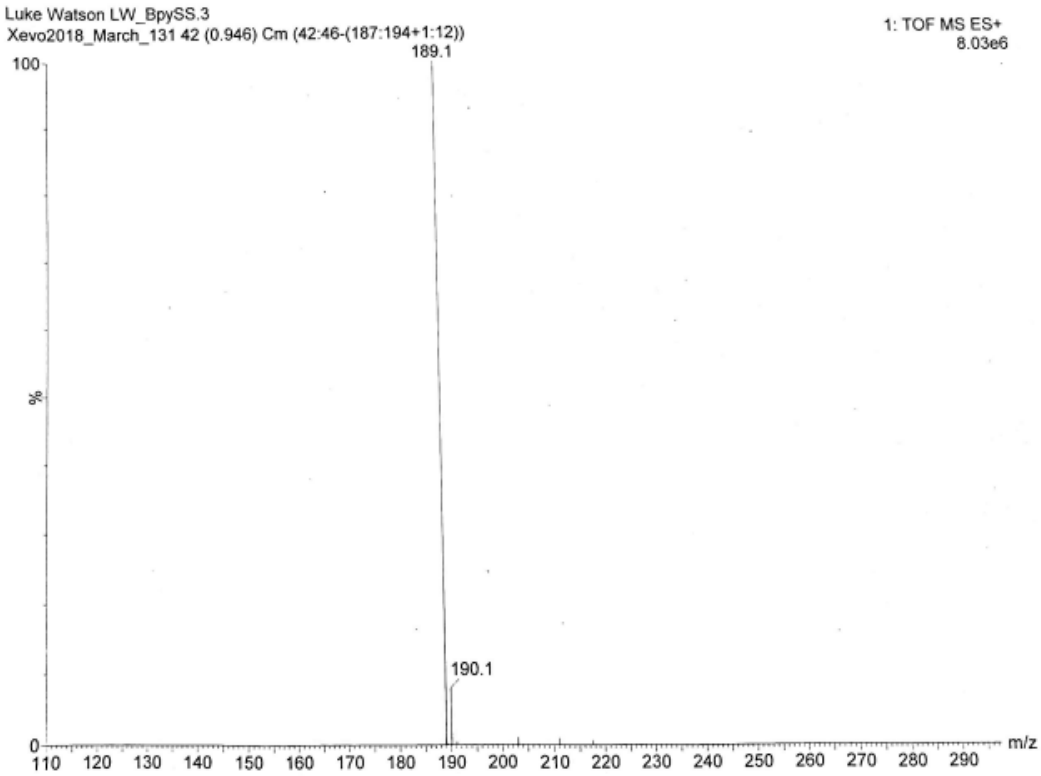

Figure 7.1.1.5. MS spectrum of BpySS.3.

BpySS.4

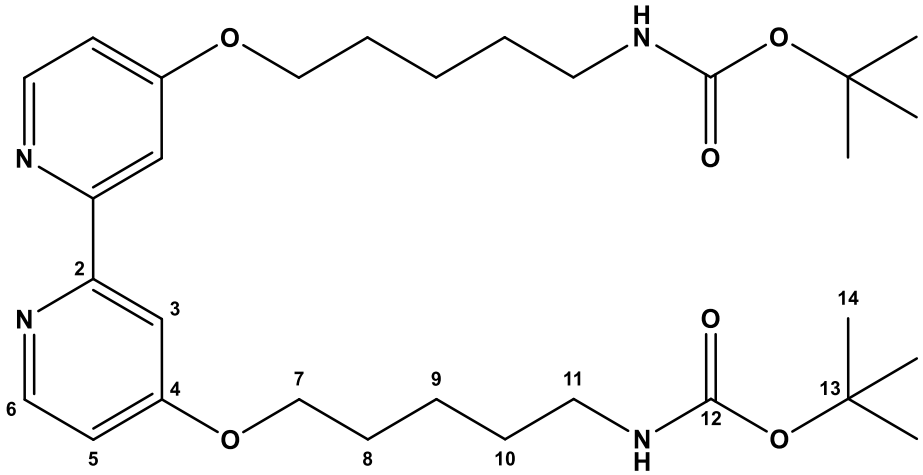

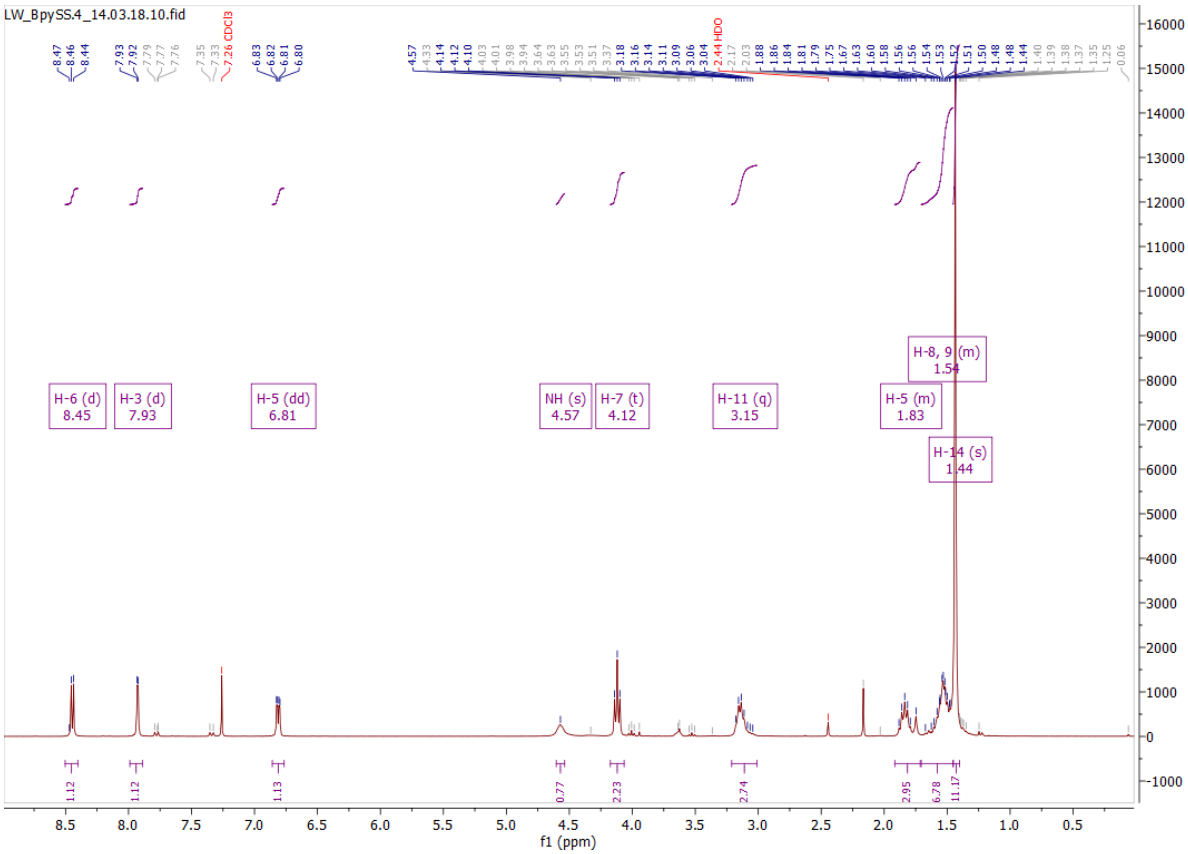

Figure 7.1.1.6. ^{1}H NMR of BpySS.4 in aerated $CDCl_3$. (δ- $CDCl_3$).

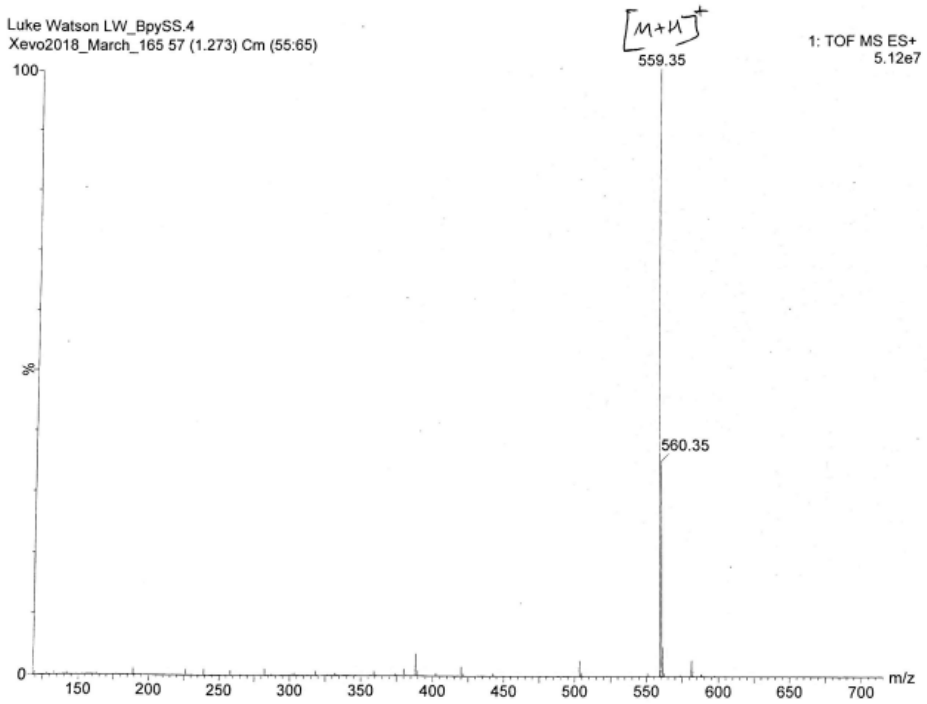

Figure 7.1.1.7. MS spectrum of BpySS.4

BpySS.5

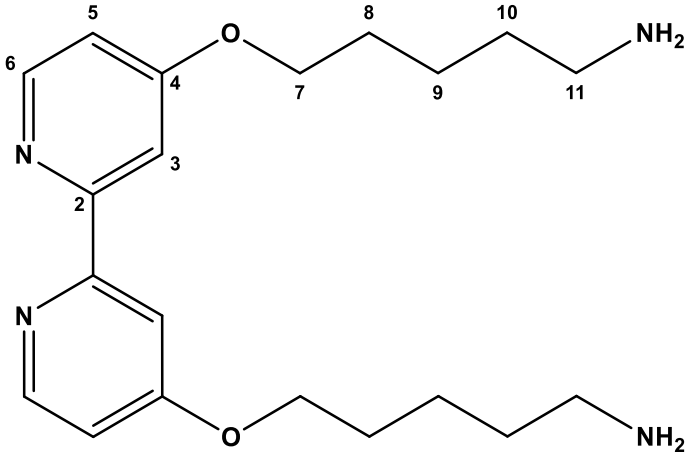

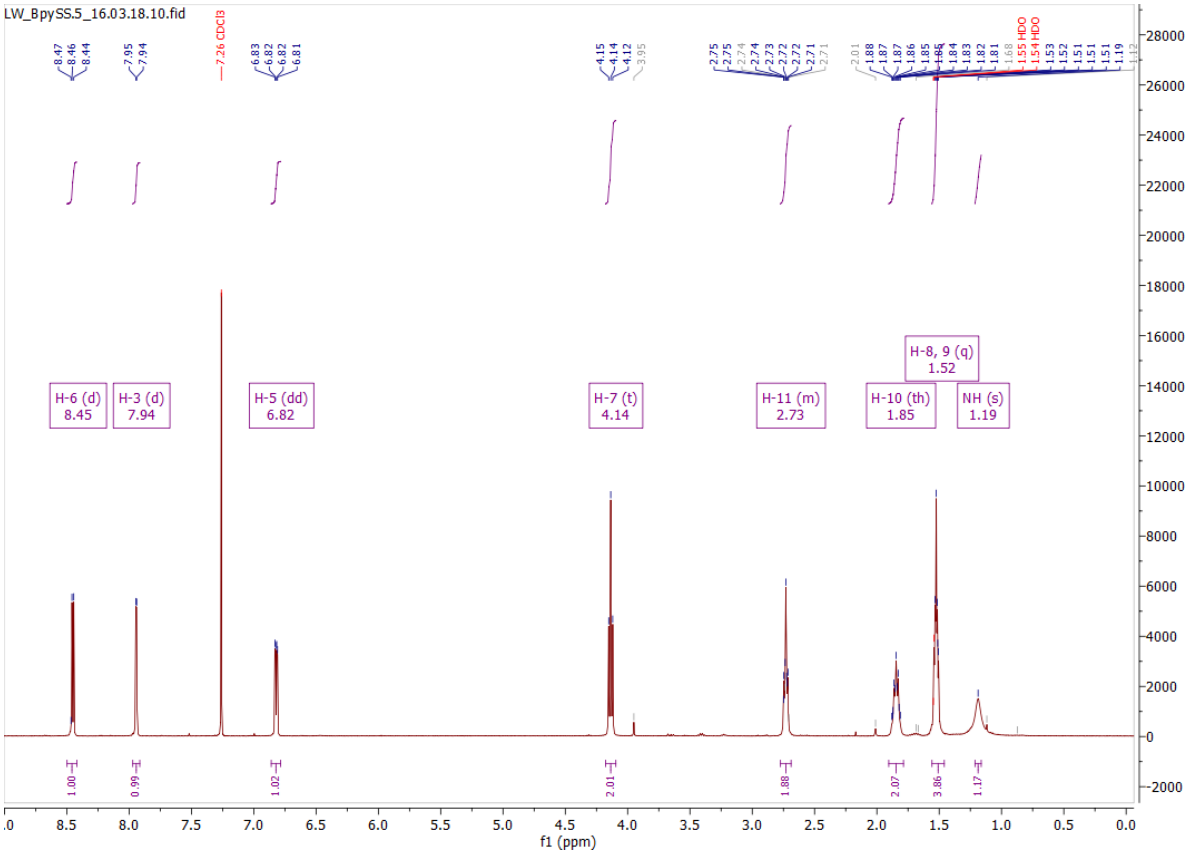

Figure 7.1.1.8. ^{1}H NMR of BpySS.5 in aerated $CDCl_3$. (δ- $CDCl_3$).

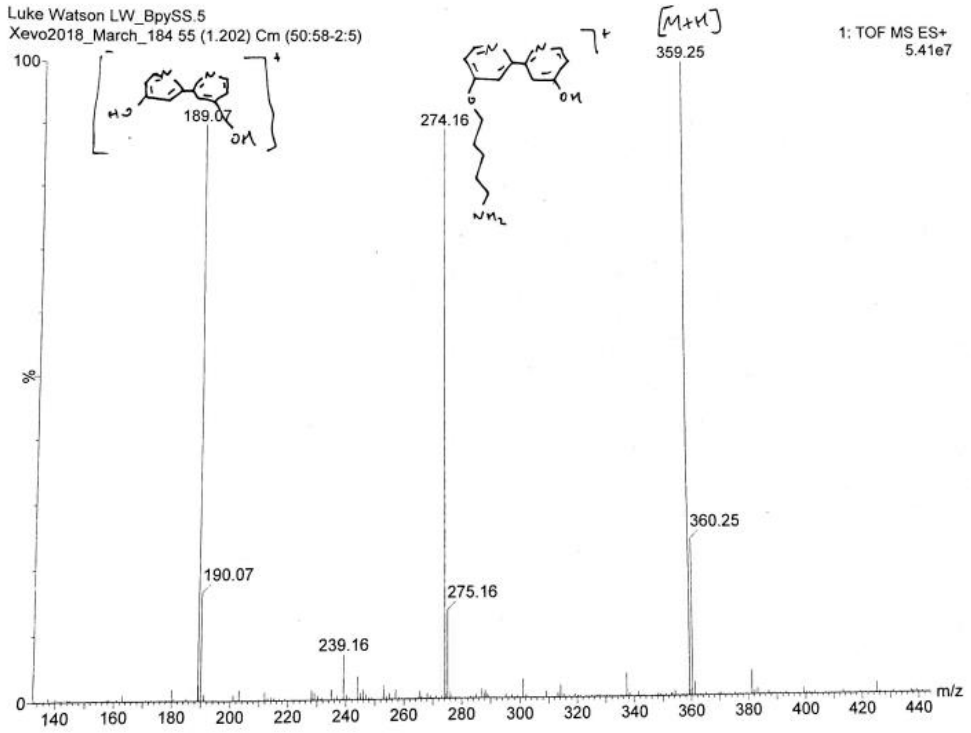

Figure 7.1.1.9. MS spectrum of BpySS.5.

BpySS.6 (BpySS ligand)

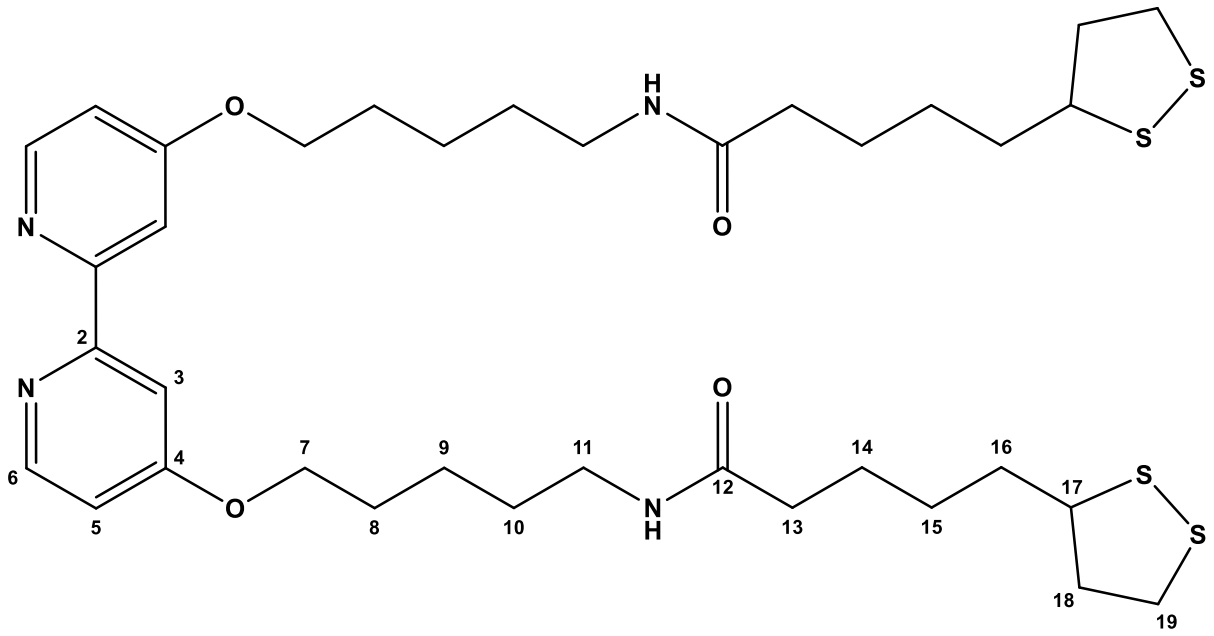

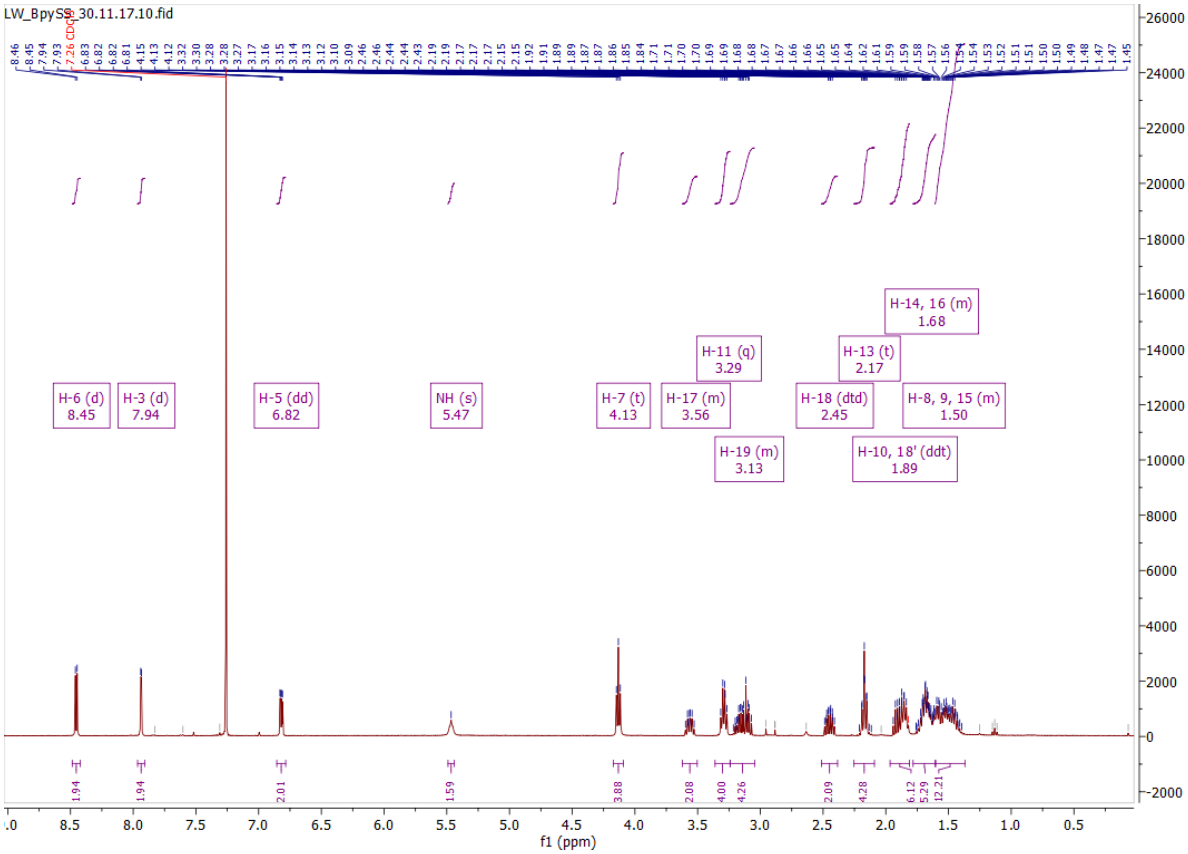

Figure 7.1.1.10. ^{1}H NMR of BpySS.6 (BpySS ligand) in aerated $CDCl_3$. (δ- $CDCl_3$).

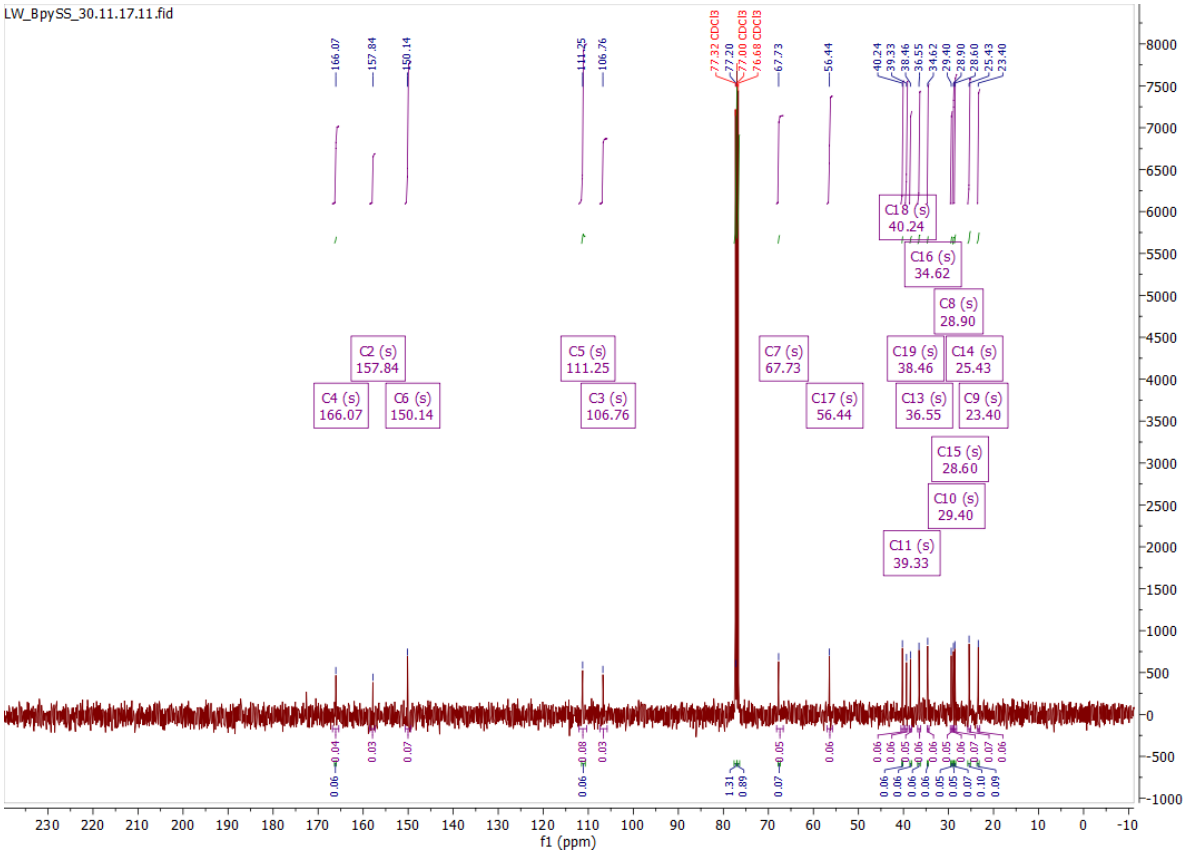

Figure 7.1.1.11. ^{13}C NMR of BpySS.6 (BpySS ligand) in aerated $CDCl_3$. (δ- $CDCl_3$).

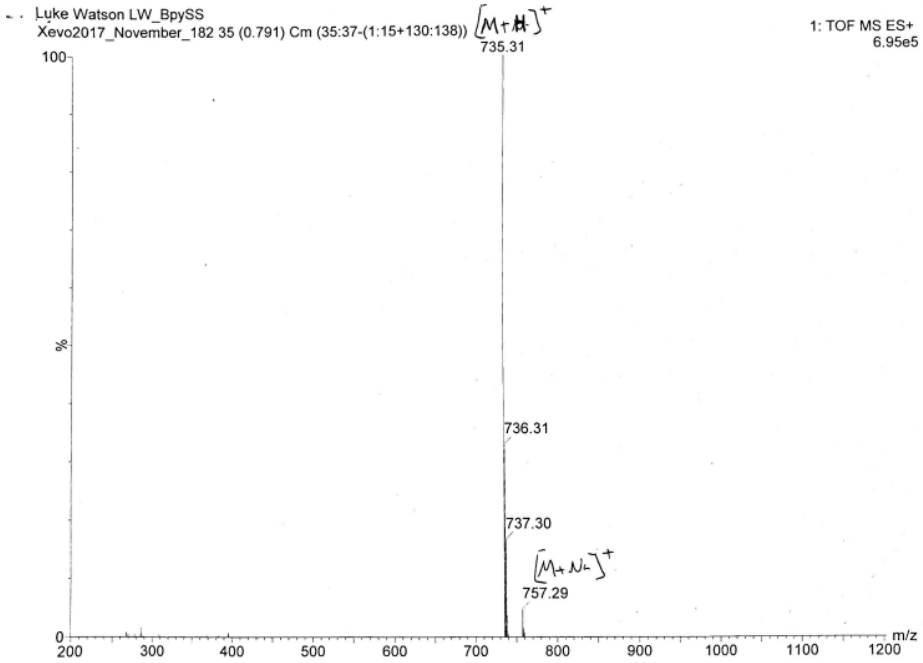

Figure 7.1.1.12. MS spectrum of BpySS.6 (BpySS ligand).

7.1.2 S8 ligand

S8.1

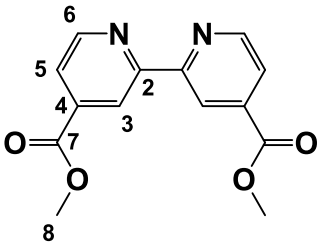

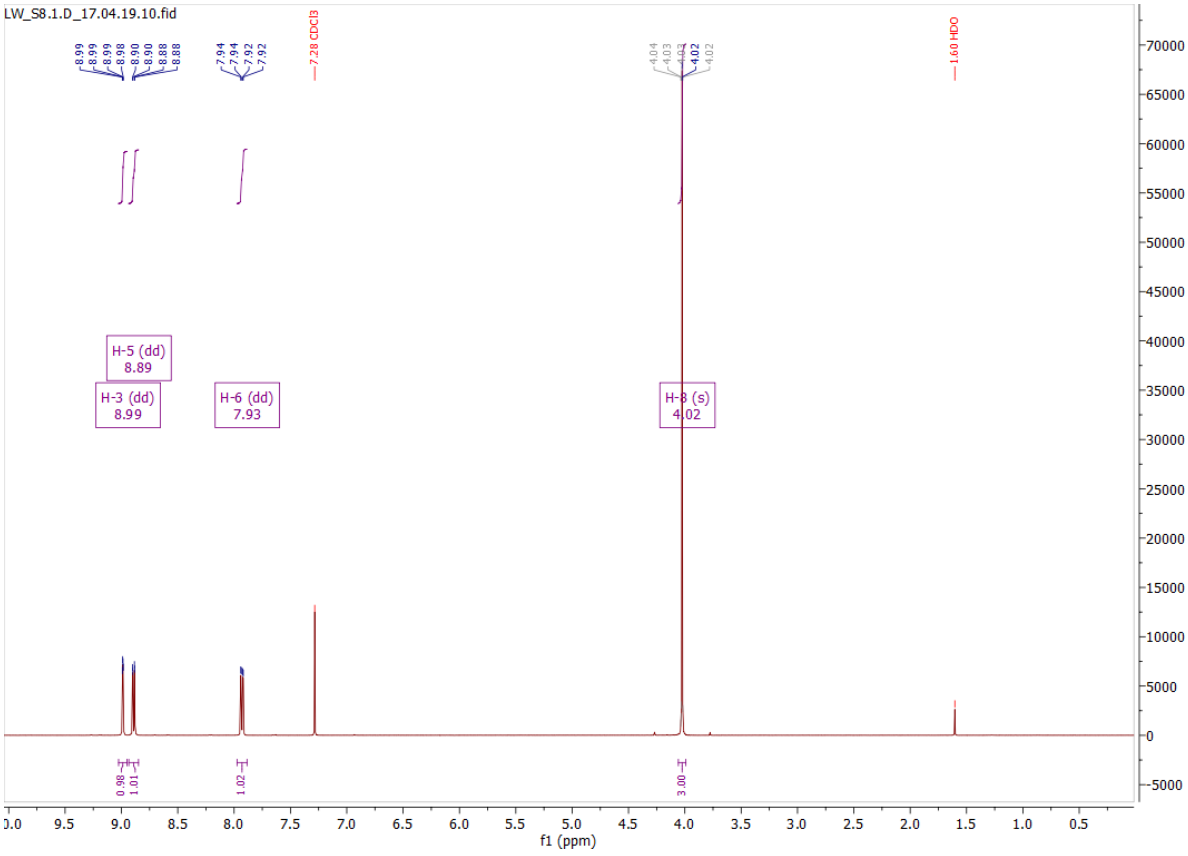

Figure 7.1.2.1. ^{1}H NMR of S8.1 in aerated $CDCl_3$. (δ- $CDCl_3$).

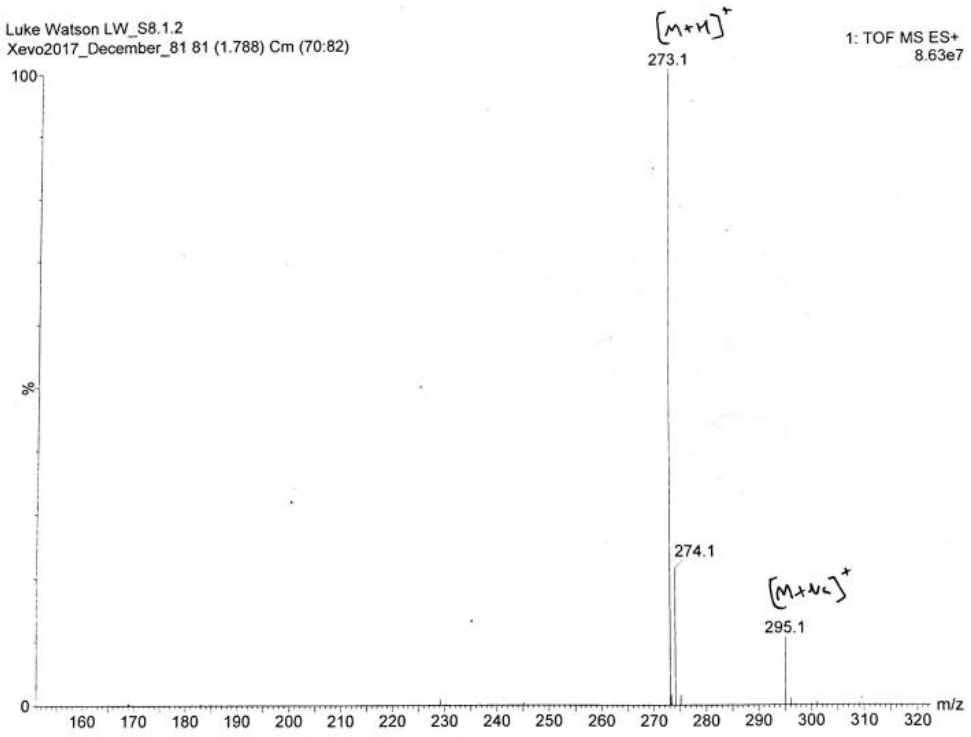

Figure 7.1.2.2. MS spectrum of S8.1.

S8.2

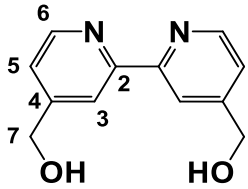

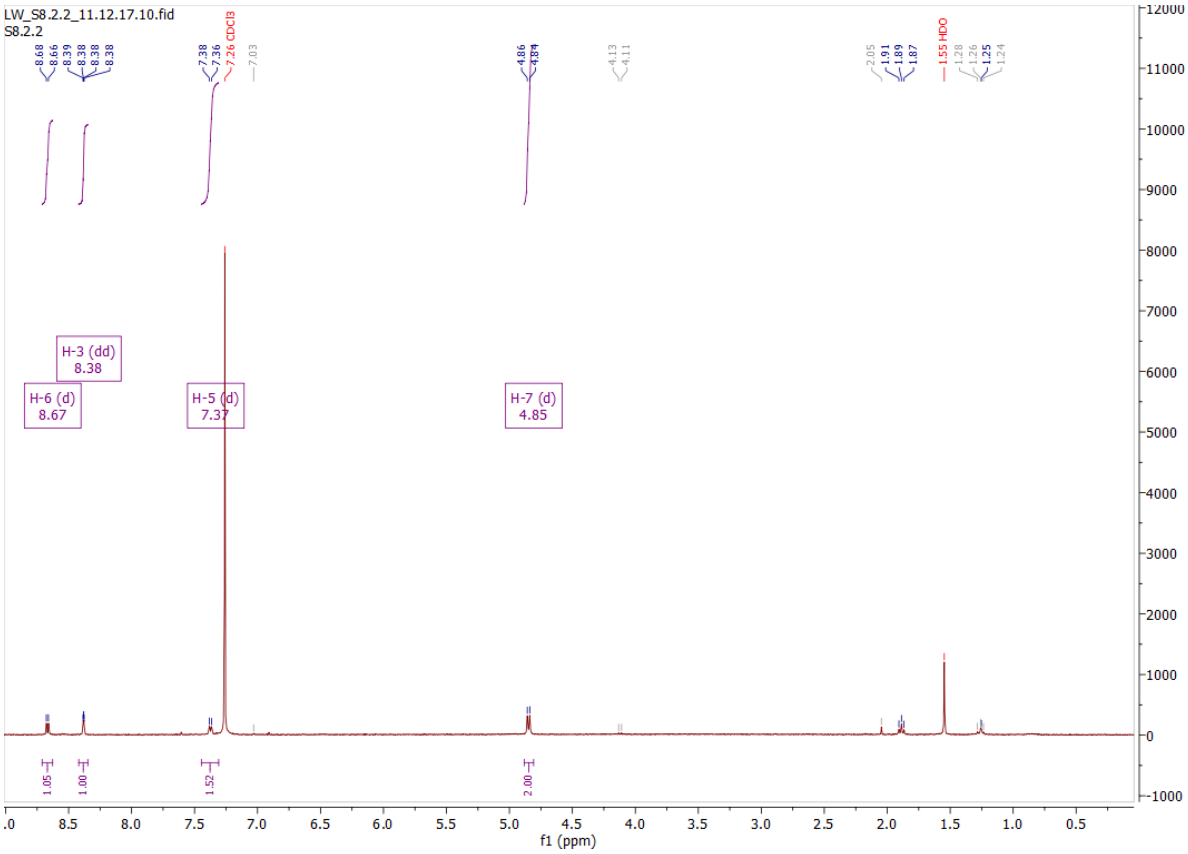

Figure 7.1.2.3. ^{1}H NMR of S8.2 in aerated $CDCl_3$. (δ- $CDCl_3$).

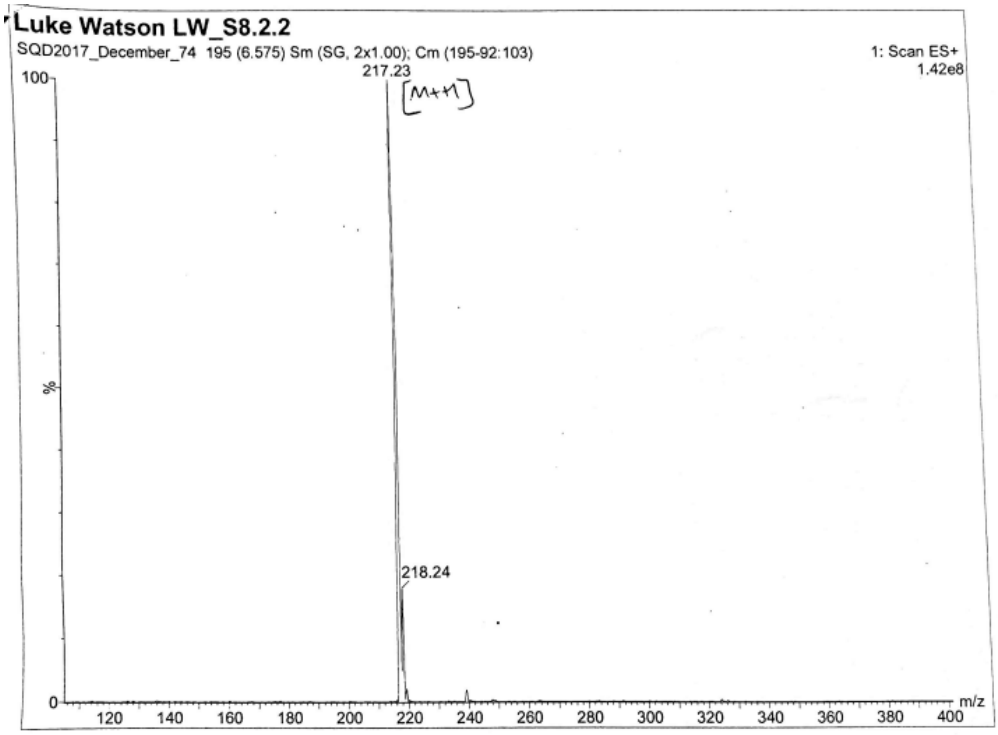

Figure 7.1.2.4. MS spectrum of S8.2.

S8.3

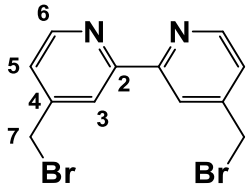

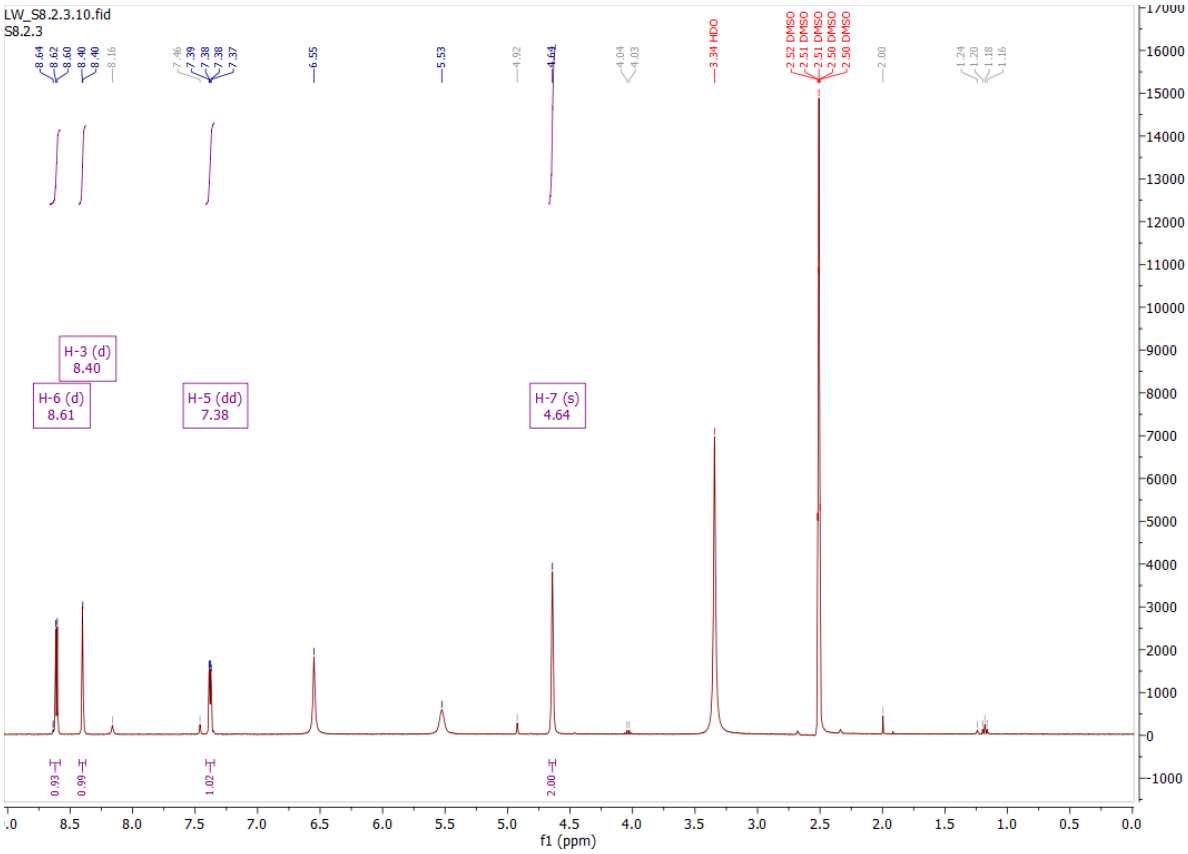

Figure 7.1.2.5.^{1}H NMR of S8.3 in aerated DMSO. (δ_6- DMSO).

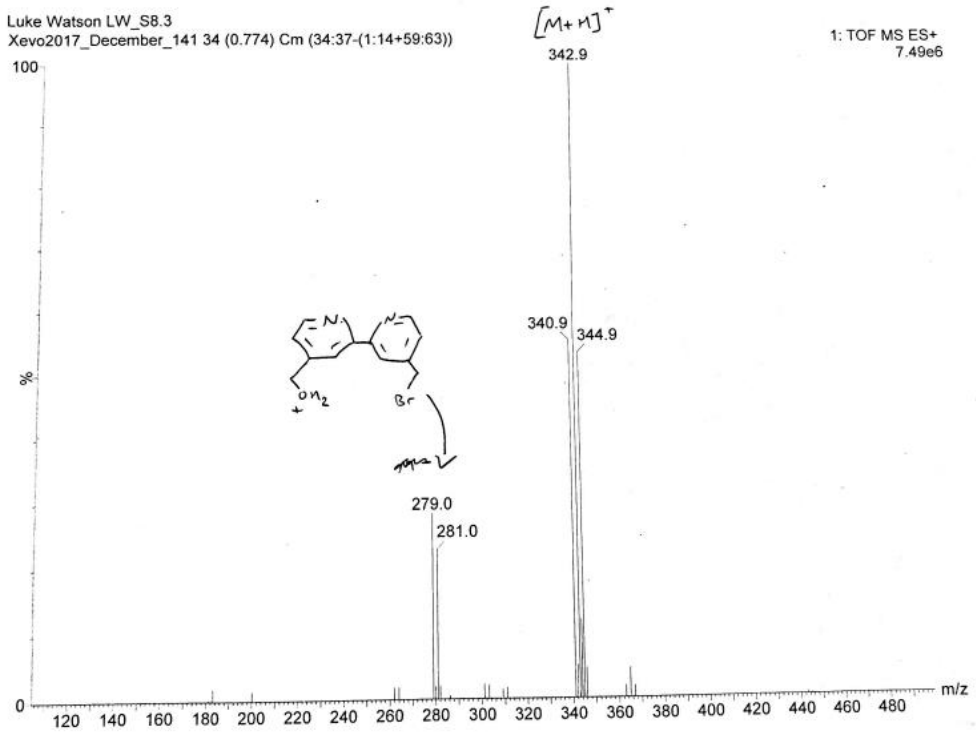

Figure 7.1.2.6. MS spectrum S8.3.

S8.4

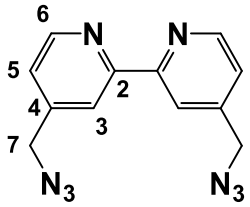

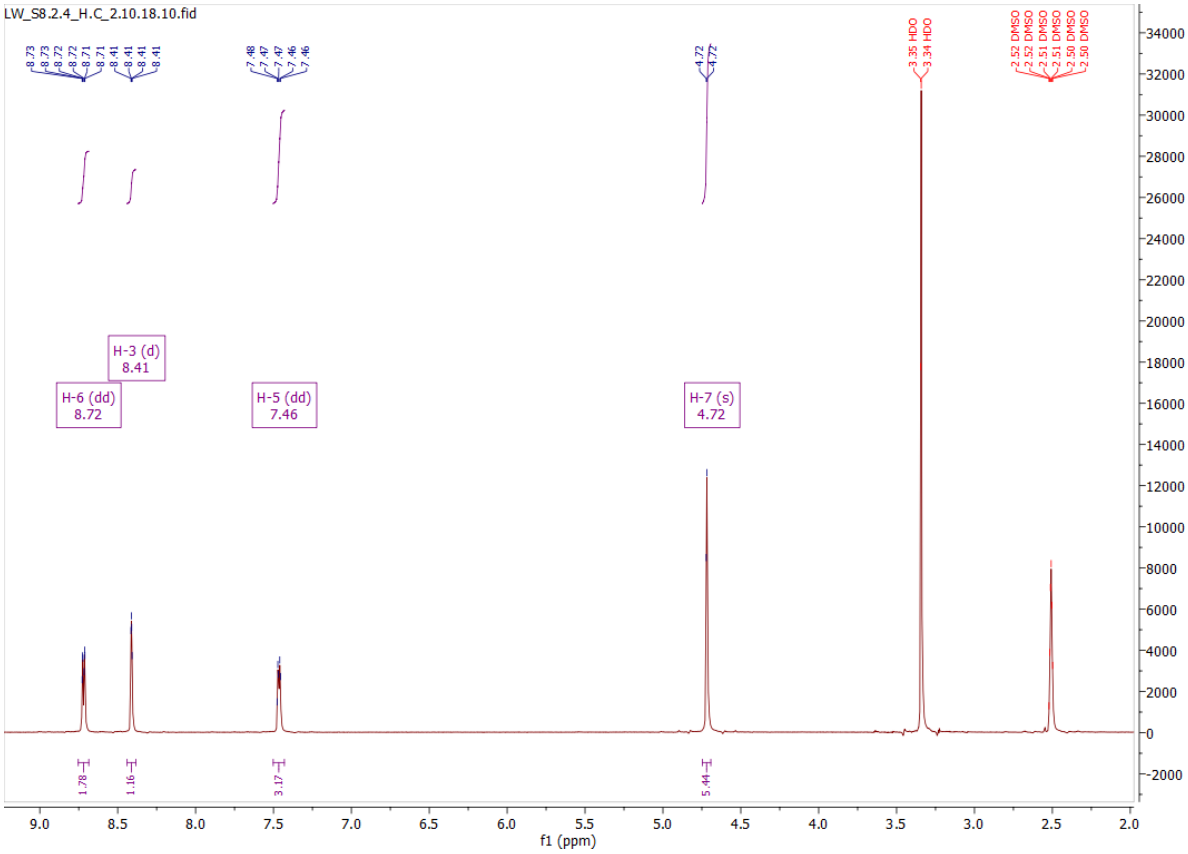

Figure 7.1.2.7. ^{1}H NMR of S8.4 in aerated DMSO. (δ_6- DMSO).

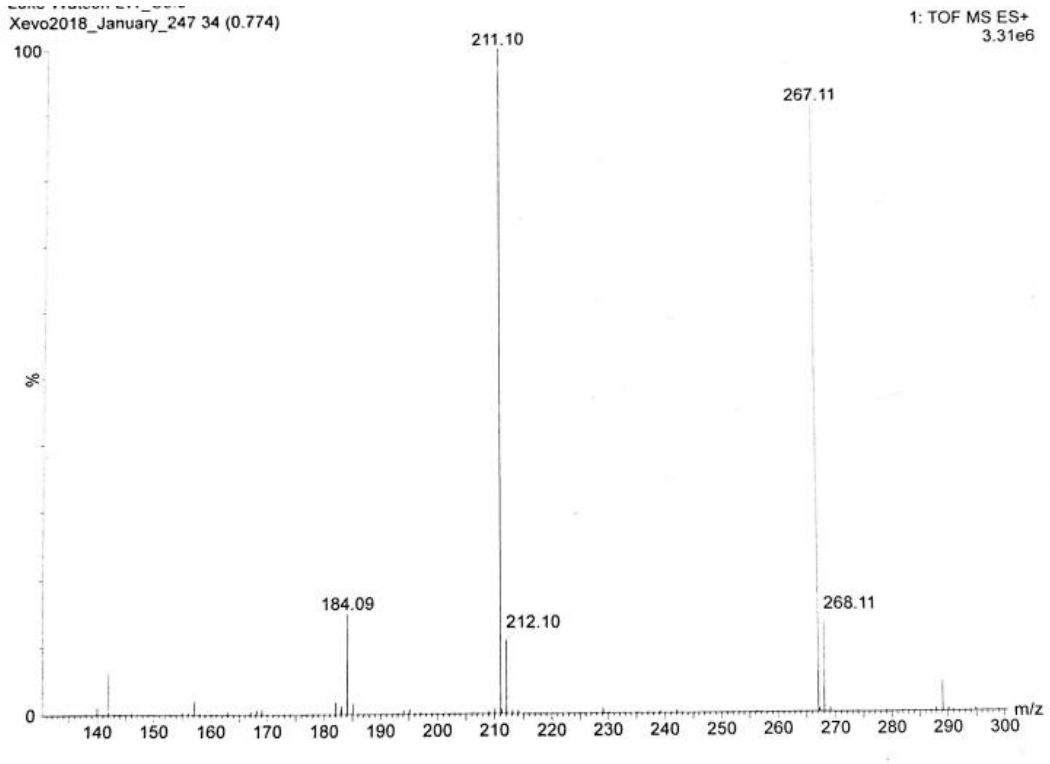

Figure 7.1.2.8. MS spectrum of S8.4.

S8.5

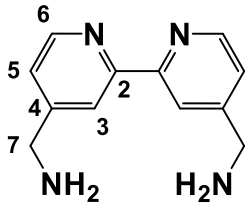

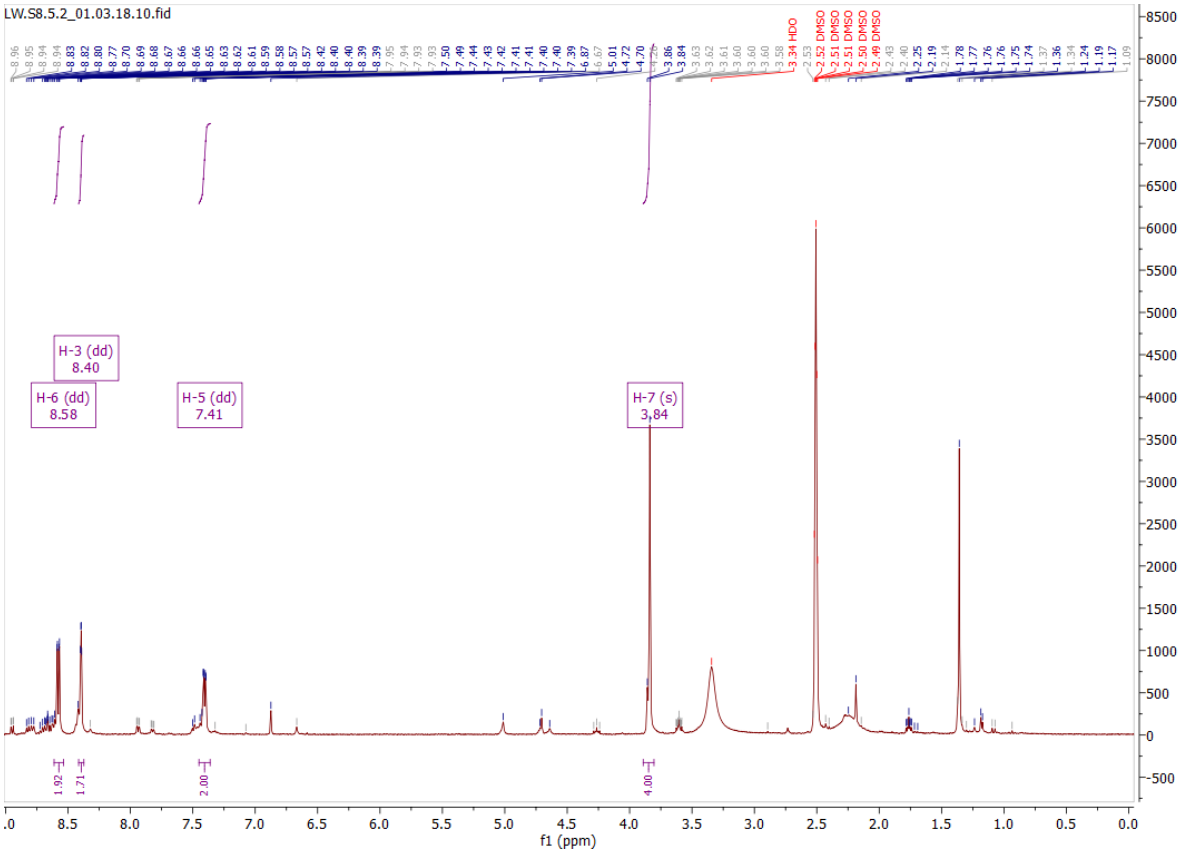

Figure 7.1.2.9. ^{1}H NMR of S8.5 in aerated DMSO. (δ_6- DMSO).

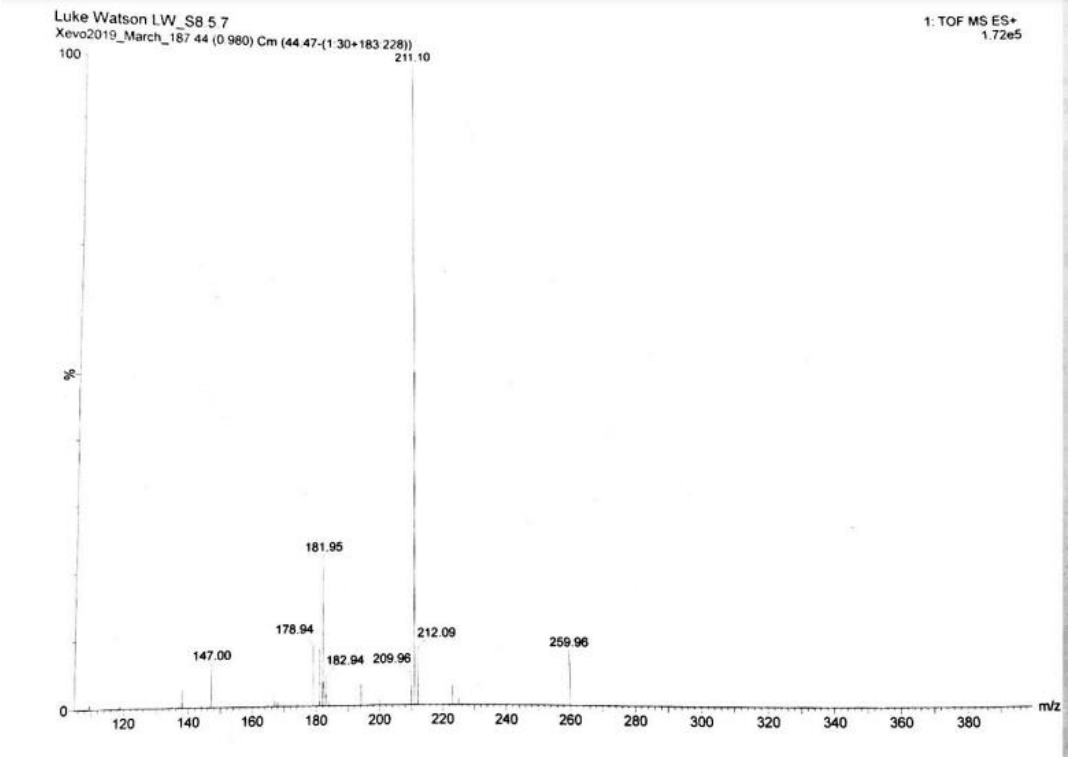

Figure 7.1.2.10. MS spectrum of S8.5.

S8.6 (S8 ligand)

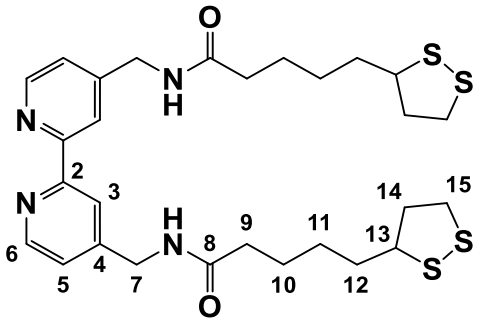

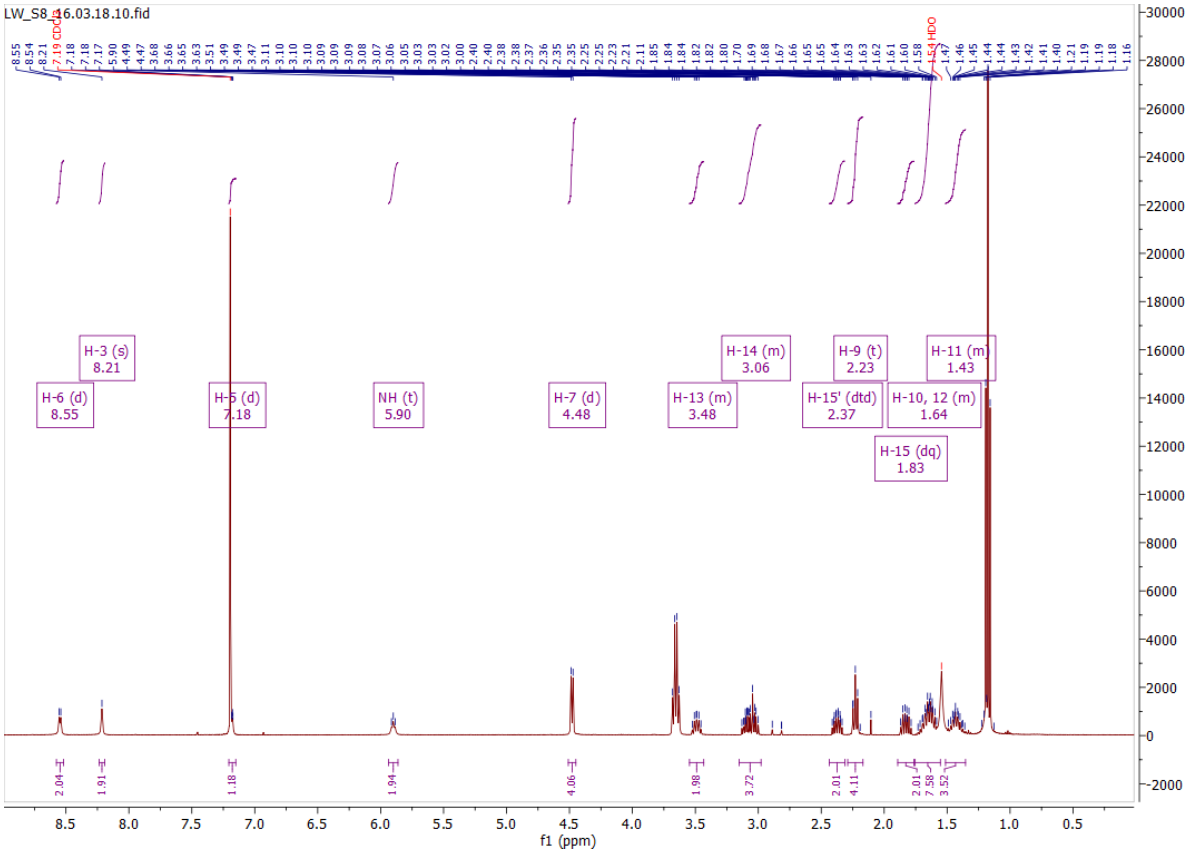

Figure 7.1.2.11. ^{1}H NMR of S8.6 (S8 ligand) in aerated $CDCl_3$. (δ-$CDCl_3$).

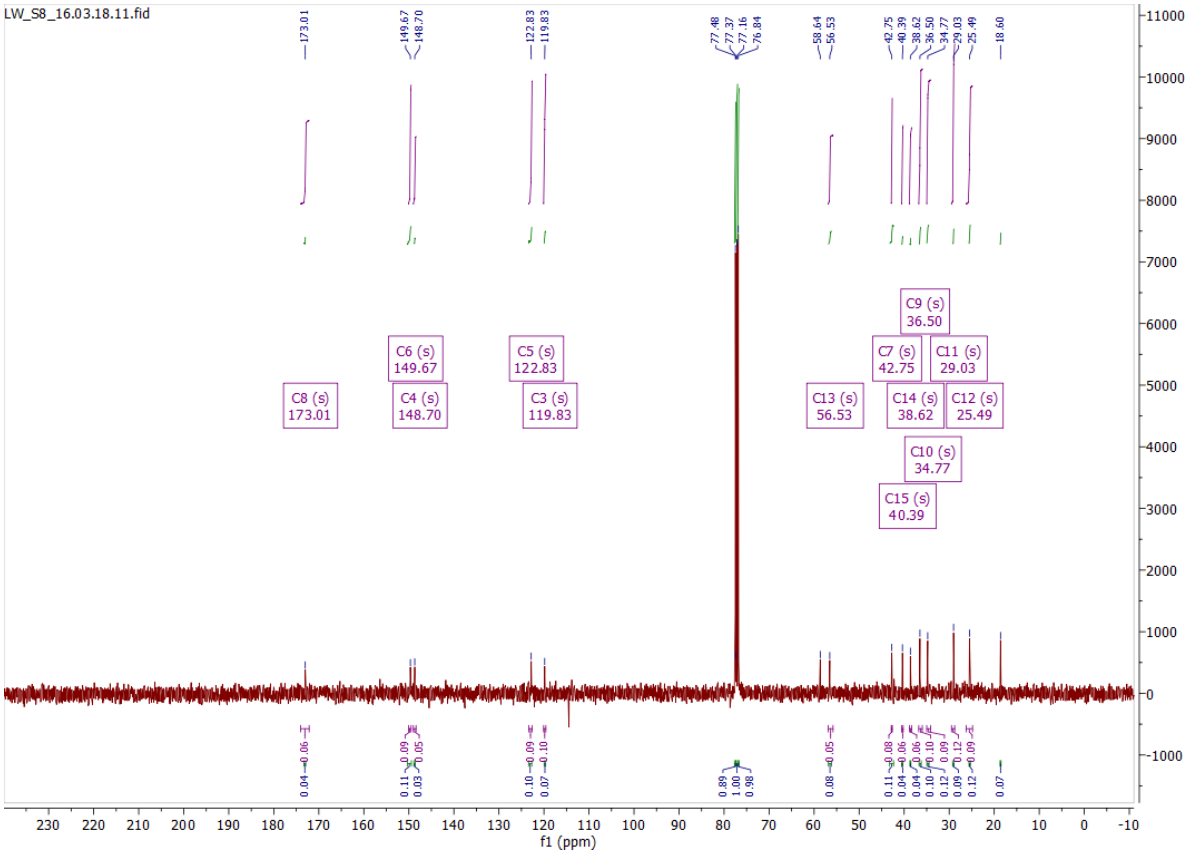

Figure 7.1.2.12. ^{13}C NMR of S8.6 (S8 ligand) in aerated $CDCl_3$. (δ-$CDCl_3$).

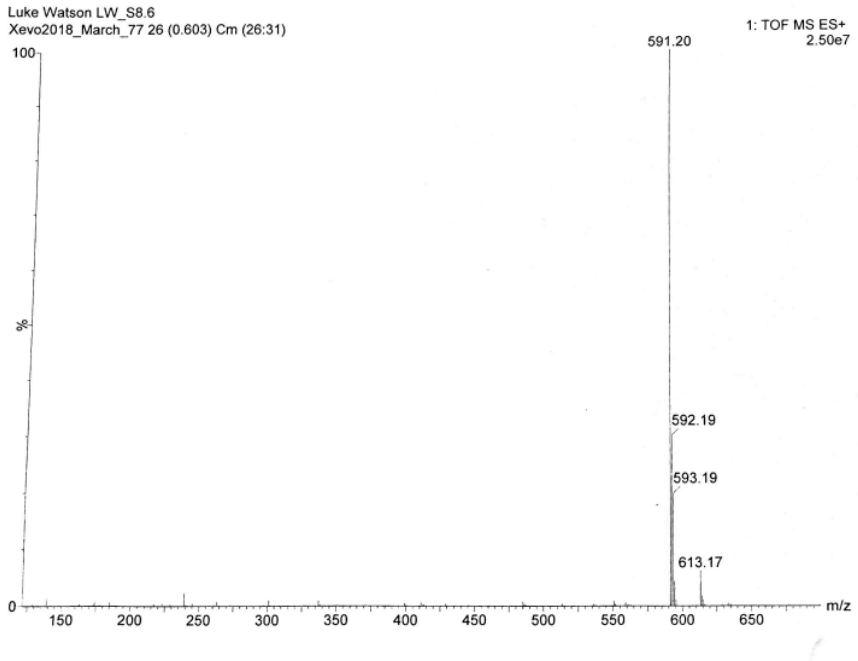

Figure 7.1.2.13. MS spectrum of S8.6 (S8 ligand).

7.1.3 $Ru(Bpy)_2Cl_2$

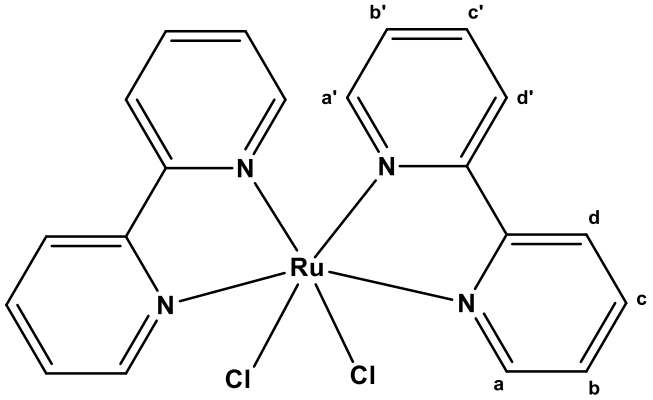

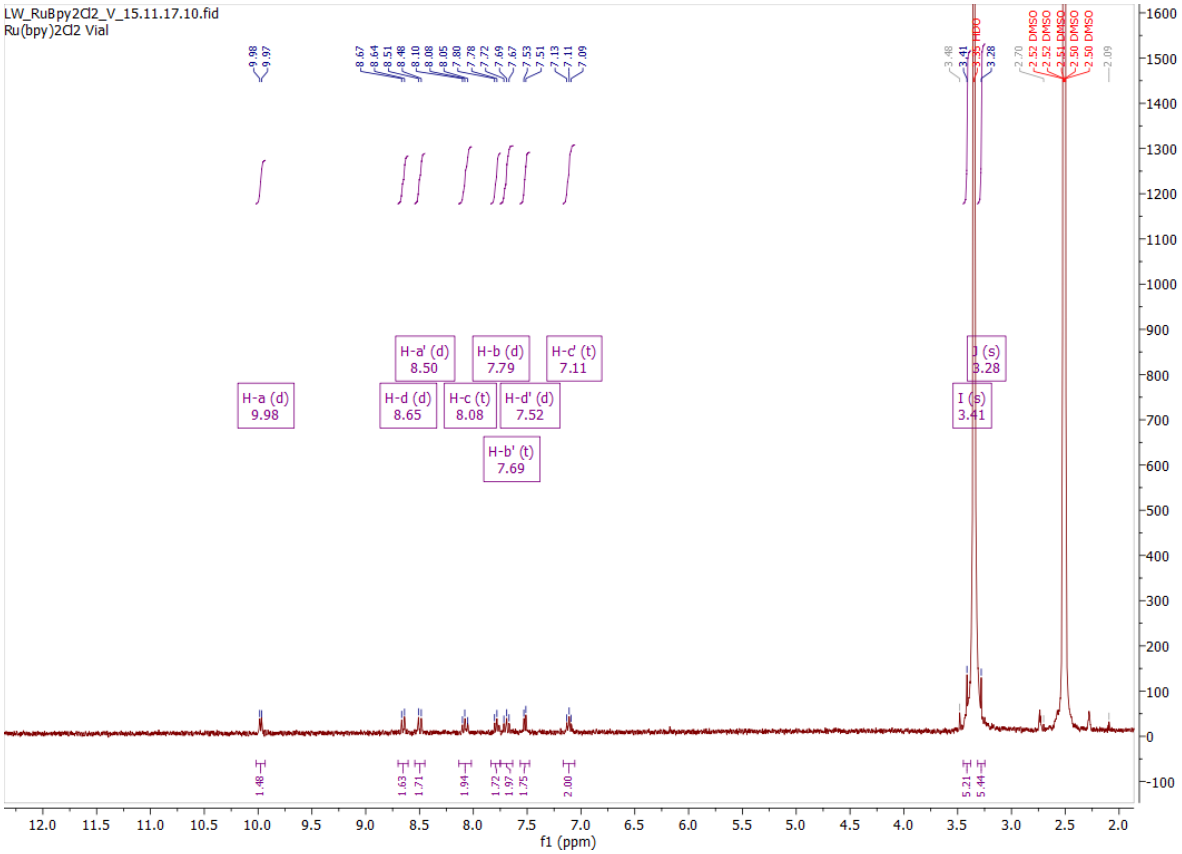

Figure 7.1.3.1. ^1H NMR of $Ru(Bpy)_2Cl_2$ in aerated DMSO. (δ_6- DMSO).

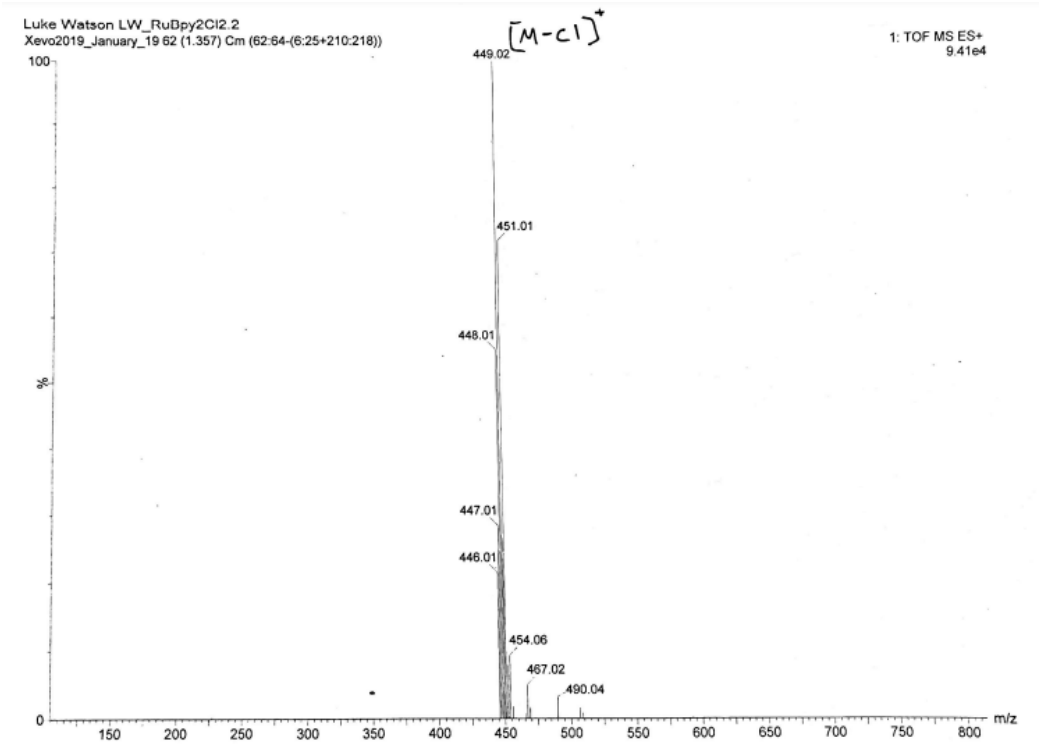

Figure 7.1.3.2. MS spectrum of $Ru(Bpy)_2Cl_2$.

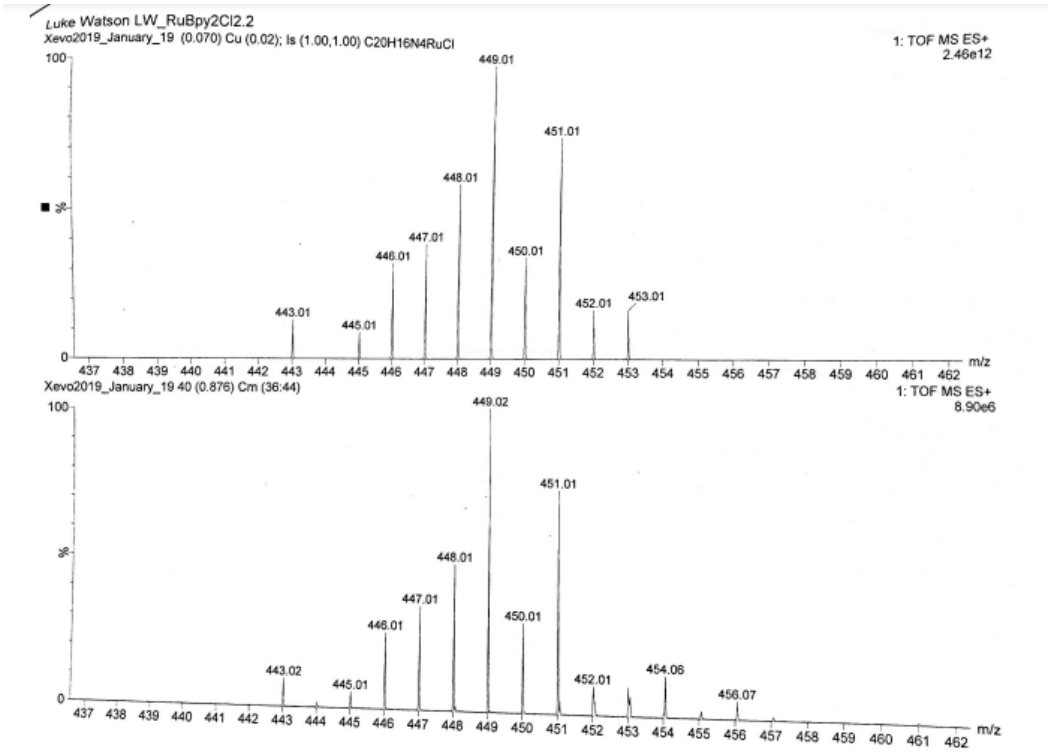

Figure 7.1.3.3. MS spectrum of theoretical mass vs experimental mass of $Ru(Bpy)_2Cl_2$.

7.1.4 $Ru(Phen)_2Cl_2$

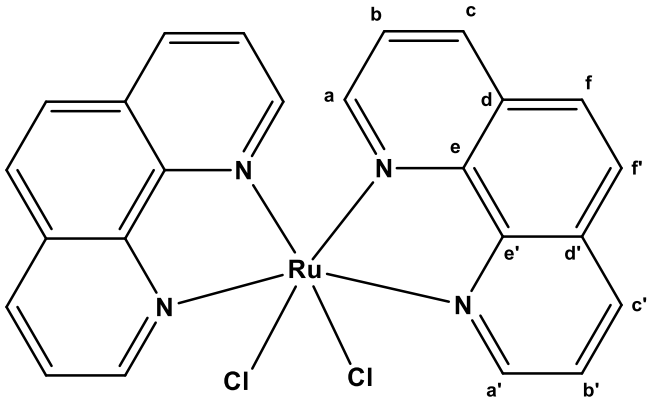

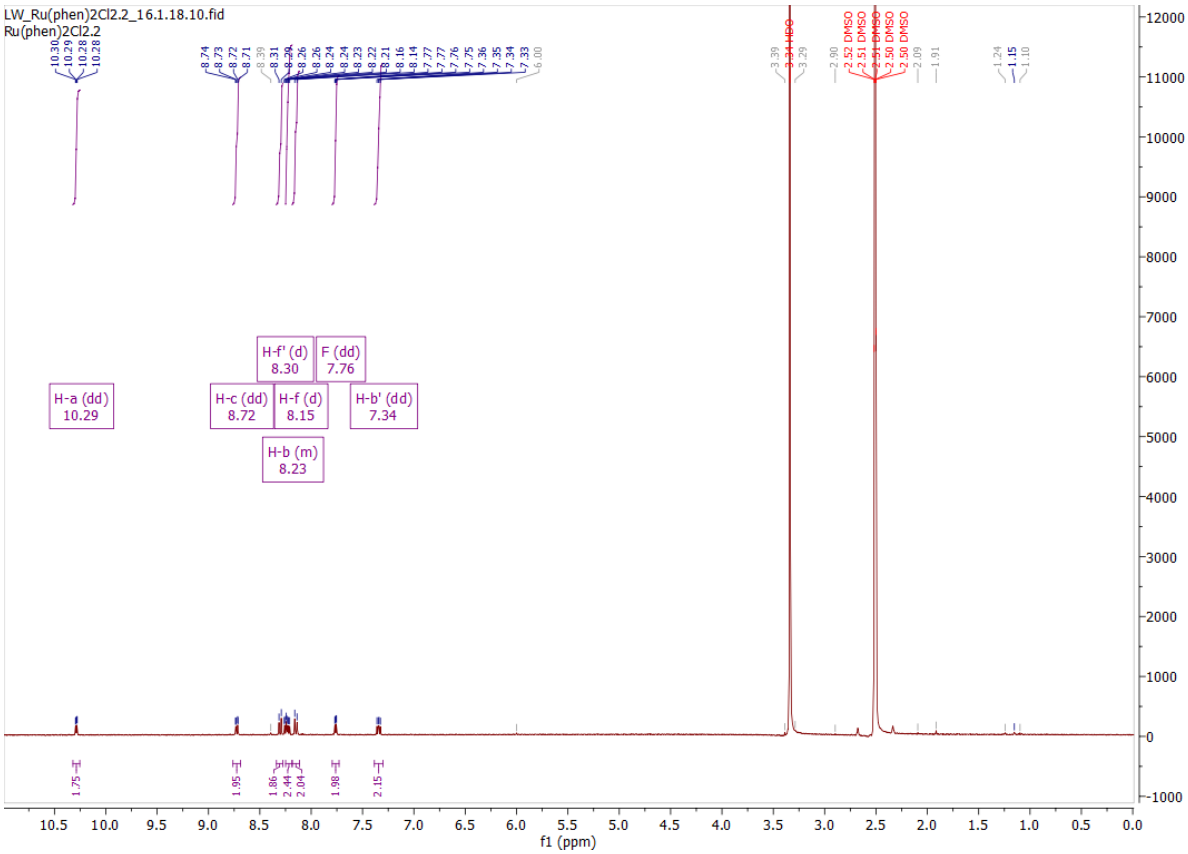

Figure 7.1.4.1. ^{1}H NMR of $Ru(Phen)_2Cl_2$ in aerated DMSO. (δ_6- DMSO).

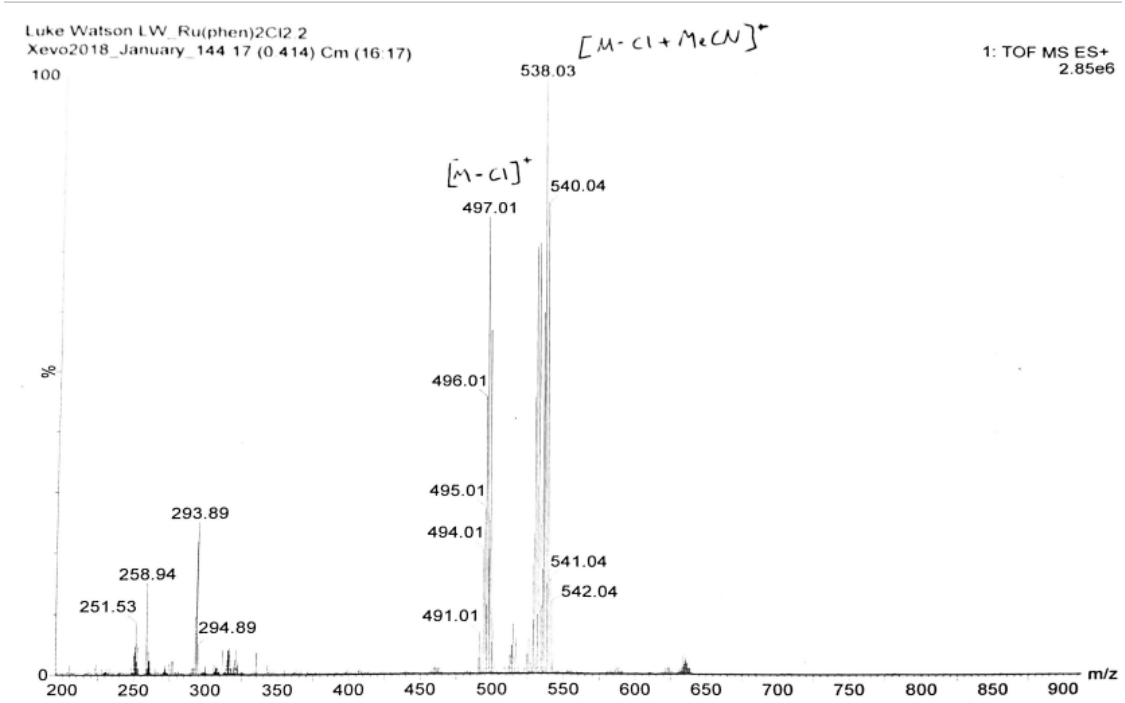

Figure 7.1.4.2. MS spectrum of Ru(Phen)$_2$Cl$_2$.

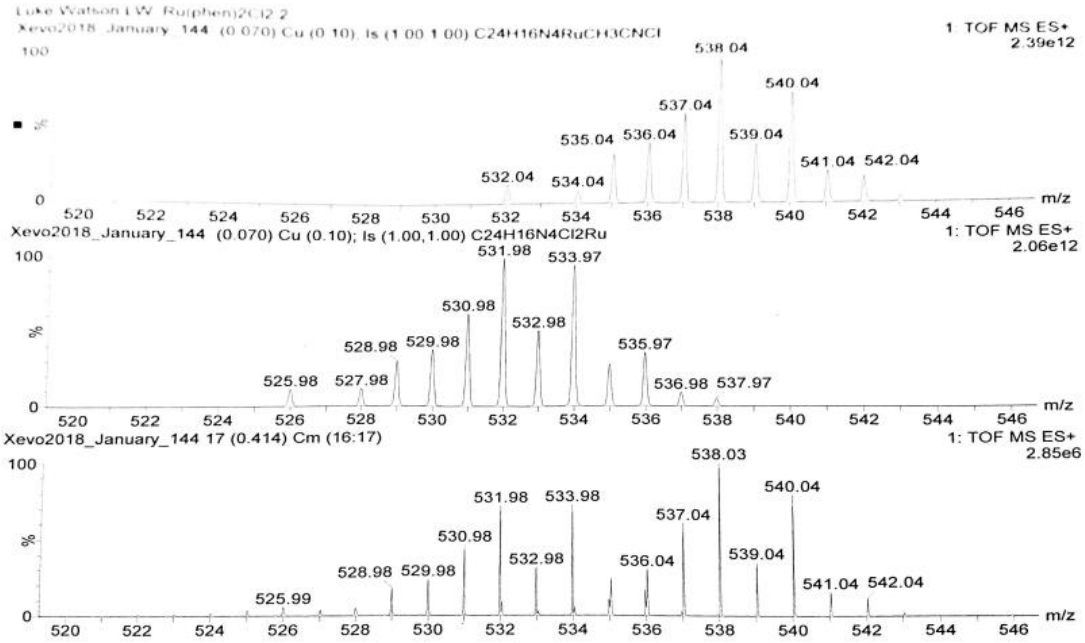

Figure 7.1.4.3. MS spectrum of Ru(Phen)$_2$Cl$_2$ of theoretical mass vs experimental mass.

7.1.5 $Os(Phen)_2Cl_2$

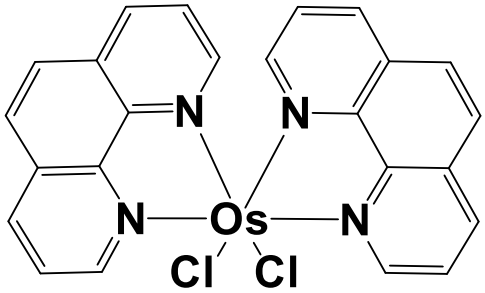

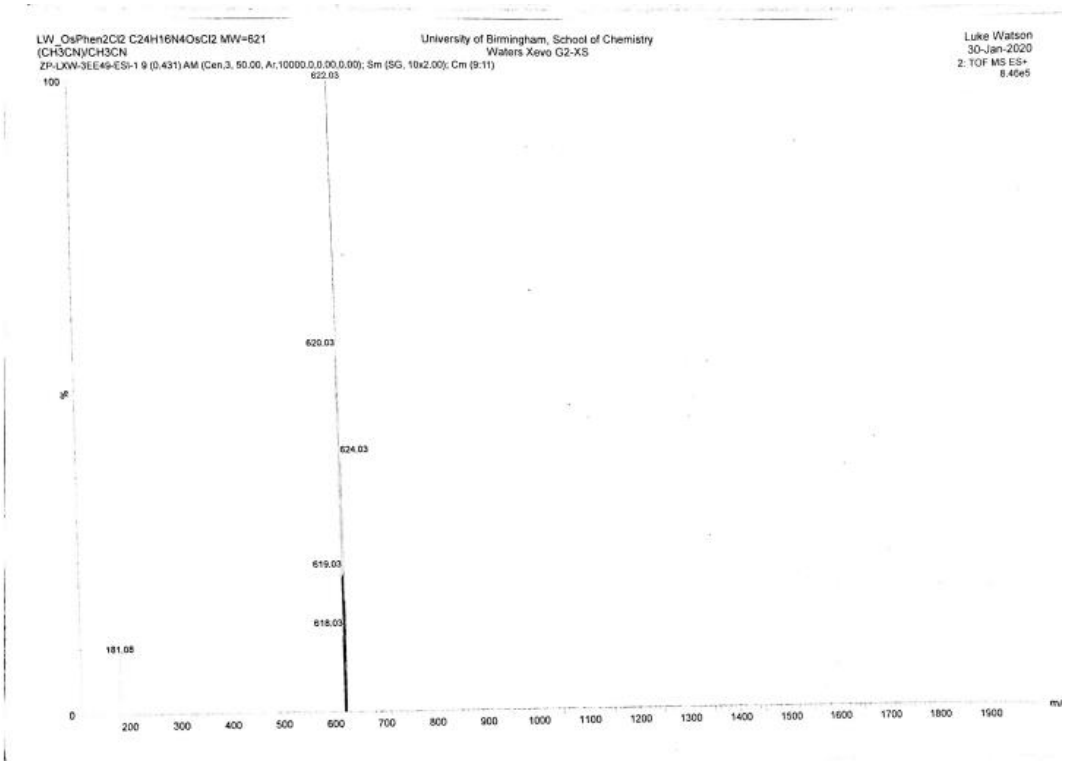

Figure 7.1.5.1. MS spectrum of $Os(Phen)_2Cl_2$.

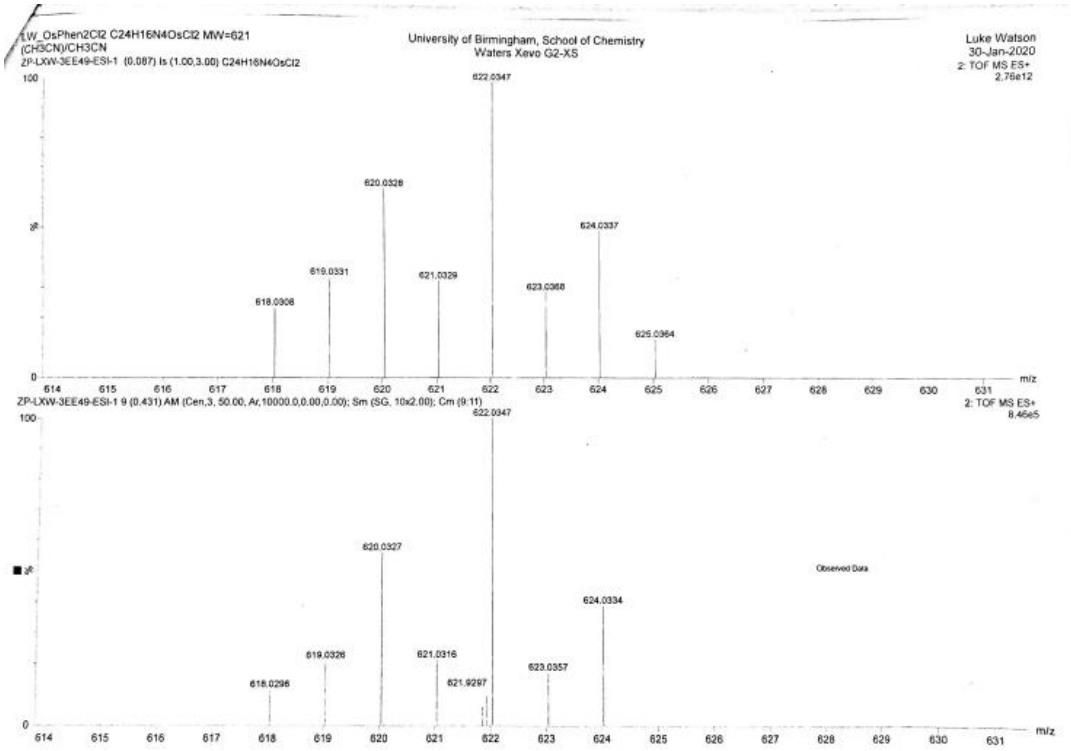

Figure 7.1.5.2. MS spectrum of $Os(Phen)_2Cl_2$ of experimental mass vs theoretical mass.

7.1.6 RuBpySS

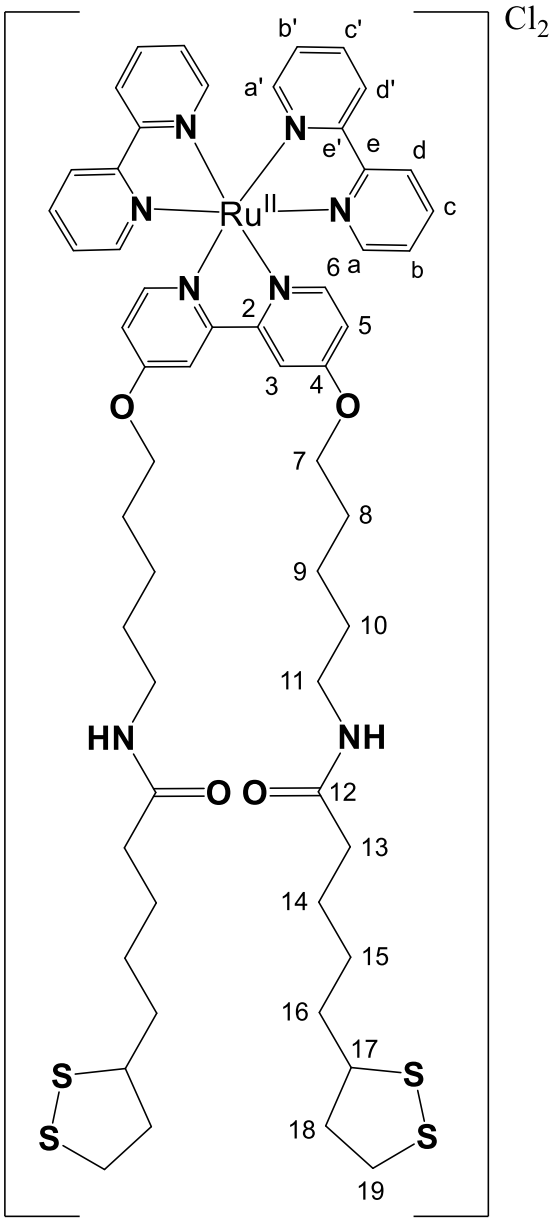
Cl2
Ru II
N
O
HN
NH
S
a'
b'
c'
d'
e'
a
b
c
d
e
2
3
4
5
6
7
8
9
10
11
12
13
14
15
16
17
18
19

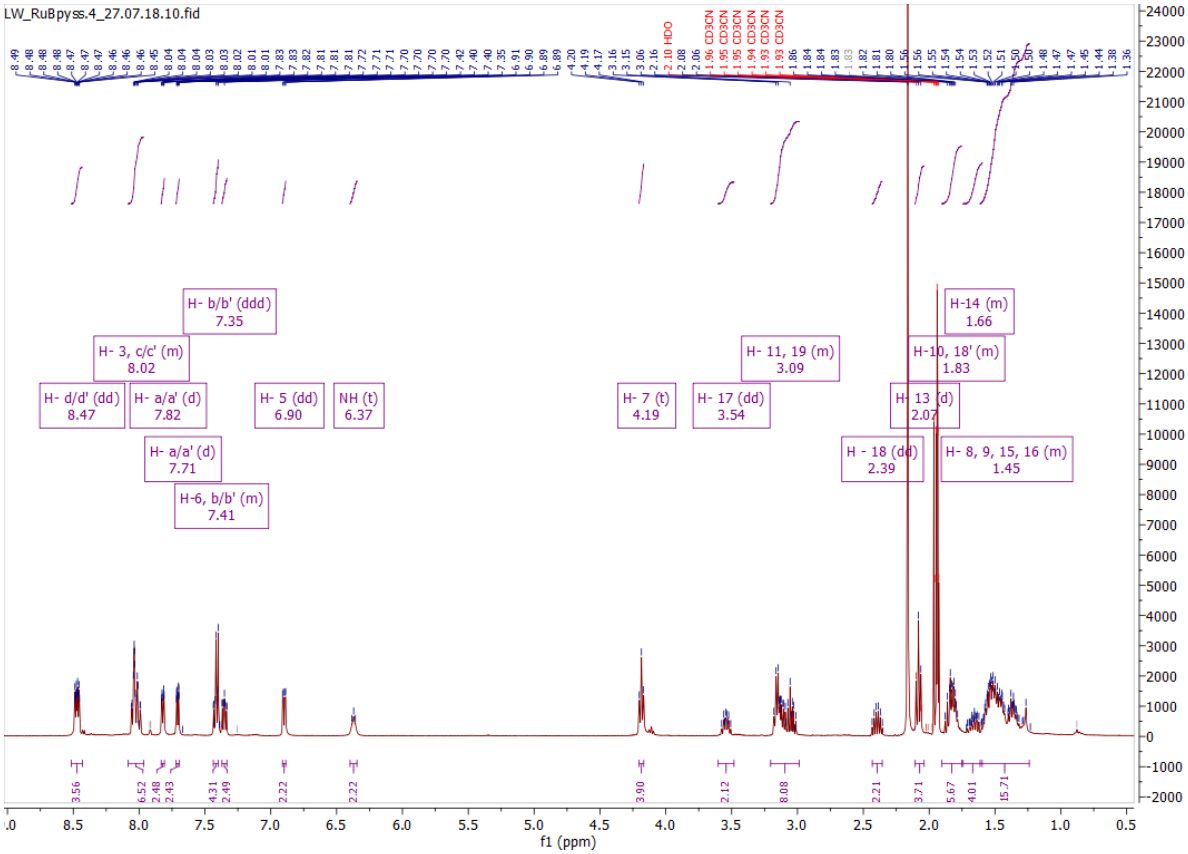

Figure 7.1.6.1. ^{1}H NMR of RuBpySS in aerated CD_3CN. (δ_3- CD_3CN).

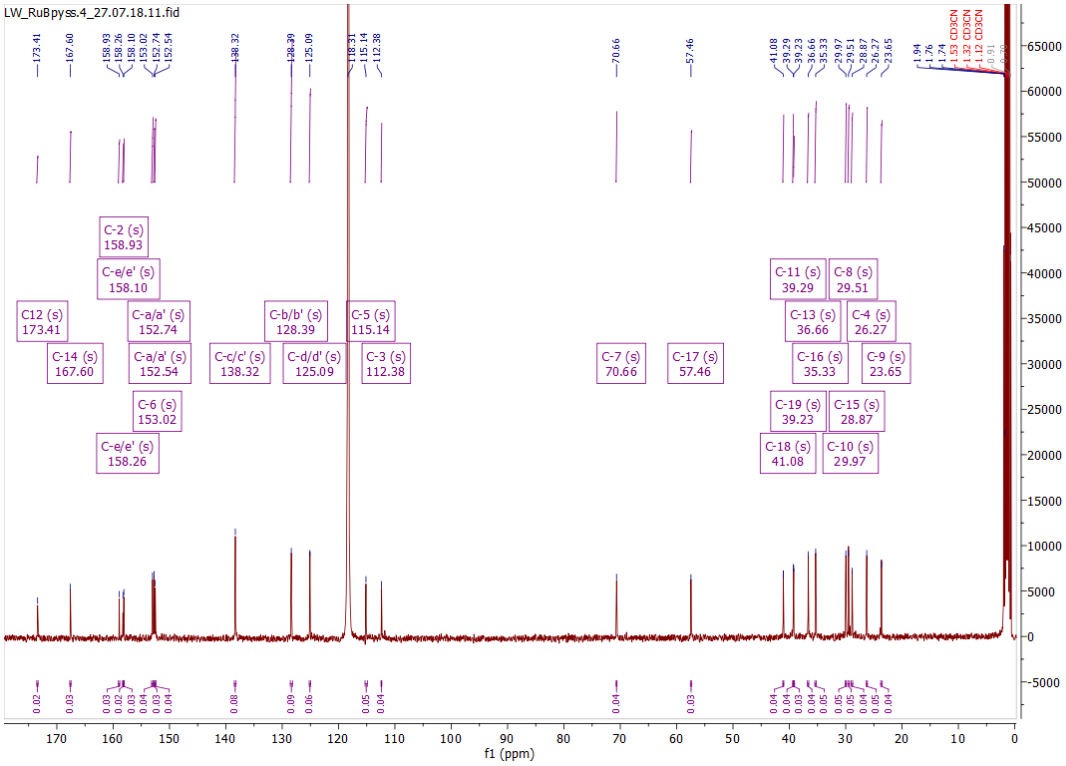

Figure 7.1.6.2. ^{13}C NMR of RuBpySS in aerated CD_3CN. (δ_3- CD_3CN).

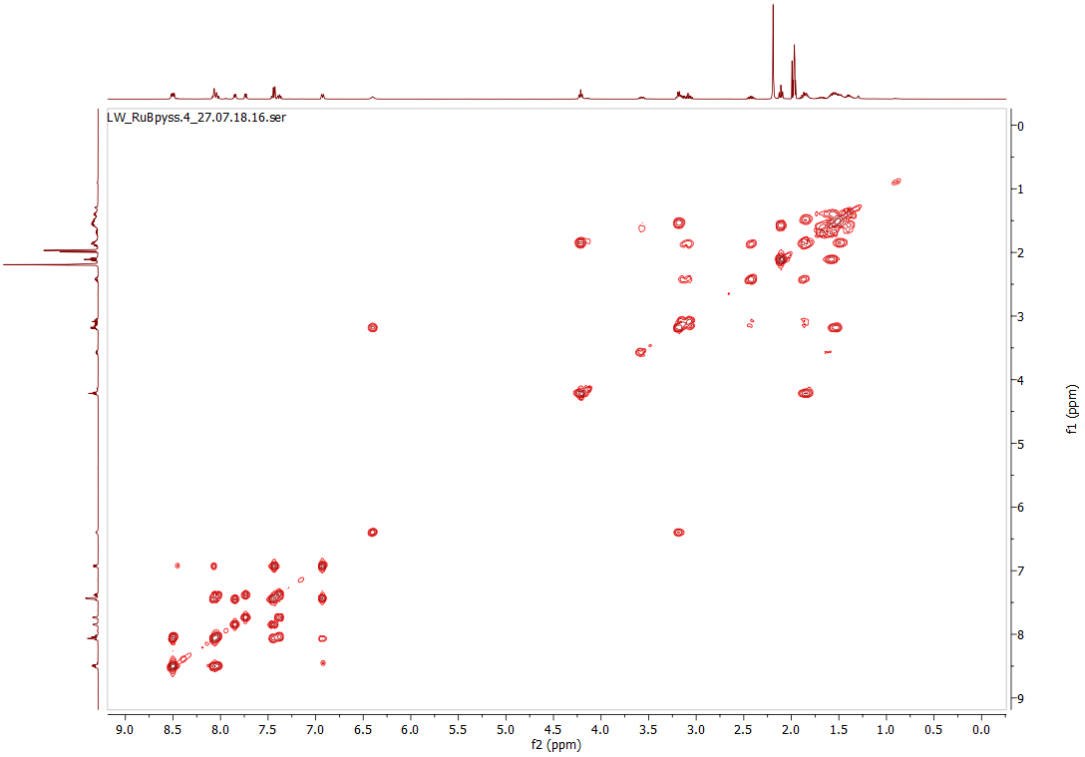

Figure 7.1.6.3. COSY spectrum of RuBpySS in aerated CD_3CN. (δ_3- CD_3CN).

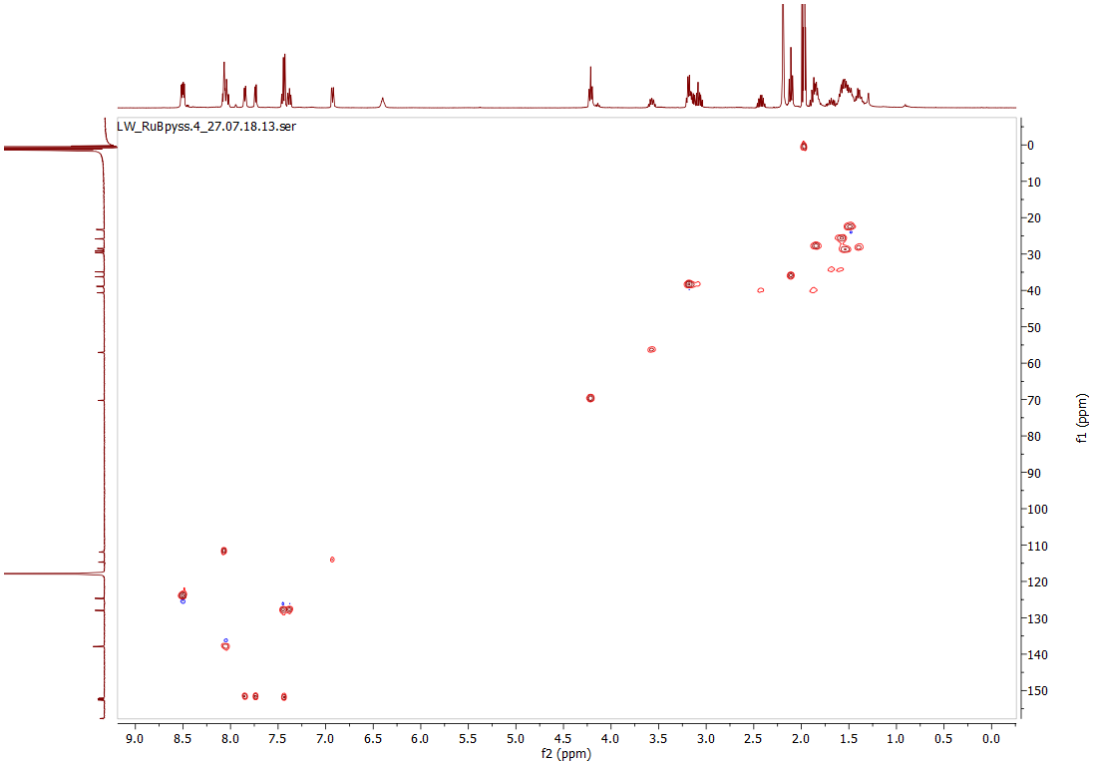

Figure 7.1.6.4. HSQC spectrum of RuBpySS in aerated CD_3CN. (δ_3- CD_3CN).

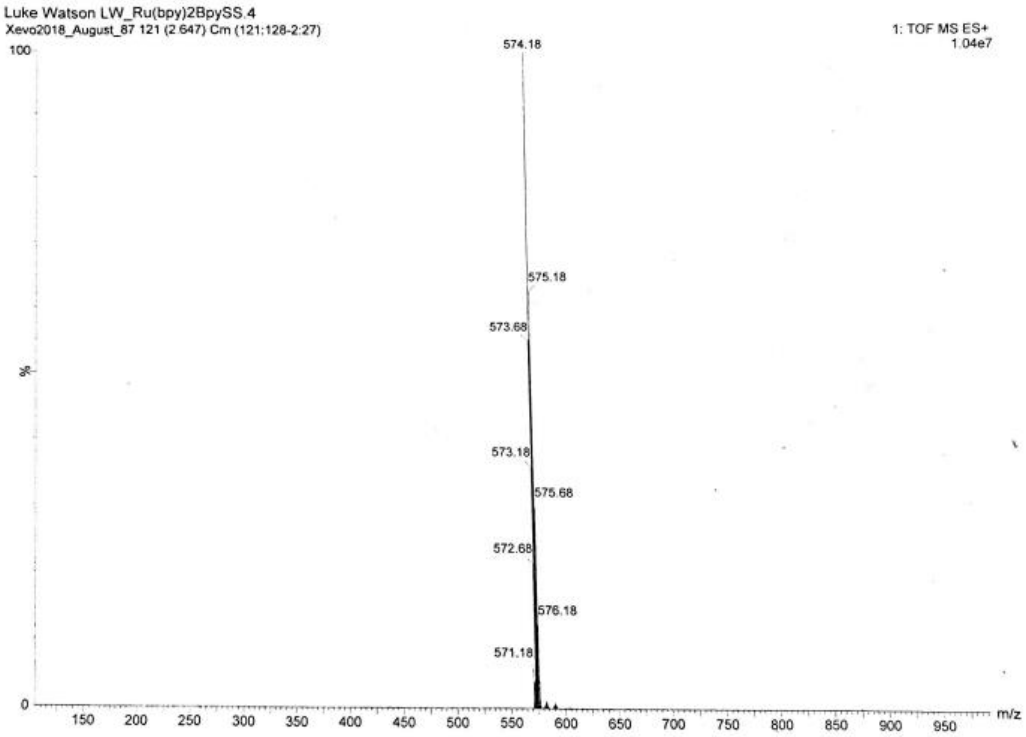

Figure 7.1.6.5. MS spectrum of RuBpySS.

7.1.7 RuPhenSS

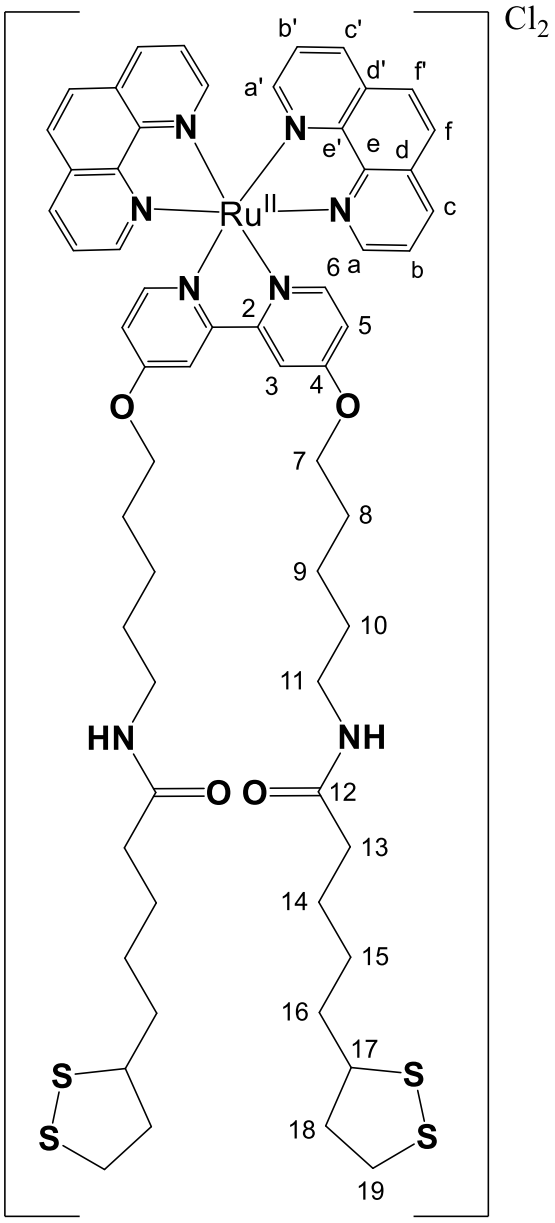

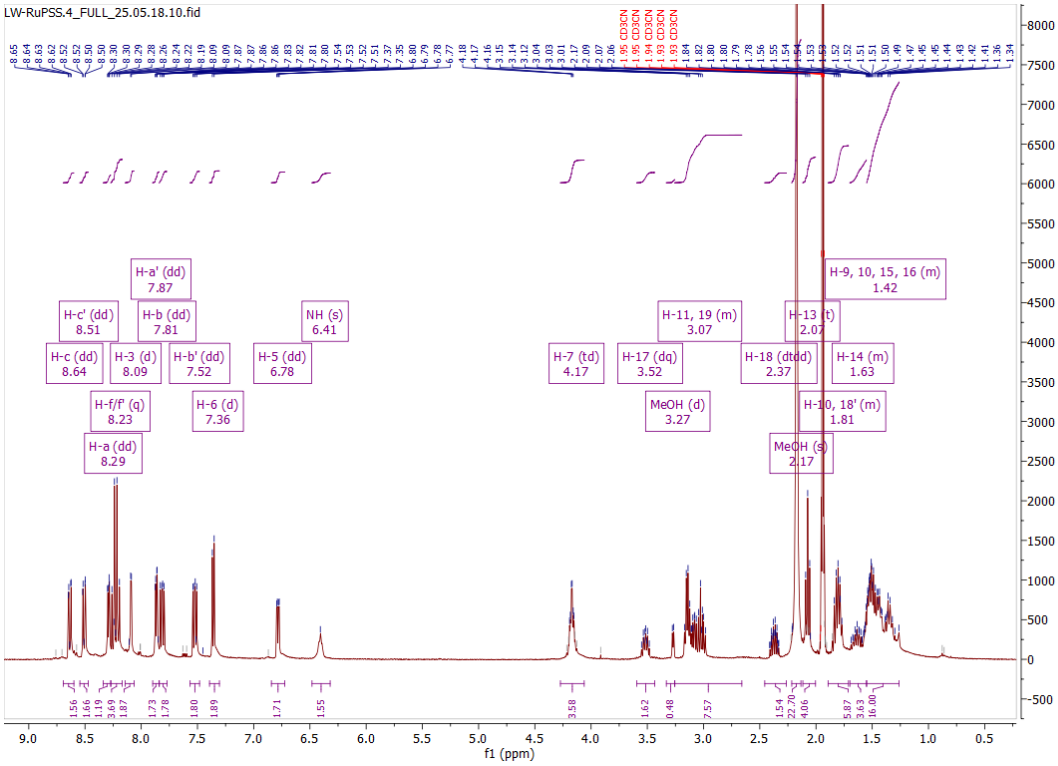

Figure 7.1.7.1. ^{1}H NMR of RuPhenSS in aerated CD3CN. (δ_3- CD_3CN).

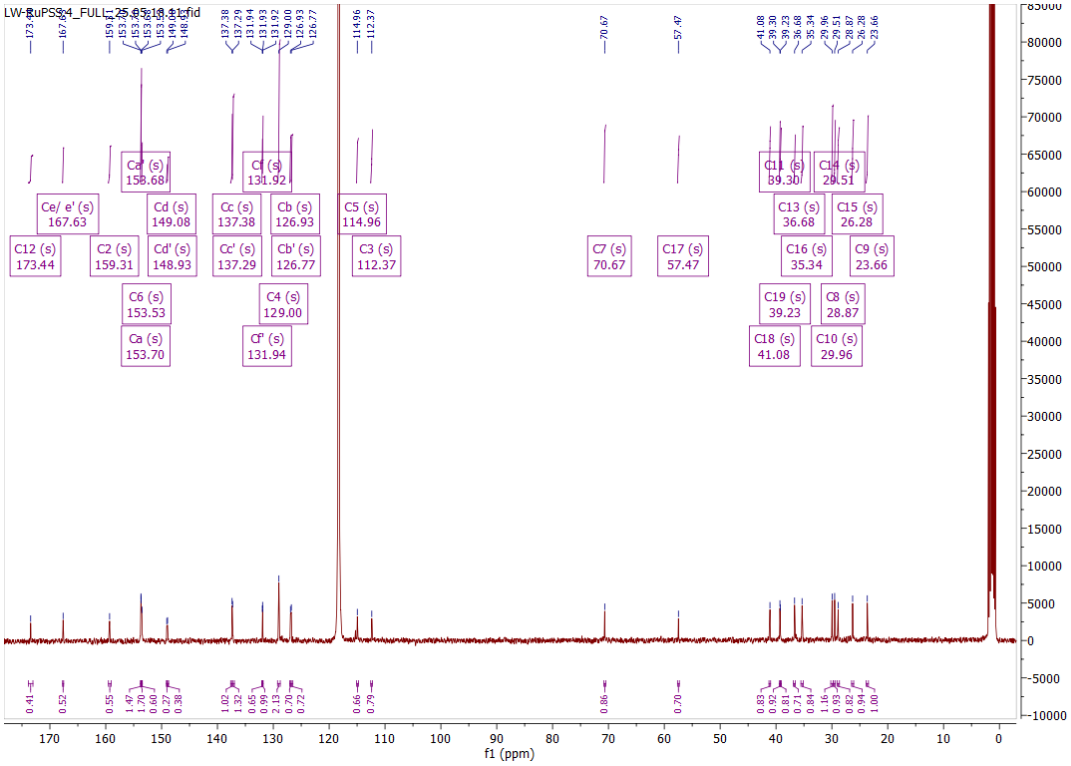

Figure 7.1.7.2. ^{13}C NMR of RuPhenSS in aerated CD_3CN. (δ_3- CD_3CN).

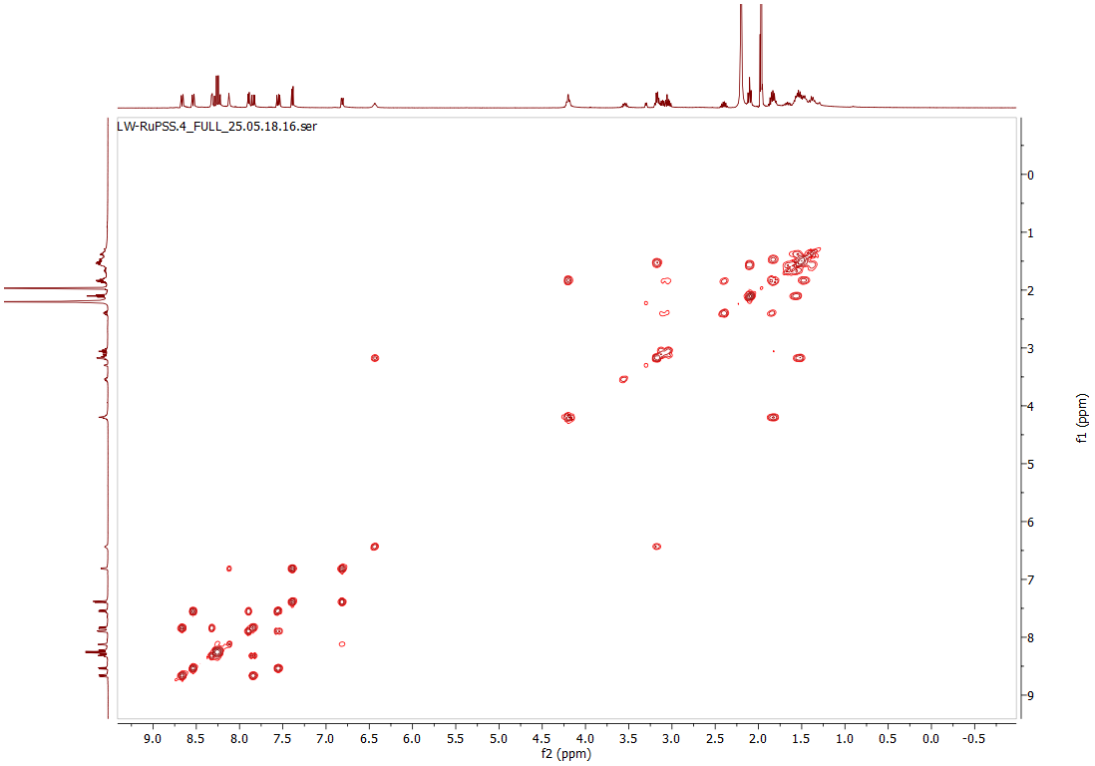

Figure 7.1.7.3. COSY spectrum of RuPhenSS in aerated CD_3CN. (δ_3- CD_3CN).

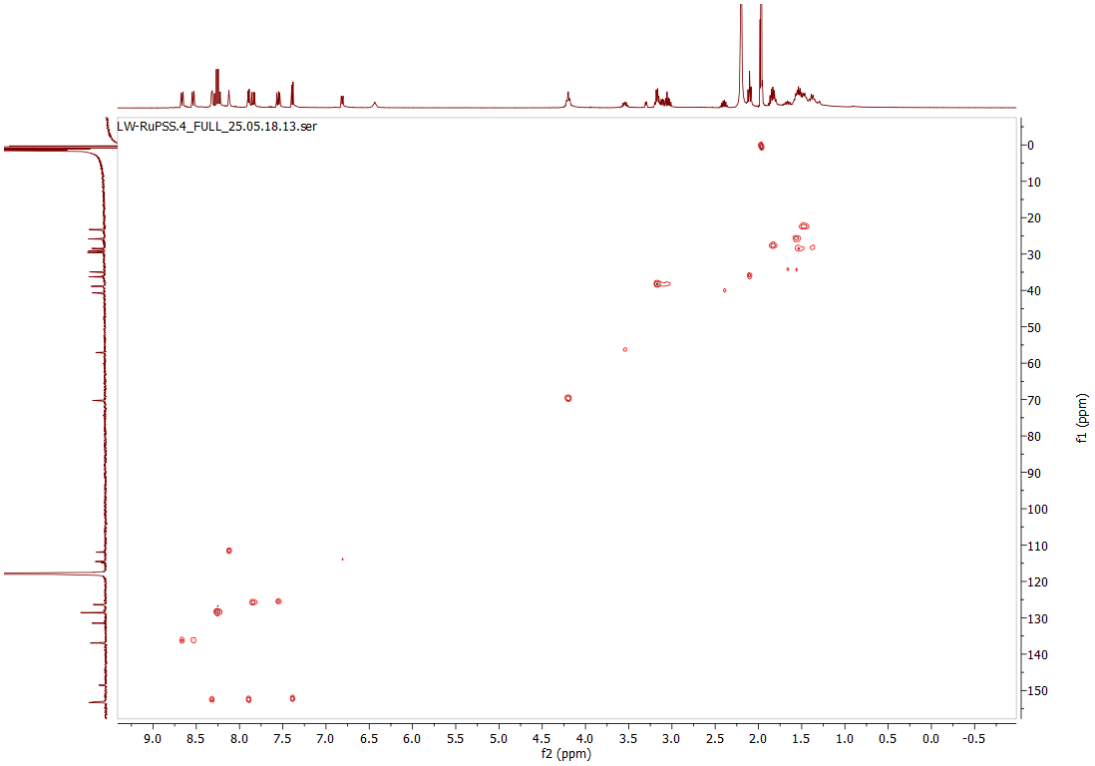

Figure 7.1.7.4. HSQC spectrum of RuPhenSS in aerated CD_3CN. (δ_3- CD_3CN).

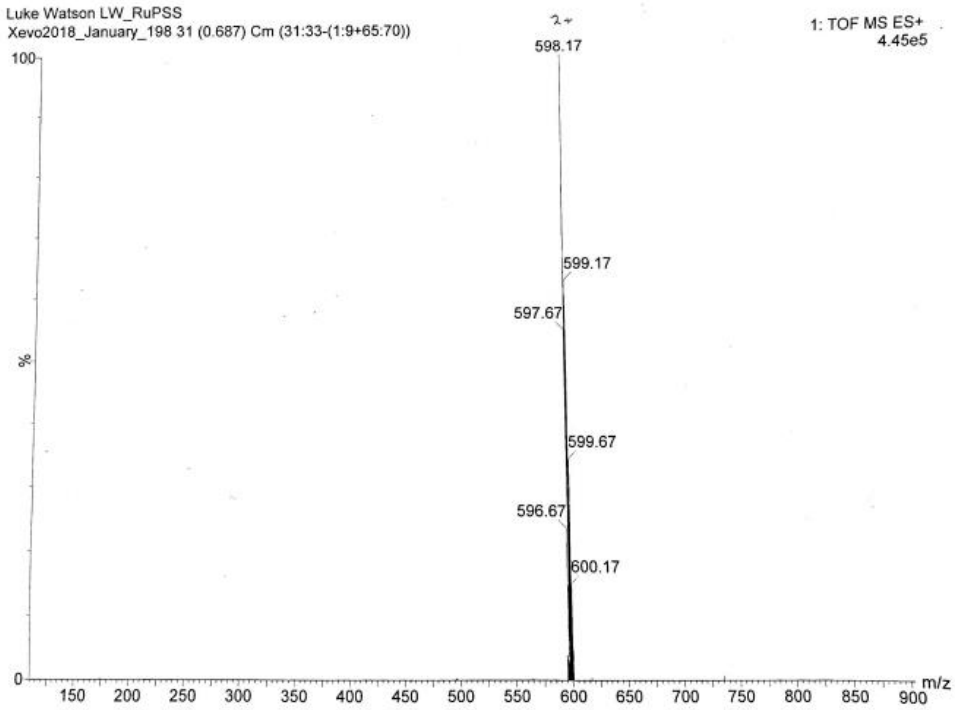

Figure 7.1.7.5. MS spectrum of RuPhenSS.

7.1.8 RuS8

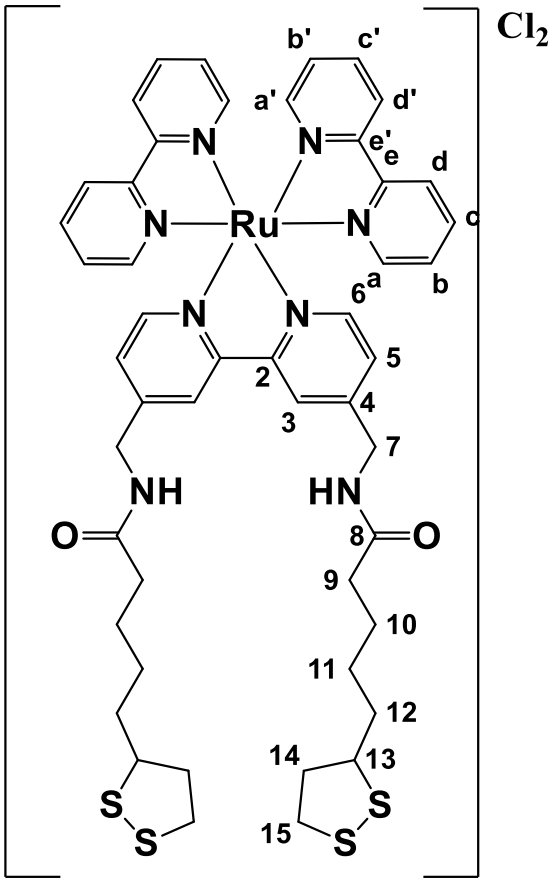
Cl2
b'
c'
a'
d'
N
N
e'
e
d
N
Ru
N
c
a
b
6
N
N
5
2
4
3
7
NH
HN
O
8
O
9
10
11
12
14
13
S
S
S
15
S

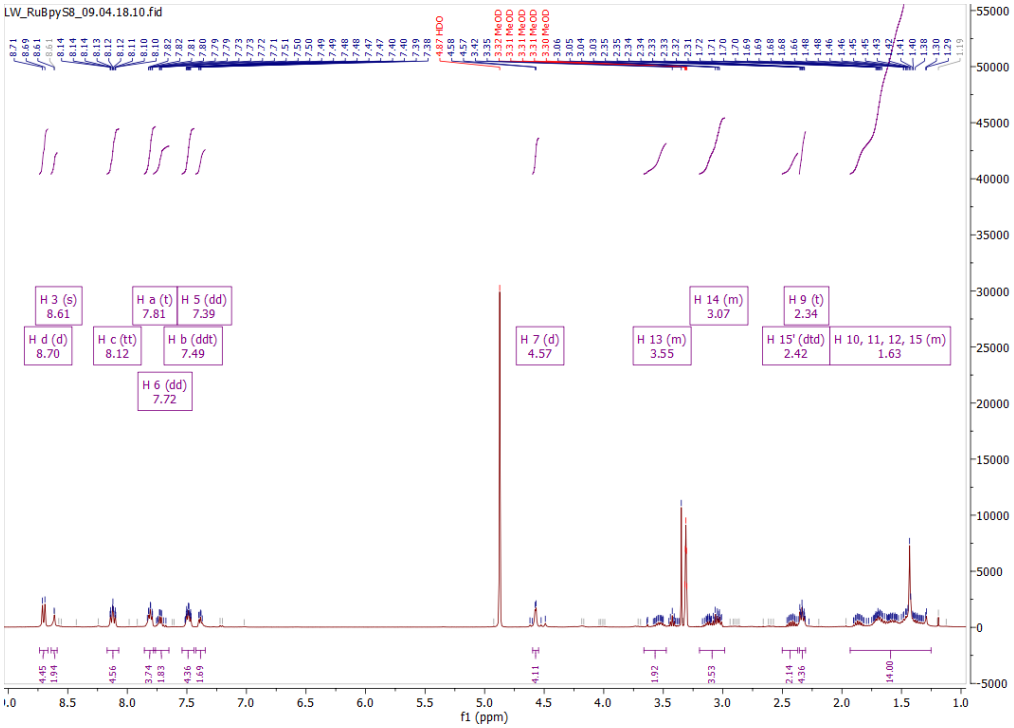

Figure 7.1.8.1. ^{1}H NMR of RuS8 in aerated MeOD. (δ- MeOD).

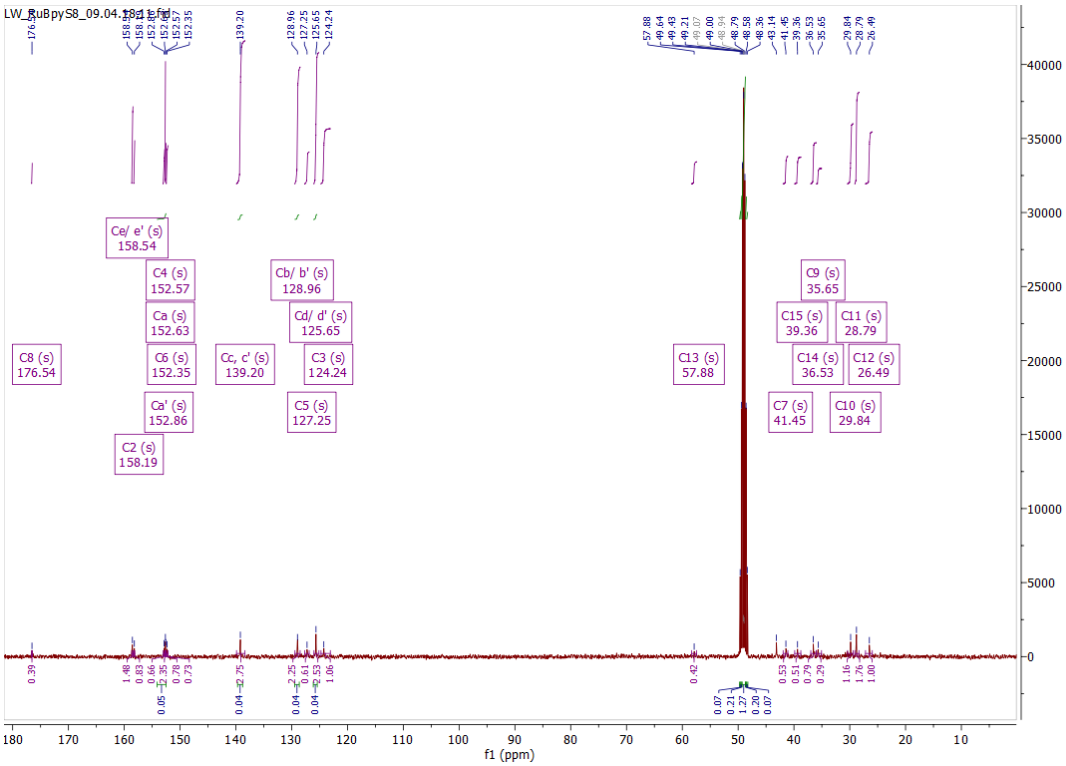

Figure 7.1.8.2. ^{13}C NMR of RuS8 in aerated MeOD. (δ- MeOD).

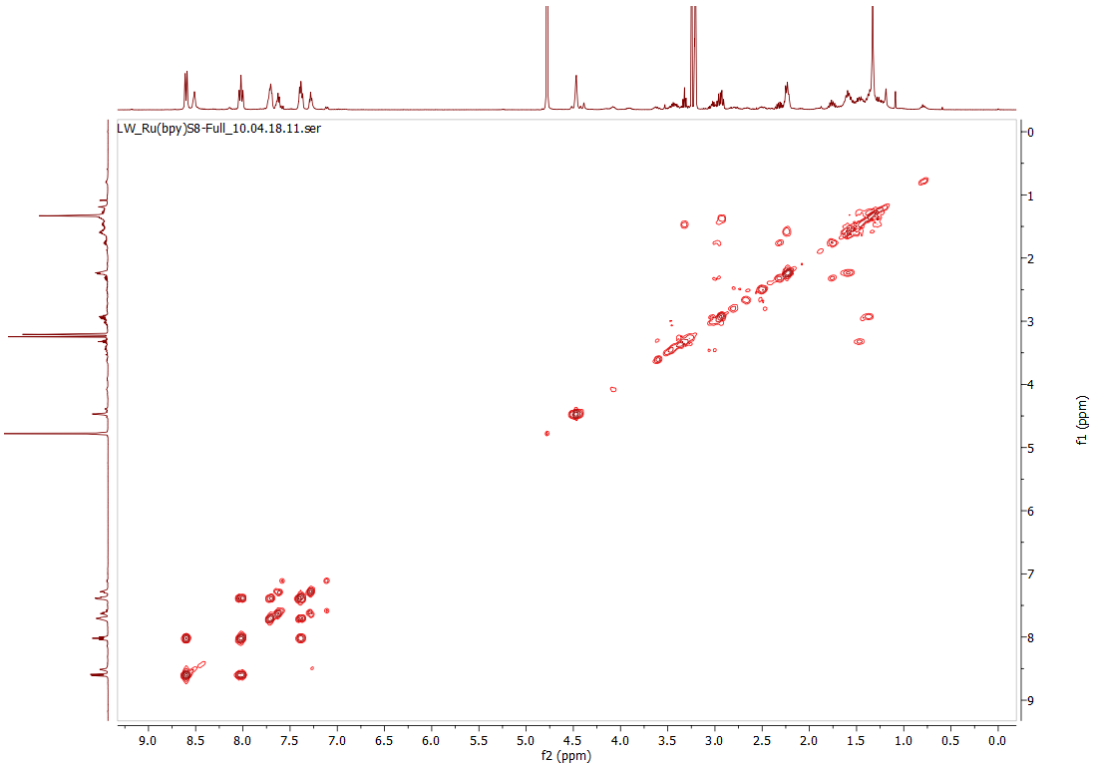

Figure 7.1.8.3. COSY spectrum of RuS8 in aerated MeOD. (δ- MeOD).

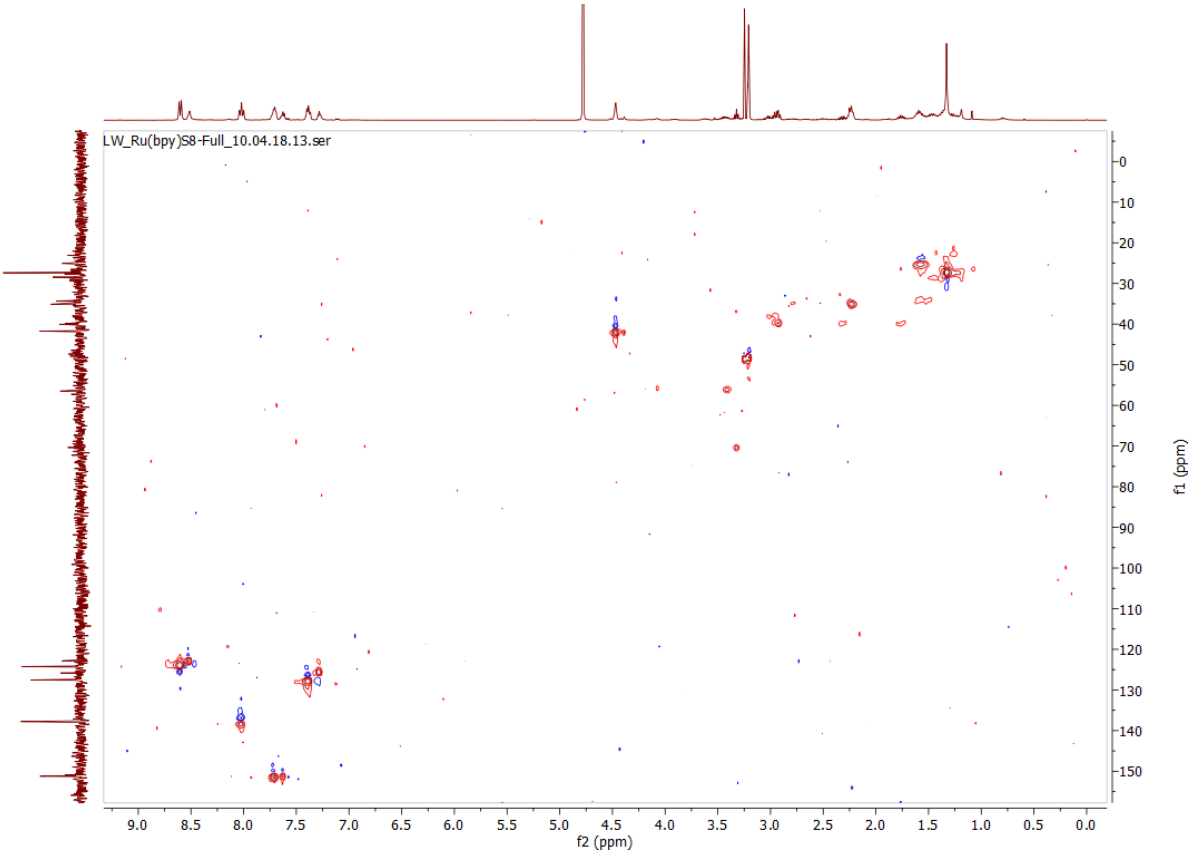

Figure 7.1.8.4. HSQC spectrum of RuS8 in aerated MeOD. (δ- MeOD).

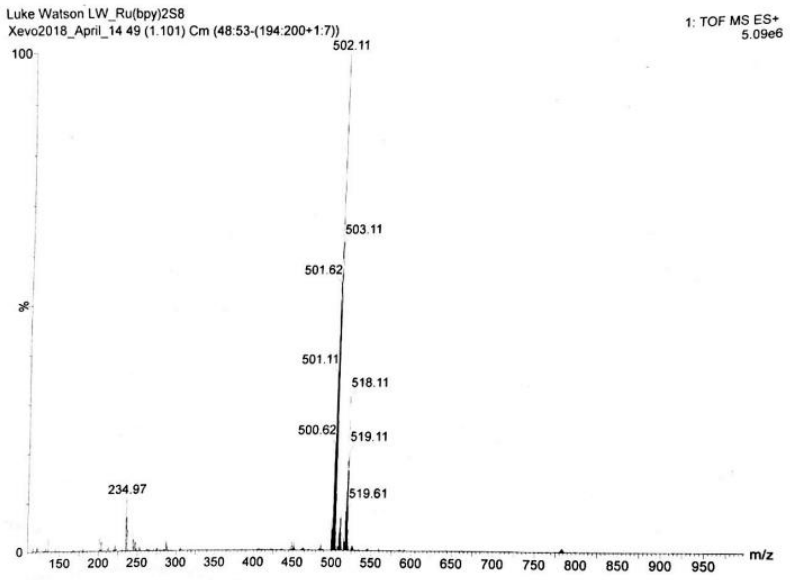

Figure 7.1.8.5. MS spectrum of RuS8.

7.1.9 OsPhenSS

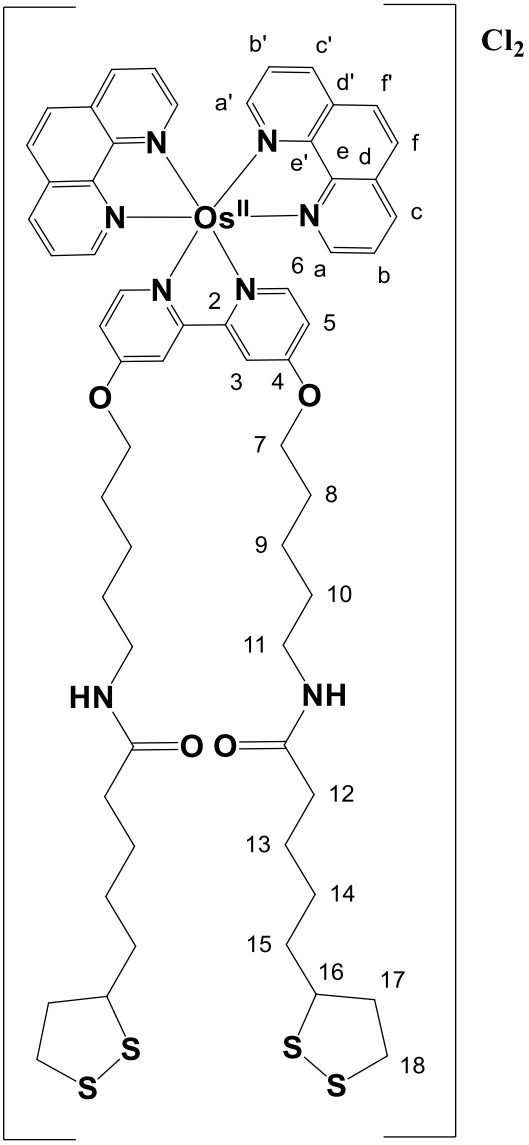

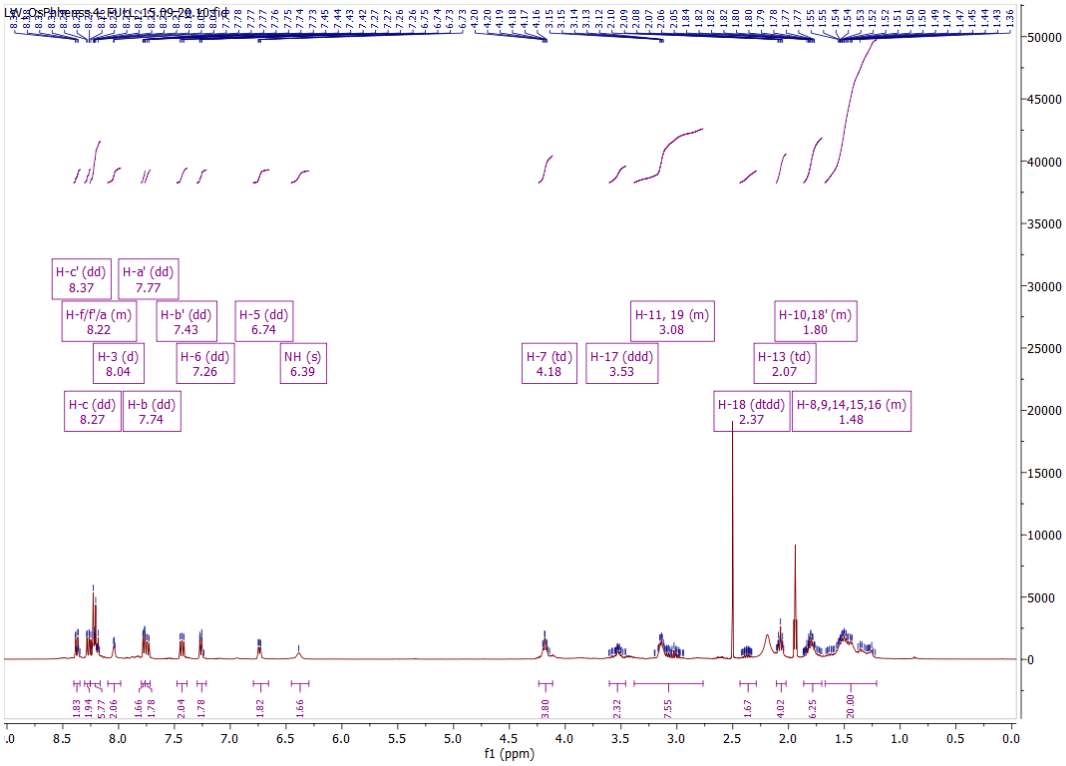

Figure 7.1.9.1. ^{1}H NMR in aerated MeCN. (δ_3- MeCN).

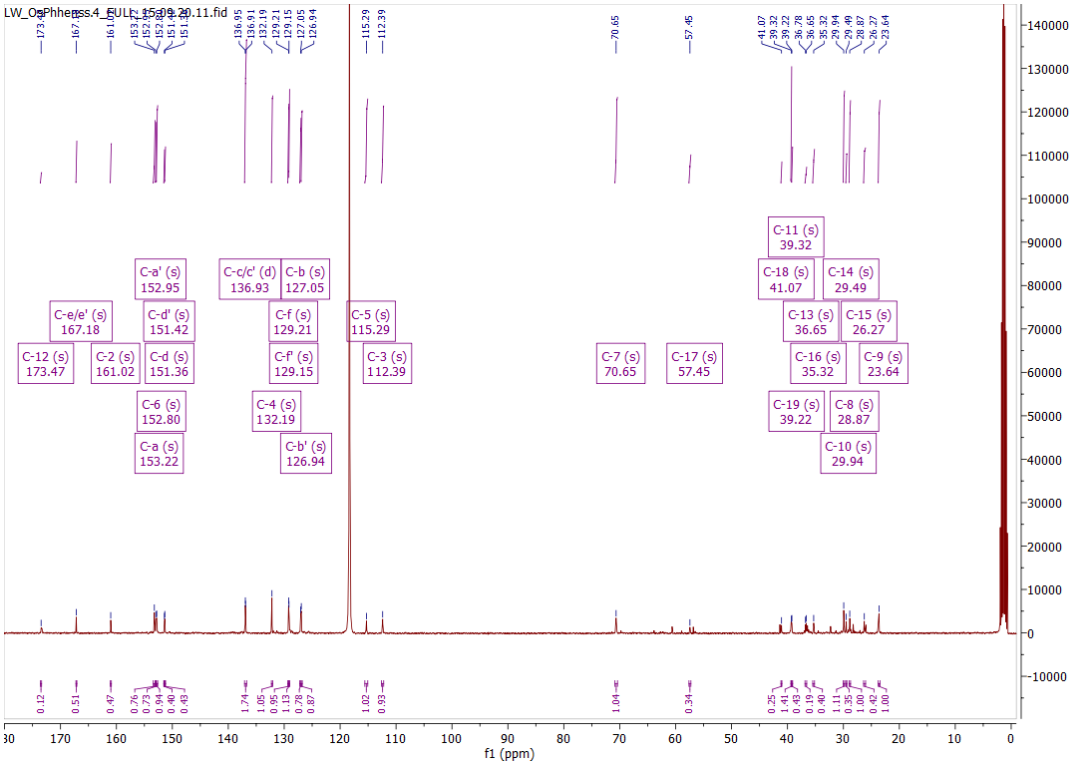

Figure 7.1.9.2. ^{13}C NMR in aerated MeCN. (δ_3- MeCN).

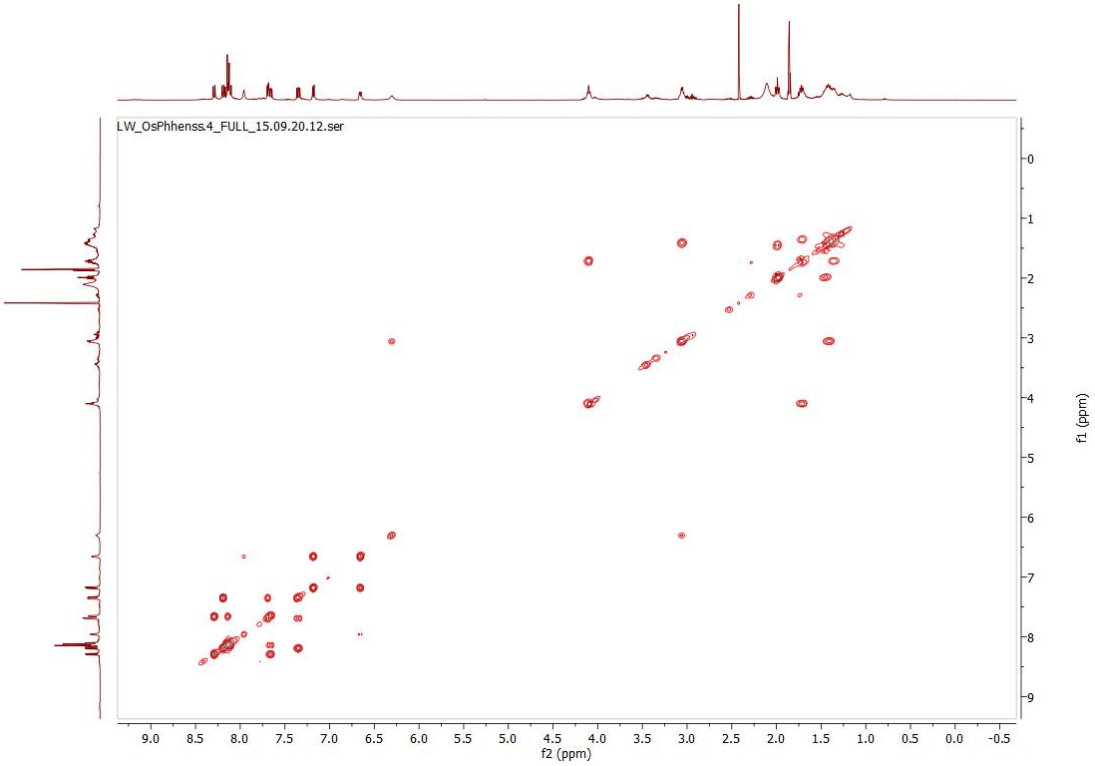

Figure 7.1.9.3. COSY spectrum of OsPhenSS in aerated MeCN. (δ_3- MeCN).

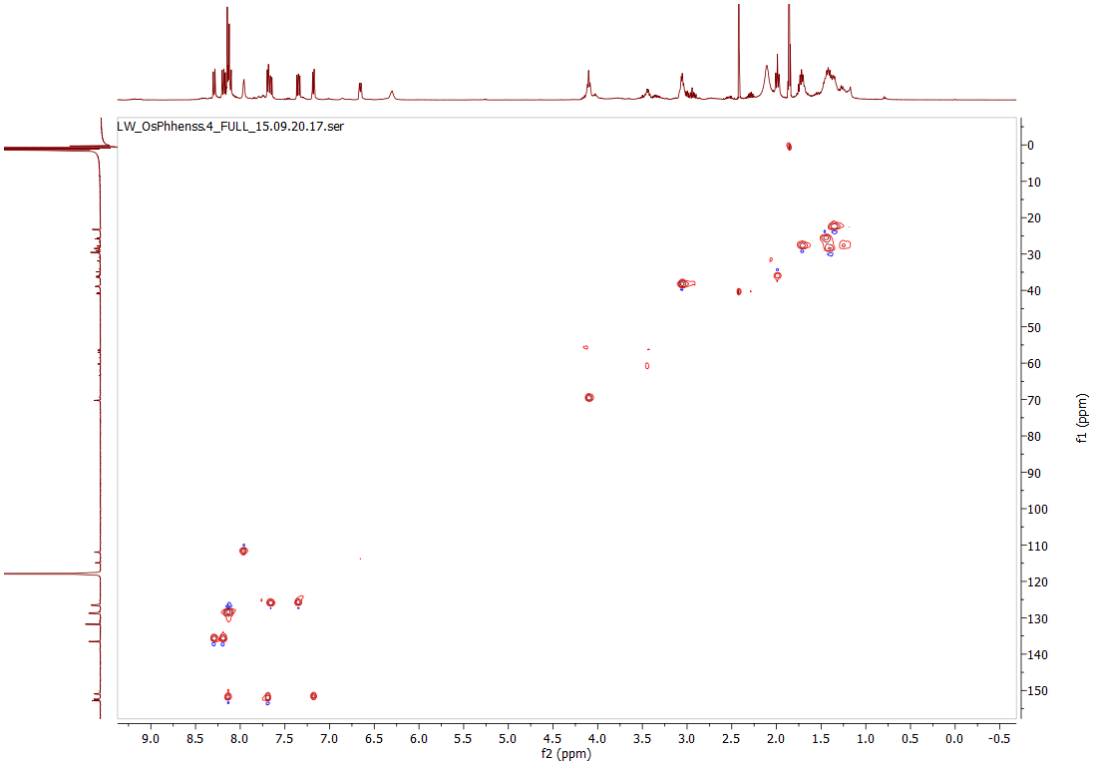

Figure 7.1.9.4. HSQC spectrum of OsPhenSS in aerated MeCN. (δ_3- MeCN).

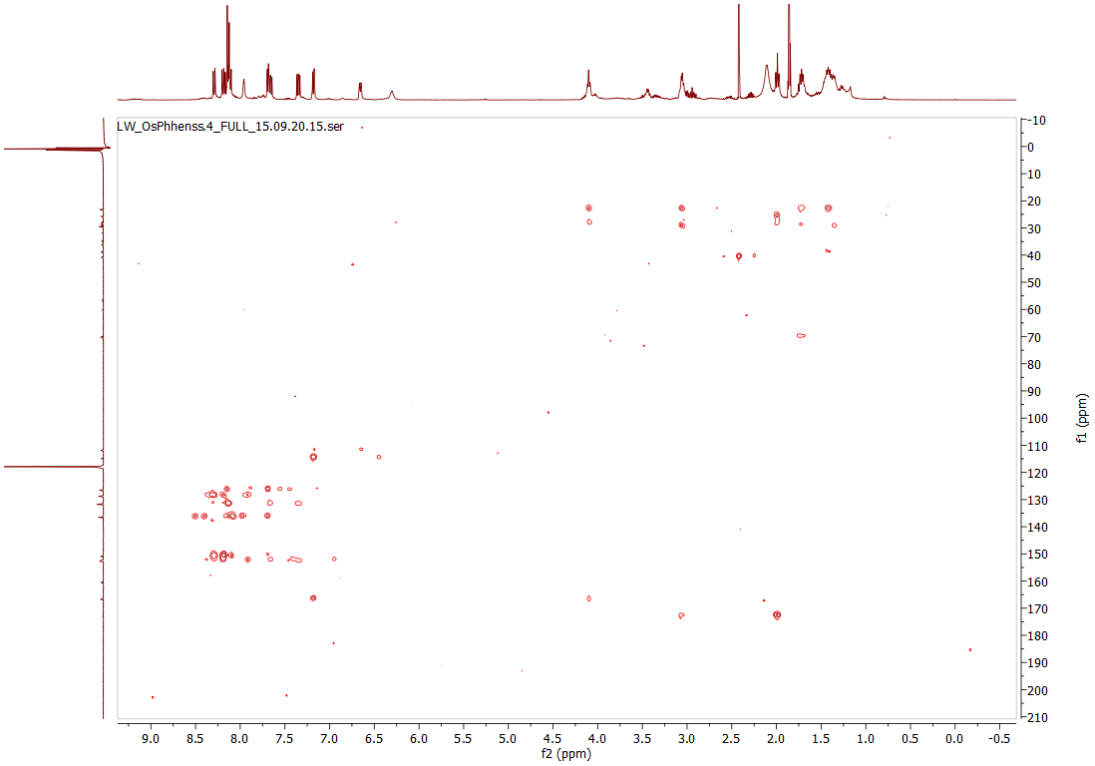

Figure 7.1.9.5. HMBC spectrum of OsPhenSS in aerated MeCN. (δ_3- MeCN).

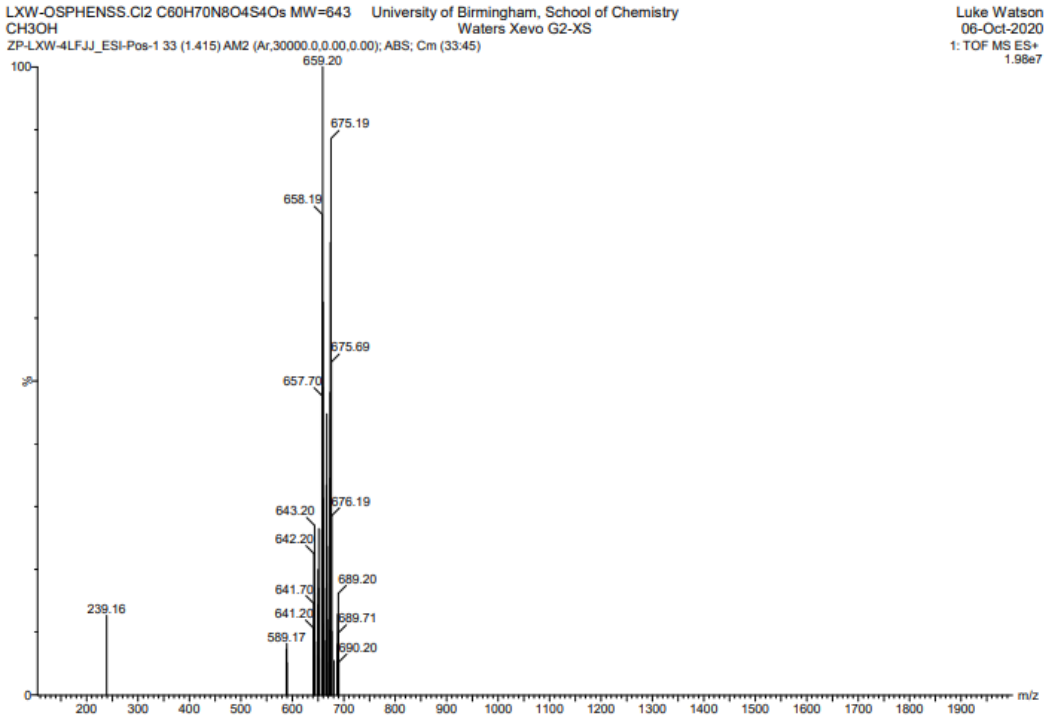

Figure 7.1.9.6. MS spectrum of OsPhenSS.

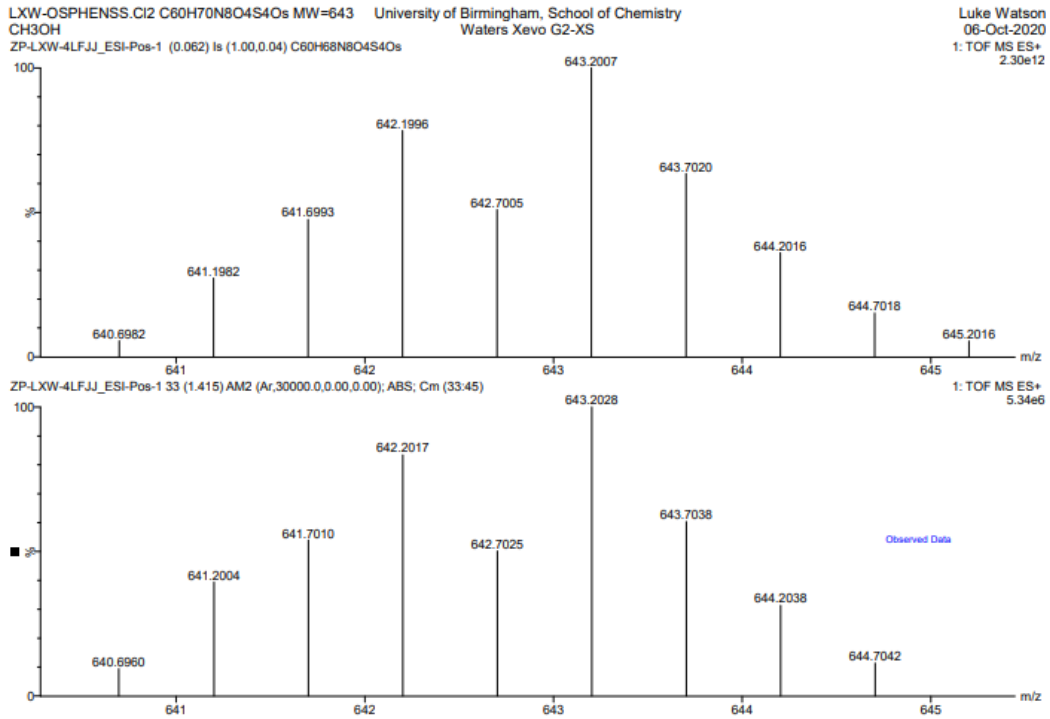

Figure 7.1.9.7. MS spectrum of OsPhenSS of theorectical mass vs experimental mass.

7.2 IR spectrum of ruthenium complexes

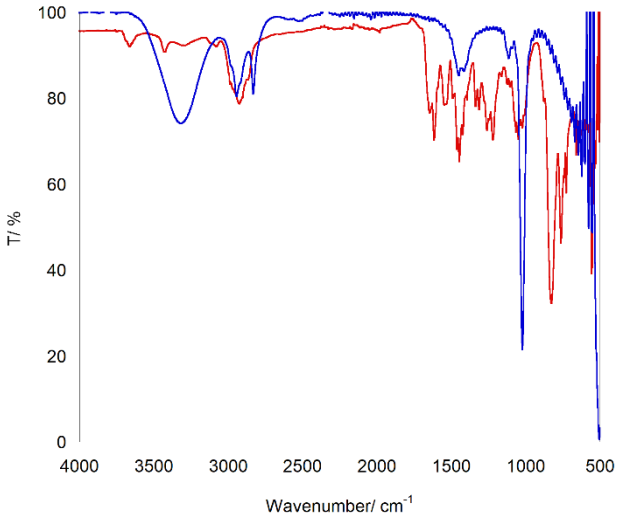

Figure 7.2.1. FTIR spectrum of RuBpySS of PF6 salt (red) and Cl salt (blue).

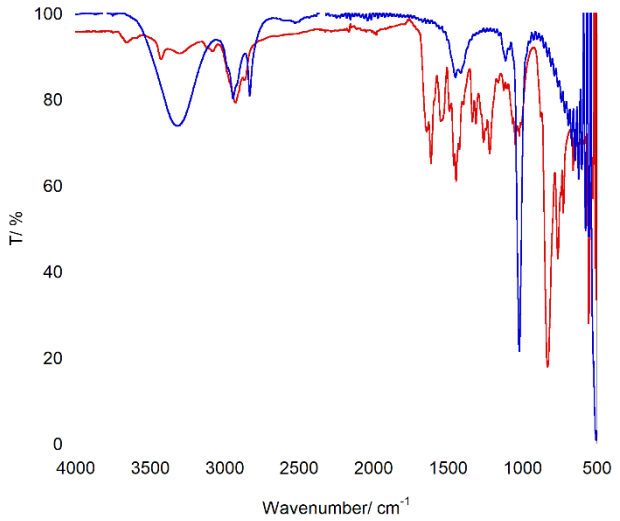

Figure 7.2.2. FTIR spectrum of RuPhenSS of PF6 salt (red) and Cl salt (blue).

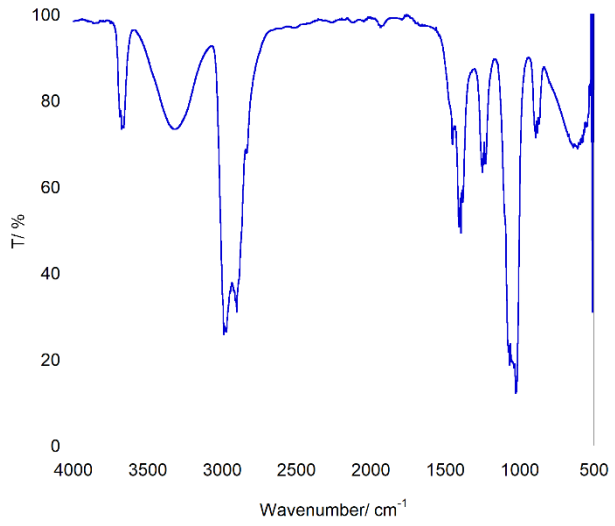

Figure 7.2.3. FTIR spectrum of RuS8 as Cl salt.

7.3 Luminescence lifetimes of ruthenium complexes (χ^2 values between 1.0 – 1.2)

7.3.1 RuBpySS (left), RuPhenSS (middle) and RuS8 (right) in aerated water

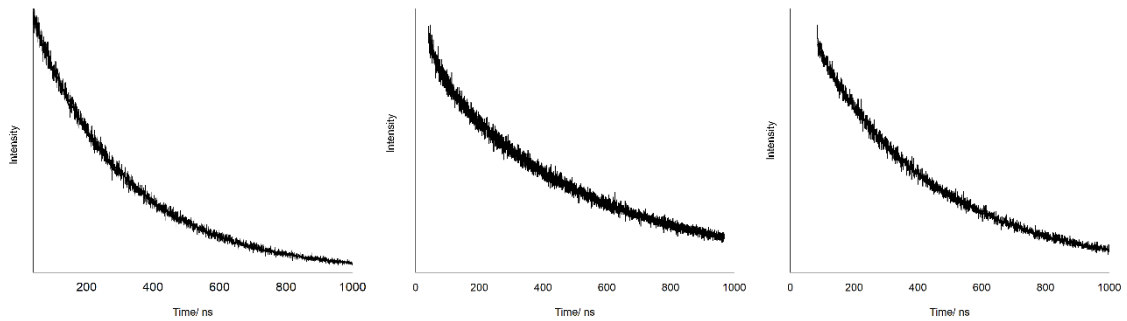

7.3.2 RuBpySS (left), RuPhenSS (middle) and RuS8 (right) in the presence of Zonyl FSA in aerated water

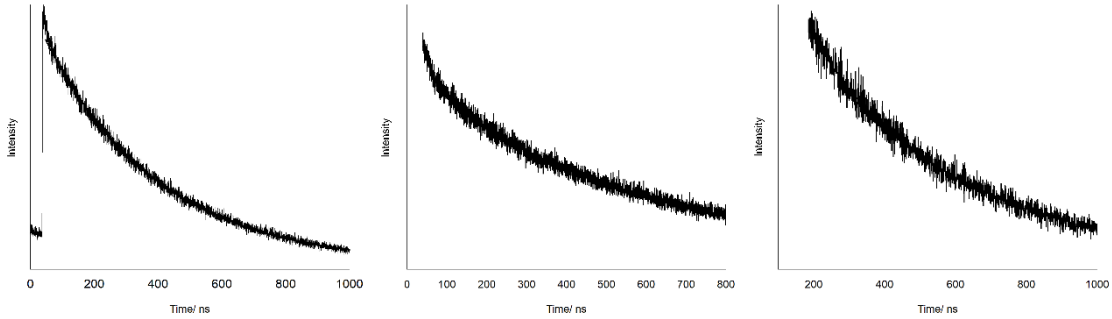

7.3.3 RuBpySS (left), RuPhenSS (middle) and RuS8 (right) on 13 nm gold nanoparticles in aerated water

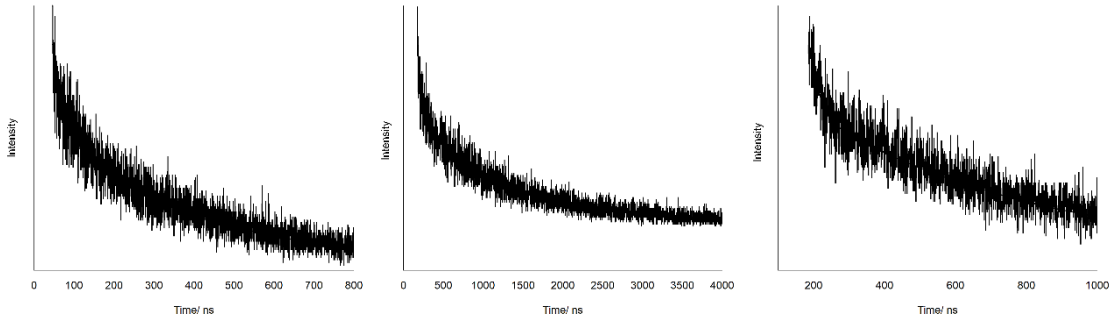

7.4 Hoescht 3368 staining of live A549 cells for RuPhenSS 13 nm and 25 nm gold nanoparticles

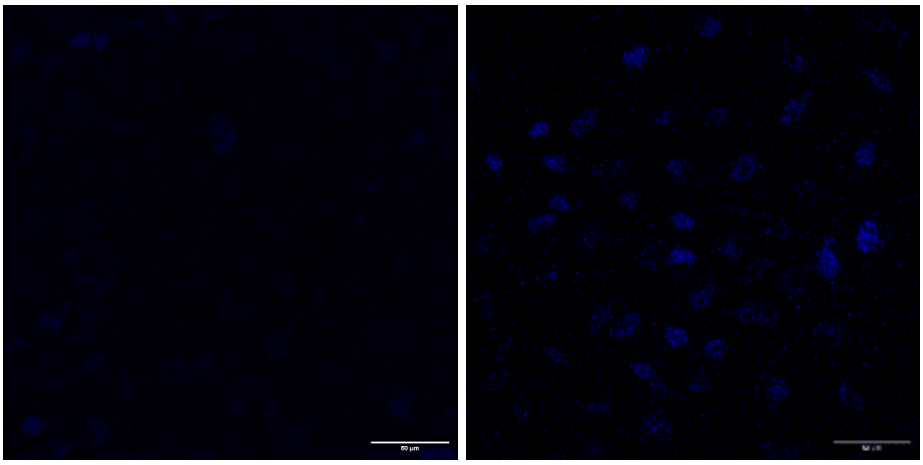

Figure 7.4.1. Hoescht 3368 staining of live A549 cells (λexc = 405 nm, λem = 420 – 460 nm) for 13 nm RuPhenSS gold nanoparticles (left) and RuPhenSS 25 nm gold nanoparticles (right).

7.5 Luminescence lifetimes of OsPhenSS (χ_2 values between 1.0 – 1.2)

7.5.1 Luminescence lifetime of OsPhenSS in aerated water

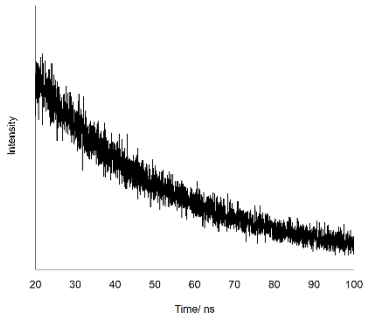

7.5.2 Luminescence lifetime of OsPhenSS in the presence of Zonyl in aerated water

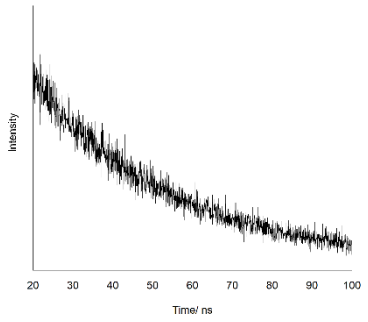

7.5.3 Luminescence lifetime of OsPhenSS on 13 nm gold nanoparticles in aerated water

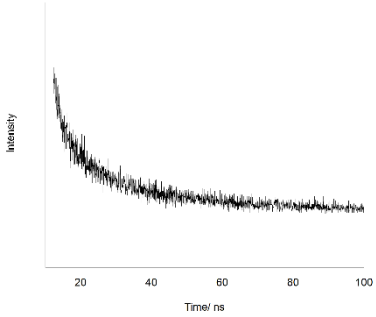

7.6 Z-stacks of RuPhenSS 25 nm gold nanoparticles in live A549 cells

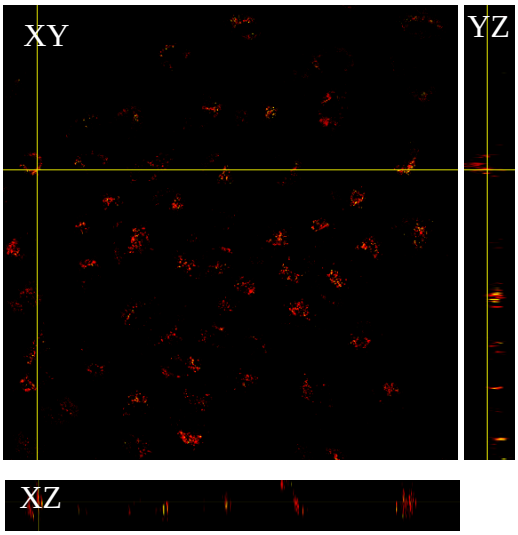

Figure 7.6.1. Orthogonal reconstruction of selected central plane from z-stack images of A549 cells showing ruthenium signal inside cells after incubation with 0.2 nM RuPhenSS•Z•AuNP25 for 18 hours at 37°C. Red channel, ruthenium emission (λ_{exc} = 488 nm, λ_{em} = 500 – 800 nm); Yellow channel, Reflectance emission (λ_{exc} = 633 nm, λ_{em} = 620 – 640 nm).

7.7 Z-stacks of OsPhenSS 25 nm gold nanoparticles in live A549 cells

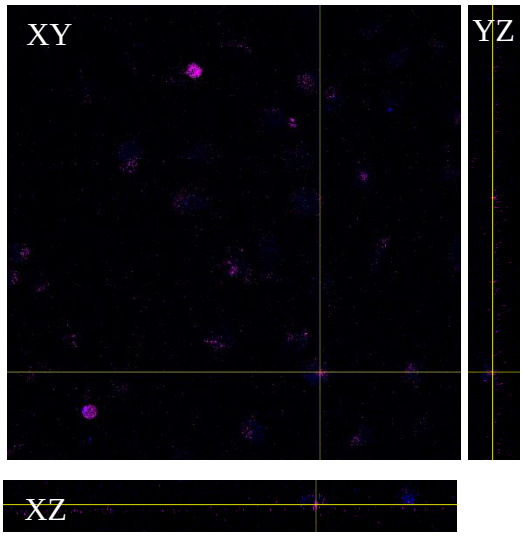

Figure 7.7.1. Orthogonal reconstruction of selected central plane from z-stack images of A549 cells showing osmium signal inside cells after incubation with 0.2 nM OsPhenSS•Z•AuNP25 for 18 hours at 37°C. Purple channel, osmium emission (λ_{exc} = 488 nm, λ_{em} = 650 – 800 nm); Blue channel, Hoescht emission (λ_{exc} = 402 nm, λ_{em} 420−470 nm)(

7.8 Fixed cell images of OsPhenSS 25 nm gold nanoparticles in A549

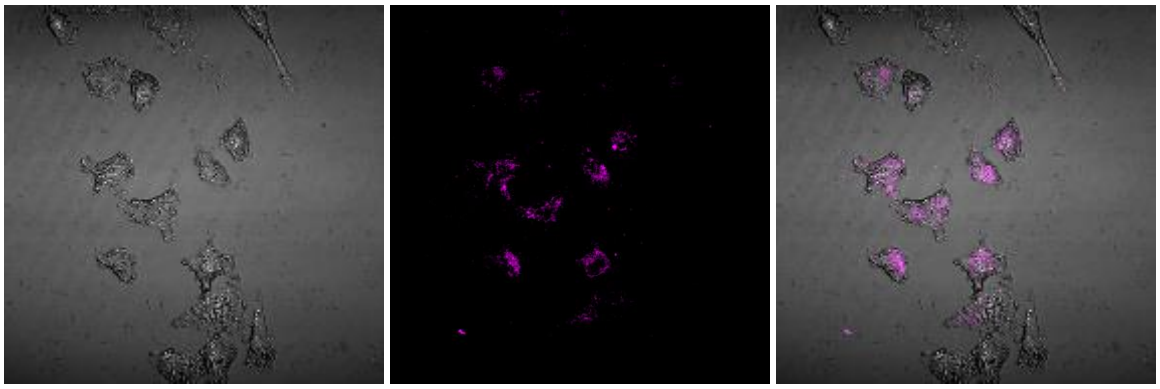

Figure 7.8.1. Confocal microscopy of gold nanoparticles in fixed A549 cells treated with 0.2 nM OsPhen.AuNP25 at 4 hours. Brightfield (left); Purple channel, OsPhen.AuNP25 emission (λexc = 488 nm, λem 650−800 nm) (middle) and overlap of brightfield and osmium emission (right).

7.9 Confocal images of RuPhenSS•PEG•AuNP and RuPhenSS•RXB•AuNP on OCI-LY3 cytospins

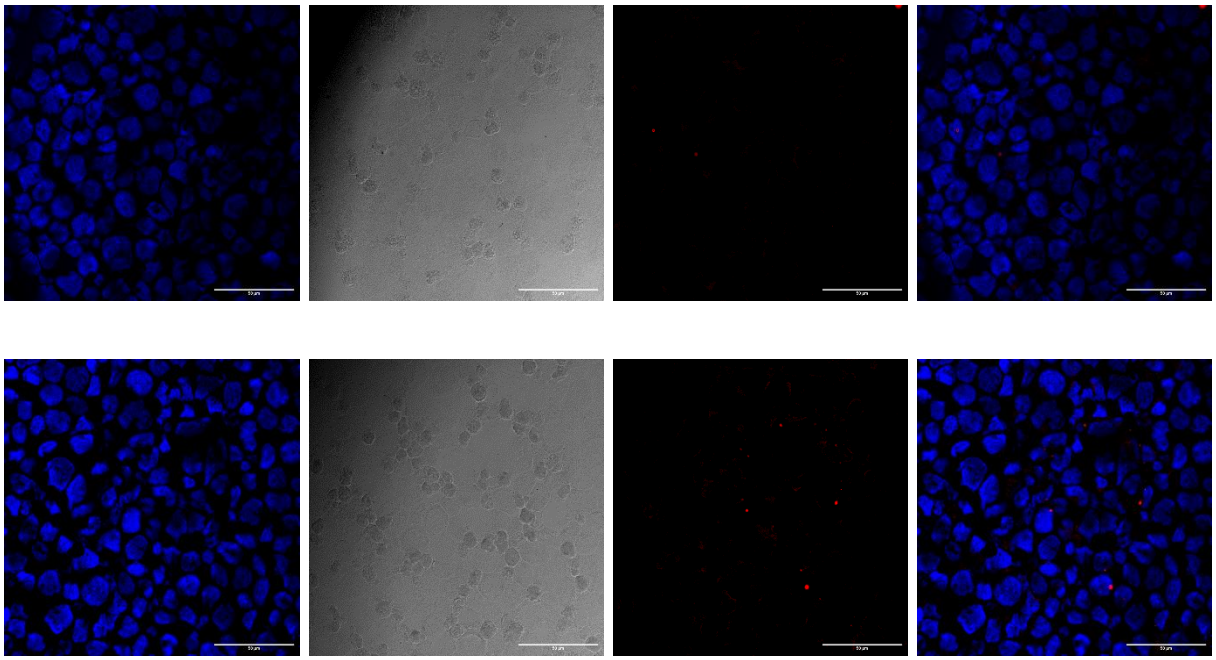

Figure 7.9.1. Confocal microscopy of particles in fixed OCI-LY3 cells from cytospins treated with 3 nM RuPhen.AuNP13 (Top) and 3 nM RuPhen-RXB-AuNP13 (Bottom) at 16 hours. Blue channel: DAPI emission (λexc = 405 nm, λem 415−460 nm) (A), Brightfield (B); Red channel: Ruthenium emission (λ_{exc} = 488 nm, λ_{em} 580−780 nm) (C), overlap of A and C (D). Scale bar = 50µm.

7.10 Images of H&E stained tonsil tissue

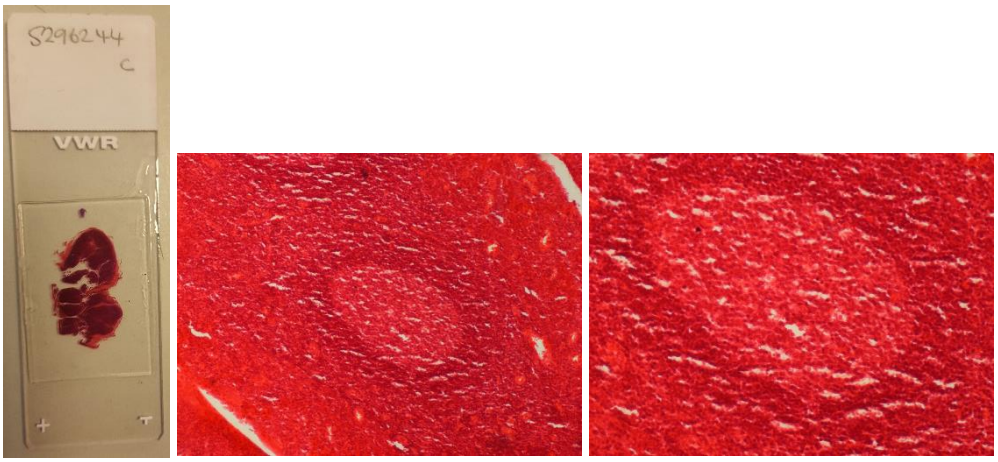

Figure 7.10.1. Image of H&E stained tonsil tissue slide (left), microscope image of H&E stained tonsil tissue showing germinal center at 10x (middle) and 20x (right) magnification.

7.11 Images of RuPhenSS•PEG•AuNP and RuPhenSS•RXB•AuNP after MSI

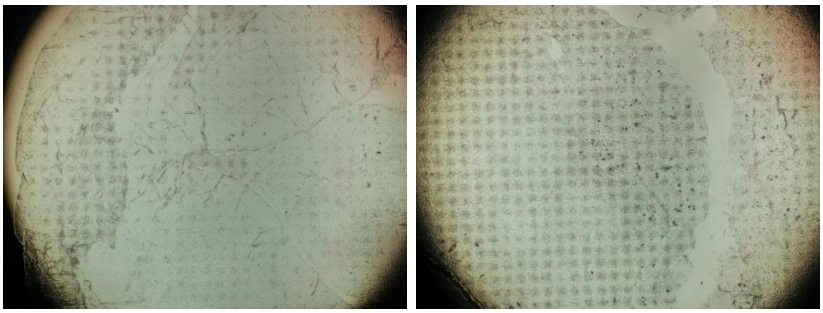

Figure 7.11.1. Microscope images post MSI of RuPhenSS•RXB•AuNP (left) and RuPhenSS•PEG•AuNP (right) showing tissue damage from rastering of laser.

7.12 Gold nanoparticle concentration calculation from UV-Vis

Rearranging the Beer-Lambert law and using the equation in 1 mL of particles gives:

$$c = \frac{A_{450}}{\varepsilon_{450}}$$

Where c is concentration, A_{450} is the absorbance value at 450 nm and ε_{450} is the molar extinction coefficient at 450 nm can yield an approximate concentration of gold nanoparticles.

7.13 Conferences and papers

Conferences:

2017 – Eurobic conference, Birmingham, UK, poster presentation "Nanoparticles for Targeting Cancer Tissue: Detection and Imaging"

2019 – PhotoUKIT conference, Lipari, Italy, poster presentation, "Luminescent Gold Nanoparticles Based on Transition Metals for Imaging"

Papers:

2021, JACS Au "Quantification by Luminescence Tracking of Red Emissive Gold Nanoparticles in Cells"